Physik-Department
Technische Universität München
Theoretische Physik

Spatiotemporal Adaptation in the Corticogeniculate Loop

Ulrich Hillenbrand

Vollständiger Abdruck der von der Fakultät für Physik der Technischen Universität München zur Erlangung des akademischen Grades eines

Doktors der Naturwissenschaften

genehmigten Dissertation.

Vorsitzender:		Univ.-Prof. Dr. M. Kleber
Prüfer der Dissertation:	1.	Univ.-Prof. Dr. J. L. van Hemmen
	2.	Univ.-Prof. Dr. E. Sackmann

Die Dissertation wurde am 29.02.2000 bei der Technischen Universität München eingereicht und durch die Fakultät für Physik am 16.01.2001 angenommen.

Acknowledgments

It is my pleasure to thank Professor Dr. J. Leo van Hemmen for cultivating an environment at his institute for creative exploration and growth of new ideas. Open-mindedness and, at the same time, a strong sense for scientific value are of particular importance and delicacy in a field at the interface between empirical biological diversity and mathematical rigor. Leo van Hemmen combines both in his attitude and has always promoted the according style of work.

Moreover, I like to thank the individuals who populated this environment. They always were supportive in that each one of them showed sincere interest in the other's scientific concerns. More subtilely, the distinguished sense of humor that we shared helped to overcome one or the other tense period.

I am especially indebted to those of my colleagues who spent a significant amount of their time on maintaining our local computer network, most notably Armin Bartsch, Moritz Franosch, and Oliver Wenisch. Without their kind support, things would have got stuck in computer trouble more than once.

Special thanks also go to Dr. Thomas Jestädt. As a decent friend, he took some pains to comment on the manuscript from the valuable perspective of the intelligent non-specialist.

I thank the Deutsche Forschungsgemeinschaft (DFG) for funding my work for its largest part (grant GRK 267), and my colleagues at the Graduiertenkolleg "Sensorische Interaktion in biologischen und technischen Systemen" for interesting discussions and insights into various methods for studying the brain.

Especially insightful was a visit to PD Dr. Esther Peterhans at the University of Zurich. I very much appreciate several discussions on experimental data and on ideas about visual motion processing.

At times it could be hard to tolerate life with a scientist, and perhaps the doctoral-researcher type is the worst company for every-day life. My wife must know about it. After all, emotion is more important than visual motion, and I am very grateful for Ania's patience and understanding during the period of my doctoral work.

Life as a doctoral researcher, very unfortunately, is rarely blessed with economic prosperity. I owe special thanks to my parents who, when times got tough, offered plentiful support both morally and materially, far beyond what one could expect from parents.

Abstract

The thalamus is the major gate to the cortex for almost all sensory signals, for input from various subcortical sources such as the cerebellum and the mammillary bodies, and for reentrant cortical information. Thalamic nuclei do not merely relay information to the cortex but perform some operation on it while being modulated by various transmitter systems and in continuous interplay with their cortical target areas. Indeed, cortical feedback to the thalamus is the anatomically dominant input to relay cells even in those thalamic nuclei that are directly driven by sensory systems. While it is well-established that the receptive fields of cortical neurons are strongly influenced by convergent thalamic inputs of different types, the modulation effected by cortical feedback in thalamic response has been difficult to interpret. Experiments and theoretical considerations have pointed to a variety of operations of the visual cortex on the visual thalamus, the lateral geniculate nucleus (LGN), such as control of binocular disparity for stereopsis (Schmielau & Singer, 1977), attention-related gating of relay cells (Sherman & Koch, 1986), gain control of relay cells (Koch, 1987), synchronizing firing of neighboring relay cells (Sillito et al., 1994; Singer, 1994), increasing visual information in relay cells' output (McClurkin et al., 1994), and switching relay cells from a detection to an analyzing mode (Godwin et al., 1996; Sherman, 1996; Sherman & Guillery, 1996). Nonetheless, the evidence for any particular function is still sparse and rather indirect to date.

Clearly, detailed concepts of the interdependency of thalamic and cortical operation could greatly advance our knowledge about complex sensory, and ultimately cognitive, processing. Here we present a novel view on the corticothalamic puzzle by proposing that *control of velocity tuning of visual cortical neurons* may be an eminent function of corticogeniculate processing.

The hypothesis is advanced by studying a model of the primary visual pathway in extensive computer simulations. At the heart of the model is a biophysical account of the electrical membrane properties of thalamic relay neurons (Huguenard & McCormick, 1992; McCormick & Huguenard, 1992) that includes 12 ionic conductances. Among the different effects that corticogeniculate feedback may have on relay cells, we focus on the modulation of their relay mode (between tonic and burst mode) by control of their resting membrane potential. Employing two distinct temporal-response types of geniculate relay neurons (lagged and nonlagged), we find that shifts in membrane potential affect the temporal response properties of relay cells in a way that alters the tuning of cortical cells for speed.

Given the loop of information from the LGN to cortical layer 4, via a variable number of synapses to layer 6, and back to the LGN, the question arises, what are likely implications of adaptive speed tuning for visual information processing? Based on some fairly general considerations concerning the nature of motion information, we devise a simple model of the corticogeniculate loop that utilizes adaptive speed tuning for the fundamental task of *segmentation* of objects in *motion*. A detailed mathematical analysis of the model's behavior is presented. Treating visual stimulation as a stochastic process that drives the adaptation dynamics, we prove the model's object-segmentation capabilities and reveal some non-intended properties, such as oscillatory responses, that are consequences of its basic design. Several aspects of the dynamics in the loop are discussed in relation to experimental data.

Contents

Chapter 1

The Thalamus

The dorsal thalamus, which forms the main mass of the diencephalon in most mammals, is the principal source of subcortical input to the cerebral cortex, and all that the cortex can do necessarily depends on this input. By way of the dorsal thalamus the cortex is informed of all sensory input, with the olfactory system as the only exception, and of activity in subcortical brain structures such as the cerebellum, the mammillary bodies, and the globus pallidus; see Jones (1985) for a summary. It is thus most evident that uncovering the relay functions of the dorsal thalamus is crucial for a deeper understanding of all sensory and cognitive processing.

In contrast to the prominent position of the thalamus in the central nervous system and the complexity of thalamic circuitry, the common, simplistic, understanding of the dorsal thalamus had been for a long time that of a faithful relay of all incoming signals to the cortex, without much processing or elaboration. It was concluded from early and more recent studies of the lateral geniculate nucleus, the part of the thalamus that relays visual information from the retina to the cortex, that the spatial characteristics of receptive fields are essentially unchanged at the retinogeniculate synapse. Those of geniculate relay cells are very similar to those of the retinal ganglion cells that provide their input (Glees & Clark, 1941; Hubel & Wiesel, 1961; Hoffmann et al., 1972). This disappointing finding was summarized by Zeki (1993): “the . . . minutely studied lateral geniculate nucleus has told us very little that is of interest about vision as a process, beyond the vague statement that it may act as a ‘sharpener’ of the visual image, a surprisingly banal function for so large and complex a structure.”

In the last decades, a rich thalamocortical network of two-way connections has been revealed and modulation of thalamic activity by inputs from the cortex, the brainstem, and the basal forebrain utilizing various transmitter systems has been identified. Furthermore, the intrinsic dynamics of thalamic relay cells and interneurons has been understood in terms of various transmembrane currents; see McCormick (1992), Guillery (1995), and Sherman & Guillery (1996) for reviews. The general pattern of thalamic activity has been shown to be related to states of arousal, wakefulness, and sleep (Livingstone & Hubel, 1981; McCarley et al., 1983; Steriade & McCarley, 1990; Steriade, 1992; Steriade et al., 1993; Steriade & Contreras, 1995). Finally, the involvement of thalamic circuits in the production of epilepsy has been suggested (Steriade & Llinás, 1988; McCormick & Feeser, 1990; Huguenard & McCormick, 1992; Steriade, 1992; Steriade et al., 1993; Huguenard & Prince, 1994; Steriade & Contreras, 1995). Despite a wealth of information on transmitters and synaptic circuits, however, it has not yet been possible to convincingly define a function, or a set of functions, for thalamocortical relay, let alone for the complex thalamocortical interplay, in the normal, awake, behaving animal. Nonetheless, in view of the complexity of the thalamocortical network one is compelled to believe that the thalamus not merely *delivers* information to the cortex but that cortical processing is somehow *entangled* with thalamic processing. Accordingly, it seems that cortical function cannot be properly understood without a clear concept of thalamic operation.

In section 1.1, we briefly outline the thalamocortical network in order to provide the more general context in which the geniculocortical system is embedded that we are going to study in this work. A summary of results on temporal response properties of thalamic relay cells that will be relevant in this study is given in section 1.2. We conclude this chapter in section 1.3 with some speculation on the function of the thalamocortical system from the literature. We also briefly outline the ideas pursued in the present work in relation to earlier functional considerations.

Most details on thalamic neurons and thalamocortical circuits that we review below and on which our modeling will be based refer to the cat's lateral geniculate nucleus, as this is the best-studied thalamic nucleus, and because vision is the sensory modality that will occupy us in the following chapters. It is often not known to what extent details observed for one specific nucleus generalize to other nuclei and species. In some cases it is evident that there are in fact internuclei and -species differences in thalamocortical circuitry. The basic outline and structural principles, however, are thought to be the same in different parts of the thalamocortical system and for different mammals.

1.1 A Hierarchy of Thalamocortical Processing

Facts about the thalamocortical system compiled in this section are collected from several reviews (Sherman & Koch, 1990; Guillery, 1995; Sherman, 1996; Sherman & Guillery, 1996). The reader is referred to these excellent reviews and to the extensive literature cited therein for more detailed information. Facts that specifically relate to the visual system and that are only briefly touched upon in this section are further elaborated in the next chapter.

Not all of what is outlined here is firmly established, and we will be accordingly careful with claims where appropriate. Generally, when emphasizing a certain structure or organizational principle in a biological system, especially the brain, one always has to be aware of the deviations that are gracefully neglected for the sake of highlighting that particular aspect of the system. This neglect is certainly permissible, if the highlighted aspect has the potential to explain the system's behavior and shed light on its function. After all, there is no understanding without the interpretation of empirical data as manifestations of underlying structures.

Throughout this work, when speaking of the 'thalamus' we really refer to the dorsal thalamus, i.e., the part of the thalamus that is the main relay of information to the cortex.

Although each part of the thalamus receives various kinds of afferents, there is always one kind of glutamatergic[1] input, coming from one particular source, that is believed to be the main driving input to the respective thalamic cells. These afferents are called the *primary afferents* of a part of thalamus. The various thalamic parts, or *nuclei*, inherit their basic function as a relay station for a particular type of information from their primary afferents. Examples are the lateral geniculate nucleus with its retinal afferents, the medial geniculate nucleus with its inferior collicular afferents, or the ventrolateral nucleus with its cerebellar afferents. Accordingly, these nuclei relay information on vision, hearing, and body motion. The retina, the inferior colliculus, and the cerebellum are all *subcortical* structures, meaning that they are not part of the cerebral cortex. Thalamic nuclei that relay information mainly from one subcortical source to the cortex are classically called *specific nuclei*. We will study the primary visual pathway with the lateral geniculate nucleus (LGN) as its thalamic relay station in the next chapter. The anatomy of the primary visual pathway up to the primary visual cortex, also called V1 or area 17, is shown in Figure 1.1. For an overview of thalamic

---

[1] Glutamate is a very common synaptic transmitter in the central nervous system. Its effect is a depolarization and, hence, excitation of the postsynaptic cell.

nuclei see Figure 1.2.

Primary thalamic afferents can be defined on the basis of morphology and fine structure of their axons and synaptic terminals, of the spatial pattern of termination on relay cells, and of their intrathalamic synaptic relations. In particular, their terminals are relatively large and contact relatively large dendritic stems of relay cells that tend to be close to the cell body. Moreover, retinogeniculate synapses frequently form triadic synaptic arrangements with geniculate interneurons, commonly in complex terminal structures called glomeruli; see the next chapter.

It turns out that different thalamic nuclei project to different cortical target areas. One nucleus, however, may project to several cortical areas. For instance, the lateral geniculate nucleus of the cat projects to areas 17, 18, and 19, although only the geniculate C-layers project to area 19. Of course, all these areas, by virtue of their geniculate input as well as intracortical connections, are functionally *visual* areas. To a first, crude, approximation, the thalamus relays a system of separate primary pathways from subcortical sources to the cortex. A graphical overview of connections between the thalamus and the cortex is given in Figure 1.2.

There are thalamic nuclei that apparently do not receive significant input from subcortical sources of a type comparable to the one provided by primary afferents. Such nuclei are classically called *non-specific nuclei* or *association nuclei*. There is now evidence that they receive their primary afferents from layer 5 of some cortical area. Such thalamic nuclei thus may relay information from one cortical area to another. Examples are the anterior thalamic nucleus, the medial thalamic nucleus, and the pulvinar; cf. Figure 1.2. A *hierarchy* of thalamic nuclei can be defined along the primary pathway of information, from a subcortical source passing through a thalamic relay nucleus to some cortical area, and then, by way of further thalamic nuclei, to different cortical areas. The nuclei that relay signals before they first hit the cortex have been termed *first-order nuclei*, those that seem to primarily pass information between cortical areas *higher-order nuclei*. The hypothesis of primary afferents of cortical origin, and thus of the hierarchy of thalamic nuclei, is due to Guillery (1995). A schematic summary of the synaptic relations in the thalamocortical system is given in Figure 1.3.

Besides the pathway that ascends along the hierarchy, there also exist descending projections. These originate from layer 6 of cortical areas and terminate in the thalamus; see Figures 1.2 and 1.3. Like in the ascending pathway, synaptic terminals of descending fibers are glutamatergic. In contrast to the primary thalamic afferents, however, the corticothalamic input from layer 6 is thought to mainly subserve a role in *modulating*, rather than *evoking*, thalamic responses.

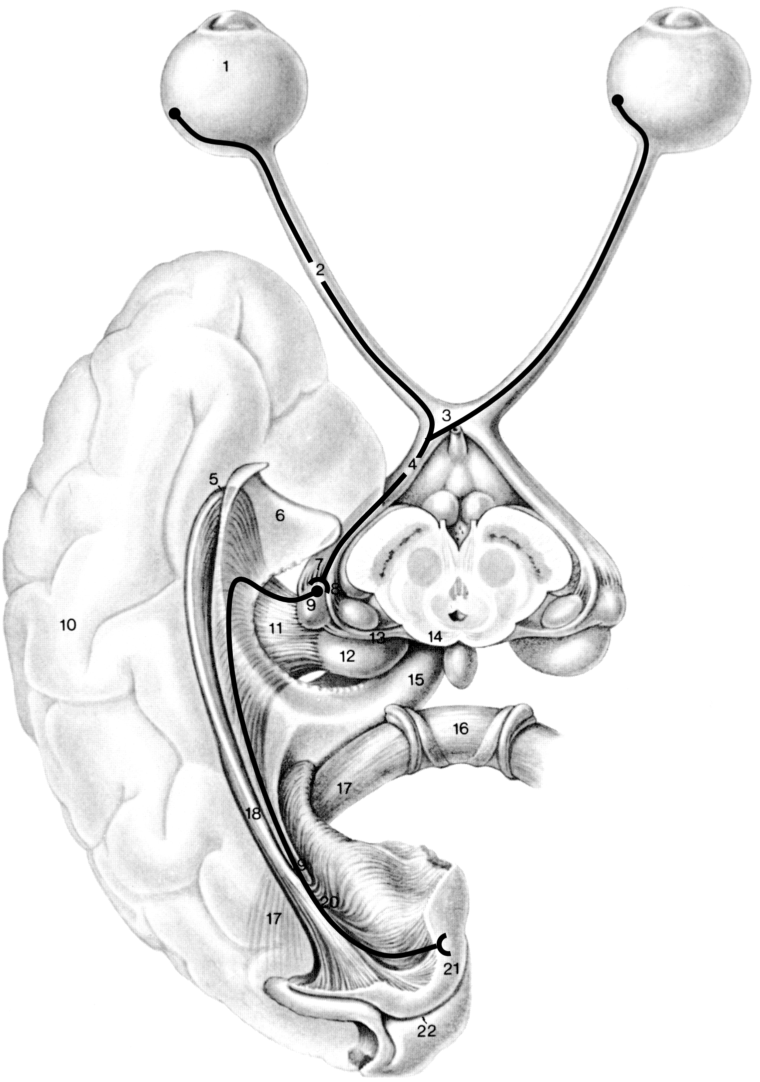

Figure 1.1: Ventral view of the human retinogeniculocortical projection which forms the primary visual pathway. It originates from the retinas (1) and passes through the optic nerve (2) to the optic chiasm (3). In the optic chiasm fibers from the left hemi-retinas of both eyes (representing the right visual hemi-field) combine and proceed through the optic tract (4) to the left lateral geniculate nucleus (9), and vice versa for fibers from the right hemi-retinas (not shown). From the lateral geniculate nucleus relay cells project via the optic radiation (11) to the primary visual cortex (21). There are alternative routes from the retinas to the cortex that are not regarded as part of the primary visual pathway (not shown). Figure adapted from Nieuwenhuys et al. (1988).

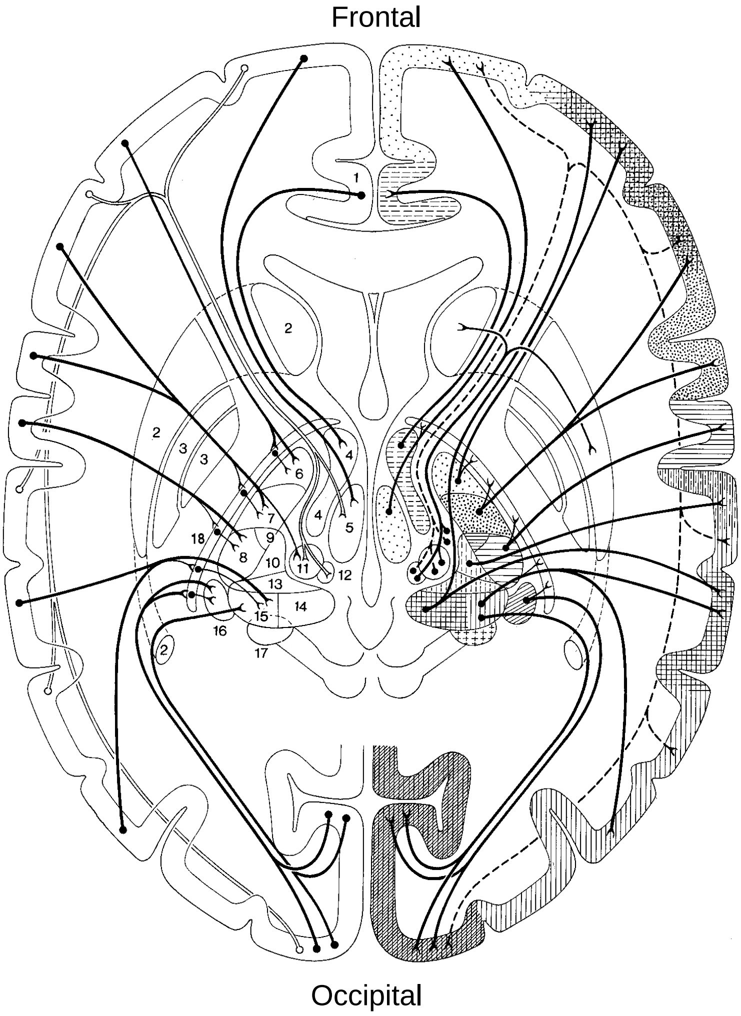
Frontal
1
2
2
3
3
4
4
5
6
7
18
8
9
10
11
12
13
14
15
16
17
2
Occipital

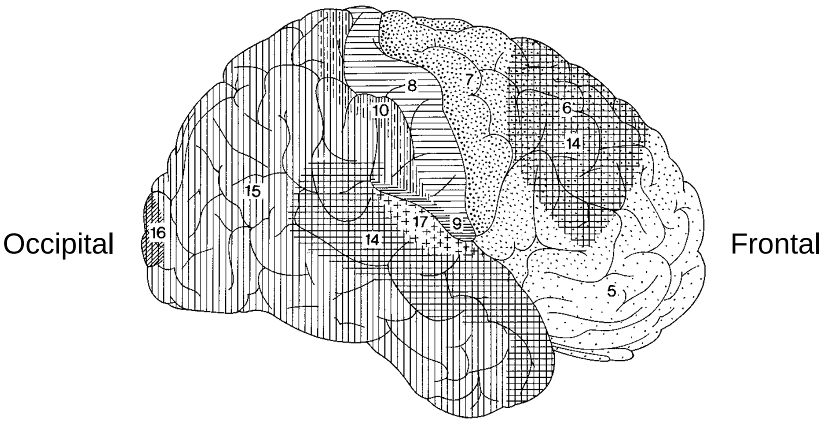
8
7
10
6
14
15
17
9
16
14
5
Occipital
Frontal

Figure 1.2: Diagrammatic horizontal section of the thalamocortical system (**top**) and lateral view of the cerebral cortex (**bottom**) in humans. In the **top** view, the left hemisphere depicts the corticothalamic, the right hemisphere the thalamocortical projections. Shadings and numbers in the **bottom** view correspond to the thalamic nuclei and their respective cortical target areas as labeled in the **top** view. The thalamic nuclei are: anterior thalamic nucleus (4), medial thalamic nucleus (5), ventroanterior nucleus (6), ventrolateral nucleus (7), ventroposterior nucleus (8,9), lateral posterior nucleus (10), centromedian nucleus (11), parafascicular nucleus (12), pulvinar (13,14,15), lateral geniculate nucleus (16), medial geniculate nucleus (17), thalamic reticular nucleus (18). Figure adapted from Nieuwenhuys et al. (1988).

One thalamic nucleus may receive layer 6 input from several cortical areas. As an example, the corticogeniculate projections in the cat arise in layer 6 of areas 17, 18, and 19. Area 19 only projects back to the geniculate C-layers from where it receives input. At present, it looks as if a thalamic nucleus receives cortical layer 6 input mainly from areas where it sends its primary projection to. This kind of cortical input thus implements *feedback* to a thalamic nucleus. The loop of the primary *geniculocortical pathway* and the *corticogeniculate feedback* will concern us throughout this work.

As for morphology and fine structure, the cortical layer 6 feedback is distinct from primary input to the thalamus, including cortical layer 5 input. In particular, their terminals are small and contact relay cells on slender, distal parts of their dendrites. They are rarely involved in synaptic triads or glomerular structures (see the next chapter) but also contact the dendritic shafts of intrathalamic interneurons. It is interesting to note that, in the LGN of the cat, corticogeniculate feedback makes the *majority* of synapses on relay cells, probably 40–50 %, outnumbering even the retinal synaptic terminals.

Although both primary afferents and cortical layer 6 feedback utilize glutamate as the transmitter at their terminals, there seems to be a difference on the receptor side. While retinal terminals and corticogeniculate feedback appear to activate the same types of AMPA/kainate and NMDA receptors[2], cortical terminals additionally activate metabotropic glutamate receptors. Metabotropic receptors initiate an intracellular second messenger cascade that, besides other effects, regulates ion channels and, hence, leads to changes

---

[2] Receptors are commonly classified and labeled by their selective agonists. Three prominent agonists that are selective for different types of glutamate receptors are AMPA (for α-amino-3-hydroxy-5-methyl-4-isoxalone propionic acid), kainate, and NMDA (for N-methyl-D-aspartate).

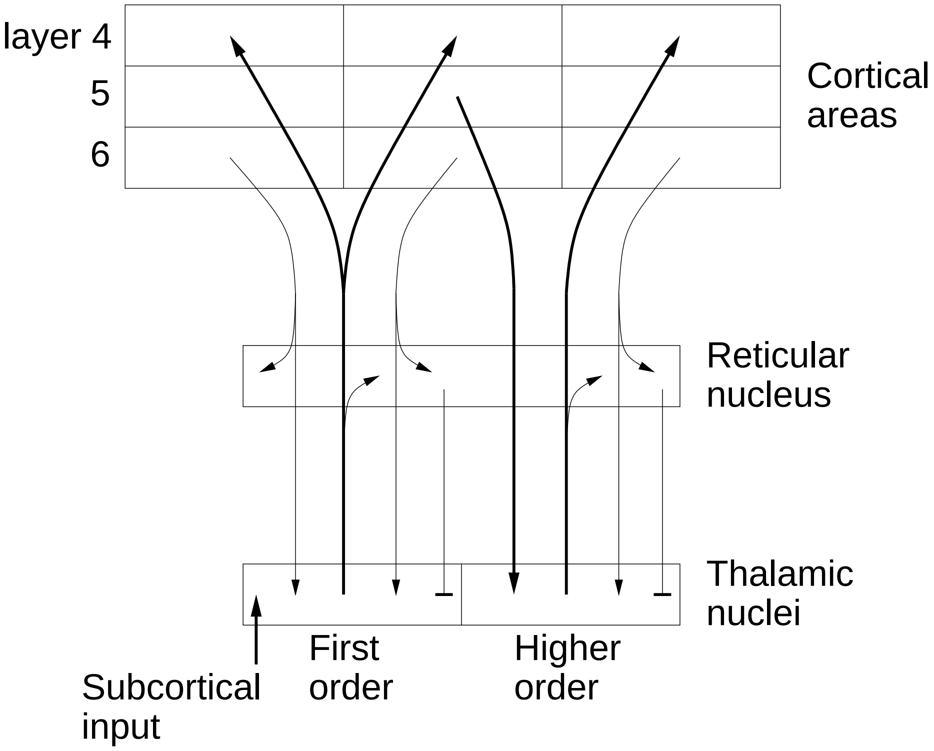

Figure 1.3: Schematic summary of connections within the thalamocortical system. The primary stream of information (bold arrows) is believed to run from sensory systems or some other subcortical region through a first-order relay nucleus to layer 4 of some cortical area, and from layer 5 of cortical areas through higher-order relay nuclei to layer 4 of further cortical areas. This primary pathway determines the gross response properties and functional specialization of thalamic and cortical cells. Reverse projections originate from layer 6 of cortical areas and terminate in those thalamic nuclei from which the areas receive projections. These feedback connections are regarded as mainly modulating thalamic responses to the primary input. Moreover, thalamocortical projections and corticothalamic projections from layer 6 send collaterals to the thalamic reticular nucleus. All these fibers form glutamatergic terminals (arrow heads). Additionally, there are GABAergic connections (bar heads) from sections of the reticular nucleus back to those thalamic nuclei from which the sections receive input.

in membrane potential; see the next chapter. In contrast, ionotropic receptors, such as AMPA/kainate and NMDA receptors, incorporate ion channels that are directly affected by receptor binding.

The three types of receptors at the corticogeniculate synapse implement three different timescales of postsynaptic effects. The fastest postsynaptic potentials are mediated by AMPA/kainate receptors and last tens of milliseconds. An intermediate timescale of postsynaptic action, hundreds of milliseconds, is provided by the NMDA receptors. The longest potentials can last for seconds and are initiated by metabotropic glutamate receptors. It remains to be elucidated which of the receptors are activated under different physiological conditions.

Another important difference between cortical layer 6 and primary afferents, including cortical layer 5 input, is that the former regularly send axon collaterals to the thalamic reticular nucleus, a sheet of GABAergic[3] neurons that is part of the ventral thalamus and lies adjacent to the dorsal thalamus; see Figures 1.2 and 1.3. In contrast, primary afferents apparently do not contact the reticular nucleus. Thalamocortical axons also produce collaterals to the reticular nucleus which, in turn, projects back to the respective thalamic nuclei. There are, therefore, distinct parts of the reticular nucleus that implement feedback inhibition to different thalamic nuclei; see Figures 1.2 and 1.3. It appears that a single section of the reticular nucleus may be involved in loops with several thalamic nuclei, and, conversely, that a single thalamic nucleus may be reciprocally connected with several parts of the reticular nucleus. This opens up the possibility for complex interactions between different thalamic nuclei via the reticular nucleus.

The sections of the reticular nucleus that reciprocally connect to the different thalamic nuclei are further structured. Different subsections may form two-way connections with different thalamic layers. In particular, the part of the reticular nucleus that is involved in the loop with the A-laminae of the cat LGN is called the perigeniculate nucleus (PGN). Through the A-laminae pass the X- and Y-streams from the retina to the cortex. They belong to the best-studied, and perhaps functionally prominent, part of the visual thalamus and will be considered in the next chapter.

All the projections that have been discussed in this section apparently share – to varying degrees – a common principle of organization, the principle of *topographic mapping*. This means that neighboring neurons that send axons along one of the projections contact neurons in the target area that

---

[3] GABA (for γ-aminobutyric acid) is a very common synaptic transmitter in the central nervous system. Its effect is usually a hyperpolarization and, hence, inhibition of the postsynaptic cell.

are likewise close to each other. In other words, these projections do not spread out very much, and maps that exist in the source area will persist in the target area. Thus, there are thalamic, reticular, and cortical maps in the system. There are indications, however, that projections between higher-order nuclei of the thalamus and the reticular nucleus may not be topographic. Furthermore, as retinal topography seems to be gradually lost in higher visual cortical areas, one may expect the thalamic primary targets of these areas to lack retinal topography as well.

1.2 Thalamic Relay Modes: The Temporal Character of the Relay

Since it today seems evident that not much spatial processing occurs at the retinogeniculate synapse, it is natural to direct attention to the temporal characteristics of the geniculate transform. A useful characterization of the temporal transformation performed by a cell, and one that will be used in this work, is its *temporal transfer function.* It fully characterizes linear transformations but can be defined for rather general transforms. Let IN(t) and OUT(t) be the time-dependent input and output rates of a neuron, respectively. Let us, more precisely, assume their Fourier series to be

$$\begin{aligned} \mathrm{IN}(t) &= F_0 + \sum_{k=1}^{\infty} F_k \sin(2\pi k f t + \phi_k) \ , && (1.1) \\ \mathrm{OUT}(t) &= G_0 + \sum_{k=1}^{\infty} G_k \sin(2\pi k f t + \psi_k) \ , && (1.2) \end{aligned}$$

with $F_1 \neq 0$, i.e., f is the fundamental frequency of the input signal. Such periodic input and output rates may be obtained in response to sinusoidal sensory stimuli, e.g., a spot of varying brightness flashed on the retina with frequency f. The rates IN(t) and OUT(t) are calculated as spike counts in time bins which should be significantly shorter than the period $1/f$. The spike counts are usually averaged over several cycles of stimulus presentation. The *amplitude-transfer function* is defined as the ratio

$$\mathrm{a}(f) := \frac{G_1}{F_1} \ , \qquad (1.3)$$

the *phase-transfer function* as the difference

$$\mathrm{p}(f) := \phi_1 - \psi_1 \ , \qquad (1.4)$$

such that negative phase transfer means phase lead over the input. While amplitude and phase transfer are usually given as functions of the fundamental input frequency f, this provides a full description of the rate transformation only in the linear case. In general, G_1/F_1 and $\phi_1 - \psi_1$ also depend on all the Fourier coefficients F_k and all the phases ϕ_k of the input signal, and a knowledge of higher harmonics in the output signal is required for complete information.

Thalamocortical relay neurons possess a characteristic blend of voltage-gated ion channels (Jahnsen & Llinás, 1984a; Jahnsen & Llinás, 1984b; Huguenard & McCormick, 1992; McCormick & Huguenard, 1992; Zhan et al., 1999) that jointly determine the timing and pattern of action potentials in response to a sensory stimulus; see the next chapter and appendix C. Depending on the initial membrane polarization, the geniculate relay neuron's response to a visual stimulus is in a range between a *tonic* and a *burst* mode (Sherman, 1996; Sherman & Guillery, 1996). The generation of *burst* spikes depends prominently on the low-threshold Ca^{2+} current, or T-current ('T' for 'transient'); see appendix A, especially Figure A.3, and appendix C, equations (C.29) through (C.33). At hyperpolarization below roughly -70 mV, the low-threshold Ca^{2+} current gets slowly de-inactivated. As the membrane repolarizes above roughly -70 mV, the current activates, followed by a rapid transition from the de-inactivated to the inactivated state, thereby producing a Ca^{2+} spike with an amplitude that depends on how long and how strongly the cell has been hyperpolarized previously. After sufficient hyperpolarization the Ca^{2+} spike will thus reach the threshold for Na^+ spiking and give rise to a *burst* of one to ten action potentials riding its crest (Jahnsen & Llinás, 1984a; Jahnsen & Llinás, 1984b; Huguenard & McCormick, 1992; McCormick & Huguenard, 1992; Zhan et al., 1999). All other action potentials, i.e., those that are not promoted by a Ca^{2+} spike and, hence, do not group into bursts, are called *tonic* spikes. Figure 1.4 shows intracellular voltage recordings of burst and tonic action potentials and of the Ca^{2+} spike.

Although the issue is still controversial, there is some evidence that a *mixture* of burst and tonic spikes may be involved in the transmission of visual signals in lightly anesthetized or awake animals (Guido et al., 1992; Guido et al., 1995; Guido & Weyand, 1995; Mukherjee & Kaplan, 1995; Sherman, 1996; Sherman & Guillery, 1996; Reinagel et al., 1999). At resting membrane potentials below -70 mV, bursting constitutes a very early part of a relay cell's response, producing a phase lead of up to a quarter cycle relative to its primary input (Lu et al., 1992; Guido et al., 1992; Mukherjee & Kaplan, 1995). At more depolarized membrane potentials, a relay cell's response is dominated by tonic spikes and is in phase with the primary input (Lu et al., 1992; Guido et al., 1992; Mukherjee & Kaplan, 1995). Figure

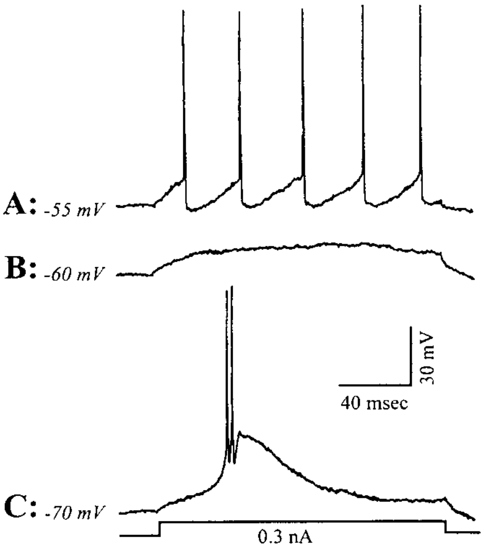

Figure 1.4: Dependence of thalamic firing mode upon membrane potential. At three different initial levels of membrane polarization, a step current of 0.3 nA is delivered; see bottom. (**A**) At −55 mV the low-threshold Ca^{2+} current is inactivated. The cell responds with tonic spiking. (**B**) At −60 mV the low-threshold Ca^{2+} current is still inactivated. The current pulse does not suffice to produce any spike (Ohmic response). (**C**) At −70 mV the low-threshold Ca^{2+} current is de-inactivated. It is activated by the depolarization caused by the current pulse. A Ca^{2+} spike is produced with a burst of two action potentials (Na^+ spikes) riding its crest. Figure adopted from Sherman (1996). See appendix A, especially Figure A.3, and appendix C, equations (C.29) through (C.33), on the dynamics of the low-threshold Ca^{2+} current.

1.5 shows typical examples of tonic and burst responses of a geniculate relay cell. Figure 1.6 presents plots of temporal transfer functions in the burst and tonic relay modes.

There is another type of geniculate relay neuron, called *lagged neuron*, that is strongly delayed in response time and phase (Mastronarde, 1987a; Humphrey & Weller, 1988a; Saul & Humphrey, 1990; Mastronarde et al., 1991). It has been speculated that in lagged cells, because of strong feedforward inhibition they are assumed to receive, burst spikes are responsible for high-activity transients seen at the cessation of their retinal input (Mastronarde, 1987a; Mastronarde, 1987b) and contribute substantially to delayed response peaks (Mastronarde, 1987b). The issue of lagged and nonlagged neurons will be covered in some detail in the next chapter.

Besides timing there are other characteristic differences in the responses of relay cells in burst and tonic mode. In particular, in the burst mode spontaneous activity is significantly lower than in the tonic mode. Furthermore,

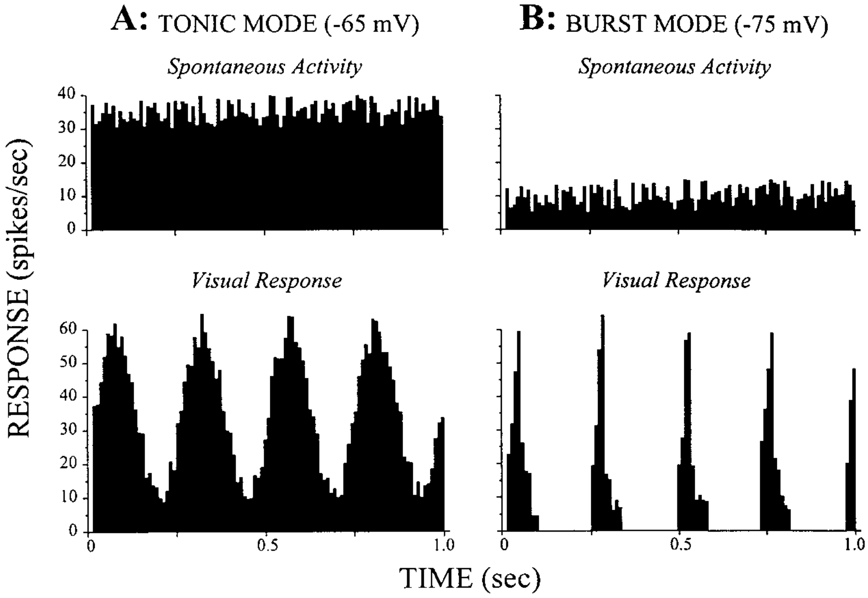

Figure 1.5: Average firing histograms of spontaneous activity (**top row**) and of responses to successive cycles of a drifting sinusoidal grating (giving rise to a 4 Hz modulation; **bottom row**) from a geniculate relay cell. (**A**) At a resting membrane potential of -65 mV the neuron is in the tonic relay mode. The spontaneous activity is high and the response profile faithfully reflects the sinusoidal input. (**B**) At a resting membrane potential of -75 mV the neuron is in the burst mode. The spontaneous discharge is low and the response starts and finishes early in the stimulus cycle. The temporal transformation performed by the bursting relay cell is more nonlinear. The resting membrane potential is controlled by current injection in this experiment. Figure adopted from Sherman (1996).

the temporal transform performed by a cell in burst mode is more nonlinear than in tonic mode; cf. Figure 1.5.

1.3 Functional Implications

The last decades have produced a wealth of data on anatomy, physiology, and pharmacology of thalamocortical circuits. Of these we can review only a very limited portion in this chapter. It has proven hard to fuse the various fragments into a unified and coherent picture, and what the thalamus might actually be doing has remained somewhat mysterious. Indeed, current ideas tend to be either much more vague or more difficult to justify than

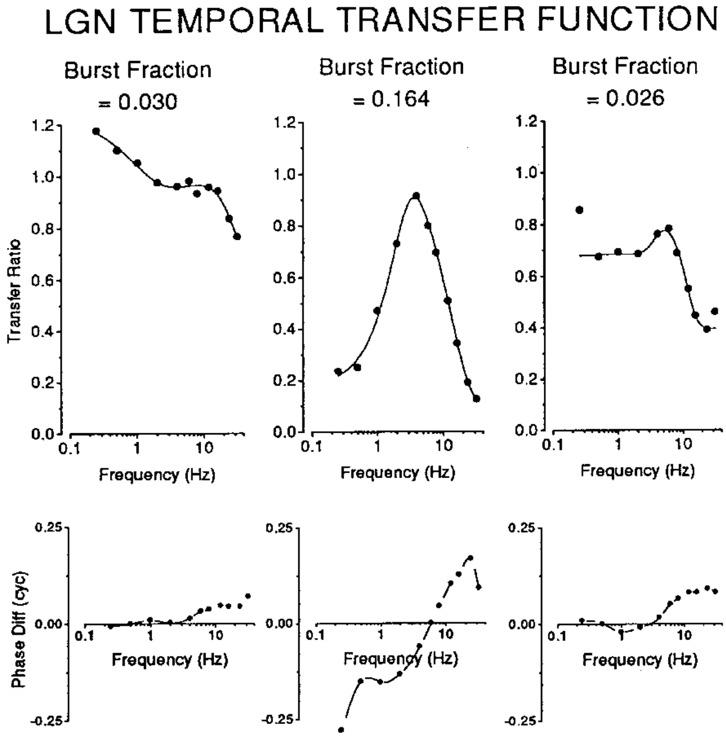

Figure 1.6: Temporal transfer functions of a geniculate relay cell as measured in an experiment at three successive times (0 hours, 1 hour, and 1.5 hours in the columns from left to right). A sinusoidal visual stimulus is applied for various frequencies f. The stimulus signal is first transformed by the retina to the geniculate input signal IN(t), and subsequently by the relay cell to OUT(t); cf. equations (1.1) and (1.2). From IN(t) and OUT(t) the transfer of amplitude [**top row**; cf. equation (1.3)] and phase [**bottom row**; cf. equation (1.4)] can be determined. In the experiment, the relay neuron switched from a tonic (**left column**) to a more bursty (**center column**), and back to a tonic (**right column**) relay mode, as indicated by the different burst fractions (proportion of burst spikes). Note the transition from a low-pass to a band-pass (**top row**), and from an in-phase response to a phase transfer with a strong slope (**bottom row**) as the cell switches from tonic to burst mode. Modulation of the relay mode is thought to be mediated by brainstem input or feedback from cortical layer 6. Figure adapted from Mukherjee & Kaplan (1995).

considerations on, e.g., function of visual cortical areas. Nonetheless, some hypotheses have been formulated that point into interesting directions.

The fundamental role of the thalamus as a gate for all kinds of subcortical information to the cortex has long been recognized. Perhaps the most general, as yet *little* appreciated, conclusion that may be drawn from the layout of the thalamocortical network as outlined here is that it also implements a major pathway for corticocortical communication (Guillery, 1995; Sherman & Guillery, 1996). This pathway would work in parallel to the one established by intracortical connections. The important question then is, what may be the difference between the two ways of corticocortical communication. It has been suggested that connections between cortical areas via the thalamus might assist the propagation of activity over long cortical distances by providing a 'high-security' link (Miller, 1996). Quite obviously, this is a topic that deserves much more attention in future research.

Confusing results have been obtained regarding the action of corticothalamic feedback originating from layer 6. Some studies have suggested a facilitation, others a suppression of geniculate relay cell firing (Kalil & Chase, 1970; Richard et al., 1975; Baker & Malpeli, 1977; Schmielau & Singer, 1977; Geisert et al., 1981; McClurkin & Marrocco, 1984; McClurkin et al., 1994). Today the pathway is often regarded as exerting a modulatory influence on thalamic response properties (Sherman & Guillery, 1996; Crick & Koch, 1998). The metabotropic glutamate receptors used in this pathway have been seen to locally switch relay cells between the burst and tonic modes of relay (McCormick & von Krosigk, 1992; Godwin et al., 1996; Sherman, 1996; Sherman & Guillery, 1996; von Krosigk et al., 1999). Indeed, geniculate relay cells in vivo are dynamic and differ individually in their degree of bursting (Lu et al., 1992; Guido et al., 1992; Mukherjee & Kaplan, 1995); cf. Figure 1.6. It has therefore been hypothesized that, by corticothalamic feedback, information on visual stimuli may be increased in the relay-cell output (McClurkin et al., 1994) and that relay cells are switched from a detection to an analyzing mode once novel and interesting stimuli are detected (Godwin et al., 1996; Sherman, 1996; Sherman & Guillery, 1996). The burst mode with its low spontaneous activity and, hence, high signal to noise ratio would be better suited for detection, while the tonic mode with its more linear transformation would provide for the fidelity of signal transmission that is required for analysis; cf. Figure 1.5; see, however, Mukherjee & Kaplan (1998). Furthermore, it has been proposed that corticogeniculate feedback modulates the spatial layout of receptive fields of cortical simple cells by exploiting the geniculate burst-tonic transition (Wörgötter et al., 1998).

Some other proposals have been made concerning the function of corticogeniculate feedback, such as control of binocular disparity for stereopsis

(Schmielau & Singer, 1977), attention-related gating of relay cells (Sherman & Koch, 1986), gain control of relay cells (Koch, 1987), and synchronizing the firing of neighboring relay cells (Sillito et al., 1994; Singer, 1994) that represent related parts of a stimulus.

It is characteristic of the corticogeniculate feedback pathway that it involves glutamatergic and GABAergic synapses with various types of receptors that converge onto single relay cells. Signals on this pathway may even pass multiple GABAergic synapses within the reticular nucleus before reaching the LGN, so that, besides excitation and inhibition of different 'flavors', disinhibition is another possible effect. One of the troubles with predicting the effects of corticogeniculate feedback is thus that they are likely to depend significantly on details of synapses made by individual axons running from the cortex to the LGN, from the cortex to the reticular nucleus, from the reticular nucleus to the LGN, and on details of connectivity within the reticular nucleus. These details are, however, not known yet. In this situation modelers must take care of the robustness of predictions or otherwise be aware of the speculative nature of their conclusions. Moreover, significant variability may exist in corticothalamic synaptic relationships that supports a corresponding multiplicity of functions. As a consequence, suggestions on the function of cortical feedback have always to be viewed as non-exclusive.

In this work we will pursue the idea that a prominent function of corticothalamic feedback is the modulation of relay modes, as has been suggested by other authors; see above. Unlike the other authors, however, we will focus on the response *timing* aspects of relay modes. In particular, in chapter 2 we explicate the causal link between the *variable response timing of geniculate relay cells* and *variable tuning of visual cortical cells for velocity* of moving features, thus identifying control of velocity tuning as a likely mode of corticogeniculate operation. The conclusions drawn in this context rely on the involvement of different relay modes in normal visual function, a question that in principle may presently be accessible to experiment. Importantly, we do not need to assume any particular detailed structure of cortical feedback connections. In chapter 3 we push the novel hypothesis on adaptive velocity tuning one step further. Based on some fairly general considerations concerning the necessities of visual information processing, we present and analyze a model of the corticogeniculate loop that implements the control of cortical velocity tuning. In its analysis we explore the model's ability of object segmentation by statistical motion analysis in the visual field. Although we try to keep the loop model as simple and generic as possible, the particular structure of the loop that we investigate has to be of a speculative nature. More general than the network structure, however, is the computational principle that it implements.

Chapter 2

Dynamic Cortical Velocity Tuning: A Role for Corticogeniculate Feedback

Most excitatory inputs to cortical cells, even to those in the thalamic recipient layers, originate from the cells' cortical neighborhood. In layer 4 of the cat's area 17, the proportion of excitatory synapses on spiny stellate cells that derive from geniculate relay neurons is estimated to be only 6 percent. There are direct indications, however, that the synapses formed with thalamic afferents are especially efficient in driving cortical cells to fire (Stratford et al., 1996; Alonso et al., 1996). Conversely, the bulk of local intracortical connections seem to mediate subthreshold modulations of the membrane potential and affect stimulus preferences only mildly (Toth et al., 1997).

Another line of research has accumulated evidence for the direct influence of geniculate input on cortical receptive field (RF) properties, both in the spatial and temporal dimension (Saul & Humphrey, 1992a; Saul & Humphrey, 1992b; Reid & Alonso, 1995; Ferster et al., 1996; Jagadeesh et al., 1997; Murthy et al., 1998; Hirsch et al., 1998). Suggested intracortical effects, on the other hand, include sharpening of tuning properties by suppressive interactions (Hammond & Pomfrett, 1990; Reid et al., 1991; Hirsch et al., 1998; Crook et al., 1998; Murthy & Humphrey, 1999), amplification of geniculate inputs by recurrent excitation (Douglas et al., 1995; Suarez et al., 1995), and normalization of responses by local interactions (Toth et al., 1997).

The above evidence may be condensed to saying that the thalamic input defines the gross RF properties of cells in the cortical recipient layers, while local cortical circuits refine and modulate their responses by amplification or inhibition. Visual neurons far away from the geniculate input stage may have response properties that heavily depend on the cortical network. Even in those neurons, however, *variations* in the geniculate input should show up in according response variations, unless the variation in the input does not reflect anything behaviorally relevant. It is thus worthwhile to study the geniculate input to the primary visual cortex, and, in particular, its *variability*, in order to learn more about cortical information processing.

The model to be developed and analyzed in this chapter addresses the geniculate contribution to spatiotemporal RFs of the visual cortex. We will be especially concerned with the question of how cortical velocity tuning may change under the influence of cortical feedback on geniculate relay cells (GRCs). In particular, we elaborate the novel hypothesis that the visual cortex controls via feedback to the lateral geniculate nucleus the temporal response properties of relay cells in a way that *alters* the tuning of cortical cells for speed.

2.1 Geniculate Input to Cortical Simple Cells

2.1.1 Spatiotemporal Receptive Fields and Velocity Tuning

Velocity selectivity or velocity tuning, taken here to mean preference for a certain speed and direction of motion of visual features, requires convergence of pathways with different spatial information and different temporal characteristics, such as delays, onto single neurons; see Figure 2.1. For higher mammals this is believed to occur in the primary visual cortex (Movshon, 1975; Orban et al., 1981a; Orban et al., 1981b). Since the early days of Hassenstein & Reichardt (1956), motion detectors in different species have been modeled along these lines, on various levels of refinement and with different neural implementations in mind; see Nakayama (1985) for a review of the classic approaches. Modern models of velocity-selective responses at the earliest cortical processing stage can be roughly divided in those which employ a purely feedforward architecture, i.e., geniculate and possibly cortical input that converges onto cortical cells (Tolhurst & Heeger, 1997; Emerson, 1997; Emerson & Huang, 1997; Wimbauer et al., 1997a; Wimbauer et al., 1997b; Murthy et al., 1998), and those which make use of recurrent intracortical circuits (Douglas et al., 1995; Suarez et al., 1995; Maex & Orban, 1996; Mineiro & Zipser, 1998). As explained above, we will adopt the view that the geniculate input characteristics are important in determining basic cortical RF properties, including spatiotemporal tuning, at least in the geniculate recipient layer 4B.

One concise description of neuronal responses to stimuli that vary in

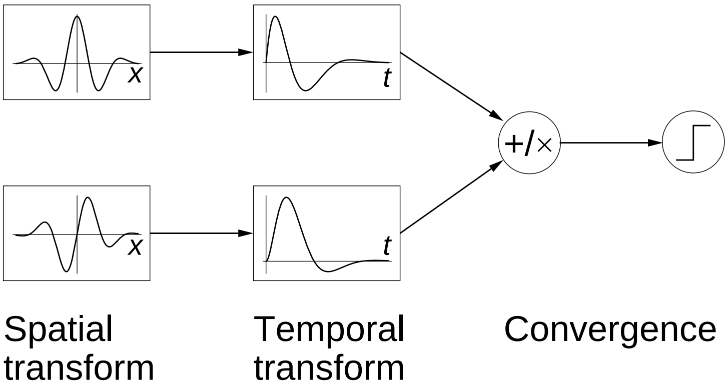

Figure 2.1: Basic structure of common models of low-level velocity selectivity; cf. Nakayama (1985). The graphs in the boxes show possible integral kernels to realize spatial and temporal filtering. A spatiotemporal signal is first spatially transformed by two different operations, e.g., as shown, by two local bandpass filters which have a phase difference of a quarter cycle. The two transformed signals are further subject to different temporal transformations, e.g., filters with different delays or, as shown, a response-phase difference of a quarter cycle. The two paths of processing are combined by summation or multiplication. The combined signal may be subject to a threshold or other nonlinear transformation to yield a velocity-selective response. Several variations of this basic structure have been investigated to fit responses of different cell types. The different transformations may be implemented by feedforward mechanisms or by recurrent circuits. Convergence may occur at the geniculocortical or at corticocortical synapses. Nonlinearities may be generated at the single-cell or network level.

time and space is given by the spatiotemporal RF; see Figure 2.2. The spatiotemporal RF is usually determined from reverse correlation experiments (DeAngelis et al., 1993; DeAngelis et al., 1995), a technique where discrete spatiotemporal white-noise stimuli are presented and the cell's output spikes are correlated to the dark and light pixels of the stimulus that occurred *prior* to a spike. In this way, data can be accumulated on how likely an output spike is produced given a dark or light local stimulus at a certain time and place in visual space. This description is especially transparent for simple cells which respond rather linearly in the space-time domain (McLean & Palmer, 1989; McLean et al., 1994; Reid et al., 1991; Albrecht & Geisler, 1991; DeAngelis et al., 1993; DeAngelis et al., 1995; Jagadeesh et al., 1993; Jagadeesh et al., 1997; Murthy et al., 1998). In that case the spatiotemporal RF determined by reverse correlation is the first-order rate response kernel of the cell, and it is all one needs to know to predict the cell's response rate to all kinds of stimuli. The best predictions of responses to moving stimuli from the spatiotemporal RF are obtained for simple cells in the geniculate recipient layer 4B (Murthy et al., 1998). For complex cells, on the other hand, higher order correlations between stimuli and output spikes must be taken into account to estimate the response to a moving stimulus.

Receptive fields of simple cells that are tuned for direction and speed have a special spatiotemporal structure. Response latency decreases gradually across their RFs in the preferred direction of motion; see Figure 2.2 **E** and **F**. Such RFs are spatiotemporally inseparable, that is, they cannot be described mathematically as a product of a spatial and a temporal function.

To avoid confusion, we point out that the term 'speed tuning' is sometimes used in a more restricted sense. Simple cells exhibit tuning for spatial and temporal frequencies[1] that results in preference for speeds of moving gratings depending on their spatial frequency. Here we will be concerned with the more natural case of stimuli having a low-pass frequency content (Field, 1994), specifically, those composed of local features such as thin bars.

2.1.2 Lagged and Nonlagged Relay Neurons

In the retina of the cat two classes of ganglion cell, the X-cells and the Y-cells, are distinguishable on the basis of their *spatial* RF properties. Since X- and Y-ganglion cells mainly project to different LGN relay cells, the X- and Y-streams remain separated in the LGN. Relay cells thus inherit RF properties of the X- or Y-type and are classified accordingly. In particular, cells of the X-type have smaller RFs and prefer higher spatial frequencies than cells of the Y-type. Moreover, X-cells perform a rather linear spatial summation of a stimulus, while Y-cells exhibit strong nonlinearities (Hubel & Wiesel, 1961; Hoffmann et al., 1972; Hochstein & Shapley, 1976b; Hochstein & Shapley, 1976a; Cleland et al., 1979). There are also some temporal response differences correlated with the X/Y-classification. In particular, Y-cells tend to respond more transiently, or more 'phasic', and to stimuli moving at higher speeds than X-cells (Cleland, 1983; Cleland et al., 1983; Cleland & Harding, 1983).

In the A-laminae of cat LGN two subclasses of relay cell have been identified within the X- and Y-classes that dramatically differ in their *temporal* response properties (Mastronarde, 1987a; Humphrey & Weller, 1988a; Saul & Humphrey, 1990; Mastronarde et al., 1991). Those that are more delayed in response time and phase have been termed *lagged*, the others *nonlagged*

---

[1] as is evident from the Fourier transform of their spatiotemporal RF

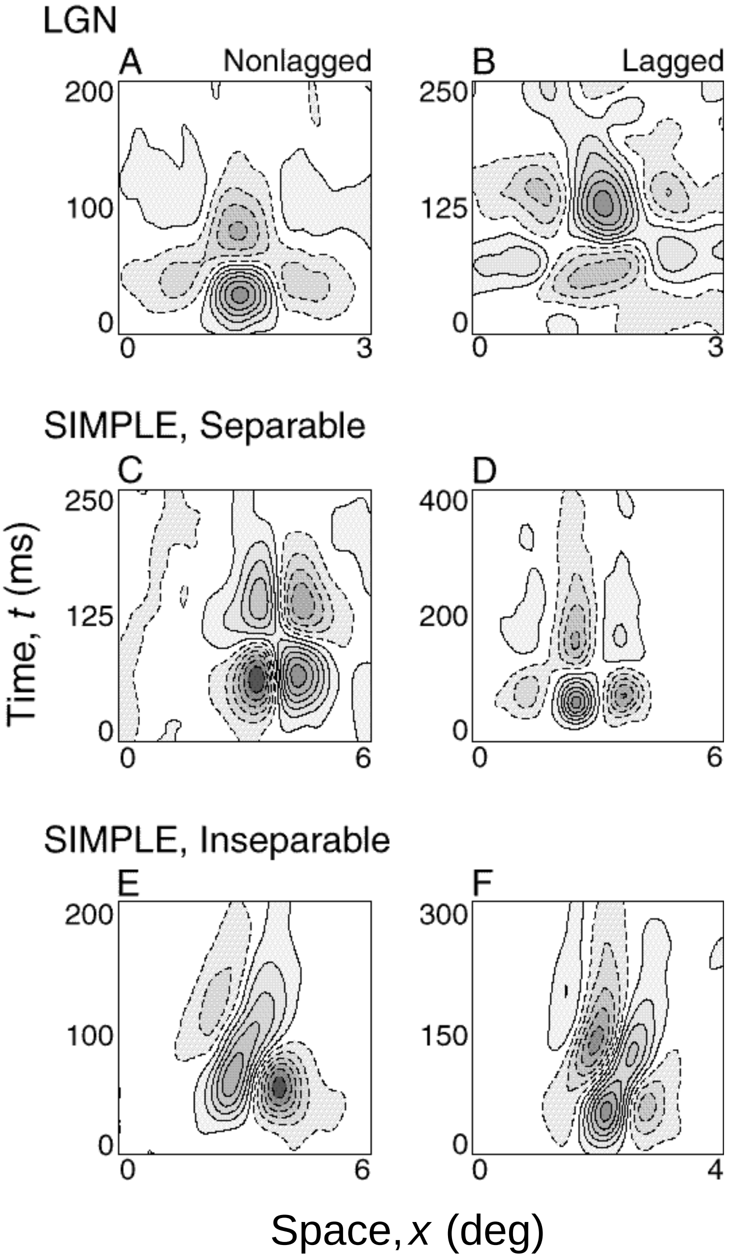

Figure 2.2: Spatiotemporal receptive field (RF) profiles for relay neurons of cat lateral geniculate nucleus (LGN) and simple cells of cat area 17. In each panel, the horizontal axis represents space (x), for the simple cells measured along a direction orthogonal to their preferred orientation, and the vertical axis represents latency (t), measured from stimulus onset. Solid contours delimit regions that are excited by bright stimuli, dashed contours indicate regions that are excited by dark stimuli. (**A**) Nonlagged on-center cell from the LGN. (**B**) Lagged on-center cell from the LGN.

Figure 2.2: (**C**) Simple cell with space-time separable RF. At $t \approx 100$ ms the two main regions simultaneously reverse their bright-dark polarity. (**D**) Another simple cell with approximately space-time separable RF. (**E**) Simple cell with space-time inseparable RF. The arrangement of the two subregions, i.e., the spatial phase of the RF, changes gradually with time. Put differently, the latency of the excitatory responses to bright and dark stimuli increases gradually across space. The tilt of the response regions in x-t-space is related to the preferred direction and speed of a stimulus. (**F**) Another simple cell with space-time inseparable RF. One possible interpretation of such RF data is that they arise from a summation of nonlagged and lagged geniculate inputs (**A**, **B**) at the cortical level. Figure adapted from DeAngelis et al. (1995).

cells. There are also very few so-called *partially lagged* neurons which on some response measures fall in between the lagged and nonlagged classes. In lagged neurons, the on-response to a flash of light is preceded by a dip in the firing rate lasting for 5 to 220 ms and there is typically a transient of high firing rate just after the offset of a prolonged light stimulus (Mastronarde, 1987a; Humphrey & Weller, 1988a); see Figure 2.3. For a moving light bar, the time lag of the on-response peak is about 100 ms after the bar has passed the RF center (Mastronarde, 1987a); see Figure 2.4. In contrast to lagged cells, the nonlagged cells' responses resemble their retinal input and show no transient at stimulus offset (Mastronarde, 1987a; Humphrey & Weller, 1988a); see Figures 2.3 and 2.4. See also Figure 2.2 **A** and **B** for a reverse correlation study of lagged and nonlagged spatiotemporal RFs.

In the temporal-frequency domain it is found that lagged and nonlagged neurons markedly differ in their response phase. Since their response phases turn out to be approximately linear functions of stimulus frequency, although with a slightly convex shape as shown in Figure 2.5, the phase-transfer functions [cf. equation (1.4)] are well characterized by their slope and their offset at 0 Hz. It is trivial to check that the slope of the phase-frequency relationship is related to the latency of the response. In fact, for any function f with Fourier transform $\hat{\mathrm{f}}$ we have

$$\mathrm{f}(t-\Delta) \propto \int_{-\infty}^{\infty} \mathrm{d}\omega\, \hat{\mathrm{f}}(\omega)\, \mathrm{e}^{-\mathrm{i}\omega(t-\Delta)} = \int_{-\infty}^{\infty} \mathrm{d}\omega\, \hat{\mathrm{f}}(\omega)\, \mathrm{e}^{\mathrm{i}\omega\Delta}\, \mathrm{e}^{-\mathrm{i}\omega t} \,. \tag{2.1}$$

Hence, $\mathrm{p}(f) = 2\pi f \Delta$ is the phase-transfer function of the operator that delays a signal by the time Δ. For that reason, the slope of the phase-transfer function devided by 2π is called *phase latency.* The offset at 0 Hz is referred to as *intrinsic* or *absolute phase.*

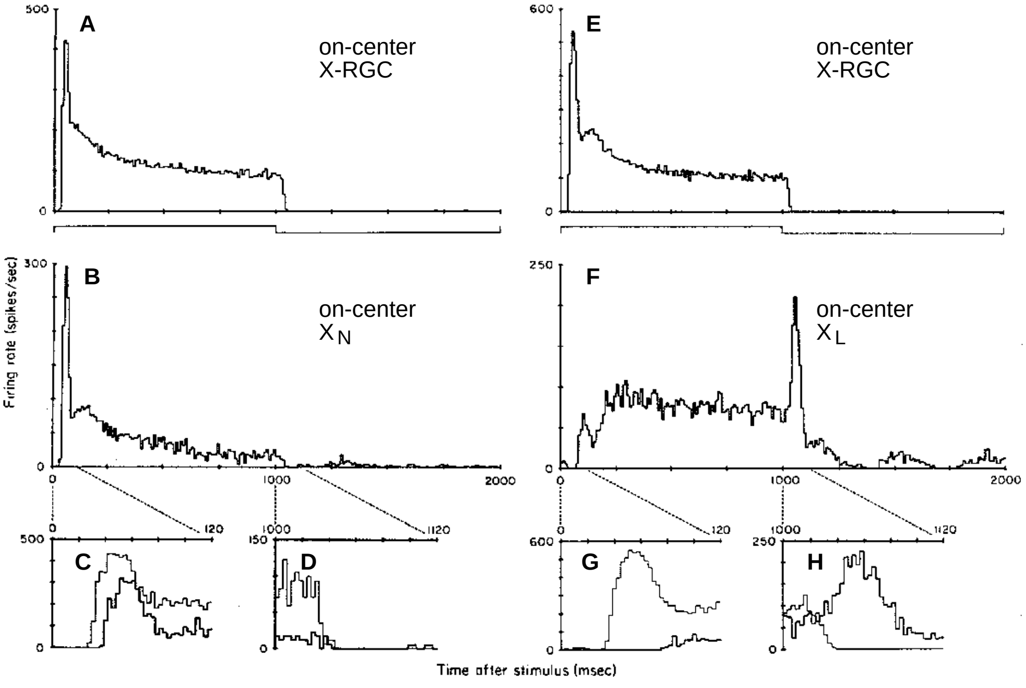

Figure 2.3: Averaged responses of lagged and nonlagged geniculate on-center X-cells (**B**, **F**) and their respective main excitatory retinal input (**A**, **E**) to a flashing central spot. The spot was on for 1 s and off for 1 s, as indicated by the traces below **A** and **E**. (**A**, **B**) Response of a nonlagged cell (X_N) and of the retinal ganglion cell (X-RGC) providing its main excitatory input. (**C**, **D**) Expanded parts of the responses in **A** and **B** at flash onset and flash offset; here thin lines show the RGC response, thick lines indicate the X_N-response. (**E**–**H**) Response of a lagged cell (X_L) and of its main excitatory retinal input (X-RGC). The bin width is 10 ms for the histograms of the entire responses and 3 ms for the expansions. The number of sweeps was 57 for the X_N-cell and 72 for the X_L-cell. Figure adapted from Mastronarde (1987a).

It turns out that lagged cells have a phase latency that is roughly 100 ms larger than, and an absolute phase that lags about a quarter cycle behind that of nonlagged cells (Saul & Humphrey, 1990); see Figure 2.5. Moreover, for the amplitude transfer [cf. equation (1.3)] it is found that lagged cells prefer lower temporal frequencies than nonlagged cells, although there is substantial overlap (Saul & Humphrey, 1990).

Unlike the X- and Y-streams of processing, which originate in the retina, the lagged and nonlagged types differentiate in the LGN. Physiological (Mas-

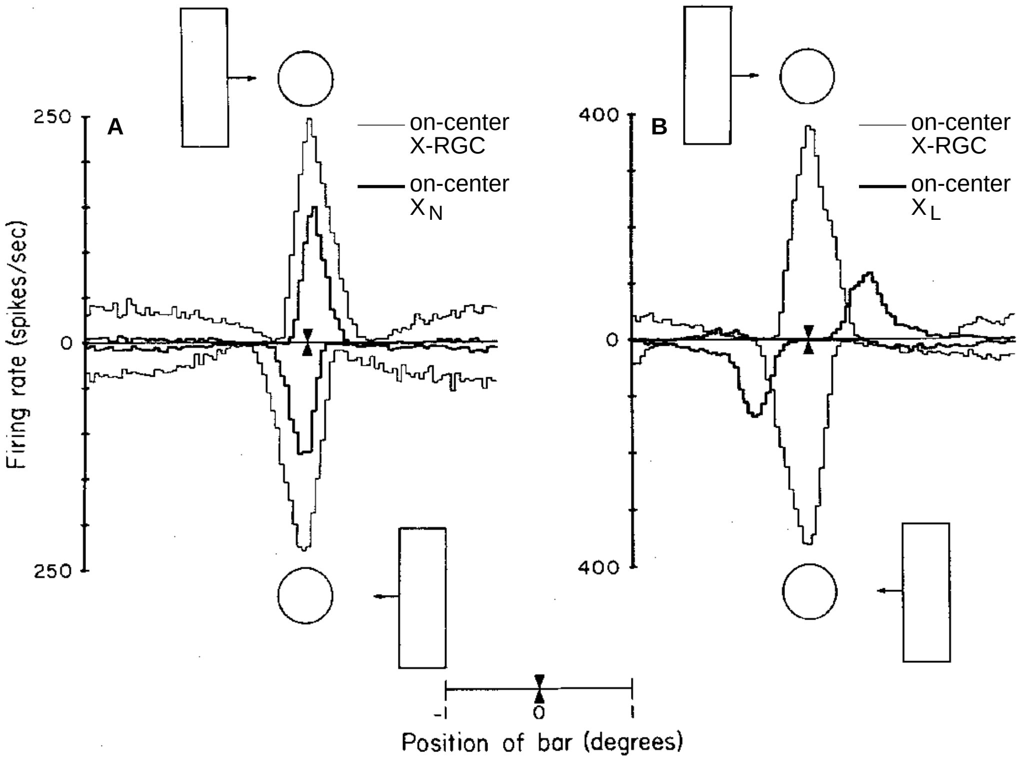

Figure 2.4: Averaged responses of nonlagged (**A**, $\mathrm{X_N}$, thick line) and lagged (**B**, $\mathrm{X_L}$, thick line) geniculate on-center X-cells and their respective main excitatory retinal input (**A** and **B**, X-RGC, thin lines) to a moving light bar. Upper and lower histograms show responses to opposite directions of motion. Double arrowheads indicate the position of the central point of the receptive fields, circles indicate the approximate size of the receptive-field centers. The width of the bar was 0.5 degrees and is drawn to scale in the figure. The bar was swept at 5 deg/s and 100 times for the $\mathrm{X_N}$-cell, 102 times for the $\mathrm{X_L}$-cell in each direction. The bin width is 10 ms. Figure adapted from Mastronarde (1987a).

tronarde, 1987b), pharmacological (Heggelund & Hartveit, 1990), and structural (Humphrey & Weller, 1988b) evidence suggests that rapid feedforward inhibition via intrageniculate interneurons plays a decisive role in shaping the lagged cells' response. According to this view, when a retinal input spike train arrives, feedforward inhibition initially prevents relay cells from firing. After some delay, inhibition declines or excitation builds up giving way to repolarization of the relay cell's membrane potential. At this point there is a low-threshold $\mathrm{Ca^{2+}}$ spike triggered by the mechanism described in section

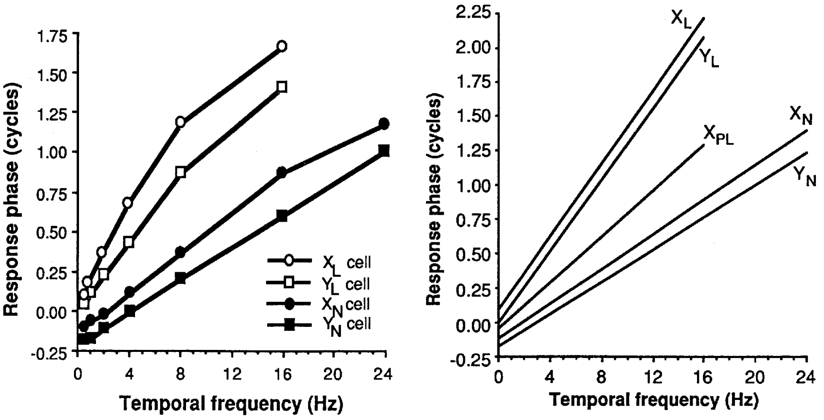

Figure 2.5: Response phase of lagged ($\mathrm{X/Y_L}$), nonlagged ($\mathrm{X/Y_N}$), and partially lagged ($\mathrm{X_{PL}}$) cells as functions of stimulus' temporal frequency. Positive response phases indicate phase lag relative to the stimulus phase. Response phases increase approximately linearly with frequency. **Left:** 4 typical cells. **Right:** Summary for a sample of cells. Lines are drawn with average slope [phase latency; $\mathrm{X_L}$: 133 ± 4 ms (33); $\mathrm{X_N}$: 63 ± 2 ms (77); $\mathrm{Y_L}$: 130 ± 14 ms (4); $\mathrm{Y_N}$: 59 ± 2 ms (30)] and offset at 0 Hz [absolute phase; $\mathrm{X_L}$: 0.096 ± 0.15 cycles (33); $\mathrm{X_N}$: -0.116 ± 0.007 cycles (76); $\mathrm{Y_L}$: -0.004 ± 0.023 cycles (4); $\mathrm{Y_N}$: -0.180 ± 0.010 cycles (27)] for each cell class [values given as *mean* ± *standard error* (*sample size*)]. Lagged and nonlagged cells are distinct, but X- and Y-cells of the same type have similar response phases. Partially lagged cells have response phases in between lagged and nonlagged cells; these cells are very rare. The phase difference between lagged and nonlagged cells is $\approx$ 0.25 cycles at low frequencies and expands to $\approx$ 0.5 cycles at 4 Hz. Figure adapted from Saul & Humphrey (1990).

1.2. The result of this series of events would be a delayed firing that starts with burst spikes. Burst spikes may also be seen in the high-activity transients just after the offset of a prolonged stimulus (Mastronarde, 1987b). We will explore the proposed mechanism of generating lagged responses in more detail below.

Some authors have additionally related differences in receptor types to the lagged-nonlagged dichotomy, suggesting that lagged responses rely more on NMDA receptors than nonlagged responses (Heggelund & Hartveit, 1990; Hartveit & Heggelund, 1990). This difference, however, could not be confirmed by Kwon et al. (1991).

Feedforward inhibition is common in X-cells, where it is anatomically concentrated in dendritic appendages called *glomeruli* (Sherman & Koch,

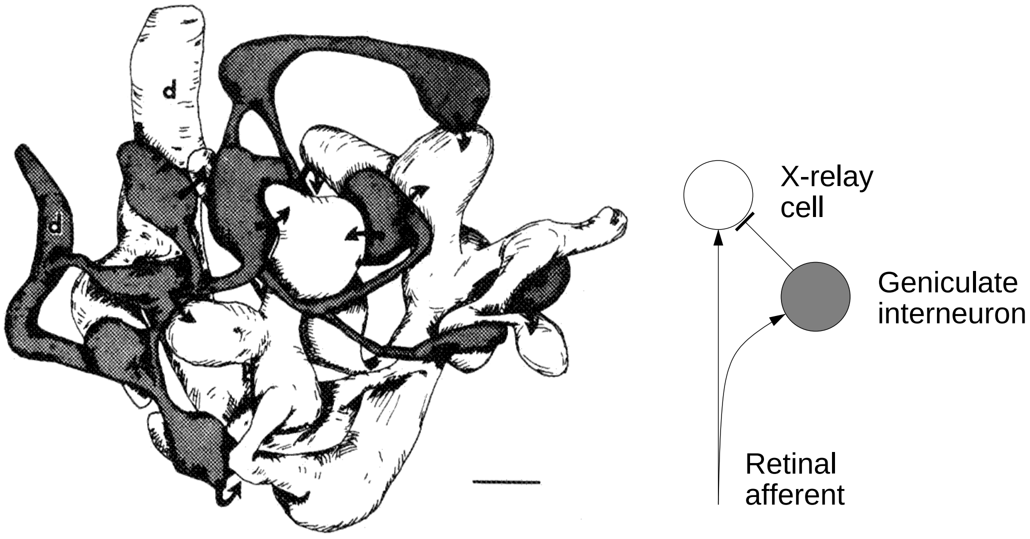

Figure 2.6: Reconstruction of a glomerular zone in the A-laminae of the cat's LGN and triadic synaptic circuit. **Left:** The stem dendrites of an interneuron and an X-relay cell are labeled "d". They both emit fine processes that are entangled with each other. The interneuron's dendrite and its process are marked by stippling, the relay cell's dendrite and its eight processes are blank. Arrows indicate dendrodendritic synapses from the interneuron to the relay cell. The scale bar represents 1.0 μm. **Right:** The synaptic triad that is realized in the glomerulus. A retinal afferent synapses on the dendrites of the relay cell and of the inhibitory geniculate interneuron, which in turn contacts the *same* relay cell dendrite. All three types of synapses coexist in close proximity in the glomerulus. Adapted from Hamos et al. (1985).

1990; Sherman & Guillery, 1996). In glomeruli, a retinal afferent synapses on the dendrites of a relay cell and of an inhibitory geniculate interneuron, which in turn contacts the *same* relay cell dendrite; see Figure 2.6. This synaptic circuit is known as *synaptic triad.* Its compact realization in glomeruli is possible because the synapse from the interneuron to the relay cell is located on the *dendrite* of the interneuron in the immediate vicinity of the contact from the retinal afferent. The synapse thus directly connects the dendrite of the interneuron to the dendrite of the relay cell and is accordingly called a *dendrodendritic* synapse. A single interneuron can in this way function as a collection of independent, very localized, feedforward inhibitors without any use of a central spike-generating mechanism at the cell's soma (Cox et al., 1998). In contrast to X-cells, glomeruli are rare on Y-cells.

Consistent with a dominant role of feedforward inhibition in the generation of lagged responses, lagged X-cells comprise about 40 % of all X-relay cells (Mastronarde, 1987a; Humphrey & Weller, 1988b), while lagged Y-cells are rather rare, accounting for roughly 5 % of all Y-cells in the A-laminae of the LGN (Saul & Humphrey, 1990; Mastronarde et al., 1991).

Layer 4B in cortical area 17 of the cat is the target of both lagged and nonlagged geniculate X-cells (Saul & Humphrey, 1992a; Jagadeesh et al., 1997; Murthy et al., 1998). The first-order spatiotemporal RFs of its direction-selective simple cells can routinely be interpreted as being composed of subregions that receive geniculate inputs alternating between lagged and nonlagged X-type (Saul & Humphrey, 1992a; Saul & Humphrey, 1992b; DeAngelis et al., 1995; Jagadeesh et al., 1997; Murthy et al., 1998); see Figures 2.2 and 2.7. This situation seems to be a natural extension to the spatiotemporal domain of the widely-accepted result that convergent and segregated geniculate on- and off-inputs outline the *spatial* structure of the simple cells' RFs (Reid & Alonso, 1995; Alonso et al., 1996; Ferster et al., 1996; Hirsch et al., 1998), giving rise to basic tuning for spatial frequency and orientation. In the spatiotemporal extension of this scenario, the gradual response latency reduction (cf. Figure 2.2) and phase advance (cf. Figure 2.7) of successive off-lagged, off-nonlagged, on-lagged, and on-nonlagged responses across the RF creates a response maximum for a certain direction and speed of motion of a properly oriented bar. This mechanism is just another implementation of the basic structure of velocity-tuned systems sketched in Figure 2.1.

As pointed out in the previous subsection, the link between the first-order spatiotemporal RF structure and responses to moving stimuli is particularly tight in the geniculate recipient layer 4B (Murthy et al., 1998). Lagged and nonlagged inputs that converge, either directly or via other cortical neurons, on simple cells are thus likely to shape the earliest level of cortical velocity selectivity (Saul & Humphrey, 1990; Saul & Humphrey, 1992a; Saul & Humphrey, 1992b; Ferster et al., 1996; Jagadeesh et al., 1997; Wimbauer et al., 1997a; Wimbauer et al., 1997b; Murthy et al., 1998). The study to follow of variable tuning of simple cells for speed is based on this assumption.

2.2 A Model of the Primary Visual Pathway

Our goal was to investigate the visual pathway from the retinal ganglion cells (RGCs) through the LGN up to cortical layer 4B as the stage where neuronal signals converge to form the first and most primitive representation of visual motion; cf. Figure 1.1 for a view of the human primary visual pathway. Importantly, the model has to allow for inclusion of effects of cortical feedback, originating from cortical layer 6, on geniculate processing. No attempt

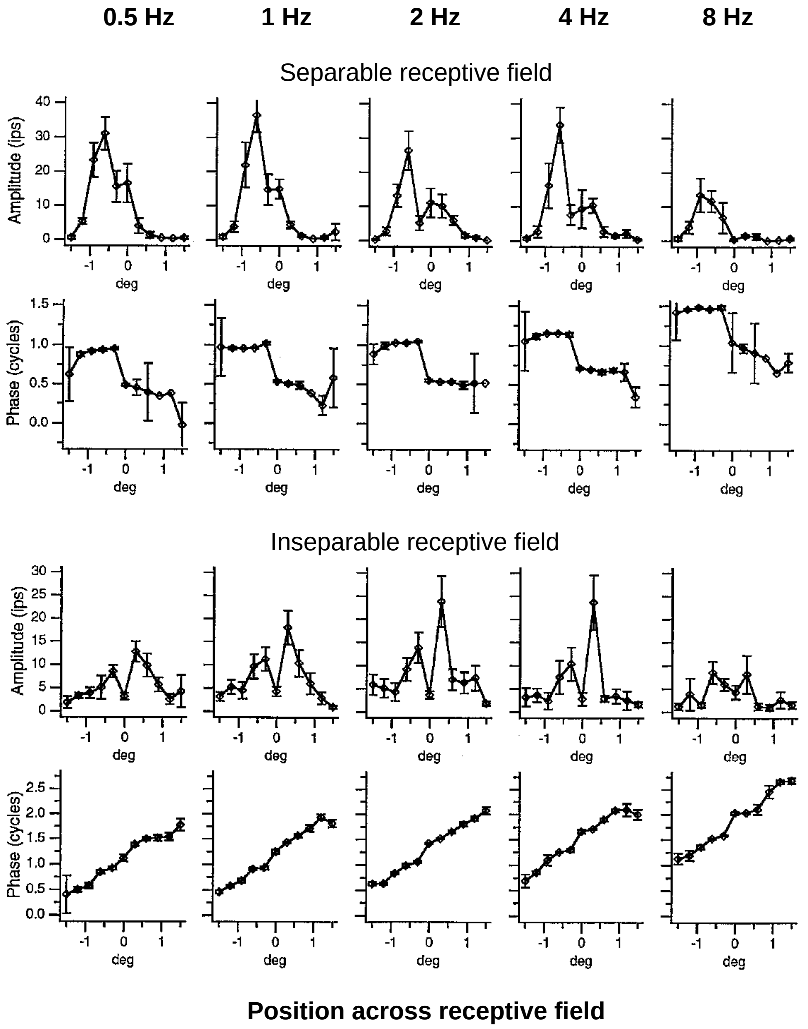

Figure 2.7: First harmonic amplitudes and phases of responses at different positions across the receptive field and for different stimulus frequencies. Means and standard errors are shown. For many of the phase values, standard errors are too small to be visible in the graphs. **Top:** Space-time separable receptive field. The response phase is rather constant across space, except for a jump of a half-cycle. This pattern is consistent with non-lagged geniculate inputs of the on- and off-types. Such a receptive field is not direction-selective; cf. Figure 2.2 **C** and **D**. **Bottom:** Space-time inseparable receptive field. There is a *gradual* increase in response phase across space, especially at low temporal frequencies. This pattern is consistent with a succession of geniculate inputs of the types off-nonlagged, off-lagged, on-nonlagged, and on-lagged; cf. Figure 2.5. Such a receptive field produces the strongest response for motion in the direction of decreasing response phase; cf. Figure 2.2 **E** and **F**. Adapted from Saul & Humphrey (1992a).

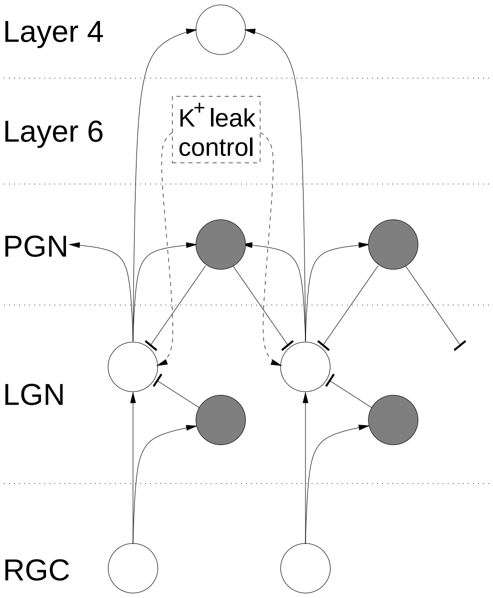

Figure 2.8: Network model of the primary visual pathway. Open/filled circles and arrow/bar heads indicate excitatory/inhibitory neurons and their respective synapses. A retinal ganglion cell (RGC) sends its axon to the lateral geniculate nucleus (LGN) and synapses excitatorily on a relay cell (open circle) and on an intrageniculate interneuron (filled circle), which in turn inhibits the same relay cell. This synaptic circuit is called 'synaptic triad'; cf. Figure 2.6. There is an inhibitory feedback loop via the perigeniculate nucleus (PGN). The relay cells' output converges in cortical layer 4. The influence of cortical feedback, originating from cortical layer 6, has been modeled as a variation of the relay cells' resting membrane potential by control of a K^+ leak current.

was made, however, to build into the model any of the intracortical processing. Doing so would necessarily have entailed many additional assumptions, many of them quite arguable, on the nature of intracortical circuits and neuron types, while obscuring the robust effect that we are going to demonstrate. The model is thus as follows.

2.2.1 Neuron and Network Models

As shown in Figure 2.8, retinal input reaches a GRC directly as excitation, and indirectly via an intrageniculate interneuron as inhibition, thus establishing the typical triadic synaptic circuit found in the glomeruli of X-GRCs (Sherman & Koch, 1990; Sherman & Guillery, 1996); cf. Figure 2.6. The temporal difference between the two afferent pathways equals the delay of the inhibitory synapse and has been taken to be 1.0 ms (Mastronarde, 1987b).

We have included feedback inhibition via the PGN (Lo & Sherman, 1994; Sherman & Guillery, 1996) in the model; see Figure 2.8. Axonal plus synaptic delays are 2.0 ms in both directions, i.e., from GRCs to PGN neurons and back.

For the GRCs we have employed the 12-channel model of Huguenard & McCormick (1992) and McCormick & Huguenard (1992) of the cat relay neuron. The neuron model includes a transient and a persistent Na^+ current, several voltage-gated K^+ currents, a voltage- and Ca^{2+}-gated K^+ current, a low- and a high-threshold Ca^{2+} current, a hyperpolarization-activated mixed cation current, and Na^+ and K^+ leak conductances. The model has been adapted to 37 degrees Celsius. In appendix A we introduce the concepts of biophysical neuron models. In appendix C we list all the ionic currents along with their mathematical description that have been implemented in the GRC model.

Intrageniculate interneurons and PGN cells, like GRCs, possess a complex blend of ionic currents. They are, however, thought to be active mainly in a tonic spiking mode during the awake state (Contreras et al., 1993; Pape et al., 1994). For an efficient usage of computational resources and time we have therefore modeled these neurons by the spike-response model (Gerstner & van Hemmen, 1992; Gerstner & van Hemmen, 1994), which gives a reasonable approximation to tonic spiking (Kistler et al., 1997). A definition of the spike-response model is given in appendix B. Using the notation introduced there, the parameters we have chosen for intrageniculate interneurons and PGN cells are given in Table 2.1. The values lie within general physiological ranges. The main difference between modeled intrageniculate and PGN cells is that the former represent in fact isolated dendritic compartments (Cox et al., 1998) (cf. subsection 2.1.2) that receive input by a single retinal afferent (see subsection 2.2.5 below), while the latter represent neurons that are driven by 100 thalamic inputs each (see subsection 2.2.4 below). The amplitude w_{exc} of responses to single input spikes has been adjusted accordingly.

There is evidence for transmission across dendrodendritic synapses between intrageniculate interneurons and GRCs without spikes (Cox et al., 1998). This question, however, is irrelevant for the present model. For a relay neuron, all that matters is the fact that an excitatory retinal input is mostly followed by an inhibitory input (Bloomfield & Sherman, 1988).

It is known that both NMDA and non-NMDA receptors contribute to retinogeniculate excitation to varying degrees, ranging from almost pure non-NMDA to almost pure NMDA-mediated responses in individual GRCs of both lagged and nonlagged varieties (Kwon et al., 1991). At least in lagged cells, however, early responses and, hence, responses to the transient stimuli that will be considered here, seem to depend to a lesser degree on the NMDA receptor type than late responses (Kwon et al., 1991). Since the essential characteristics of lagged and nonlagged responses apparently do not depend on the special properties of NMDA receptors – an assumption con-

Intrageniculate interneurons					
θ	w_{exc}	w_{ref}	τ_{exc}	τ_{ref}	T_{ref}
1.0	1.5	1.5	3.0 ms	10.0 ms	2.0 ms

PGN neurons					
θ	w_{exc}	w_{ref}	τ_{exc}	τ_{ref}	T_{ref}
depending on scenario	0.1	1.0	3.0 ms	10.0 ms	2.0 ms

Table 2.1: Spike-response model parameters for intrageniculate interneurons and neurons of the perigeniculate nucleus (PGN). See appendix B for an explanation of the parameters. For PGN neurons the threshold θ has been varied for different scenarios of PGN-feedback inhibition and is given with the results for the respective scenario in subsection 2.3.2. When comparing w_{exc} for intrageniculate and PGN neurons, it is important to note that the former represent in fact isolated dendritic compartments (Cox et al., 1998) that receive input by a single retinal afferent (see Figure 2.6 and subsection 2.2.5), while the latter represent neurons that are driven by 100 thalamic inputs each (see subsection 2.2.4).

firmed by our results (see subsection 2.3.1) – we have chosen the postsynaptic conductances in GRCs to be entirely of the non-NMDA type.

The time course of postsynaptic conductance change in GRCs following reception of an input spike at time t_{in} has been modeled by an alpha function,

$$g_{\mathrm{syn}}(t) \;=\; g_{\mathrm{synmax}}\,\frac{t-t_{\mathrm{in}}}{\tau}\,\exp\!\Big(1-\frac{t-t_{\mathrm{in}}}{\tau}\Big)\;\Theta(t-t_{\mathrm{in}})\;, \tag{2.2}$$

where Θ is the Heaviside function, i.e.,

$$\Theta(t) \;:=\; \begin{cases} 1 & \text{for } t>0, \\ 0 & \text{elsewhere.} \end{cases} \tag{2.3}$$

A plot of g_{syn} is given in Figure 2.9. More generally, if input spikes arrive at times t_i, we assume a superposition

$$g_{\mathrm{syn}}(t) \;=\; g_{\mathrm{synmax}}\sum_{i=1}^{\infty}\frac{t-t_i}{\tau}\,\exp\!\Big(1-\frac{t-t_i}{\tau}\Big)\;\Theta(t-t_i)\;, \tag{2.4}$$

which for the purpose of computer simulation is best described by the linear, second-order differential equation

$$\frac{\mathrm{d}g_{\mathrm{syn}}}{\mathrm{d}t} \;=\; -\frac{1}{\tau}g_{\mathrm{syn}}+\frac{\mathrm{e}}{\tau}h\;, \tag{2.5}$$

$$\frac{\mathrm{d}h}{\mathrm{d}t} \;=\; -\frac{1}{\tau}h+g_{\mathrm{synmax}}\sum_{i=1}^{\infty}\delta(t-t_i)\;. \tag{2.6}$$

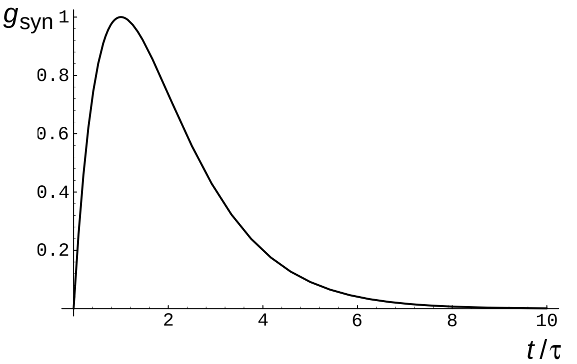

Figure 2.9: Time course of postsynaptic conductance change in modeled geniculate relay cells following reception of a single input spike at time zero (alpha function). Multiple input spikes produce a superposition of such responses; see equation (2.4). The parameter τ is the rise time of the alpha function.

Here δ denotes the Dirac-delta function. Its effect is to step up the auxiliary variable h by g_{synmax} at the times t_i. The synaptic current is

$$I_{\mathrm{syn}} = g_{\mathrm{syn}}(t)\,(V_{\mathrm{syn}} - V) \ , \tag{2.7}$$

where V is the relay cell's membrane potential and V_{syn} is the reversal potential for the synaptic current. In the model, there is an excitatory and an inhibitory synaptic current for relay cells; cf. Figure 2.8. For excitation, the rise time τ has been chosen to be 0.4 ms (Mukherjee & Kaplan, 1995), for inhibition it is 0.8 ms. The latter value was estimated from the relative durations of S potentials recorded at excitatory and inhibitory geniculate synapses (Mastronarde, 1987b) and was found to reproduce the rise times of inhibitory postsynaptic potentials recorded in relay cells following stimulation of the optic chiasm (Bloomfield & Sherman, 1988). The reversal potential V_{syn} is for excitation 0 mV, for inhibition -85.8 mV (Bal et al., 1995). The effects of different values for the peak conductance g_{synmax} of a unary postsynaptic event will be investigated in subsection 2.3.1.

2.2.2 Lagged and Nonlagged Responses

It is important to verify that typical lagged and nonlagged responses can be reproduced within the framework of our model. As will be described in detail in subsection 2.3.1, we have found typical lagged responses for strong feedforward inhibition with weak feedforward excitation, in agreement with Mastronarde (1987b), Humphrey & Weller (1988b), and Heggelund & Hartveit (1990). On the other hand, typical nonlagged responses are produced by weak feedforward inhibition with strong feedforward excitation. We have therefore implemented lagged and nonlagged relay cells in the model by varying the rel-

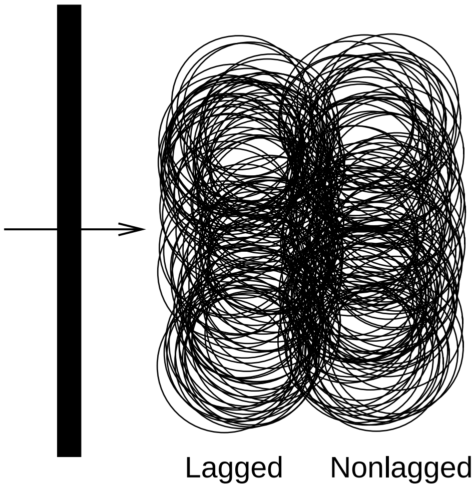

Figure 2.10: Arrangement in visual space of the receptive field (RF) centers of the 100 lagged and 100 nonlagged relay cells comprised in the model of the lateral geniculate nucleus. These relay cells are envisaged to project onto the same cortical simple cell and create an on- or off-region of the simple cell's RF. In the simulations, the diameter of a single lagged or nonlagged RF center is 0.5 degrees. Results for rescaled versions of this geometry can be derived straightforwardly from the simulations; see subsection 2.4.1. The bar and arrow on the left indicate preferred orientation and direction of motion, respectively.

ative strengths of feedforward excitation and feedforward inhibition exerted on a relay cell in the synaptic triad; cf. Figures 2.6 and 2.8.

2.2.3 Spatial Layout of Receptive Fields

The model system comprises 100 lagged and 100 nonlagged relay neurons. Their RF centers are 0.5 degrees in diameter (Cleland et al., 1979) and are spatially arranged in a lagged and a nonlagged cluster subtending 0.7 degrees each and displaced by 0.45 degrees; see Figure 2.10. More precisely, the central points of the RFs of lagged and nonlagged cells are uniformly distributed within two separate intervals of 0.2 degrees each along a certain axis, which will be the axis of bar motion during stimulation; cf. subsection 2.2.5. The RFs' offsets in the direction orthogonal to this axis, i.e., in the direction that defines the preferred orientation of the bulk RF, are irrelevant as long as the stimulus bar is long enough to pass through all RFs of the relay cells in one sweep. In fact, the bar used in the simulations is much longer than typical RFs of simple cells; see subsection 2.2.5.

The layout of geniculate inputs shown in Figure 2.10 matches the basic structure of a single on- or off-region in an RF of a directional simple cell in cortical layer 4B onto which the GRCs are envisaged to project (Saul & Humphrey, 1992a; Saul & Humphrey, 1992b; DeAngelis et al., 1995; Jagadeesh et al., 1997; Murthy et al., 1998); cf. Figure 2.8. To complete the geniculate input to an RF of this type, this lagged-nonlagged unit would have to be repeated with alternating on-off-polarity and a spatial offset that would determine the simple cell's preference for some spatial frequency; cf. Figures 2.2 and 2.7. Since we are not concerned here with effects of spatial frequency (see remark at the end of subsection 2.1.1), omission of the other on/off-regions does not affect our conclusions. Results for rescaled RF geometries can be derived straightforwardly from the simulations; see subsection 2.4.1.

The number of 200 geniculate cells contributing to a simple cell's RF has been estimated roughly from Ahmed et al. (1994). Only its order of magnitude matters.

2.2.4 Geniculate-Perigeniculate Loops

Connections between PGN neurons and GRCs are all to all within, and separate for the lagged and nonlagged populations. This synaptic separation of the lagged and the nonlagged pathways was implemented solely to allow for independent simulation of the two. Although an inhibitory coupling of lagged and nonlagged cells could in reality cause some anti-correlation of their firing, there is no evidence for anti-correlation of GRCs. Any such effects thus seem negligible. In any case, they would not affect our conclusions.

Effectively, the LGN-PGN interaction can be simulated by a lagged and a nonlagged loop that each includes only one PGN neuron of the spike-response-model type, representing an arbitrary number of real PGN neurons; cf. appendix B. The peak synaptic conductance for the inhibitory synapse of the two effective PGN neurons on their geniculate targets are $g_{\text{synmax}} = 0.05\mu\text{S}$, a value in between what we have assumed for the feed-forward inhibition received by lagged and nonlagged neurons; see results in subsection 2.3.1.

2.2.5 Retinal Input

The input to GRCs and intrageniculate interneurons has been modeled as a set of Poisson spike trains with time-varying firing rates. For investigation of the temporal transfer characteristics of lagged and nonlagged neurons, these rates varied sinusoidally between 0 and 100 spikes/s (amplitude 50 spikes/s, DC component 50 spikes/s) at a range of temporal frequencies. Before any responses to sinusoidal stimuli have been collected, the stimuli were presented for 1 second, that is, depending on the frequency, between 1 and 11 cycles. We have recorded the response for the following 100 seconds of stimulus presentation.

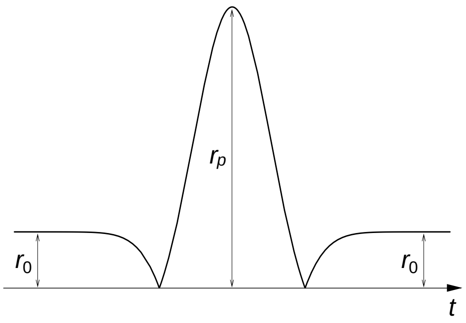

Figure 2.11: Time-dependent rate response to a moving bar of a retinal ganglion cell; cf. equation (2.8). This firing rate has been used in the simulations to generate input spikes to geniculate relay cells by an inhomogeneous Poisson process. The peak rate r_p and the width of the response peak have been adjusted for different bar speeds to fit the data of Cleland & Harding (1983). The background rate r_0 is taken to be 38 spikes/s (Mastronarde, 1987b).

For studying the responses to moving bars, rates have been fitted to recordings from retinal ganglion cells in response to moving, thin (0.1 degrees), long (10 degrees) bars (Cleland & Harding, 1983). The fit for a single retinal ganglion cell is of the form

$$\mathrm{r}(t) = \left| (r_p + r_0)\, \exp\!\left[-\left(\frac{t}{w}\right)^2 \right] - r_0 \right| , \tag{2.8}$$

where r_p is the peak rate, r_0 is the background rate, and w is a width parameter; see Figure 2.11. For the different speeds of bar motion used in the simulations, r_p and w have been chosen to fit the data of Cleland & Harding (1983) while $r_0 = 38$ spikes/s (Mastronarde, 1987b). Each pair of interneuron and GRC in a synaptic triad receive input from one retinal ganglion cell (Mastronarde, 1987b). Different interneuron-GRC pairs received retinal input from statistically independent sources; cf. Figure 2.8.

We have studied bar responses of single lagged and nonlagged neurons as well as of the entire population of 100 lagged and 100 nonlagged neurons in the geniculate model. Accordingly, bars were moved across single RFs of relay cells or the whole bulk RF in the preferred and anti-preferred directions; see Figure 2.10. Bar motion always started $3\,w$ [cf. equation (2.8)] before it hit the first RF center, and stopped $3\,w$ after it had passed the last RF center. There was a 1 second interval of stimulation with the background activity (38 spikes/s) between bar sweeps.

2.2.6 Cortical Feedback

Cortical feedback to the A-laminae of the LGN, arising mainly from layer 6 of area 17 (Sherman, 1996; Sherman & Guillery, 1996), can locally modulate the response mode (cf. section 1.2) of relay cells by shifting their membrane potentials on a time scale that is long as compared to retinal inputs. This may occur directly through the action of metabotropic glutamate and NMDA receptors (McCormick & von Krosigk, 1992; Godwin et al., 1996; Sherman, 1996; Sherman & Guillery, 1996; von Krosigk et al., 1999) and indirectly via the PGN or geniculate interneurons by activation of $\mathrm{GABA_B}$ receptors of relay cells (Crunelli & Leresche, 1991; Sherman & Guillery, 1996; von Krosigk et al., 1999).

Metabotropic glutamate receptors effect a closing of $\mathrm{K^+}$ leak channels and a membrane depolarization, while $\mathrm{GABA_B}$ receptors effect an opening of $\mathrm{K^+}$ leak channels and a membrane hyperpolarization. Accordingly, we have incorporated the influence of cortical feedback to the thalamus by varying the $\mathrm{K^+}$ leak conductance g_{Kleak} of GRCs [cf. equation (C.45) in appendix C]; see Figure 2.8. The resulting stationary membrane potential in the absence of any retinal input will be called *resting membrane potential* in this chapter. All GRCs, lagged and nonlagged, have been assigned the same resting membrane potential; here we assume a uniform action of cortical feedback on the scale of single RFs in area 17. By varying the resting membrane potential we investigate a strictly modulatory role of corticogeniculate feedback, as opposed to the retinal inputs that drive relay cells to fire; cf. Sherman & Guillery (1996), Crick & Koch (1998), and section 1.1.

For every single stimulus presentation (cf. subsection 2.2.5) we have kept the $\mathrm{K^+}$ leak conductance constant. This is justified by the slow action, compared to typical passage times of local stimulus features through RFs, of the metabotropic receptors, ranging from hundreds of milliseconds for $\mathrm{GABA_B}$ to seconds for metabotropic glutamate receptors (von Krosigk et al., 1999). Nonetheless, it is clear that dynamics in the corticogeniculate pathway may produce effects for slow-moving stimuli that we here cannot account for.

The PGN, and more generally the thalamic reticular nucleus, implements both an indirect corticothalamic feedback pathway and a disynaptic inhibitory feedback loop to relay cells (Lo & Sherman, 1994; Sherman, 1996; Sherman & Guillery, 1996). This double role suggests possible interactions between the two functions; see Figure 2.12. Depending on whether or not individual PGN neurons engage in both types of circuitry and on the connections between different PGN neurons, the strength of the disynaptic feedback inhibition exerted by PGN neurons on GRCs may be modulated by cortical feedback. The efficiency of the LGN-PGN loop may thus *covary* with the

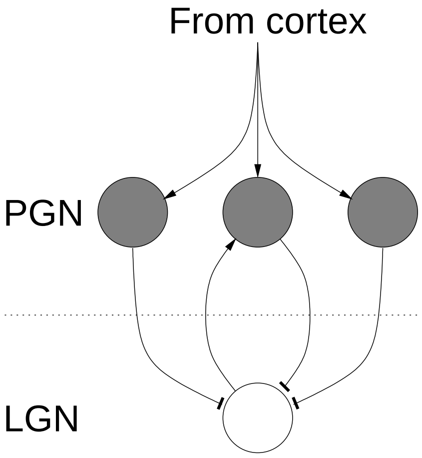

Figure 2.12: Possible interaction between the corticogeniculate pathway and the inhibitory feedback loop from the perigeniculate nucleus (PGN) back to the lateral geniculate nucleus (LGN). Same conventions as in Figure 2.8. At a higher level of cortical input, PGN neurons become more active or more excitable. More active PGN neurons shift LGN relay neurons to a more hyperpolarized level, while more excitable PGN neurons in the feedback loop increase the loop's efficiency.

GRCs' resting membrane potential.

Since cortical feedback to the thalamus and reticular nucleus is exclusively excitatory, stronger feedback makes PGN neurons more active or more excitable. More active PGN neurons hyperpolarize LGN relay cells, establishing an indirect inhibitory pathway from the cortex to the LGN. At the same time, more excitable PGN neurons that are part of a LGN-PGN-LGN synaptic loop give rise to more efficient feedback inhibition of GRCs; cf. Figure 2.12. One may speculate, therefore, that a *lower* GRC membrane potential correlates with a *more efficient* PGN-feedback inhibition.

The conclusion on the sign of correlation between GRC membrane potential and efficiency of PGN-feedback inhibition remains valid even if intra-PGN inhibition is taken into account, as long as cortical input and intra-PGN connections are assumed nondiscriminatory between neurons that do and neurons that do not involve in LGN-PGN loops. We, therefore, concentrate on investigating the effects of such a correlation.

In the model, different levels of PGN excitability are realized by adjusting the firing threshold of PGN neurons. Lower thresholds simulate more excitable neurons and, hence, implement more efficient feedback inhibition; cf. appendix B.

Due to the immense simulation times involved it has been impossible to systematically scan a certain parameter region of LGN-PGN interaction. Rather, we had to focus on a few interesting scenarios. The following scenarios of LGN-PGN interaction will be compared: no PGN feedback, three scenarios of PGN feedback increasing with GRC hyperpolarization, and constant PGN feedback. Our primary concern will be to evaluate the different scenarios for their potential to generate input to cortical neurons that is *directionally biased* and *tuned for speed*, with a significant *range* of speed preferences realized by cortical control.

2.2.7 Data Analysis

We collected spike times with 0.1 ms resolution. Spikes of single relay neurons in response to moving bars were counted in bins of 5 ms, a timescale relevant to postsynaptic integration, for variable synaptic excitatory and inhibitory input strengths. The bin counts have been averaged over 100 bar sweeps at each velocity and synaptic setting.

Spikes of single lagged and nonlagged neurons in response to sinusoidal stimulation with variable frequency f were counted in a time window of 5 ms shifted by steps of 1 ms. The spike counts were averaged over all cycles of the stimulus presented within 100 seconds of stimulation. For the resulting spike-count functions (of time within one period of input oscillation) we determined the amplitude $G_1(f)$ and the phase $\psi_1(f)$ of their first Fourier component; cf. equations (1.1) and (1.2). With the amplitude F_1 (= 50 spikes/s; see subsection 2.2.5) and the phase ϕ_1 of the sinusoidal input rate, we have calculated the amplitude-transfer function $\mathrm{a}(f) = G_1(f)/F_1$ and the phase-transfer function $\mathrm{p}(f) = \phi_1 - \psi_1(f)$, i.e., negative phase transfer means phase lead over the input; cf. equations (1.3) and (1.4).

For the investigation of velocity tuning, spikes of all 100 lagged/nonlagged relay cells were pooled. For each velocity v of bar motion tested, we calculated the total lagged/nonlagged response rates $\mathrm{r}_{\mathrm{l}}(v,t)/\mathrm{r}_{\mathrm{nl}}(v,t)$ as spike counts in 5 ms windows shifted by steps of 1 ms, i.e., $t = 1, 2, \ldots$ ms. The velocity tuning of the pooled lagged/nonlagged peak rate per neuron is

$$\mathrm{R}_\ell(v) \;=\; \frac{1}{100} \max_{t \in [t_\mathrm{i}, t_\mathrm{f}]} \mathrm{r}_\ell(v,t) \;, \quad \ell = \mathrm{l}, \mathrm{nl} \;, \tag{2.9}$$

where the times t_i and t_f are chosen such that all of the response to a bar sweep lies in the interval $[t_\mathrm{i}, t_\mathrm{f}]$.

We are primarily interested in the *total geniculate input* to a cortical simple cell onto which the GRCs are envisaged to project. To this end, we shifted lagged spikes by 2 ms to later times in order to account for the fact that the lagged cells' conduction times to cortex are slightly longer than those of the nonlagged cells (Mastronarde, 1987a; Humphrey & Weller, 1988a). Furthermore, although lagged responses in the LGN tend to be weaker than nonlagged responses (Mastronarde, 1987a; Humphrey & Weller, 1988a; Saul & Humphrey, 1990), they appear to be about equally effective in driving cortical simple cells (Saul & Humphrey, 1992a). The reason for this may lie in more efficient or numerous synapses of lagged cells than of nonlagged cells on cortical simple cells. In any case, it is beyond the scope of this work.

For the present study, we simply introduce a relative weight $\rho_\mathrm{l} > 1$ of the lagged spikes with respect to the nonlagged spikes. Using this weight we have calculated the velocity tuning of the effective geniculate input to a cortical cell,

$$\mathrm{R}(v) \;=\; \frac{1}{100} \max_{t\in[t_\mathrm{i},t_\mathrm{f}]} \left[\rho_\mathrm{l}\, \mathrm{r}_\mathrm{l}(v, t - 2\,\mathrm{ms}) + \mathrm{r}_\mathrm{nl}(v,t)\right] \ . \tag{2.10}$$

The peak input rate $\mathrm{R}(v)$ per lagged-nonlagged pair is correlated with simple-cell activity because postsynaptic potentials are summed almost linearly in simple cells (Jagadeesh et al., 1993; Kontsevich, 1995; Jagadeesh et al., 1997).

Means and standard errors have been estimated from a sample of 30 bar sweeps at each bar velocity. We have interpolated the sample-mean tuning curves $\langle \mathrm{R}(v)\rangle$ with second-order polynomials to determine the *preferred velocities* as the *maxima* of the interpolated functions $\langle \mathrm{R}(v)\rangle$. One quantity of particular interest is the *range of preferred velocities* that can be realized by cortical control, that is, by varying the GRCs' resting membrane potential.

The relative weight ρ_l in equation (2.10) is determined for different scenarios of PGN-feedback inhibition so as to *maximize* the *range* of preferred velocities at fixed ρ_l. In this way we obtain a measure of the influence of the different PGN scenarios on the lagged-nonlagged activity balance. A value of ρ_l that is close to one means that lagged and nonlagged responses arrive at the cortex in a near-optimal balance, while a value much larger than one implies that cortical synapses have to compensate a lot of nonlagged dominance for *optimal* control over speed tuning. Moreover, the maximal range of preferred velocities that can be achieved with a certain PGN scenario quantifies the fitness of that PGN scenario for the hypothetical function of *dynamic* velocity tuning.

The geniculate input rate $\mathrm{R}(v)$ to a cortical neuron depends on (i) the magnitude of the pooled lagged and nonlagged response peaks, $\mathrm{R}_\mathrm{l}(v)$ and $\mathrm{R}_\mathrm{nl}(v)$, respectively, and (ii) their relative timing. To differentiate between these two factors we have determined the times $\mathrm{t}_\mathrm{l}(v)$ and $\mathrm{t}_\mathrm{nl}(v)$ of the maxima of the lagged and nonlagged response rates, respectively,

$$\mathrm{t}_\ell(v) \;=\; \arg \max_{t\in[t_\mathrm{i},t_\mathrm{f}]} \mathrm{r}_\ell(v,t) \ , \quad \ell = \mathrm{l}, \mathrm{nl} \ , \tag{2.11}$$

and calculated the peak-time differences $\mathrm{t}_\mathrm{nl}(v) - \mathrm{t}_\mathrm{l}(v)$ as a function of the bar velocity v.

The times of the lagged/nonlagged response maxima relative to the time when the stimulus bar passes the *center* of the lagged/nonlagged RF clusters[2]

---

[2] Retinogeniculate transmission delays are set to zero in the model. Such delays would merely result in a temporal shift of the input spikes to the LGN and, hence, of all subsequent dynamics.

(cf. Figure 2.10) are denoted by $\mathrm{T}_{\mathrm{l}}(v)/\mathrm{T}_{\mathrm{nl}}(v)$.

2.2.8 Numerics

The model is described by a high-dimensional system of nonlinear, coupled, stochastic differential equations; cf. appendices A, B, and C. In fact, there are 23 equations per thalamic relay neuron, and 3 equations per spike-response neuron. The lagged and nonlagged pathways may be solved independently, resulting in two systems of far more than 2000 coupled equations each. The stochastic drive of the system is delivered by the Poissonian spike trains that model the retinal input applied to the excitatory synapses of the relay cells, expressed as a sum of delta functions in equation (2.6), and to the intrathalamic interneurons; cf. Figure 2.8 and subsection 2.2.5. Of course, there is no way of treating this system analytically.

In the computer simulations spikes were detected and transmitted between neurons with a temporal resolution of 0.1 ms. As is explained in appendix B, the spike-response neurons produce a spike when their membrane potential rises above a certain threshold; cf. Table 2.1. In the GRC model, on the other hand, spikes arise from the differential equations. For the *detection* of spikes, however, a threshold criterion for the GRCs' membrane potential has to be defined. We have set this threshold at -30 mV. At this voltage the Na^+ channel is already activated and the Na^+ current invariably produces a spike[3]; cf. Figure A.2 in appendix A and equation (C.1) in appendix C.

For numerical integration of the GRCs' dynamics we used an adaptive fifth-order Runge-Kutta algorithm[4]. The maximal time step was 0.02 ms and was scaled down to satisfy upper bounds on the estimated error per time step. Increasing or decreasing those bounds by a factor of 10 had negligible effects on the time course of the membrane potential of a GRC, and no effect on spike timing within the temporal resolution of 0.1 ms we used for detection and transmission. The dynamics of spike-response neurons has been solved by exact integrals.

Each simulation started with a 3 second period without any stimulus to allow the GRCs' dynamics to converge on its stationary (resting) state. Simulations were mostly run on an IBM SP2 parallel computer to simulate all the bar sweeps needed for a good statistics in parallel.

---

[3] Alternatively, a threshold criterion may be defined for the activation gate of I_{Na}.

[4] Note that, because of discontinuities in the system of differential equations (cf. appendix C), more sophisticated and faster methods of integration are not safely applicable.

2.3 Results

We first address the response properties of single relay neurons in the model, and then turn to the total geniculate input to a cortical neuron.

2.3.1 Lagged and Nonlagged Relay Neurons

We have checked whether both lagged- and nonlagged-type responses could be reproduced within our model by simply varying the synaptic strengths of feedforward excitation and feedforward inhibition of relay neurons; see Figure 2.8. Varying the peak postsynaptic conductances g_{synmax} [cf. equation (2.4)] for excitation and inhibition and stimulating with a bar moving at 4 deg/s we found a lagged-nonlagged transition that is analogous to a first-order phase transition in response timing; see Figure 2.13 for an example at a resting membrane potential of -65 mV. At strong excitation and weak inhibition there is a response peak with zero delay relative to the input peak. As the excitation is reduced and the inhibition increased, this nonlagged peak shrinks while a lagged peak develops. The latter invariably has a delay of roughly 100 ms relative to the input peak, a value consistent with experimental data (Mastronarde, 1987a); cf. Figure 2.4. At strong inhibition and weak excitation the lagged peak is the dominant part of the response.

We have also checked the dependence of relay-cell responses upon their resting membrane potential. The peak postsynaptic conductances g_{synmax} for the lagged cell have now been fixed at 0.0125 μS for excitation and at 0.25 μS for inhibition; for the nonlagged cell they have been fixed at 0.05 μS for excitation and at 0.0125 μS for inhibition; cf. Figure 2.13. In Figure 2.14 we show the bar response (4 deg/s) and the temporal transfer of amplitude and phase of a lagged and a nonlagged neuron for the resting membrane potentials -72 mV and -61 mV. Again, the response data agree well with experiments (Mastronarde, 1987a; Saul & Humphrey, 1990; Lu et al., 1992; Guido et al., 1992; Mukherjee & Kaplan, 1995). They are to be compared to the experimental data shown in Figures 1.6, 2.4, and 2.5. Also compare the nonlagged bar responses to the grating responses shown in Figure 1.5. Note that Figure 2.5 does not show the phase-transfer functions of lagged and nonlagged neurons, but rather the phases of their output rates, i.e., not with the phases of their retinal inputs subtracted. However, since lagged and nonlagged neurons receive the same type of retinal input, the phase difference between lagged and nonlagged outputs shown in Figure 2.5 should be comparable to the difference in their phase-transfer functions displayed in the right column of Figure 2.14. In particular, the lagged cell's response shows a phase lag relative to the input that increases with frequency; the

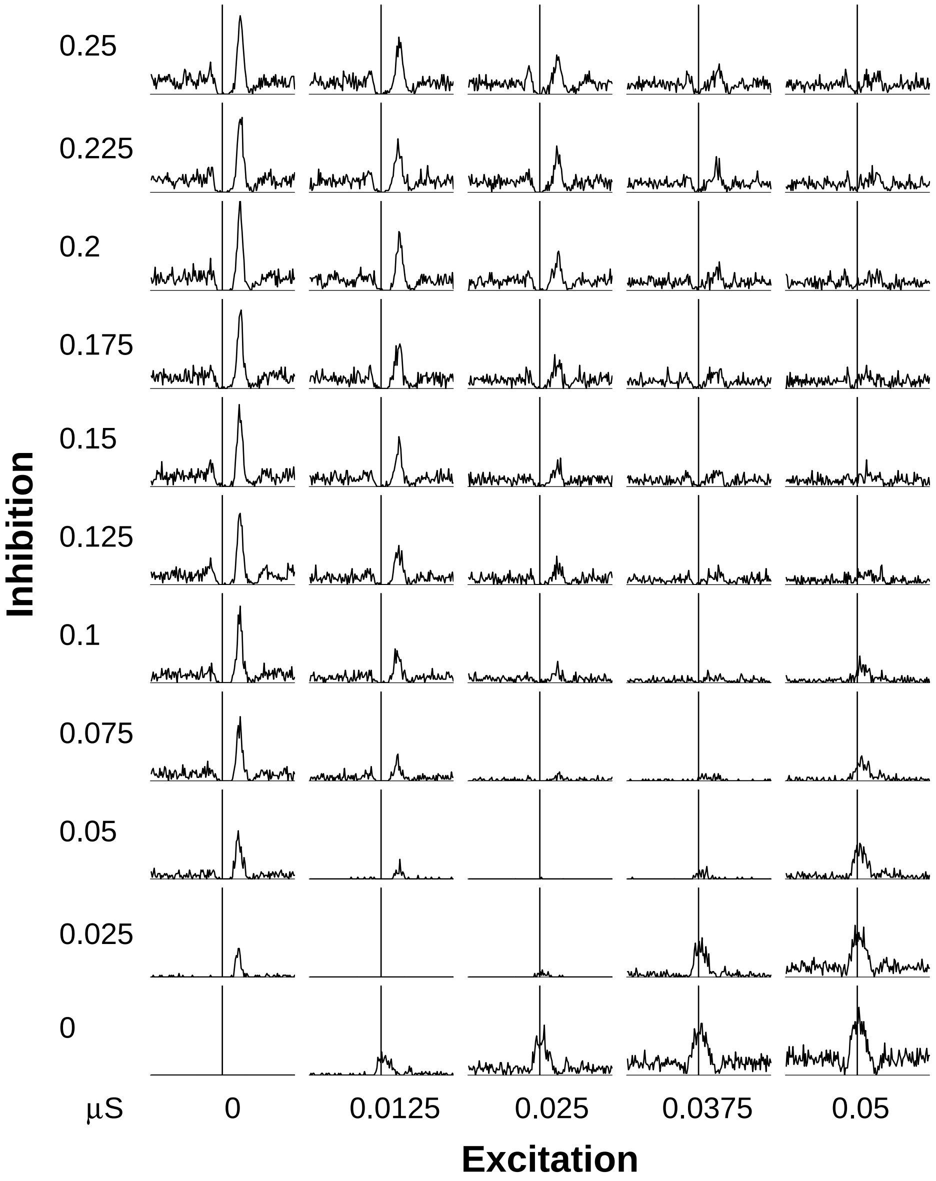

Figure 2.13: Dependence of moving-bar response of single modeled relay neurons upon the strengths of feedforward excitation and feedforward inhibition. In each plot the horizontal axis spans 750 ms; the vertical axis indicates the time of the retinal input peak and spans 100 spikes/s. Across the whole array of plots the peak postsynaptic conductances g_{synmax} (equation 2.4) vary for excitation horizontally from 0 to 0.05 μS, and for inhibition vertically from 0 to 0.25 μS. The regions of lagged- and nonlagged-type responses in this parameter space are at low excitation with high inhibition and at high excitation with low inhibition, respectively. The resting membrane potential is -65 mV. Responses are averaged over 100 bar sweeps.

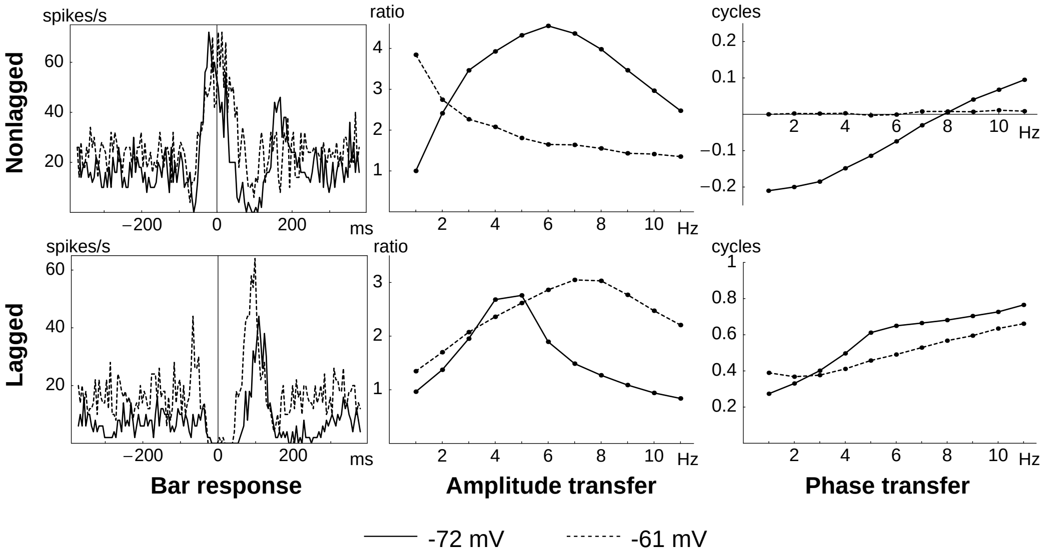

Figure 2.14: Dependence of moving-bar response and temporal transfer function of single modeled relay neurons upon their resting membrane potential. Typical nonlagged responses (top row, $g_{\mathrm{synmax}} = 0.05 \mu\mathrm{S}$ for excitation and 0.0125 μS for inhibition) and lagged responses (bottom row, $g_{\mathrm{synmax}} = 0.0125 \mu\mathrm{S}$ for excitation and 0.25 μS for inhibition; cf. Figure 2.13) have been reproduced at the two resting membrane potentials -72 mV (solid lines) and -61 mV (dashed lines). For the bar responses (leftmost column; averaged over 100 bar sweeps) the time of the retinal input peak has been set to zero. As the membrane is *hyperpolarized*, the nonlagged bar-response peak shifts to *earlier* times. Conversely, the lagged bar response shifts to *later* times. The changes in bar-response timing are also reflected in corresponding changes in the phase-transfer functions (rightmost column; note the different scales on the "cycles" axes for nonlagged and lagged cells).

nonlagged cell goes through a transition from a low-pass and in-phase relay mode to a band-pass and phase-lead (at frequencies < 8 Hz) relay mode as the membrane hyperpolarizes. The former corresponds to the tonic, the latter to the burst relay mode. Note that the slope of the phase-transfer function of lagged cells, that is, their phase latency (cf. subsection 2.1.2), is roughly twice the slope of the nonlagged phase transfer in the burst mode.

Remarkably, as the resting membrane potential is varied, the timing of the bar response shifts in *opposite* directions for lagged and nonlagged cells; cf. Figure 2.14 left column. Increasing hyperpolarization shifts the lagged response peak to *later* times, while the nonlagged response peak moves to *earlier* times. In view of what we have reported on relay modes and lagged

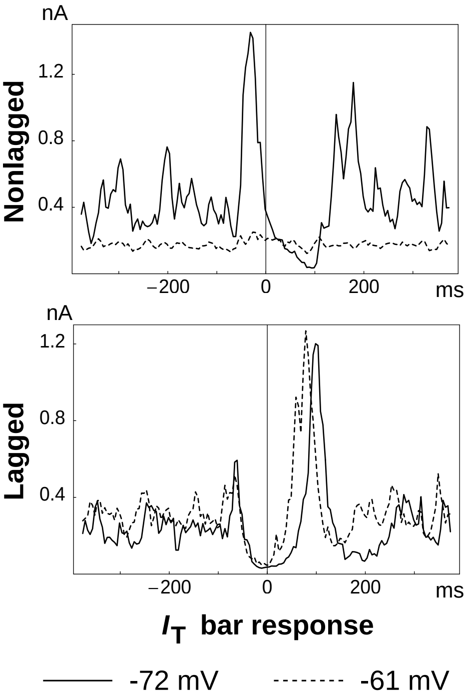

Figure 2.15: Transient and low-threshold Ca^{2+} current I_T (cf. appendix C) associated with the bar stimulus scenarios shown in Figure 2.14 leftmost column (averaged over 100 bar sweeps). High I_T indicates burst spikes mediated by underlying Ca^{2+} spikes; cf. section 1.2. For the nonlagged neuron at a resting membrane potential of −61 mV I_T is always small and does not contribute to the response. In the remaining cases the timing of the response shown in the leftmost column of Figure 2.14 can be seen to be largely determined by I_T.

cells in section 1.2 and subsection 2.1.2, respectively, it seems likely that the low-threshold Ca^{2+} current I_T [cf. Figure A.3 in appendix A and equations (C.29) through (C.33) in appendix C] is in part responsible for the GRCs' response timing. In Figure 2.15 we show simulated traces of I_T for the moving-bar scenarios. For nonlagged neurons, the current is insignificant at −61 mV, but exhibits a pronounced peak at the start of the response to the bar at −72 mV. The peak of I_T confirms the nature of the early response component seen in Figure 2.14 top left column as Ca^{2+}-mediated burst spikes (cf. section 1.2), in agreement with Lu et al. (1992), Guido et al. (1992), and Mukherjee & Kaplan (1995). For lagged neurons, on the other hand, we see that the timing of the I_T peak faithfully reflects the timing of the response peak at both resting membrane potentials. In fact, the profile of the I_T traces resembles the one of the spike rates, indicating that the Ca^{2+} current promotes firing throughout the transient responses simulated here. This result is consistent with a hypothesis by Mastronarde (1987b). We discuss the significance of burst spikes for the timing effect in subsection 2.4.2.

The reason for the opposite shifts of lagged and nonlagged response timing, then, lies in the interaction of the low-threshold Ca^{2+} current I_T with the different levels of inhibition received by lagged and nonlagged neurons. With only weak feedforward inhibition, nonlagged neurons respond to retinal input with immediate depolarization, eventually reaching the activation threshold for the Ca^{2+} current. If the Ca^{2+} current is in the de-inactivated state, it will boost depolarization and give rise to an early burst component of the visual response. The lower the resting membrane potential, the more de-inactivated and, hence, stronger the Ca^{2+} current will be, and the stronger the early burst relative to the late tonic response component. Lagged neurons, on the other hand, receive strong feedforward inhibition and, hence, initially respond to retinal input with hyperpolarization. Repolarization occurs when inhibition gets weaker. This may result either from cessation of retinal input or from adaptation, i.e., 'fatigue', of the inhibitory input to GRCs; cf. Figure 2.8. With the Ca^{2+} current I_{T} being de-inactivated by the excursion of the membrane potential to low values, lagged spiking starts with burst spikes as soon as the voltage reaches the Ca^{2+}-activation threshold. This will take longer, if the resting membrane potential is lower, leading to the shift in response timing with membrane polarization observed here.

Adaptation of inhibition is implemented in the present model by the refractoriness of the spike-response neurons that represent the inhibitory interneurons; see appendix B. The refractory potential saturates, however, on a timescale much shorter than the delay of the lagged response of roughly 100 ms; cf. Table 2.1 and Figure 2.14. Its role in generating a response delay for lagged neurons in our model can thus be only very limited.

It is important to note that the lagged on-response is *different* from a nonlagged off-response. A nonlagged off-response produces a phase lag of half a cycle relative to the nonlagged on-response at all frequencies. The right column of Figure 2.14 shows that this is not true for the simulated lagged response. Rather, the phase-transfer function has a significantly higher slope, i.e., a higher phase latency (cf. subsection 2.1.2), for the lagged response than for the nonlagged response at both resting membrane potentials. In the next subsection we will moreover show that lagged cells produce a delay of moving-bar responses that does not vanish at high speeds. This fixed delay component must be largely determined by the internal neuronal dynamics of the ion currents, notably of I_{T}, that follows hyperpolarization.

For the remaining simulations of this chapter we have always set the peak postsynaptic conductances for lagged and nonlagged neurons to the values used for the data shown in Figures 2.14 and 2.15.

2.3.2 Total Geniculate Input to the Cortex

Lagged and nonlagged responses have to be combined so as to yield a velocity-selective input to a cortical neuron; cf. Figure 2.1. We are here interested in the potential of convergent lagged and nonlagged responses to produce direction selectivity and speed tuning that *varies* with the GRCs' membrane polarization under cortical control.

As explained in subsection 2.2.1, we compare different scenarios of LGN-PGN interaction. The efficiency of the inhibitory PGN-feedback loop is varied by adjusting the firing threshold of PGN neurons. We here express firing thresholds in PGN neurons in units of the amplitudes of unary excitatory postsynaptic potentials w_{exc}, i.e., the synaptic potentials initiated in PGN cells by a single geniculate input spike; cf. appendix B. When interpreting these threshold values, one has to take into account that each PGN neuron receives input from 100 geniculate relay neurons.

For brevity, the scenarios are denoted by the sequence of pairs of PGN-threshold values $(\theta_{\mathrm{l}}, \theta_{\mathrm{nl}})$ for the lagged and nonlagged feedback loop, respectively, at the GRC resting membrane potentials -76 mV, -72 mV, -66.5 mV, and -61 mV. No PGN feedback is labeled by a threshold value of ∞. Note, however, that a finite value of ≈ 100 has virtually the same effect as no PGN, since it requires all 100 presynaptic GRCs to fire at average once within a time window shorter than 10 ms (with a rise time of postsynaptic potentials of 3 ms; see Table 2.1) in order to produce an output spike in PGN neurons. This event his highly unlikely, given the typical response rates of relay cells (cf. Figure 2.14 left column) and the fact that the 100 GRCs of lagged and nonlagged types reach their peak rate at slightly different times; cf. Figure 2.10.

PGN Thresholds $(\infty, \infty), (\infty, \infty), (\infty, \infty), (\infty, \infty)$

For different values of the resting membrane potential, Figure 2.16 shows at the top the times T_{l} and T_{nl} of the peak of the lagged and nonlagged population responses to a moving bar. With the exception of the highest speed tested, the lagged population responds between roughly 50 and 200 ms *after* the bar has passed the center of the cluster. At the highest speed ($2^{4.5} \approx 22.6$ deg/s) and resting membrane potentials of -72 mV and -76 mV the lagged response is so weak that a peak is hardly discernible; see the center of Figure 2.16 first column.

The response time T_{l} is dependent on the bar speed and on the cells' resting membrane potential. The dependence on bar speed can easily be understood as being the result of the bar traversing the lagged RFs at different speed in different time plus a constant delay. The presence of a fixed delay component is in agreement with Mastronarde (1987a). The dependence on the resting membrane potential is the same effect as the one already seen in Figure 2.14 for the single-neuron response. The lagged population response shifts to *later* times as the membrane is *hyperpolarized.*

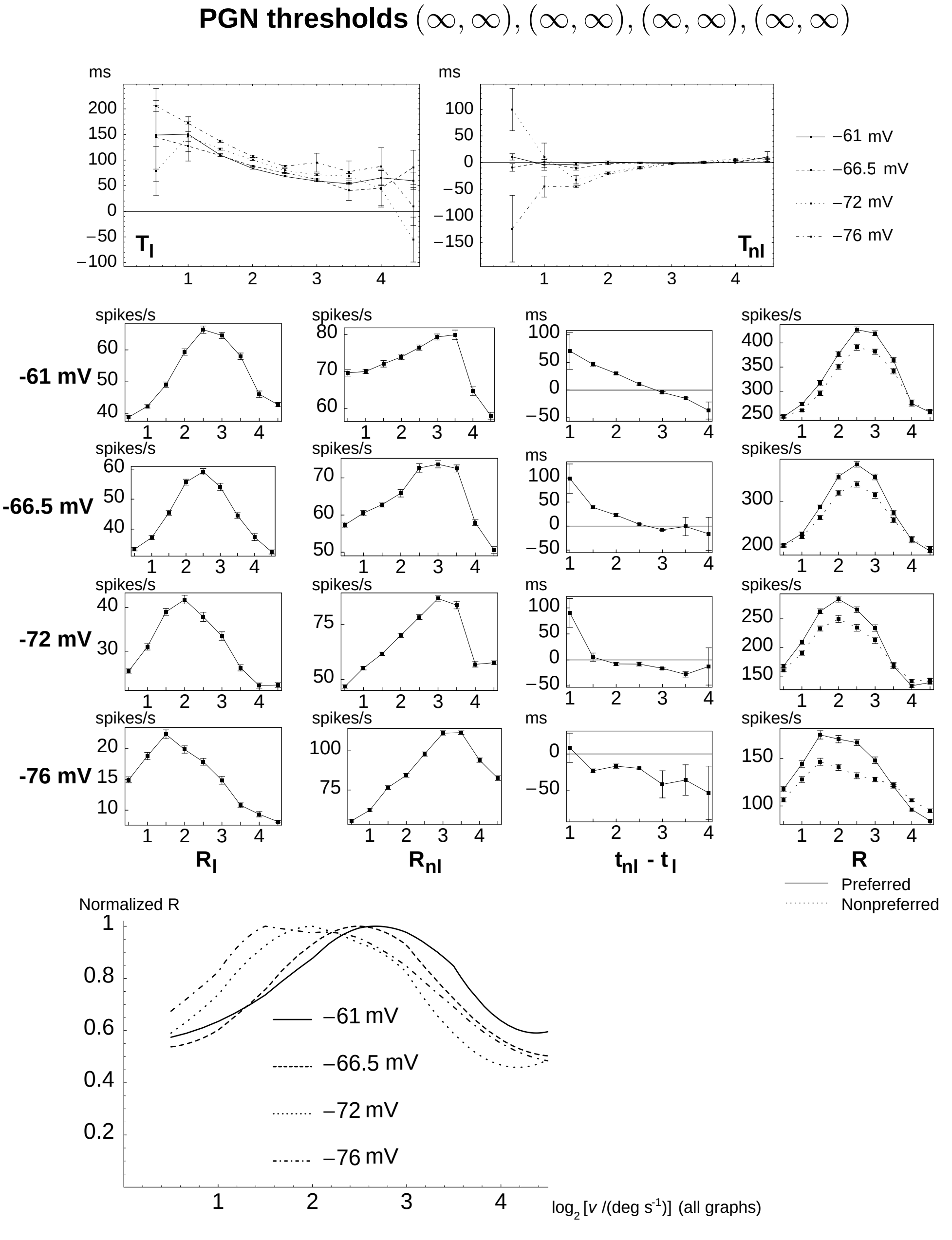

Figure 2.16: Numerical simulation of geniculate moving-bar response and input to cortex for the scenario without perigeniculate (PGN) feedback. At the **top** of the figure the peak response times of the lagged population (T_l) and of the nonlagged population (T_{nl}) are plotted as functions of the bar velocity for the resting membrane potentials indicated. The time of maximal retinal input to the center of the lagged and nonlagged populations, respectively, has been set to zero.

Figure 2.16: The array of plots in the **center** of the figure shows in the columns from left to right the peak response rate of the lagged population (R_l), of the nonlagged population (R_{nl}), their peak-time difference ($t_{nl} - t_l$) for the preferred direction, and the peak of the total geniculate input (R) to a cortical cell for the preferred (solid lines) and nonpreferred (dotted lines) direction of motion. At the **bottom** of the figure we present second-order polynomial fits to the normalized means of the total geniculate input rates R. As the membrane is *hyperpolarized*, the total geniculate input to a cortical cell and, hence, that cortical cell prefer progressively *lower* speeds. In this scenario, the dynamic range of the preferred speeds is 1.17 octaves at a lagged weight of $\rho_l = 5.5$. The horizontal axes show the logarithm (base 2) of speed in all graphs. The bars in the graphs are standard errors. Means and standard errors are estimated from 30 bar sweeps.

The nonlagged population response time T_{nl} depends as well on speed and membrane potential. With the exception of the lowest speed tested ($2^{0.5} \approx 1.4$ deg/s), where response peaks are lowest and hardly discernible at −72 mV (see the center of Figure 2.16 second column), the nonlagged population responds *before* or *when* the bar passes the center of the cluster. The population response peak is *earlier* at more *hyperpolarized* membrane potentials, as already seen in Figure 2.14 for the single-neuron response. Unlike for the lagged neurons, however, the difference between input and output peak timing vanishes at high speeds, i.e., there is no constant offset in peak timing for nonlagged cells, regardless of their membrane potential.

It is worth noting that in a *population* of nonlagged neurons that receive retinal input at slightly different times, like the 100 nonlagged neurons with spatially scattered RFs in the present simulation (cf. Figure 2.10), the *varying relative strengths* of early burst and late tonic response components leads to a more or less *gradual time shift* of the population response maximum with membrane polarization (cf. Figures 2.16 through 2.20 top right), despite the fact that the timing of burst and tonic response components in every single neuron is rather invariable.

At the center of Figure 2.16 we show for the four geniculate resting membrane potentials tested in the columns from left to right the velocity tuning of the lagged population (R_l), of the nonlagged population (R_{nl}), the peak-time differences ($t_{nl} - t_l$) of their responses for the preferred direction, and the tuning of the total geniculate input (R) to a cortical cell for the preferred and nonpreferred direction of motion. As in vivo, the lagged cells prefer lower velocities and have lower peak firing rates than the nonlagged cells (Mastronarde, 1987a; Humphrey & Weller, 1988a; Saul & Humphrey, 1990). The key observation, however, is that the maximum of the *total geniculate input rate* to a cortical neuron shifts to *lower velocities* as the membrane potential *hyperpolarizes*; see the center of Figure 2.16 right column.

At the bottom of Figure 2.16 we show second-order polynomial fits to the normalized means of total geniculate input rates for the same values of the resting membrane potential. The dynamic range of the speeds preferred by the geniculate input to a cortical neuron, and hence by that cortical neuron, is 1.17 octaves at a lagged weight of $\rho_{\mathrm{l}} = 5.5$; cf. subsection 2.2.7 for any details concerning the data analysis.

Perhaps with the exception of the case −76 mV, the total geniculate input rate R assumes its maximum at a velocity of bar motion where the peak discharges of the lagged and nonlagged neurons *coincide*, i.e., where $\mathrm{t_{nl}} - \mathrm{t_l} \approx 0$. The shift of the maximum with hyperpolarization to lower velocities is produced by a corresponding shift of the peak-time differences $\mathrm{t_{nl}} - \mathrm{t_l}$ and of the lagged tuning $\mathrm{R_l}$, while the maximum of the nonlagged tuning $\mathrm{R_{nl}}$ remains essentially unchanged. The shift of the peak-time differences, in turn, is a reflection of the opposite shifts in bar-response timing of the lagged and nonlagged populations shown at the top of Figure 2.16. At the lowest and highest bar speed tested the response timing is often not very reliable; cf. 2.16 top. We therefore have generally discarded the values of the peak-time differences at the lowest and highest speed.

Not surprisingly, the total geniculate input rate R is higher for the direction of bar motion where $\mathrm{t_{nl}} - \mathrm{t_l}$ assumes lower values. In other words, the direction preferred is the one where the lagged cells receive their retinal input before the nonlagged cells; cf. Figure 2.10 and the center of Figure 2.16 rightmost column. The rather high value of the lagged weight $\rho_{\mathrm{l}} = 5.5$, however, results in a dominance of the lagged contribution to the total geniculate input at high membrane potentials. Dominance of either component attenuates the effect of the relative *timing* of both components on the total geniculate input rate R and, hence, the directional bias of geniculate input to the cortex. The input to a cortical neuron is thus less sensitive to the direction of motion at more depolarized geniculate levels, if one considers the ratios of response rates in both directions; cf. Figure 2.16 rightmost column.

As explained in subsection 2.2.7, ρ_{l} is determined so as to maximize the range of preferred speeds that are realized by variations in geniculate resting membrane potential. The high value of ρ_{l} results from the dramatic drop in response amplitude of lagged cells with hyperpolarization; cf. center of Figure 2.16 first column. To obtain a broad range of tuning the nonlagged dominance at low membrane potentials has to be compensated, e.g., by a high value of ρ_{l}. In the following we explore a potential role of PGN feedback in moderating lagged-nonlagged differences in response amplitude. In particular, in the constant-PGN-feedback scenario we set the firing threshold lower for the PGN neurons feeding back onto nonlagged cells than for those feeding back onto lagged cells. Feedback inhibition will thus be ineffective for lagged cells at low membrane potentials, and more efficient for nonlagged than for lagged cells at all membrane potentials.

PGN Thresholds $(40, 10), (40, 10), (40, 10), (40, 10)$

We found that for these threshold settings for the PGN neurons no PGN spikes are produced in the lagged loop at resting membrane potentials of -76 mV and -72 mV. The corresponding data from the previous scenario have therefore been re-used for the present scenario[5].

Figure 2.17 summarizes the results in the same way the previous scenario was illustrated. While the response timing of lagged and nonlagged populations is essentially the same as without the PGN, the response amplitudes of the nonlagged population is strongly reduced at -76 mV and -72 mV. With the PGN feedback, the dynamic range of the speeds preferred by the total geniculate input to the cortex is 1.31 octaves at a lagged weight of $\rho_\mathrm{l} = 2.7$. Lagged and nonlagged responses are thus more balanced and allow for a larger range of velocity tuning than without PGN feedback. Moreover, because of the smaller lagged weight, the cortical input discriminates better between the preferred and the nonpreferred direction of motion.

At high resting membrane potentials the presence of PGN-feedback inhibition as applied here does not have a very strong effect on lagged and nonlagged response rates; cf. Figures 2.16 and 2.17 first and second columns. This suggests for the following studies, where feedback inhibition will be weaker for higher membrane potentials (cf. subsection 2.2.1), to re-use for -66.5 mV and -61 mV the data collected without any PGN and vary the strength of feedback at -76 mV, looking for a balancing effect of the PGN on lagged and nonlagged activity.

PGN Thresholds $(10, 10), (40, 40), (\infty, \infty), (\infty, \infty)$

Figure 2.18 summarizes the results in the same way the previous scenarios were illustrated. While the response timing of lagged and nonlagged populations is essentially the same as without the PGN, the response amplitudes of both lagged and nonlagged populations are reduced at -76 mV, but much more so for the nonlagged population. With the PGN feedback of the present

---

[5] To check consistency with the present scenario, we fed the lagged spikes from the previous scenario into a PGN neuron of this scenario. We found that no PGN spikes were produced.

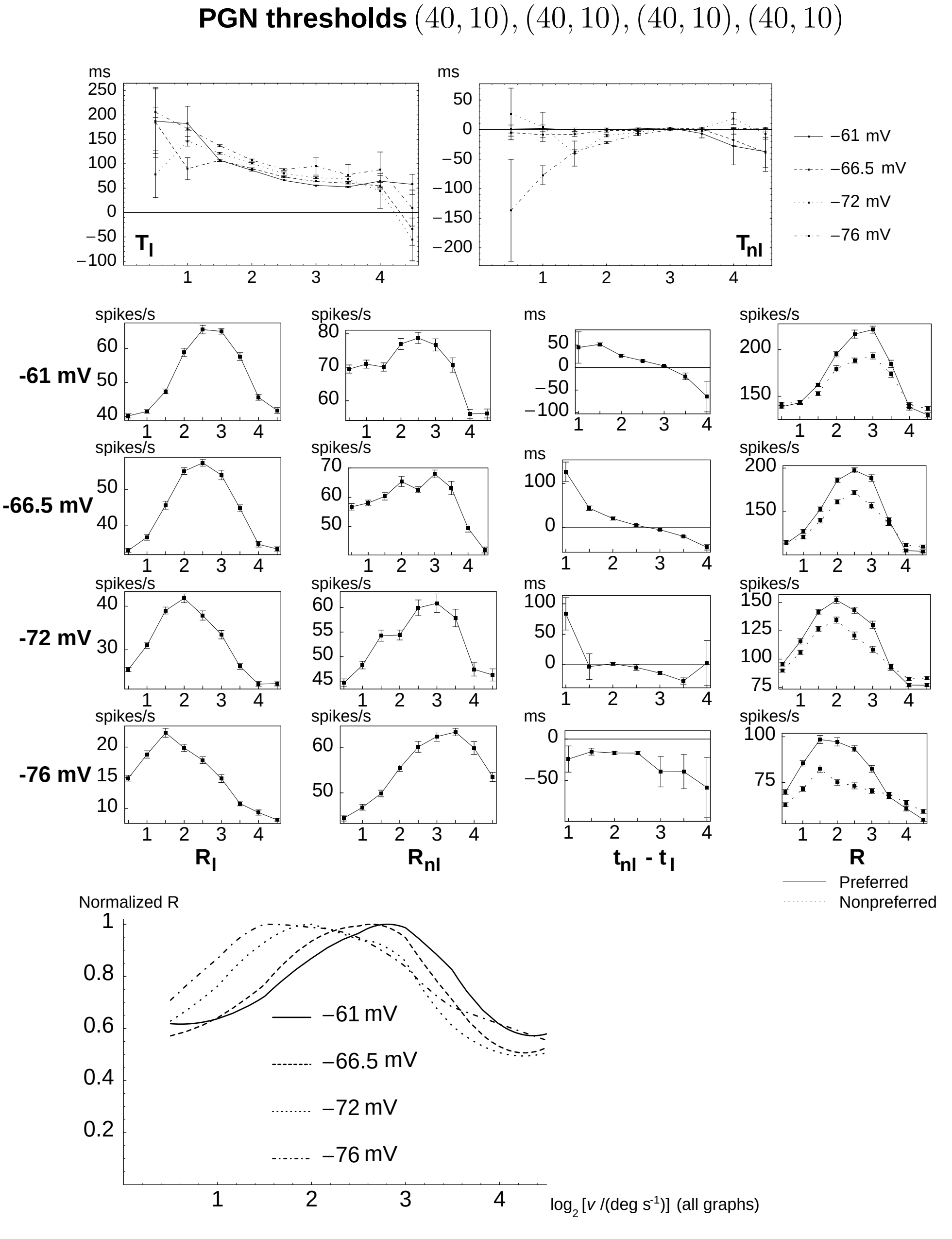

Figure 2.17: Numerical simulation of geniculate moving-bar response and input to cortex. In this scenario, perigeniculate (PGN) thresholds are 40 and 10 amplitudes of unary postsynaptic potentials for the lagged and nonlagged loop, respectively, at all resting membrane potentials. Same arrangement and conventions as in Figure 2.16. In this scenario, the dynamic range of the speeds preferred by the total geniculate input to the cortex is 1.31 octaves at a lagged weight of $\rho_l = 2.7$.

scenario, the dynamic range of the speeds preferred by the total geniculate input to the cortex is 1.16 octaves at a lagged weight of $\rho_\mathrm{l} = 7.3$. The dynamic range of tuning is thus similar to the scenario without PGN feedback. This dynamic range, however, is reached here at an even higher value of ρ_l than without the PGN. This may seem surprising at first sight, given that we successfully reduced the dominance of the nonlagged over the lagged peak response at -76 mV from a factor of roughly 5 without the PGN to slightly above 3 in the present scenario; cf. center of Figures 2.16 and 2.18 first and second columns. The reason for the still higher value of ρ_l lies in the fact that lagged and nonlagged populations do not assume their response maxima at the same speed. PGN-feedback inhibition thus has its strongest reductive effect on the firing rate at *different* speeds for lagged and nonlagged cells. It turns out that the present scenario of PGN feedback does moderate lagged-nonlagged activity differences, but yields a *less* balanced input to cortical cells as far as dynamic velocity tuning is concerned. Because of the high value of ρ_l, the directional bias is only weak in the total geniculate input to cortex; cf. center of Figure 2.18 rightmost column.

PGN Thresholds $(20, 20), (40, 40), (\infty, \infty), (\infty, \infty)$

Figure 2.19 summarizes the results in the same way the previous scenarios were illustrated. Again, the response timing of lagged and nonlagged populations is essentially the same as without the PGN. Not surprisingly, lagged and nonlagged responses at -76 mV are higher than in the previous scenario. The dynamic range of the speeds preferred by the total geniculate input to the cortex is 0.81 octaves at a lagged weight of $\rho_\mathrm{l} = 18.0$. The excessively large value of ρ_l means that the total geniculate input (R) to the cortex consists of almost only the lagged component; cf. the leftmost and the rightmost columns of the center of Figure 2.19. Accordingly, the range of dynamic tuning is nearly the one of the lagged population alone, and virtually no direction selectivity is produced for the input to cortex. In the present scenario, the lagged and nonlagged populations together do not achieve a significantly larger tuning range for speed than the lagged cells alone.

PGN Thresholds $(30, 30), (40, 40), (\infty, \infty), (\infty, \infty)$

Figure 2.20 summarizes the results in the same way the previous scenarios were illustrated. Again, the response timing of lagged and nonlagged populations is essentially the same as without the PGN. Not surprisingly, lagged and nonlagged responses at -76 mV are even higher than in the previous scenario. The dynamic range of the speeds preferred by the total geniculate

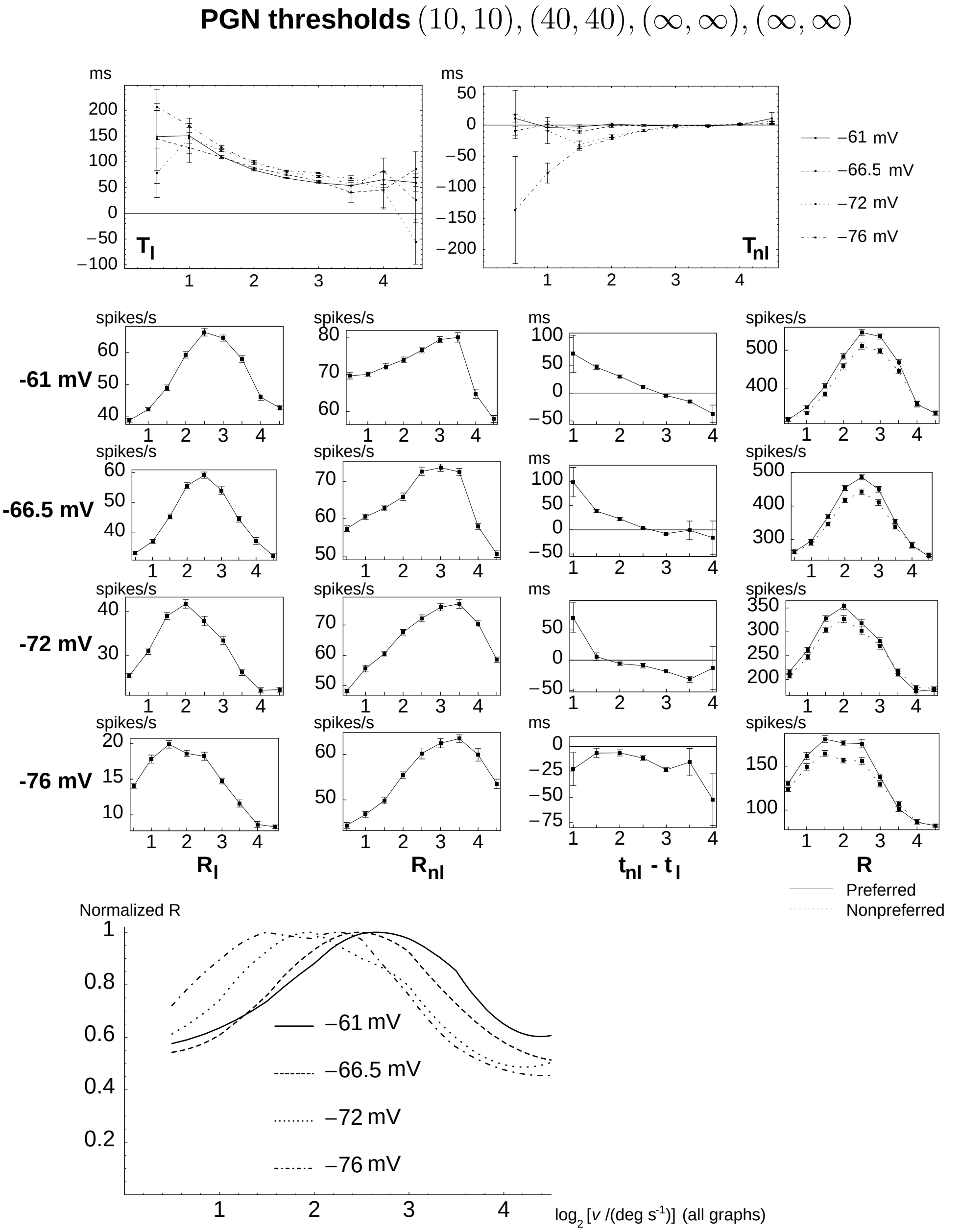

Figure 2.18: Numerical simulation of geniculate moving-bar response and input to cortex. In this scenario, perigeniculate (PGN) thresholds are 10 and 40 amplitudes of unary postsynaptic potentials at resting membrane potentials of -76 mV and -72 mV, respectively, and there is no PGN feedback at -66.5 mV and -61 mV for both lagged and nonlagged populations. Same arrangement and conventions as in Figure 2.16. In this scenario, the dynamic range of the speeds preferred by the total geniculate input to the cortex is 1.16 octaves at a lagged weight of $\rho_l = 7.3$.

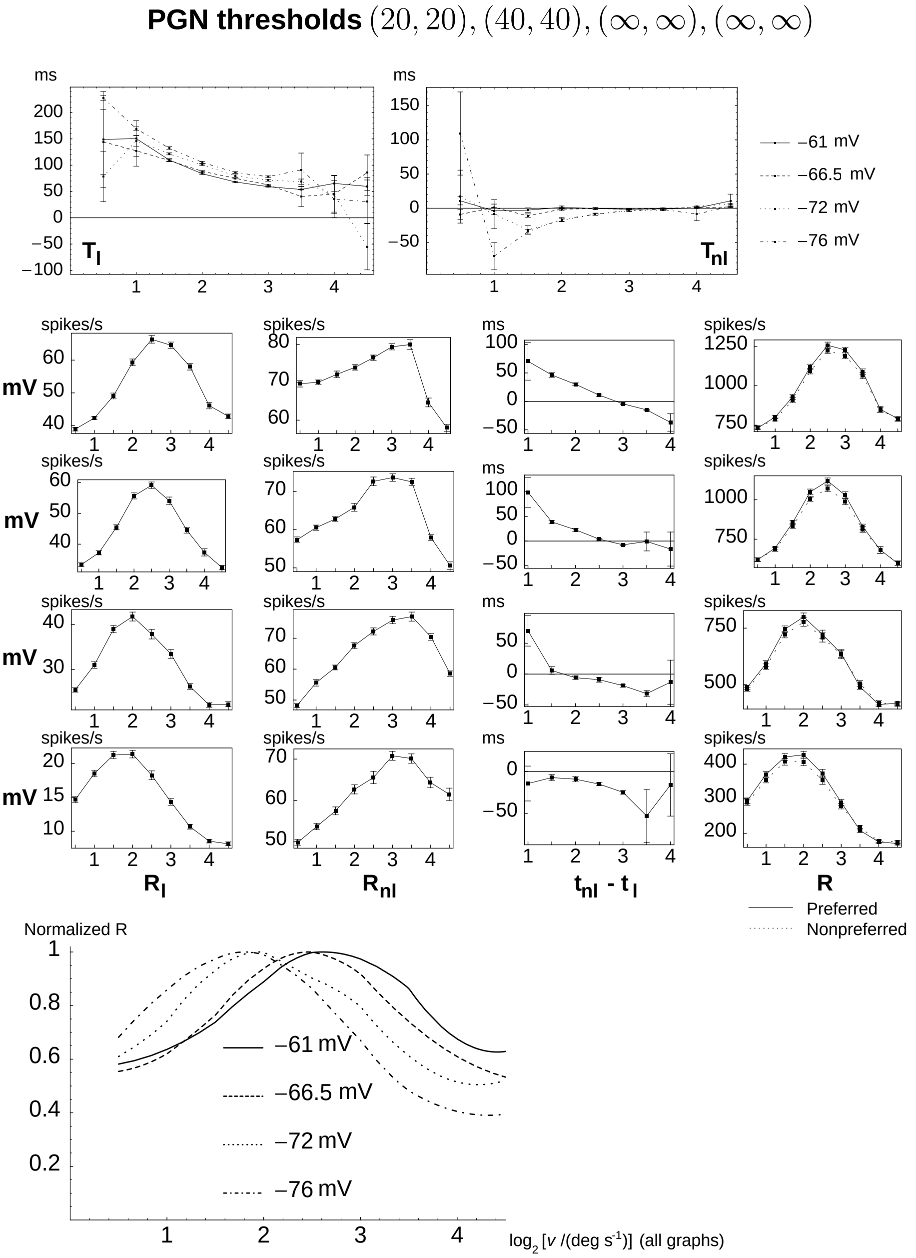

Figure 2.19: Numerical simulation of geniculate moving-bar response and input to cortex. In this scenario, perigeniculate (PGN) thresholds are 20 and 40 amplitudes of unary postsynaptic potentials at resting membrane potentials of −76 mV and −72 mV, respectively, and there is no PGN feedback at −66.5 mV and −61 mV for both lagged and nonlagged populations. Same arrangement and conventions as in Figure 2.16. In this scenario, the dynamic range of the speeds preferred by the total geniculate input to the cortex is 0.81 octaves at a lagged weight of $\rho_l = 18.0$.

Figure 2.19: The lagged responses contribute almost all of the activity to R. The dynamic range of preferred speeds is maximized by the lagged responses virtually alone. Directional selectivity of input to the cortex is essentially lost in this way.

input to the cortex is 1.18 octaves at a lagged weight of $\rho_l = 4.5$. Lagged and nonlagged responses are thus slightly more balanced than without the PGN and speed tuning varies over a slightly larger range. Moreover, at higher resting membrane potentials there is slightly more directional bias of the input rate R to a cortical neuron.

2.4 Discussion

The main point made by our modeling is that one should expect a modulatory influence of cortical feedback on the *spatiotemporal* RF structure of simple cells. More precisely, we observe a shift in the time to the bar-response peak that is *opposite* for lagged and nonlagged cells; cf. left column of Figure 2.14 and top graphs in Figures 2.16, 2.17, 2.18, 2.19, 2.20. Assuming (i) an RF layout as usually found for direction-selective simple cells in area 17, and (ii) an influence of *convergent* geniculate lagged and nonlagged inputs on this RF structure, it follows that the observed shifts in response timing and shifts in lagged tuning for speed affect cortical speed tuning. Shifts in preferred speed of the geniculate input to a cortical neuron of more than one octave are easily produced in simulations. To the best of our knowledge, nobody has looked for such an effect yet.

2.4.1 Relation to Cortical Velocity Tuning

We have investigated the geniculate input to simple cells, which clearly cannot be compared with their output directly. Because of intracortical processing we cannot expect to reproduce tuning widths and direction selectivity indices of cortical neurons. Rather, the tuning width of geniculate input is likely to be larger and its directional selectivity weaker than of a cortical neuron's output; cf. the beginning of this chapter. Indeed, superficial inspection of the rightmost column in the center of Figures 2.16, 2.17, 2.18, 2.19, 2.20 reveals that the directional bias of R tends to be rather weak compared to what is observed for directional cells in areas 17 and 18 of the cat (Orban et al., 1981a). On the other hand, the tuning width of R is relatively narrow (Orban et al., 1981b), instead of wide. This theoretical result may be rec-

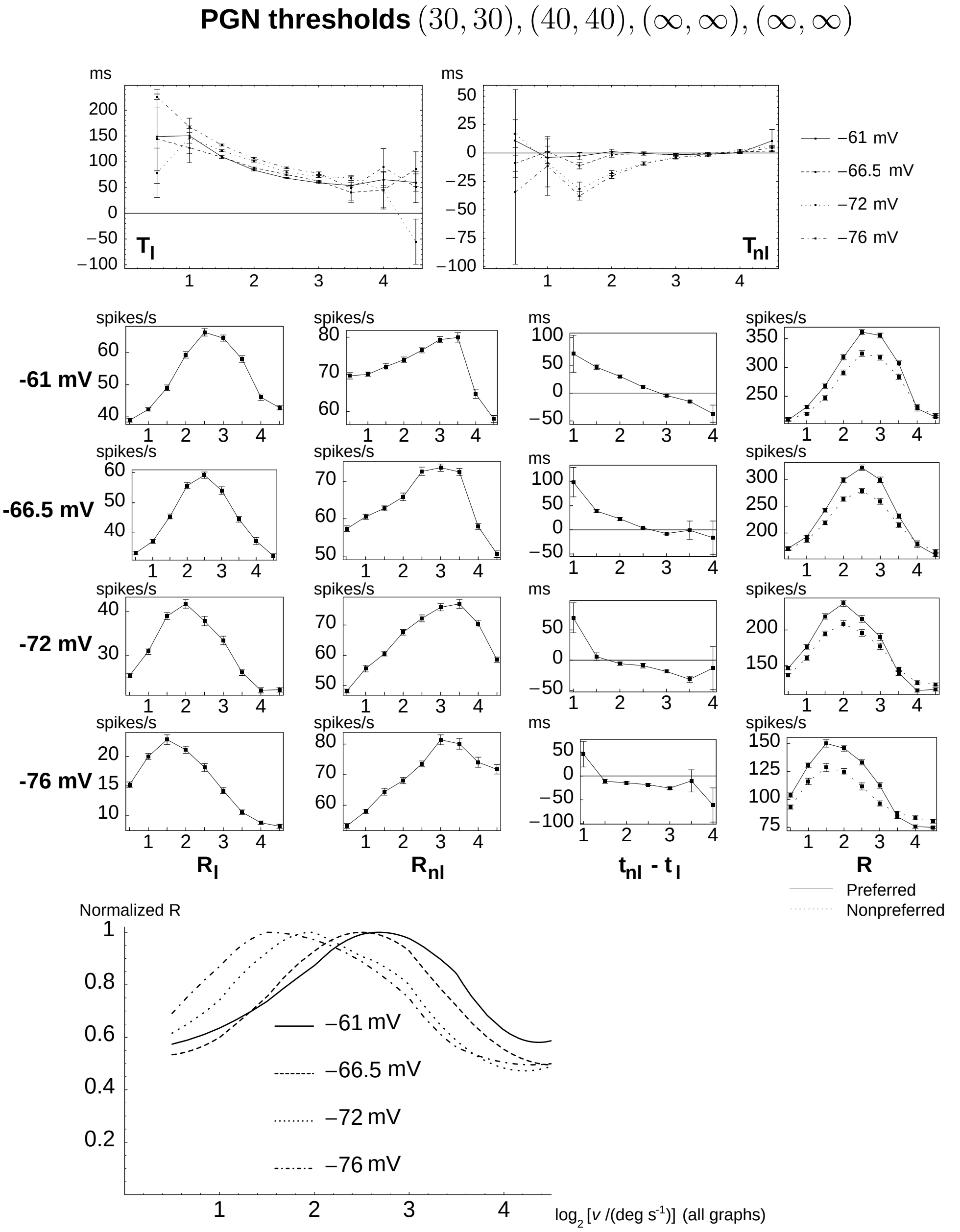

PGN thresholds $(30,30),(40,40),(\infty,\infty),(\infty,\infty)$

Figure 2.20: Numerical simulation of geniculate moving-bar response and input to cortex. In this scenario, perigeniculate (PGN) thresholds are 30 and 40 amplitudes of unary postsynaptic potentials at resting membrane potentials of −76 mV and −72 mV, respectively, and there is no PGN feedback at −66.5 mV and −61 mV for both lagged and nonlagged populations. Same arrangement and conventions as in Figure 2.16. In this scenario, the dynamic range of the speeds preferred by the total geniculate input to the cortex is 1.18 octaves at a lagged weight of $\rho_l = 4.5$.

onciled with experiment in the following ways. First, we have simulated the ideal case of equal resting membrane potential, and hence lagged and nonlagged response timing, for all of the GRCs. Scattered values of membrane potentials will produce less sharply tuned profiles for R. Second, if it is true that velocity tuning is not a *static* but a *dynamic* property of cortical cells, as is proposed in this work, measured – *effective* – tuning widths should be larger than the width of the tuning under static conditions as simulated here; see the next chapter.

Quantitative comparison of the tuning of R with cortical velocity tuning is, for the above reasons, problematic. Nonetheless, it is interesting to note that, much like velocity tuning in areas 17 and 18 (Orban et al., 1981b), the dynamic range of the modeled geniculate input, i.e., the difference between the highest and the lowest response values on each tuning curve R(v), decreases and the tuning width, measured in octaves at the rate half way between the maximum and the minimum of R(v), increases with decreasing optimal velocity in all scenarios[6]; see rightmost column in the center of Figures 2.16, 2.17, 2.18, 2.19, 2.20. Moreover, the range of preferred velocities lies within the range observed for velocity-tuned cells (Orban et al., 1981b).

Because the speed preferred by retinal ganglion cells scales linearly with their RF size (Cleland & Harding, 1983), rescaled versions of the RF geometry shown in Figure 2.10 produce accordingly shifted tuning curves (on a logarithmic speed scale). In particular, we retrieve the positive correlation between RF size and preferred speed found in areas 17 and 18 (Orban et al., 1981b) from the geniculate input.

2.4.2 Role of Relay Modes

The results presented here depend upon the special biophysical properties of thalamic relay cells that were reviewed in section 1.2. In particular, we have found different relay modes to give rise to changes in the temporal transformation performed by relay cells that support shifts in tuning for speed at the cortical level. Analogously, it has been proposed that corticogeniculate feedback modulates the *spatial* layout of simple-cell RFs by exploiting the thalamic burst-tonic transition of relay modes (Wörgötter et al., 1998).

The effects of lagged and nonlagged response timing in the present model are dependent on the low-threshold Ca^{2+} current and ensuing burst spikes. The significance of our results for visual processing in the awake, behaving animal, then, is subject to the occurrence of burst spikes under such conditions. As mentioned in section 1.2, this issue is still under much debate. For

---

[6] The correlation with tuning width was significant only in area 18 (Orban et al., 1981b).

nonlagged cells burst spikes will have a role in normal vision only, if their membrane potential gets enough hyperpolarized. For lagged cells it cannot presently be settled, if their (transient) responses are indeed supported by the low-threshold Ca^{2+} current as was seen in the simulations. If this will turn out to be wrong, the effect of cortical input on lagged response timing could be different from what we have observed. In this regard it would be interesting to study the effect of additional NMDA channels at the synapses of retinal afferents on GRCs; cf. Heggelund & Hartveit (1990) and Hartveit & Heggelund (1990). Nonetheless, the data on response timing of the modeled lagged cells suggest that some essential aspect of the true lagged mechanism has been captured in the model.

2.4.3 Role of the Perigeniculate Nucleus

We have seen that feedback inhibition by the LGN-PGN-LGN loop may increase the range of speed tuning that is realized under cortical control. It may also bring the levels of lagged and nonlagged activity that arrive at geniculocortical synapses closer to the balance that is needed for a maximal range of tuning. The type of feedback loop most adequate for this function would be more efficient for the nonlagged cells than for the lagged cells. Higher efficiency could either result from higher excitability of the involved PGN neurons, or from stronger or more numerous synapses between nonlagged cells and PGN neurons. At present there are no data available to check such an implication.

2.4.4 Variability of Geniculate Response Strength

Responses of X-relay cells to moving bars and textures are on average reduced after ablation of the visual cortex in cats (Gulyas et al., 1990). This is consistent with what we observe in our simulations of relay cells, assuming a depolarizing net effect of cortical feedback on relay neurons (Funke & Eysel, 1992; Wörgötter et al., 1998) and a lagged proportion of 40 % amongst X-relay cells (Mastronarde, 1987a; Humphrey & Weller, 1988b). In fact, the response rates of lagged neurons decrease drastically with progressive hyperpolarization; cf. center of Figures 2.16, 2.17, 2.18, 2.19, 2.20 leftmost column.

The question arises of how the visual cortex would deal with the resulting differences in the maximal geniculate input activity (cf. center of Figures 2.16, 2.17, 2.18, 2.19, 2.20 rightmost column) in a way that preserves the speed tuning of the afferent signal for a wide range of geniculate membrane polarizations. In principle this is straightforward since it is area 17 itself that modulates the membrane potential of relay cells. By a similar mechanism it could likewise adjust the responsiveness of layer 4B neurons to geniculate input. An appropriate modulatory signal could most easily be derived from the same layer 6 neurons that project to the LGN, or from their neighbors that share the same information on the actual corticothalamic feedback. In this context it is very interesting that layer 6 neurons that project to the LGN indeed send axon collaterals specifically to layer 4 (Katz, 1987).

2.4.5 Other Types of Corticogeniculate Feedback

In the model we have considered only one type of cortical input to the LGN, namely, the input mediated by metabotropic receptors that slowly control a K^+ leak conductance on GRCs. As reviewed in chapter 1, there are other cortical inputs, mediated by ionotropic receptors, that act on the much shorter timescale of the retinal inputs. While such cortical feedback certainly influences the detailed temporal pattern of geniculate spiking [see, e.g., Sillito et al. (1994)], it seems unlikely that they affect the gross timing of a transient response peak on a timescale of several 10 ms. An interesting exception is perhaps NMDA receptor-mediated feedback, with time constants in-between those of metabotropic and (ionotropic) AMPA/kainate or $\mathrm{GABA_A}$ responses. In future work it would be, therefore, interesting to include NMDA channels at corticothalamic synapses in the model.

We have presented arguments for the existence of a particular dynamic gating mechanism for thalamocortical information transfer, namely, for the transfer of information on visual motion. New experiments are required to check the implications directly. If the proposed mechanism turns out to be effective in awake, behaving animals, it will have important, as yet unrecognized, consequences for motion processing. In the next chapter we address the key question of how this gating can be controlled so as to perform biologically plausible computations.

Chapter 3

Object Segmentation by Adaptive Velocity Tuning: A Hypothesis on the Function of the Corticogeniculate Loop

In the previous chapter we have provided support for the adaptivity of cortical speed tuning under the control of corticogeniculate feedback. The question then arises, given the loop of information from the lateral geniculate nucleus (LGN) to cortical layer 4, via a variable number of synapses to layer 6, and back to the LGN (Katz, 1987; Sherman & Guillery, 1996), what are likely implications for visual information processing? Based on some fairly general considerations concerning the nature of motion information, we devise a simple model of the corticogeniculate loop that utilizes adaptive speed tuning for the fundamental task of *segmentation* of objects in *motion*. A detailed mathematical analysis of the model's behavior is presented. Treating visual stimulation as a stochastic process that drives the adaptation dynamics, we proof the model's object-segmentation capabilities and reveal some non-intended properties that are consequences of its basic design. Several aspects of the dynamics in the loop are discussed in relation to experimental data.

3.1 On Monkeys, Leopards, and other Objects in Motion

Imagine yourself being a monkey sitting in the high grass of the savanna, enjoying to get deloused by some fellow monkey, and perhaps dreaming of a banana. As you are watching the scene you turn your head and move your eyes, causing the image of grass and trees to shift over the retina in one direction or the other. Furthermore, the grass is moved by the wind, such that there is an ongoing jumble of motion even during fixation. However, you are not confused by all this. You are perceiving the world as stable and peaceful. There is nothing to attract your attention and to disturb your relaxation. Unluckily, some hundred meters away there is a leopard lurking in the high grass, greedy of some monkey meat. Since it is in camouflage you cannot see it against the yellow grass. Suddenly the leopard starts moving. It is not possible from your position to view it as a whole. There is no continuous surface, no closed contour. All you can now see are scattered bits and pieces moving behind the grass. What has really changed on your retina is the *statistics* of local motion signals. There is suddenly some component in the global density of local velocity measures which derives from scattered leopard features moving into the leopard direction at the leopard speed. Now, if evolution was any good for you, your attention is drawn to that truly significant statistical feature. Your visual system assumes all the bits and pieces sharing the same velocity to belong together. At a glance you are able to tell from their spatial distribution the size and approximate shape of that thing they belong to – and decide to escape.

There is a rich and classical psychophysical literature on the power of motion as a cue for grouping distributed features into the percept of a single entity, e.g., by Gestalt psychologists (Wertheimer, 1923; Koffka, 1935; Wertheimer, 1958), but see also Julesz (1971) and Johansson (1973). Indeed, objects that are merged with their background suddenly pop out, and sparsely distributed features which seem completely meaningless in their spatial arrangement miraculously make sense once they move. This effect works for simple coherent translational motion, i.e., with all the features sharing a common velocity, as well as for complex relative motion of features that arises from motion of objects in depth or even motion of different body parts of a walking animal. So there is good reason for confidence for the monkey's life above.

The model to be presented and analyzed in this chapter makes a suggestion as to the biological mechanisms involved in the solution to the monkey's computational problem outlined above. While motion is quite a universal cue for object segmentation, applicable to simple and complex situations, we here restrict ourselves to the discussion of a rather simple case: coherent translatory movement of spatially distributed features. This restriction allows for a clear exposition of the mechanism we propose. At the same time, it avoids speculation on the biological implementation of more complex segmentation tasks that probably involve many different areas of the visual cortex. Nonetheless, the principle of scene segmentation by adaptive tuning that is put forth in this chapter lends itself to multiple generalizations within and beyond the domain of motion processing.

3.2 Data Reduction and Object Segmentation by Motion Processing

It is often assumed that motion processing, analogous to other visual submodalities, at some low level is performed by a set of speed-tuned neurons (for various locations and directions of motion) with speed tuning curves densely sampling the entire velocity space of interest; see Figure 3.1 top. A system like this can represent the motion of all the local features in the visual field simultaneously and with high fidelity. However, this cannot be the ultimate goal of sensory processing. Instead, the input has to be *reduced* so as to only reflect the behaviorally relevant aspects of the stimulus, commonly referred to as *objects*. Thus some mechanism of selection and segmentation of the input data would still be needed to operate on the output of an abundance of velocity-tuned neurons.

For a brain (and an artificial vision system) it is certainly desirable to perform a computational task with a minimal amount of hardware. In particular, processing related to data reduction is combined most elegantly with a reduction of the hardware that would be needed for an unreduced representation since this minimizes the amount of idle components, i.e., neurons. It is thus favorable to have only *a few* velocity-tuned neurons with velocity preferences coarsely distributed in velocity space but being smartly adaptive. When being presented a moving stimulus their speed tuning curves shift so as to cluster around some *relevant* speed, the speed of an object; see Figure 3.1 bottom. In this way the representation of something relevant is *enhanced* while that of other, irrelevant features moving at different speeds is *suppressed*. An analogous scheme of adaptation might, of course, be useful to other submodalities like orientation, texture or color. Here we will confine ourself to motion processing.

The question arises: What is the basis for a system early in the visual pathway to estimate which velocity is important to behavior, which moving features are, and which are not object-related? Let us consider a stimulus like the one shown at the top of Figure 3.2. It consists of a group of scattered local features such as dots or bars, some of which move from left to right, others from right to left at various speeds. Amongst them is a subset that move at a *common* speed from left to right. It is a reasonable hypothesis for

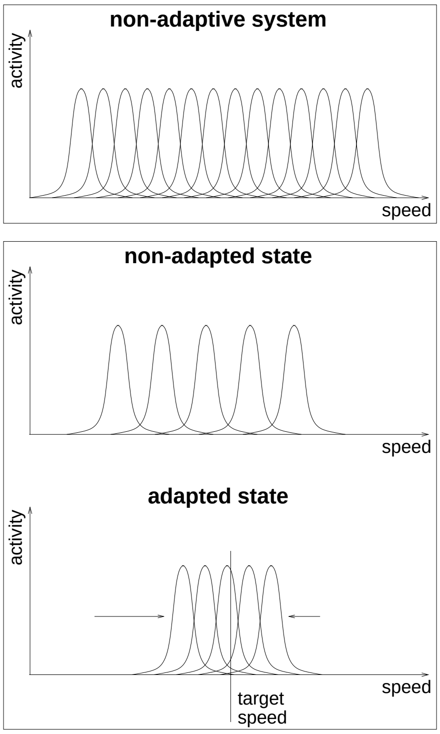

Figure 3.1: The rationale of adaptive speed tuning. The tuning curves schematically represent the peak response rate of a cortical neuron as a function of the speed of a local feature passing its receptive field. The corresponding neuron ensemble has to be replicated for multiple retinal locations and directions of motion. To be prepared to encode any possible object motion with high fidelity, a non-adaptive system needs a lot of neurons with speed tuning curves densely sampling some adequate range of speeds (**top frame**). In contrast, a system of neurons with speed tuning that adapt to the actual stimulus does the same job with only a few neurons (**bottom frame**), provided its "target speed" is the speed of the object in the stimulus. At the same time such a system performs reduction of the input data by neglecting irrelevant features moving at different speeds and segmentation of the object against a background. Data reduction and object segmentation still remain to be done with the output of the non-adaptive system.

a visual system to make that all those features that share the *same* velocity belong to the *same* entity and, hence, form an object. The bottom of Figure 3.2 shows the density of velocities in that kind of stimulus. It consists of two components. One, arising from incoherent motion, is *symmetrical* with respect to the two directions of motion; the other, representing the velocity of the coherently moving subset of features, constitutes an *asymmetric* peak. In order to exploit motion information for object segmentation the visual system has to detect and tune in to the *asymmetric* component of the velocity density. In this way coherently moving features acquire an enhanced representation while incoherent motion is suppressed.

In the motion system noise originates from neuronal activity and from ocular microtremor (Eizenman et al., 1985; Spauschus et al., 1999; Bolger et al., 1999). It is interesting to note that motion noise, by contributing directionally unbiased (false) motion signals, is part of the symmetric com-

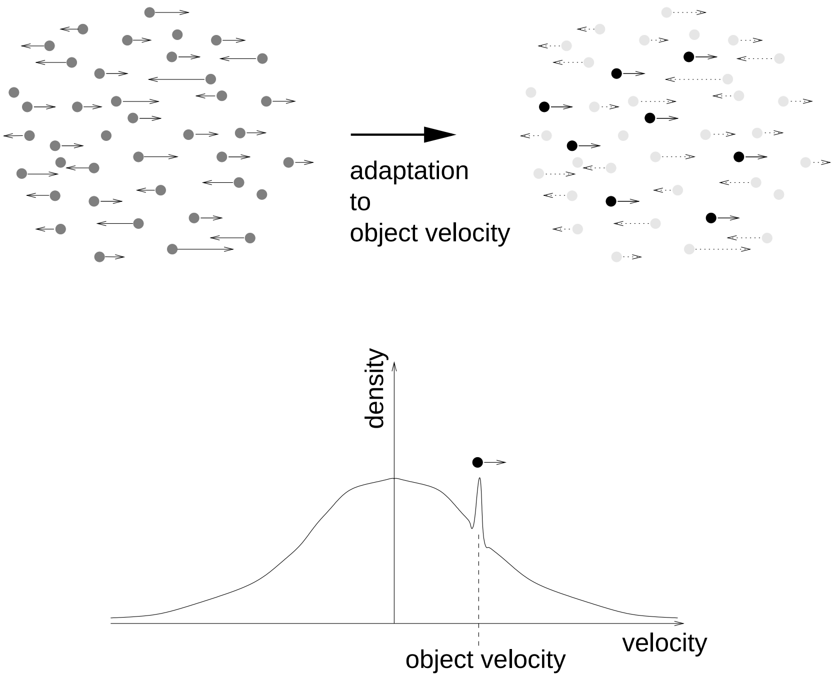

Figure 3.2: Selection of an object by coherence of motion. A collection of local features (depicted as dots, **top left**) is moving from left to right and from right to left at various speeds (depicted as arrows). A subset of them is moving at a *common* speed from left to right. The velocity density (**bottom**) of this type of stimulus consists of two components: one symmetrical with respect to the two directions of motion and one asymmetrical. The former derives from the incoherent, the latter from the coherent motion and is the statistical signature of a moving object. After adaptation of cortical velocity tuning to the asymmetric component, coherently moving features are prominent in cortical representation, whereas other features are suppressed (**top right**).

ponent of the velocity density. Noise *reduction* is thus a direct consequence of the proposed principle of object segmentation. We shall take a closer look at motion induced by ocular microtremor in subsection 3.5.3 of the discussion.

Evidently, detection of the *statistical* signature of an object in the *motion* domain requires sampling of local velocity measurements from an extended visual field, spanning several receptive fields (RFs) of cells in the primary visual cortex. Local motion information is thus to be spread either by lateral intracortical interactions, or by divergence in the corticogeniculate feedback pathway.

The stimulus scenario of Figure 3.2 is effectively one-dimensional as there are only parallel and anti-parallel velocity vectors. It generalizes, however, trivially to the two-dimensional situation, where object features give rise to an *anisotropic* peak in the bivariate velocity density. The stimulus scenario is, then, general enough to include as special cases an object moving across an incoherently moving or stationary background, an object moving in isolation without any background, and translation of a stationary scene as induced by head or eye movement.

Yet one might argue that the stimulus condition depicted in Figure 3.2 is somewhat too restricted since natural scenes do not merely consist of objects moving across incoherent or stationary backgrounds. In fact, several objects moving around often partially occlude each other, or self-movement induces motion of both an object and a background. Cats and primates, however, have a sophisticated repertoire of eye movements to track objects in motion[1] (Krauzlis, 1994). These eye movements bring the image of one out of several moving components to rest on the retina. A stationary object is analyzed by neurons preferring stationary features, mostly in the area centralis, while an overlapping object in motion may be segmented in the manner just described. Under free-viewing conditions a scene rich in moving objects could be sequentially analyzed. A plausible schedule for this analysis is that a moving object is first segmented in retinal motion and then tracked, since without prior segmentation the target of tracking would be unclear. Moreover, the statistical analysis described may be carried out in different populations of neurons in several regions and on several spatial scales of the visual field.

3.3 A Model of the Corticogeniculate Loop

Since many details of corticothalamic circuits are not known yet and since we aim at a thorough analytical treatment of the closed-loop system for general stimulus statistics we have kept the modeling at this point at a more abstract level than in the previous chapter. Moreover, the underlying principles are best exposed by a *simple* model.

The membrane potential of geniculate relay cells (GRCs) is assumed to be modulated by feedback from cortical layer 6. The postsynaptic potential evoked in GRCs by a burst of layer 6 action potentials fired around time t_i is

$$\mathrm{PSP}(t - t_i - d_i) := \frac{t - t_i - d_i}{\tau} \exp\left(1 - \frac{t - t_i - d_i}{\tau}\right) \Theta(t - t_i - d_i) \ , \quad (3.1)$$

---

[1] although cats cannot track very small targets

that is, an alpha function. Θ is the Heaviside function [cf. equation (2.3)] and $d_i > 0$ describes a corticothalamic delay. We are interested here specifically in the slow, modulatory effect of cortical input, mediated by NMDA and metabotropic glutamate receptors in the case of depolarization, and by $\mathrm{GABA_B}$ receptors for hyperpolarization. The rise time τ for combinations of NMDA and metabotropic glutamate receptor responses and for $\mathrm{GABA_B}$ receptor responses may be several 100 ms (von Krosigk et al., 1999), but is kept as a free parameter in the model, i.e., we do not specify a numerical value for τ throughout the analysis. The corticothalamic delays d_i are at least one order of magnitude smaller than τ. In particular, for layer 6 projection neurons that are visually responsive and thus relevant to our model, they are mostly below 10 ms (Tsumoto et al., 1978; Tsumoto & Suda, 1980).

As pointed out above, cortical feedback signals that carry information on local velocity measurements need to be sampled from an extended visual field, spanning several RFs of cells in the primary visual cortex. Let us label all events of cortical responses to local features within the entire population of layer 6 neurons that feed back onto GRCs by an index i according to their temporal order, i.e., $t_1 < t_2 < \ldots$. Let furthermore $\mathrm{N}(t)$ be the number of such events until time t. The slow dynamics of a GRC's membrane potential under cortical control then is

$$V(t) \;=\; \sum_{i=1}^{\mathrm{N}(t)} A_i \, \mathrm{PSP}(t - t_i - d_i) + V_0 \;, \tag{3.2}$$

where A_i is the amplitude of the ith event of cortical feedback that depends on the firing rate of a layer 6 neuron at time t_i. In this formulation the size of the layer 6 population in the adaptive system, and hence of the visual field from which motion information is integrated, is represented by the number of response events per time: the rate of events increases with the area from which motion is sampled. Lateral spread of information on local motion may be implemented either by intracortical connections, or by divergence in the corticogeniculate feedback pathway. The right side of Figure 3.3 illustrates the global connectivity of the model system.

Superimposed on the slow, cortically controlled dynamics (3.2) of the GRCs' membrane potential is the relatively fast dynamics triggered by retinal input. The latter has been modeled in the previous chapter. In the present model it will not enter explicitly. Here we only care for cortical control and for the cortical *effect* of retinal input that has been investigated in the previous chapter, that is, dynamic velocity tuning.

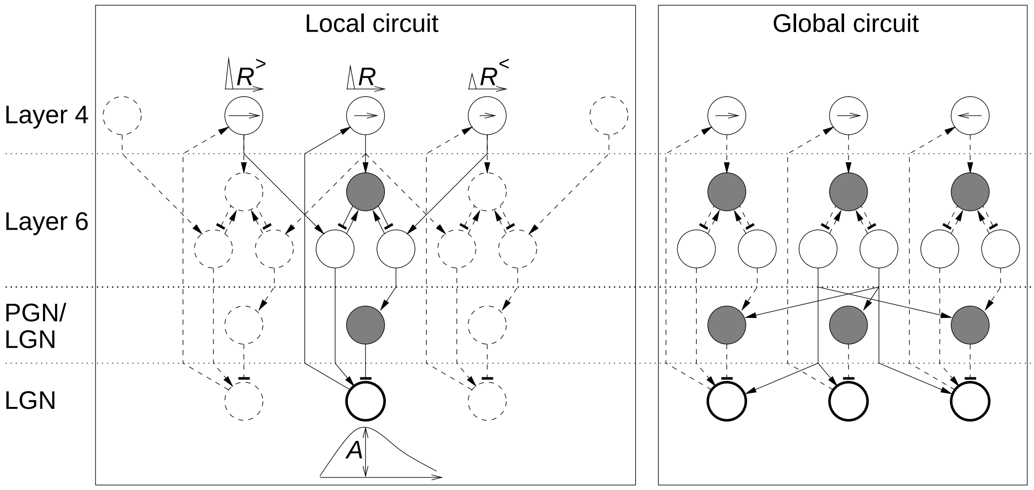

Figure 3.3: Model of corticogeniculate loop. Open/filled circles and arrow/bar heads indicate excitatory/inhibitory neurons and their respective synapses. The thick circles symbolize *all* geniculate relay cells (GRCs), lagged and nonlagged, which project to a particular cortical layer 4 cell (cf. Figure 2.10), as indicated by the long upward arrows. On the left we show a local piece of circuit (**Local circuit**). The cells depicted here in layer 4 have coinciding receptive fields, the same preferred direction but different preferred speed of motion, as indicated by the arrows of different length (a longer arrow means a higher preferred speed). The temporal responses of these cells to a moving feature have different rate amplitudes (top; amplitudes $R^>$, R, $R^<$). Cortical feedback to the lateral geniculate nucleus (LGN), originating from layer 6, modulates the membrane potential of GRCs. Direct feedback depolarizes, indirect feedback via the perigeniculate nucleus (PGN) or geniculate interneurons hyperpolarizes the membrane of relay cells. The net effect is a slow postsynaptic potential of amplitude A in GRCs (bottom). Simulation of the local circuit shows that A is well-described by equation (3.10). The dashed parts of the local circuit indicate the analogous connections that feed back to GRCs which provide input to the other local layer 4 neurons. At the right of the figure we sketch the global, or long-range, connectivity of the system (**Global circuit**). The local circuit, shown here only for one speed-tuned layer 4 neuron, is replicated for different retinal positions and two opposite directions of motion (arrows). Local circuits with identical speed tuning in layer 4 are globally interconnected by divergence in the feedback pathway. Excitatory and inhibitory inputs to the GRCs are interchanged for feedback from cortical neurons with opposite direction preferences, as indicated once for each type of feedback connection by the solid arrows.

Figure 3.3: Because of the long-range connections, each GRC receives modulatory input from cortical cells jointly representing an extended visual field, with antagonism between the two direction populations. Note that, rather than by divergence in the corticogeniculate projection, the same function could alternatively be implemented by lateral intracortical connections.

3.3.1 Dynamic Velocity Tuning

Cortical response rates in layer 4 to moving visual features such as bars are assumed to follow some kind of velocity-tuning function. In the previous chapter we have demonstrated that the velocity that produces the maximal convergent input from lagged and nonlagged geniculate relay cells is, not surprisingly, close to the velocity that yields *coincident* lagged and nonlagged response peaks, corresponding to $\mathrm{t}_{\mathrm{nl}}(v) - \mathrm{t}_{\mathrm{l}}(v) = 0$; cf. third column of the central array of plots in Figures 2.16, 2.17, 2.18, and 2.20. In this spirit we define a layer 4 cell's response rate to a feature passing its RF with velocity v in the cell's preferred direction as

$$R \;=\; \mathrm{f}[|\mathrm{t}_{\mathrm{nl}}(v) - \mathrm{t}_{\mathrm{l}}(v)|] \;, \tag{3.3}$$

where f is some positive, monotonically decreasing function. We choose f to take values between zero and one. For analytical treatment there will be some further restriction on f, to be formulated in subsection 3.3.4. Moreover, we assume layer 4 cells not to respond to features moving into their null direction. Note that we do not model the time course of the cortical response. Stimulation and response are rather treated as one instantaneous event. This approximation is acceptable as long as single cortical response periods are brief compared to the time scale of change of cortical tuning properties, that is, GRC membrane potentials.

By looking at the third column of the central array of plots in Figures 2.16, 2.17, 2.18, and 2.20, we see that the simulation data are roughly consistent with

$$[\mathrm{t}_{\mathrm{nl}} - \mathrm{t}_{\mathrm{l}}]\,(v, V) \;=\; \mathrm{s}(v) - \mathrm{c}(V) \;, \tag{3.4}$$

where s and c are monotonically decreasing functions of the stimulus velocity v and the relay cells' membrane potential V, respectively. This approximation seems to be better at higher membrane potentials. Velocity tuning is thus given by

$$R \;=\; \mathrm{f}[|\mathrm{s}(v) - \mathrm{c}(V)|] \;. \tag{3.5}$$

Note that this family of functions is rather general in that it fits a large set of velocity-tuning characteristics.

To obtain a physical interpretation of $\mathrm{s}(v)$ and $\mathrm{c}(V)$, we note that the naive understanding of the velocity-dependence of $\mathrm{t}_{\mathrm{nl}}(v) - \mathrm{t}_{\mathrm{l}}(v)$ is that it arises from the visual feature crossing the lagged-nonlagged compound RF (see Figure 2.10) in a time proportional to $1/v$. Rewriting equation (3.4) as

$$\mathrm{c}(V) \;=\; \mathrm{t}_{\mathrm{l}} - (\mathrm{t}_{\mathrm{nl}} - \mathrm{s}) \;, \tag{3.6}$$

it is evident that if s is the time it takes the visual feature to travel from the lagged RFs to the nonlagged RFs, c is the difference in response times intrinsic to the lagged and nonlagged populations. Appealing to this interpretation, we will write

$$s_i := \mathrm{s}(v_i) \;, \quad \mathrm{RTD}(t) := \mathrm{c}[V(t)] \;, \quad R_i := \mathrm{f}[|s_i - \mathrm{RTD}(t_i)|] \;, \tag{3.7}$$

and refer to s_i as the *stimulus passage time* and to $\mathrm{RTD}(t)$ as the (dynamic) *response time difference* (RTD) between the lagged and nonlagged populations. As above, the index i enumerates the stimulus/response events in temporal order. The response of a layer 4 neuron is thus maximal, if the stimulus passage time equals the lagged-nonlagged RTD.

We will use the simplest approximation for the dependence of the response time difference on the membrane potential,

$$\mathrm{RTD}(t) \;=\; -\chi V(t) + \mathrm{RTD}_0 \;, \tag{3.8}$$

that is, a linear function of V with slope $-\chi < 0$ and offset RTD_0.

3.3.2 Control of Velocity Tuning

In order to close the corticogeniculate loop, and the system of equations, we need a transformation of the layer 4 responses R_i to the feedback signals of layer 6 cells, which in turn determine the amplitudes of postsynaptic potentials A_i in GRCs. To this end, we have analyzed a simple implementation of cortical control. The rationale is that each cortical response R_i to a stimulus s_i triggers a postsynaptic potential of amplitude A_i through feedback, either directly (depolarization, $A_i > 0$), or via the PGN or geniculate interneurons (hyperpolarization, $A_i < 0$), such that the response time difference $\mathrm{RTD}(t)$ is pulled *closer* to the stimulus passage time s_i,

$$|s_i - [\mathrm{RTD}(t) + \chi A_i \mathrm{PSP}(t - t_i - d_i)]| \;>\; |s_i - \mathrm{RTD}(t)| \quad \text{for } t > t_i + d_i . \tag{3.9}$$

To understand the last inequality, note that $\mathrm{RTD}(t) + \chi A_i \mathrm{PSP}(t - t_i - d_i)$ is the RTD as it would be *without* the feedback signal initiated by s_i.

For the computation of the feedback signal a layer 4 cell's response activity serves as a measure of the amount of mismatch between RTD(t_i) and s_i: low activity indicates large mismatch, high activity signals a good match; cf. equation (3.5). The sign of mismatch is computed by comparing the outputs of layer 4 cells preferring the same direction but different speeds, corresponding to different values of V_0 in equation (3.2). A simple network of spike-response neurons, shown on the left of Figure 3.3, approximates these principles and provides the corresponding feedback signals to the LGN. More precisely, computer simulations of this network that are summarized in Figure 3.4 (see appendix F for details on the computer simulations) show that the amplitudes A_i are well described by

$$A_i \,=\, \gamma\, \mathrm{A}(R_i)\, \sigma(R_i^{>} - R_i^{<}) \ , \tag{3.10}$$

where A is some positive, monotonically decreasing function, σ is a sigmoidal function running between -1 and $+1$ with $\sigma(0) = 0$, and $R_i^{>}$, $R_i^{<}$ are response rates of layer 4 cells tuned to higher and lower speeds than the cell producing the response R_i. The factor $\gamma > 0$ describes the overall strength of cortical feedback to the LGN. To implement feedback control as outlined above, we require that $\mathrm{A}(1) = 0$, since $R_i = 1$ has been chosen as the maximum response; cf. last subsection. Moreover, we realistically have to assume some finite maximum value $\mathrm{A}(0) < \infty$, since corticothalamic neurons are not able to produce feedback amplitudes beyond some maximum. Equation (3.10) is the relation we used between layer 4 responses and amplitudes of GRC potentials. Note that it is the result of a simple transformation of the layer 4 activity to the feedback signals of layer 6 cells; cf. Figure 3.3 left. Although a LGN-layer-4-layer-6-LGN loop of synaptic connections is indeed supported by anatomical data (Katz, 1987; Sherman & Guillery, 1996), our aim was primarily to investigate a network as simple as possible that can do the necessary computation.

3.3.3 Complete System Dynamics

For the above control mechanism to work, sets of cortical layer 4 neurons are required that have overlapping RFs and *differ* in speed tuning. It is not necessary, but conceptually most straightforward, to assume the same set of n classes of neurons, defined by the initial values $V_0^{(c)}$ [cf. equation (3.2)] of their membrane potentials $V^{(c)}$, $c = 1, 2, \ldots, n$, to represent each retinal location. Accordingly, we have n dynamic variables $V^{(c)}(t)$ and $\mathrm{RTD}^{(c)}(t)$, and n series of cortical layer 4 responses $R_i^{(c)}$ and of thalamic PSP amplitudes $A_i^{(c)}$. There is, of course, only one series of stimulus passage times s_i

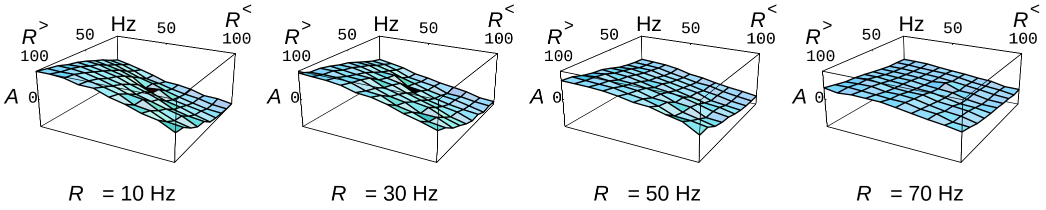

$R = 10$ Hz $R = 30$ Hz $R = 50$ Hz $R = 70$ Hz

Figure 3.4: Simulation of the amplitudes of corticothalamic postsynaptic potentials as produced by the local network shown in Figure 3.3 left. For each layer 4 neuron depicted in Figure 3.3 left we implemented 10 neurons in the simulations. The average amplitudes A (100 sweeps) are plotted in arbitrary units as function of layer 4 response amplitudes $R^>$ and $R^<$ for values of $R = 10, 30, 50, 70$ Hz. Layer 4 activity was generated as a set of Poisson spike trains with triangular time course of the rates, as sketched at the top of Figure 3.3 left. The amplitude A is well-described by equation (3.10). See appendix F for details on the computer simulations.

for the whole system. The different classes of neurons are coupled by the network computing the cortical feedback signal (cf. Figure 3.3 left), which is mathematically embodied by equation (3.10).

We want to restrict our attention to cortical neurons that prefer one out of two opposite directions of motion. For each class c of cortical neurons there are two variants selective for the two opposite directions, to be labeled by the superscripts $(c, +)$ and $(c, -)$. The interaction between the "+" and the "−" population is taken to be such that features moving in opposite directions elicit PSP amplitudes A_i of opposite signs in each GRC. This kind of antagonism ensures that the average adaptation to incoherent, directionally unbiased motion is zero (see section 3.4) and, hence, is vital to object segmentation. Measuring stimulus passage times s_i as positive in the "+" and negative in the "−" direction, and numbering neuron classes such that

$$\left|\mathrm{RTD}^{(c,\pm)}(0)\right| < \left|\mathrm{RTD}^{(c',\pm)}(0)\right| \quad \text{for } c > c', \tag{3.11}$$

the system dynamics is described by the equations

$$\begin{aligned}
V^{(c,\pm)}(t) &= \pm \sum_{i=1}^{\mathrm{N}(t)} (\mathrm{sgn} s_i) A_i^{(c)} \, \mathrm{PSP}(t - t_i - d_i) + V_0^{(c)} \;, & (3.12)\\
R_i^{(c)} &= \mathrm{f}\left[\left|s_i - \mathrm{RTD}^{(c,\mathrm{sgn} s_i)}(t_i)\right|\right] \;, & (3.13)\\
\mathrm{RTD}^{(c,\pm)}(t) &= \pm\left[-\chi V^{(c,\pm)}(t) + \mathrm{RTD}_0\right] \;, & (3.14)\\
A_i^{(c)} &= \gamma \, \mathrm{A}(R_i^{(c)}) \, \sigma(R_i^{(c+1)} - R_i^{(c-1)}) \;. & (3.15)
\end{aligned}$$

In the last equation one may define $c_0 \equiv c_1$ and $c_{n+1} \equiv c_n$ to deal with the lowest and highest values of the class index. The stimulus passage times s_i and the times t_i of the cortical responses are stochastic variables and depend on the statistics of the stimulus. Adaptation of velocity tuning and the dynamics of cortical responses are thus described as a stochastic process driven by the stimulus. Figure 3.3 attempts to give a picture of the complete system of the corticothalamic loop.

Strictly speaking, the above dynamics adapts stimulus-passage-time tuning rather than velocity tuning. To achieve the desired result, viz., adaptation to a particular object *velocity*, RF sizes have to be taken into account. Either only layer 4 cells with roughly the same RF size contribute to, and participate in, each adaptation process, or the RTD and hence the PSP amplitudes A_i are scaled to compensate for variations in RF size across visual space. For a brain to develop such systems some sort of activity-driven learning is probably required. Learning to see may thus mean to transfer the coherence of objects into synaptic circuits.

3.3.4 Analytical Treatment

The precise shapes of the functions f, A, and σ are unimportant, as long as the combination $\mathrm{A} \circ \mathrm{f}$ can be approximated reasonably well by a linear function within a relevant range of values. A full analytical treatment is possible for the limiting cases

$$\mathrm{A}[\mathrm{f}(|\,\cdot\,|)] = |\,\cdot\,| \,, \quad \sigma(\,\cdot\,) = \mathrm{sgn}(\,\cdot\,) \,. \tag{3.16}$$

With these idealizations and as long as the speed preferences of neurons retain their order, i.e.,

$$\left|\mathrm{RTD}^{(c,\pm)}(t)\right| < \left|\mathrm{RTD}^{(c',\pm)}(t)\right| \quad \text{for } c > c',\, t > 0, \tag{3.17}$$

equation (3.15) simplifies so as to give

$$A_i^{(c)} = \gamma\,(\mathrm{sgn} s_i) \left[\mathrm{RTD}^{(c,\mathrm{sgn} s_i)}(t_i) - s_i\right] \,. \tag{3.18}$$

The dynamics of the different classes c decouple and the class superscript c can be dropped. Combining equations (3.12), (3.13), (3.14), and (3.18), and dropping the class superscript c we get

$$\mathrm{RTD}^{(\pm)}(t) = \chi\gamma \sum_{i=1}^{\mathrm{N}(t)} \left[s_i - \mathrm{RTD}^{(\mathrm{sgn} s_i)}(t_i)\right] \mathrm{PSP}(t - t_i - d_i) \underbrace{\pm (-\chi V_0 + \mathrm{RTD}_0)}_{=\mathrm{RTD}^{(\pm)}(0)} \,. \tag{3.19}$$

If, on the other hand, condition (3.17) is violated, i.e., if speed preferences *cross* in the course of adaptation, the system will produce PSP amplitudes $A_i^{(c)}$ of the wrong sign [cf. equation (3.15)] and adaptation will be disrupted. Stimulus conditions under which crossing is likely to occur are derived in subsection 3.4.7. Note, however, that, because of the finite slope of the sigmoidal σ at zero, PSP amplitudes $A_i^{(c)}$ get small, if the RTDs of classes $c-1$ and $c+1$ come close to each other; cf. equation (3.15). This fact endows the true system dynamics with a certain robustness to disruption of adaptation by crossing of RTDs.

3.3.5 Computer Simulations

Computer simulations were run using

$$\mathrm{A}[\mathrm{f}(|\ \cdot\ |)] = \begin{cases} |\ \cdot\ | & \text{if } |\ \cdot\ | < p, \\ p & \text{elsewhere,} \end{cases} \qquad \sigma(\ \cdot\ ) = \tanh(q\ \cdot\ )\ , \tag{3.20}$$

with positive parameters p and q. See appendix G for details.

3.4 Analysis and Results

In this section we derive analytic results on the dynamics of the above model. We moreover illustrate the results by computer simulations wherever appropriate.

In the first subsection we derive integral equations for the moments of the RTDs, which arguably is the ‘obvious’ approach to the problem. The solution that can be obtained in this way, however, has a drawback in that it does not tell what individual trajectories look like. In the second subsection we therefore cast the dynamic equations in the form of a Markov chain. Making use of the Markov property in the remaining subsections we gain insight not only in the *statistics* of RTD dynamics, but also in the temporal pattern of *individual* trajectories. Another significant advantage of the Markov formulation is that it allows us to give far-reaching results without specifying the stochastic process that underlies the stimulus presented to the system.

3.4.1 Integral Equations for the Moments of Response Time Differences

We start by reformulating equation (3.19). Absorbing $\chi > 0$ into $\gamma > 0$ and introducing the notation

$$\Delta \ := \ \mathrm{RTD}^{(+)}(0)\ , \tag{3.21}$$

$$x(t) \; := \; \mathrm{RTD}^{(+)}(t) - \Delta \; , \tag{3.22}$$

we can write

$$\mathrm{RTD}^{(\pm)}(t) \; = \; x(t) \pm \Delta \tag{3.23}$$

and formulate the dynamics (3.19) as

$$\begin{aligned} x(t) \; &= \; \sum_{i=1}^{\mathrm{N}(t)} A_i \, \mathrm{PSP}(t - t_i - d_i) \; , &(3.24)\\ A_i \; &= \; \mathrm{F}[x(t_i), s_i] \; , &(3.25)\end{aligned}$$

with

$$\mathrm{F}(x, s) \; := \; \gamma \, [s - (\mathrm{sgn} s) \, \Delta - x] \; . \tag{3.26}$$

We can now derive integral equations for the moments of x and, hence, of $\mathrm{RTD}^{(\pm)}$ as a function of time.

Let $\mathrm{f}_1(t)$ and $\mathrm{f}_2(t, t')$ be the one- and two-point distribution functions, respectively, of the point process that describes the times of cortical responses to stimulus features. We use the notation

$$\begin{aligned} \langle \mathrm{g}(s) \rangle \; &:= \; \int_{-\infty}^{\infty} \mathrm{d}s \, \mathrm{v}(s) \, \mathrm{g}(s) \; , &(3.27)\\ \langle \mathrm{g}[x(t)] \rangle \; &:= \; \int_{-\infty}^{\infty} \mathrm{d}x \, \mathrm{p}_t(x) \, \mathrm{g}[x(t)] \; , &(3.28)\end{aligned}$$

where $\mathrm{v}(s)$ is the density of stimulus passage times, $\mathrm{p}_t(x)$ the density of x at time t, and g is some function on the reals for which the integrals are defined. The temporal evolution of the first moment of x is governed by the integral equation

$$\langle x(t) \rangle \; = \; \int_0^{\infty} \mathrm{d}t' \, \mathrm{f}_1(t') \; \langle A \rangle_{t'} \; \langle \mathrm{PSP}(t - t') \rangle \; , \tag{3.29}$$

with

$$\begin{aligned} \langle A \rangle_t \; &:= \; \int_{-\infty}^{\infty} \mathrm{d}A \, \mathrm{p}(A|t) \, A \; , &(3.30)\\ \langle \mathrm{PSP}(t) \rangle \; &:= \; \int_0^{\infty} \mathrm{d}d \, \mathrm{w}(d) \, \mathrm{PSP}(t - d) \; , &(3.31)\end{aligned}$$

where $\mathrm{w}(d)$ denotes the density of corticothalamic delays and $\mathrm{p}(A|t)$ the conditional probability of having an amplitude A of a corticothalamic PSP, given that there is cortical input to the thalamus at time t. This conditional probability can be written as

$$\mathrm{p}(A|t) \; = \; \int_{-\infty}^{\infty} \mathrm{d}x \, \mathrm{p}_t(x) \int_{-\infty}^{\infty} \mathrm{d}s \, \mathrm{v}(s) \, \delta[A - \mathrm{F}(x, s)] \; ; \tag{3.32}$$

cf. equation (3.25). Here δ is the Dirac delta function. Substituting equations (3.26), (3.30), and (3.32) into (3.29), we get

$$\langle x(t)\rangle = \gamma \int_0^\infty \mathrm{d}t'\, \mathrm{f}_1(t')\, \left(\langle s\rangle - \mu\,\Delta - \langle x(t')\rangle\right) \langle \mathrm{PSP}(t-t')\rangle \;, \tag{3.33}$$

where we have introduced the difference μ between the statistical weights of motion in the two opposite directions,

$$\mu := \int_0^\infty \mathrm{d}s\, \mathrm{v}(s) - \int_{-\infty}^0 \mathrm{d}s\, \mathrm{v}(s) \;. \tag{3.34}$$

Analogously, the dynamics of the second moments of x is governed by

$$\left\langle x(t)\, x(\hat{t})\right\rangle = \int_0^\infty \mathrm{d}t'\, \mathrm{f}_1(t')\, \left\langle A^2\right\rangle_{t'} \left\langle \mathrm{PSP}(t-t')\, \mathrm{PSP}(\hat{t}-t')\right\rangle \tag{3.35}$$

$$+ \int_0^\infty \mathrm{d}t' \int_0^\infty \mathrm{d}t''\, \mathrm{f}_2(t',t'')\, \langle A\rangle_{t'}\, \langle A\rangle_{t''}\, \langle \mathrm{PSP}(t-t')\rangle \left\langle \mathrm{PSP}(\hat{t}-t'')\right\rangle \;.$$

Here we have assumed that stimulus passage times and corticothalamic delays are sampled from their respective densities *independently* at each event of cortical response. This assumption is justified for the chronological sequence of *all* stimulus/response events in an extended retinal region. Spatiotemporal correlations that may be present in the stimulus do not show up since passage-time samples are mixed in the sequence irrespective of retinal location.

In an analogous manner integral equations can be formulated for higher-order moments of x. Since F is a linear function of x, it is possible to successively solve for the moments up to any order, starting with the first order, equation (3.33). The integral equations may be solved by Laplace transform.

In the next subsection we will develop an alternative formulation of the system dynamics that is based on a Markov chain. The advantage over the present formulation is that, by exploiting the Markov property of the dynamics, we gain insight not only in the dynamics of the moments, but also in the behavior of *individual realizations* of $x(t)$. Moreover, while in the present formulation of the problem it is necessary to specify the distribution functions $\mathrm{f}_1(t)$, $\mathrm{f}_2(t,t')$, etc. in order to proceed, we will see that it is possible to derive far-reaching results within the Markov formulation without specifying the stochastic process underlying the stimulus.

3.4.2 Markov Formulation of the Dynamics of Response Time Differences

As in the last subsection, we start by reformulating equation (3.19). We absorb $\chi > 0$ into $\gamma > 0$ and introduce the notation

$$\begin{aligned}
\Delta &:= \mathrm{RTD}^{(+)}(0)\ , && (3.36)\\
x_i &:= \mathrm{RTD}^{(+)}(t_i) - \Delta\ , && (3.37)\\
r_i &:= t_{i+1} - t_i\ , && (3.38)
\end{aligned}$$

such that we have

$$\mathrm{RTD}^{(\pm)}(t_i) = x_i \pm \Delta\ . \qquad (3.39)$$

As noted above, the corticothalamic delays d_i are more than one order of magnitude smaller than the rise time τ of corticothalamic PSPs (Tsumoto et al., 1978; Tsumoto & Suda, 1980; von Krosigk et al., 1999). We hence neglect for the moment corticothalamic delays, i.e., we set $d_i = 0$ for all i. In subsection 3.4.8 we consider first-order corrections due to the delays and proof structural stability of the dynamics without the delays as analyzed here.

Neglecting the delays we get from equation (3.19)

$$\begin{aligned}
x_j &= \frac{\mathrm{e}\gamma}{\tau}\sum_{i=1}^{j-1}\left[s_i - (\mathrm{sgn} s_i)\,\Delta - x_i\right]\left(\sum_{i'=i}^{j-1} r_{i'}\right)\ \exp\left(-\frac{1}{\tau}\sum_{i''=i}^{j-1} r_{i''}\right)\\
&= \frac{\mathrm{e}\gamma}{\tau}\sum_{i=1}^{j-2}\left[s_i - (\mathrm{sgn} s_i)\,\Delta - x_i\right]\left(\sum_{i'=i}^{j-1} r_{i'}\right)\ \exp\left(-\frac{1}{\tau}\sum_{i''=i}^{j-1} r_{i''}\right)\\
&\quad + \frac{\mathrm{e}\gamma}{\tau}\left[s_{j-1} - (\mathrm{sgn} s_{j-1})\,\Delta - x_{j-1}\right] r_{j-1}\mathrm{e}^{-r_{j-1}/\tau}\\
&= \frac{\mathrm{e}\gamma}{\tau}\sum_{i=1}^{j-2}\left[s_i - (\mathrm{sgn} s_i)\,\Delta - x_i\right]\left(\sum_{i'=i}^{j-2} r_{i'}\right)\ \exp\left(-\frac{1}{\tau}\sum_{i''=i}^{j-1} r_{i''}\right)\\
&\quad + \frac{\mathrm{e}\gamma}{\tau}\sum_{i=1}^{j-2}\left[s_i - (\mathrm{sgn} s_i)\,\Delta - x_i\right]\ r_{j-1}\ \exp\left(-\frac{1}{\tau}\sum_{i''=i}^{j-1} r_{i''}\right)\\
&\quad + \frac{\mathrm{e}\gamma}{\tau}\left[s_{j-1} - (\mathrm{sgn} s_{j-1})\,\Delta - x_{j-1}\right] r_{j-1}\mathrm{e}^{-r_{j-1}/\tau}\\
&= x_{j-1}\mathrm{e}^{-r_{j-1}/\tau} + y_{j-1}\frac{\mathrm{e}r_{j-1}}{\tau}\mathrm{e}^{-r_{j-1}/\tau} \qquad (3.40)\\
&\quad + \frac{\mathrm{e}\gamma}{\tau}\left[s_{j-1} - (\mathrm{sgn} s_{j-1})\,\Delta - x_{j-1}\right] r_{j-1}\mathrm{e}^{-r_{j-1}/\tau}\ ,
\end{aligned}$$

with

$$y_j := \gamma\sum_{i=1}^{j-1}\left[s_i - (\mathrm{sgn} s_i)\,\Delta - x_i\right]\exp\left(-\frac{1}{\tau}\sum_{i'=i}^{j-1} r_{i'}\right)\ . \qquad (3.41)$$

We can now reformulate the dynamics (3.19) of the RTDs at the discrete times t_j as an iteration of a combination of two stochastic maps $\mathcal{R}(r)$ and $\mathcal{S}(s)$,

$$\begin{pmatrix} x_j \\ y_j \end{pmatrix} = \mathcal{R}(r_{j-1}) \circ \mathcal{S}(s_{j-1}) \begin{pmatrix} x_{j-1} \\ y_{j-1} \end{pmatrix} , \quad x_0 = y_0 = 0 , \tag{3.42}$$

$$\mathcal{S}(s): \quad \begin{pmatrix} x \\ y \end{pmatrix} \mapsto \begin{pmatrix} x \\ y + \gamma\{s - [x + (\mathrm{sgn} s)\Delta]\} \end{pmatrix} , \tag{3.43}$$

$$\mathcal{R}(r): \quad \begin{pmatrix} x \\ y \end{pmatrix} \mapsto \begin{pmatrix} \left(x + \mathrm{e} y \frac{r}{\tau}\right) \mathrm{e}^{-r/\tau} \\ y \mathrm{e}^{-r/\tau} \end{pmatrix} . \tag{3.44}$$

The *interstimulus times* r_j and the *stimulus passage times* s_j are stochastic variables, drawn independently from densities $\mathrm{u}(r)$ on $\mathbb{R}_+$ and $\mathrm{v}(s)$ on $\mathbb{R}$, respectively. These densities are determined by the stimulus. Note that although there may well be correlations between the interstimulus and passage times as sampled by one individual cortical neuron, they do not show up when sampling the sequence of all stimulus events in an extended retinal region irrespective of location. Similarly, r_j and s_j are independent of $r_{j'}$ and $s_{j'}$ $(j \neq j')$, respectively.

We point out that nothing is lost in calculating the RTDs at the discrete times t_j only [cf. equation (3.39)], since these are the times when any of the layer 4 cells respond. At all other times the state of adaptation, i.e., the RTD, of these neurons is irrelevant for any kind of processing. The times t_j of responses are also stimulus-driven stochastic variables and may be incorporated by extending the system (3.42) with the equation

$$t_j = t_{j-1} + r_{j-1} . \tag{3.45}$$

This equation may be solved independently of (3.42). In particular,

$$\langle t_j \rangle = j \langle r \rangle = j \int_0^\infty \mathrm{d}r \, \mathrm{u}(r) \, r . \tag{3.46}$$

We decompose the passage time density v into the two parts corresponding to the two opposite directions of motion,

$$\mathrm{v}(s) = \mu_+ \mathrm{v}_+(s) + \mu_- \mathrm{v}_-(s) , \tag{3.47}$$

with

$$\mu_\pm := \int_{-\infty}^{\infty} \mathrm{d}s \, \mathrm{v}(s) \, \Theta(\pm s) , \quad \mathrm{v}_\pm(s) := \begin{cases} \frac{\mathrm{v}(s)\,\Theta(\pm s)}{\mu_\pm} & \text{for } \mu_\pm > 0, \\ 0 & \text{for } \mu_\pm = 0. \end{cases} \tag{3.48}$$

We will deal with mean values of the types

$$\begin{aligned}\langle \mathrm{g}(s)\rangle &:= \int_{-\infty}^{\infty} \mathrm{d}s'\, \mathrm{v}(s')\, \mathrm{g}(s')\ , && (3.49)\\ \langle \mathrm{g}(s)\rangle_{\pm} &:= \int_{-\infty}^{\infty} \mathrm{d}s'\, \mathrm{v}_{\pm}(s')\, \mathrm{g}(s')\ , && (3.50)\\ \langle \mathrm{g}(r)\rangle &:= \int_{0}^{\infty} \mathrm{d}r'\, \mathrm{u}(r')\, \mathrm{g}(r')\ , && (3.51)\end{aligned}$$

with g being some function on the reals for which the integrals are defined.

The dynamics (3.42) is a Markov chain. The transition probability corresponding to $\mathcal{S}(s)$ is

$$\begin{aligned}\mathrm{p}_{\mathcal{S}}(x,y|x',y') \ =\ & \mu_{+}\int_{-\infty}^{\infty} \mathrm{d}s\, \mathrm{v}_{+}(s)\, \delta(x-x')\, \delta[y-y'-\gamma(s-x'-\Delta)]\\ & +\mu_{-}\int_{-\infty}^{\infty} \mathrm{d}s\, \mathrm{v}_{-}(s)\, \delta(x-x')\, \delta[y-y'-\gamma(s-x'+\Delta)]\ , \qquad (3.52)\end{aligned}$$

the one corresponding to $\mathcal{R}(r)$ is

$$\mathrm{p}_{\mathcal{R}}(x,y|x',y') \ =\ \int_{0}^{\infty} \mathrm{d}r\, \mathrm{u}(r)\, \delta\Big[x-\Big(x'+\mathrm{e}y'\frac{r}{\tau}\Big)\,\mathrm{e}^{-r/\tau}\Big]\ \delta\Big(y-y'\mathrm{e}^{-r/\tau}\Big)\ . \qquad (3.53)$$

We want to know how the moments of x and y change under the action of $\mathcal{R}(r)\circ\mathcal{S}(s)$. Let $\mathrm{p}(x,y)$ be a joint probability density for x and y. Then are

$$\langle x^n y^m\rangle := \int_{-\infty}^{\infty}\mathrm{d}x'\int_{-\infty}^{\infty}\mathrm{d}y'\, \mathrm{p}(x',y')\, x'^n y'^m\ , \quad n,m\ \in\ \mathbb{N}\ , \qquad (3.54)$$

the moments. For the action of $\mathcal{S}(s)$ we get

$$\begin{aligned}&\langle x^n y^m\rangle_{\mathcal{S}} && (3.55)\\ &:= \int_{-\infty}^{\infty}\mathrm{d}\bar{x}\int_{-\infty}^{\infty}\mathrm{d}\bar{y}\int_{-\infty}^{\infty}\mathrm{d}x'\int_{-\infty}^{\infty}\mathrm{d}y'\, \mathrm{p}_{\mathcal{S}}(\bar{x},\bar{y}|x',y')\, \mathrm{p}(x',y')\, \bar{x}^n\bar{y}^m\\ &= \mu_{+}\int_{-\infty}^{\infty}\mathrm{d}x'\int_{-\infty}^{\infty}\mathrm{d}y'\int_{-\infty}^{\infty}\mathrm{d}s\, \mathrm{p}(x',y')\, \mathrm{v}_{+}(s)x'^n\, [y'+\gamma(s-x'-\Delta)]^m\\ &\quad +\mu_{-}\int_{-\infty}^{\infty}\mathrm{d}x'\int_{-\infty}^{\infty}\mathrm{d}y'\int_{-\infty}^{\infty}\mathrm{d}s\, \mathrm{p}(x',y')\, \mathrm{v}_{-}(s)x'^n\, [y'+\gamma(s-x'+\Delta)]^m\\ &= \sum_{\substack{h+i+j+k=m\\ j\ \mathrm{even}}} \binom{m}{h,i,j,k}(-1)^i\gamma^{h+i+j}\Delta^j\left\langle s^h\right\rangle\left\langle x^{n+i}y^k\right\rangle\\ &\quad + \sum_{\substack{h+i+j+k=m\\ j\ \mathrm{odd}}} \binom{m}{h,i,j,k}(-1)^{i+1}\gamma^{h+i+j}\Delta^j\left(\mu_{+}\left\langle s^h\right\rangle_{+}-\mu_{-}\left\langle s^h\right\rangle_{-}\right)\left\langle x^{n+i}y^k\right\rangle\ ,\end{aligned}$$

with polynomial coefficients ($h, i, j, k, m \in \mathbb{N}$)

$$\binom{m}{h,i,j,k} := \frac{m!}{h!\,i!\,j!\,k!} \ , \quad h+i+j+k=m \ . \tag{3.56}$$

The action of $\mathcal{R}(r)$ yields

$$\begin{aligned} &\langle x^n y^m \rangle_{\mathcal{R}} \\ := \ & \int_{-\infty}^{\infty} \mathrm{d}\bar{x} \int_{-\infty}^{\infty} \mathrm{d}\bar{y} \int_{-\infty}^{\infty} \mathrm{d}x' \int_{-\infty}^{\infty} \mathrm{d}y' \, \mathrm{p}_{\mathcal{R}}(\bar{x}, \bar{y} | x', y') \, \mathrm{p}(x', y') \, \bar{x}^n \bar{y}^m \\ = \ & \int_{-\infty}^{\infty} \mathrm{d}x' \int_{-\infty}^{\infty} \mathrm{d}y' \int_{0}^{\infty} \mathrm{d}r \, \mathrm{p}(x', y') \, \mathrm{u}(r) \left(x' + \mathrm{e}y' \frac{r}{\tau} \right)^n \mathrm{e}^{-nr/\tau} y'^m \mathrm{e}^{-mr/\tau} \\ = \ & \sum_{k=0}^{n} \binom{n}{k} \left\langle \left(\frac{\mathrm{e}r}{\tau} \right)^k \mathrm{e}^{-(n+m)r/\tau} \right\rangle \left\langle x^{n-k} y^{m+k} \right\rangle \ . \end{aligned} \tag{3.57}$$

Let $\mathrm{p}_t(x, y)$ be the joint probability density of x and y at time t. In combining equations (3.55) and (3.57) we can write down iteration equations for the moments,

$$\langle x^n y^m \rangle_j := \int_{-\infty}^{\infty} \mathrm{d}x' \int_{-\infty}^{\infty} \mathrm{d}y' \, \mathrm{p}_{t_j}(x', y') \, x'^n y'^m \ . \tag{3.58}$$

The iterations can be solved successively for all n and m, starting with the first moments. We shall solve for the first two moments, i.e., for $\langle x^n y^m \rangle_j$ with $n+m=1$ and $n+m=2$.

Note that the ensemble averages (3.58) are not taken at constant time t, but rather at a constant number j of *stimulus/response events*, irrespective of the time t_j.

All analysis of the system that follows below is based on the Markov formulation of the dynamics developed in this subsection. The power of this approach will become apparent as we derive results on the moments of x and y for general stimulus statistics, and in particular in subsection 3.4.5 where we make assertions on the temporal pattern of *individual* trajectories of RTDs.

3.4.3 Mean Adaptation Dynamics

Let us choose the direction of positive passage times as the one of object motion. Introducing the statistical weight $\mu := \mu_+ - \mu_- \in [0, 1]$ of the object in the stimulus we decompose the passage time density according to

$$\mathrm{v}(s) = \mu \mathrm{v}_o(s) + (1-\mu) \mathrm{v}_b(s) \ , \tag{3.59}$$

with v_o being the *object* and v_b the *background* component; cf. Figure 3.2. We use the notation

$$\langle \mathrm{g}(s) \rangle_{o/b} := \int_{-\infty}^{\infty} \mathrm{d}s \, \mathrm{v}_{o/b}(s) \, \mathrm{g}(s) \ . \tag{3.60}$$

Since v_b is symmetric, $\langle s \rangle_b = 0$ and $\langle s \rangle = \mu \langle s \rangle_o$.

Let us assume for convenience that $\langle s \rangle_o \neq \Delta$, i.e., that the neurons are initially not optimally adapted to the object speed. All results to be derived, however, will be valid without this restriction. Transforming from the means of x and y introduced in subsection 3.4.2 [cf. definition (3.58)] to new dynamic variables

$$\alpha_j := \frac{\langle x \rangle_j}{\langle s \rangle_o - \Delta} \ , \quad \beta_j := \frac{\langle y \rangle_j}{\langle s \rangle_o - \Delta} \ , \tag{3.61}$$

we can write the mean RTD [cf. equation (3.39)] as

$$\left\langle \mathrm{RTD}^{(\pm)}(t_j) \right\rangle = \langle x \rangle_j \pm \Delta = (1 \mp \alpha_j)(\pm\Delta) + \alpha_j \langle s \rangle_o \ . \tag{3.62}$$

We call α_j the *mean degree of adaptation* to the object speed. For $\alpha_j = 0$ there is no adaptation at all, for $\alpha_j = 1$ neurons selective for the "+" direction, that is, the direction of object motion, have their mean preference at the object speed. The iteration dynamics of the mean values obtained from equations (3.55) and (3.57) in terms of α_j and β_j is

$$\begin{pmatrix} \alpha_j \\ \beta_j \end{pmatrix} = \underbrace{\begin{pmatrix} a_1 - \gamma b_1 & b_1 \\ -\gamma a_1 & a_1 \end{pmatrix}}_{=:M_1} \begin{pmatrix} \alpha_{j-1} \\ \beta_{j-1} \end{pmatrix} + \mu\gamma \begin{pmatrix} b_1 \\ a_1 \end{pmatrix} \ , \tag{3.63}$$

with the stimulus parameters

$$\left. \begin{array}{lcl} a_1 & := & \left\langle \mathrm{e}^{-r/\tau} \right\rangle \\ b_1 & := & \left\langle \frac{r}{\tau} \mathrm{e}^{1-r/\tau} \right\rangle \end{array} \right\} \in (0,1) \ . \tag{3.64}$$

From equation (3.63) it follows that there is no dependence of α_j upon Δ, the initial RTD. Thus all neurons have the same mean degree of adaptation, irrespective of their initial tuning.

The dynamics of α_j, β_j depend on the eigenvalues of M_1, and thus on the stimulus parameters a_1, b_1. The eigenvalues are

$$\lambda_{1/2} := a_1 - \frac{\gamma b_1}{2} \pm \frac{1}{2} \sqrt{\gamma^2 b_1^2 - 4\gamma a_1 b_1} \ . \tag{3.65}$$

For convergence of the dynamics we require that

$$\left| \lambda_{1/2} \right| < 1 \quad \Longleftrightarrow \quad \gamma b_1 < (a_1 + 1)^2 \ . \tag{3.66}$$

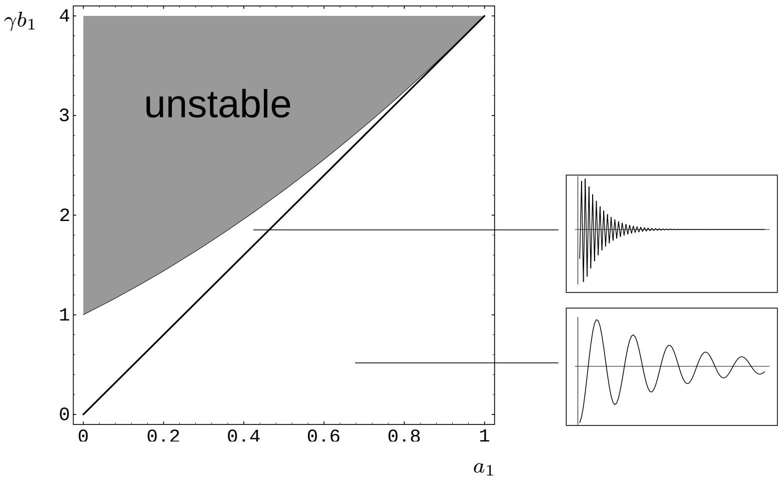

Figure 3.5: Parameter space for the stimulus statistics determining the dynamics of mean response time differences (RTDs). The dynamics converges for $(a_1 + 1)^2 > \gamma b_1$. For $\gamma b_1 < 4a_1$, the two eigenvalues given by equation (3.65) are complex conjugate. For $(a_1 + 1)^2 > \gamma b_1 > 4a_1$, they are real and negative. The corresponding type of mean dynamics is depicted for both of these regimes. In subsection 3.4.4 we show that only the case $\gamma b_1 < 4a_1$ is associated with finite variances of the RTDs.

Figure 3.5 shows the parameter regions of convergence and divergence. In this parameter space the vicinity of the point $a_1 = 1$, $b_1 = 0$ is occupied by stimuli that are fast or dense on the retina, as in both cases the interstimulus times r are short. Very sparse and slow stimuli, on the other hand, occupy the region around the point $a_1 = 0$, $b_1 = 0$.

By inspection of Figure 3.5 it is clear that there are three ways to ensure convergence to a finite mean degree of adaptation: (i) by making the overall strength of feedback to the LGN γ sufficiently small, (ii) by making the rise time τ of the corticothalamic PSPs sufficiently large, or (iii) by sufficiently extending the retinal region from which the local velocity measures are sampled. In subsection 3.4.7 we will show, however, that if $\mu > 1/2$, approaching the point $a_1 = 1$, $b_1 = 0$ is likely to result in crossing of the RTDs, i.e., violation of condition (3.17) with subsequent disruption of the adaptation process.

From equation (3.63) it is easy to calculate the asymptotic values

$$\alpha \ := \ \alpha_\infty \ = \ \frac{\mu\gamma b_1}{\gamma b_1 + (1 - a_1)^2} \ , \tag{3.67}$$

$$\beta \ := \ \beta_\infty \ = \ \frac{\mu\gamma(1 - a_1)a_1}{\gamma b_1 + (1 - a_1)^2} \tag{3.68}$$

for the regime of convergence. The relevant quantity is the asymptotic mean degree of adaptation $\alpha \in [0, 1]$. By inspection of equation (3.62), it follows that the preferences of the neurons encoding motion in the direction of the object at average *converge* to the vicinity of the object's speed, conforming to our computational goal of object segmentation. Neurons encoding the opposite direction of motion, on the other hand, at average *diverge* from the object's speed – and from each other. This fact implies that in the "$-$" direction there is no speed for moving features to elicit a strong response in all neurons representing the features' location. The ensemble activity in the "$-$" population of neurons is thus lower than in the "+" population.

A contour plot of α as a function of a_1 and γb_1 is shown in the left graph of Figure 3.6. Assuming the times t_j of cortical stimulation by local features to be compatible with a Poisson process, we show in appendix D that the stimulus parameters a_1, b_1 lie on a parabola, plotted in the left graph of Figure 3.6 for different feedback strengths γ. For Poisson statistics of the times t_j, the asymptotic mean degree of adaptation α behaves as shown in the right graph of the figure. Not surprisingly, adaptation gets stronger with increasing a_1, that is, for denser or faster stimuli, and with increasing feedback strength γ. Moreover, α is proportional to μ, the statistical weight of the object component in the stimulus. Hence, the larger or faster the object, the stronger the average attraction of speed preferences to the object's speed.

For $\gamma b_1 < 4a_1$ the eigenvalues $\lambda_{1/2}$ are complex conjugate. In the next subsection we will show that only then the variance of the RTDs converges. As depicted in Figure 3.5, in this regime the mean RTDs converge in a damped oscillation. In fact, if G is the matrix that diagonalizes M_1, i.e., GM_1G^{-1} is diagonal, and

$$K := \begin{pmatrix} 1 & 1 \\ \mathrm{i} & -\mathrm{i} \end{pmatrix} , \tag{3.69}$$

the matrix KG is real and we have

$$M_1^j = a_1^j G^{-1} K^{-1} \begin{pmatrix} \cos(j\phi) & -\sin(j\phi) \\ \sin(j\phi) & \cos(j\phi) \end{pmatrix} KG , \quad \text{with} \quad \phi := \arg(\lambda_1) . \tag{3.70}$$

The iteration dynamics (3.63) is solved by

$$\begin{pmatrix} \alpha_j \\ \beta_j \end{pmatrix} = \begin{pmatrix} \alpha \\ \beta \end{pmatrix} - M_1^j \begin{pmatrix} \alpha \\ \beta \end{pmatrix} , \tag{3.71}$$

that is, a spiral motion around the center (α, β). Its angular period is,

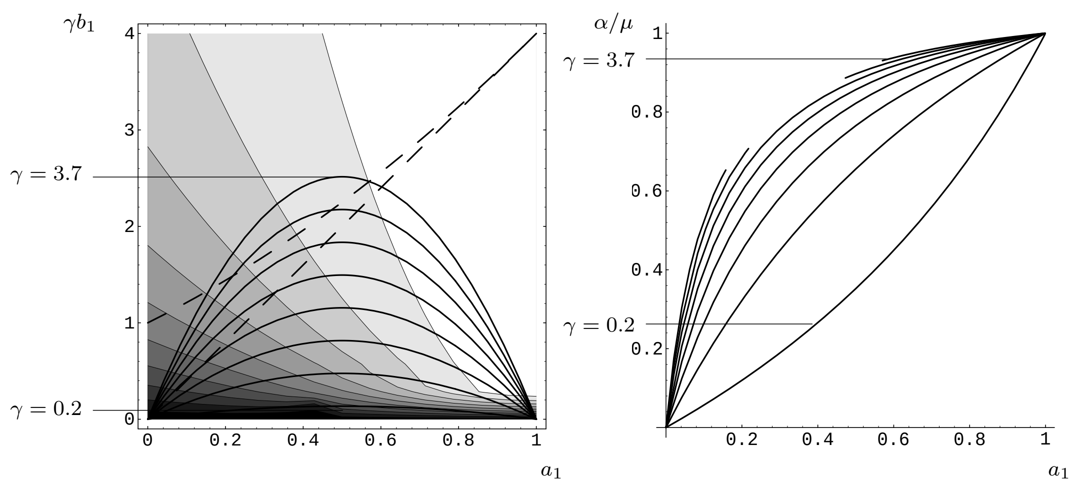

Figure 3.6: The asymptotic mean degree of adaptation α in units of the object weight μ is shown as a contour plot on the left. Dashed lines delimit the regions of different mean dynamics defined in Figure 3.5. Assuming Poisson statistics for cortical response times to stimulus features, the stimulus parameters a_1, b_1 lie on the parabolas plotted in the left graph for $\gamma = 0.2, 0.7, \ldots, 3.7$. In the right graph we show α/μ for Poisson statistics and the same values of γ as those on the left. The curves are interrupted where $(a_1+1)^2 < \gamma b_1$ such that the mean dynamics is divergent.

measured in the number of stimulus/response events,

$$P = \frac{2\pi}{\arg(\lambda_1)} \ , \tag{3.72}$$

and averages in real time to

$$\langle T \rangle = P \, \langle r \rangle \ . \tag{3.73}$$

Thus $\langle T \rangle$ is the mean period of the mean RTD. It also is, however, the mean period of the covariance function

$$\begin{aligned} \operatorname{cov}(x_j, x_{j+k}) &:= \left\langle \left(x_j - \langle x \rangle_j\right) \left(x_{j+k} - \langle x \rangle_{j+k}\right) \right\rangle \qquad (3.74) \\ &= \int_{-\infty}^{\infty} \mathrm{d}x \int_{-\infty}^{\infty} \mathrm{d}y \int_{-\infty}^{\infty} \mathrm{d}x' \int_{-\infty}^{\infty} \mathrm{d}y' \, \mathrm{p}_k(x, y | x', y') \, \mathrm{p}_{t_j}(x', y') \\ &\quad \times \ \left(x - \langle x \rangle_{j+k}\right) \left(x' - \langle x \rangle_j\right) \ , \end{aligned}$$

where

$$\mathrm{p}_1(x, y | x', y') \ := \ \int_{-\infty}^{\infty} \mathrm{d}x'' \int_{-\infty}^{\infty} \mathrm{d}y'' \, \mathrm{p}_{\mathcal{R}}(x, y | x'', y'') \, \mathrm{p}_{\mathcal{S}}(x'', y'' | x', y') \ , \tag{3.75}$$

$$\begin{aligned}\mathrm{p}_k(x,y|x',y') \;&:=\; \int_{-\infty}^{\infty}\mathrm{d}x''\int_{-\infty}^{\infty}\mathrm{d}y''\,\mathrm{p}_1(x,y|x'',y'')\,\mathrm{p}_{k-1}(x'',y''|x',y')\ , \\ &\text{for } k>1,\end{aligned} \tag{3.76}$$

by the following argument. Denoting the affine-linear map

$$\begin{pmatrix}\langle x\rangle_{j-1}\\ \langle y\rangle_{j-1}\end{pmatrix} \mapsto \begin{pmatrix}\langle x\rangle_{j}\\ \langle y\rangle_{j}\end{pmatrix}\ , \tag{3.77}$$

defined in equation (3.63), by $\mathrm{L}\equiv(\mathrm{L}_x,\mathrm{L}_y)$, and its k-fold iteration by $\mathrm{L}^k\equiv(\mathrm{L}_x^k,\mathrm{L}_y^k)$, we can write [cf. equation (3.74)]

$$\int_{-\infty}^{\infty}\mathrm{d}x\int_{-\infty}^{\infty}\mathrm{d}y\,\mathrm{p}_k(x,y|x',y')\,\left(x-\langle x\rangle_{j+k}\right) \;=\; \mathrm{L}_x^k(x',y')-\langle x\rangle_{j+k}\ . \tag{3.78}$$

Evidently, this expression, taken as a discrete function of k, performs a damped oscillation with period P; cf. equation (3.72). Substituting back into the covariance function (3.74), we see that it has the same period. In particular, the asymptotic covariance function $\lim_{j\to\infty}\mathrm{cov}(x_j,x_{j+k})$ alternates between phases of correlation and anti-correlation with period P. In subsection 3.4.5 we will show that under certain conditions these oscillations of the RTDs never die out for *individual realizations* of the adaptation process. The damping of the *mean* oscillation is then due to a loss of phase coherence with time.

For a Poisson process generating the stimulus/response times t_j, the mean oscillation period is given by

$$\left\langle\frac{T}{\tau}\right\rangle = \tag{3.79}$$

$$\begin{cases} 2\pi\left\langle\frac{r}{\tau}\right\rangle\Big/\arctan\left[\frac{\sqrt{\mathrm{e}\gamma\langle r/\tau\rangle[(4-\mathrm{e}\gamma)\langle r/\tau\rangle+4]}}{(2-\mathrm{e}\gamma)\langle r/\tau\rangle+2}\right] & \text{for } (2-\mathrm{e}\gamma)\left\langle\frac{r}{\tau}\right\rangle+2>0,\\ 2\pi\left\langle\frac{r}{\tau}\right\rangle\Big/\left\{\pi+\arctan\left[\frac{\sqrt{\mathrm{e}\gamma\langle r/\tau\rangle[(4-\mathrm{e}\gamma)\langle r/\tau\rangle+4]}}{(2-\mathrm{e}\gamma)\langle r/\tau\rangle+2}\right]\right\} & \text{elsewhere;}\end{cases}$$

see appendix D. In Figure 3.7 we show plots of $\langle T/\tau\rangle$ for different γ both as function of $\langle r/\tau\rangle$ and a_1. For $\langle r/\tau\rangle > 4/(\mathrm{e}\gamma-4)$ or, equivalently, $a_1 < 1-4/(\mathrm{e}\gamma)$, the stimulus enters the regime where $\lambda_{1/2}$ are real and negative, and the mean period ends up on the curve

$$\left\langle\frac{T}{\tau}\right\rangle = 2\left\langle\frac{r}{\tau}\right\rangle = 2\left(\frac{1}{a_1}-1\right)\ , \tag{3.80}$$

plotted with the dashed lines in Figure 3.7. For $\langle r/\tau\rangle\to 0$ or, equivalently, $a_1\to 1$, i.e., at high stimulus density or speed, $\langle T/\tau\rangle$ approaches zero. In particular, $\langle T\rangle$ can be much shorter than the rise time τ of a corticothalamic PSP.

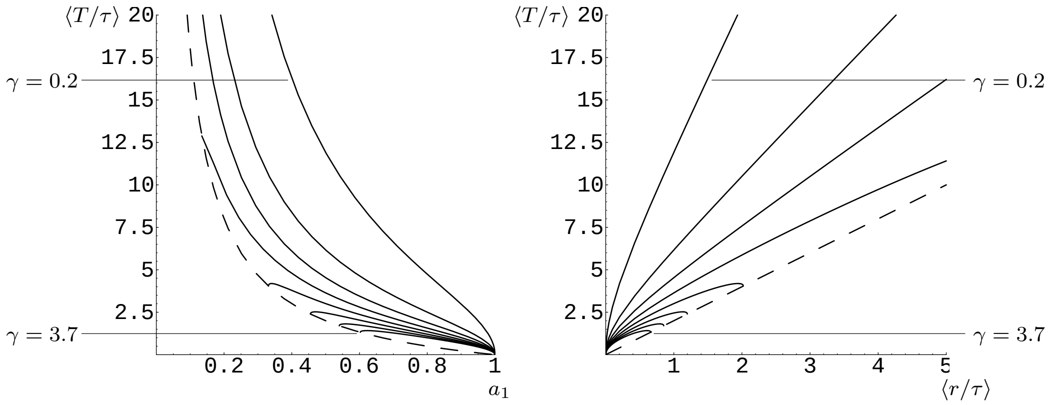

Figure 3.7: Mean oscillation period $\langle T \rangle$ of response time differences (RTDs) in units of the rise time τ of corticothalamic postsynaptic potentials as a function of the stimulus parameters a_1 (left) and $\langle r/\tau \rangle$ (right). For the curves we assume Poisson statistics for cortical response events to stimulus features and $\gamma = 0.2, 0.7, \ldots, 3.7$; cf. Figure 3.6. The mean oscillation period lies on the dashed curves for $a_1 < 1 - 4/(\mathrm{e}\gamma)$ or, equivalently, $\langle r/\tau \rangle > 4/(\mathrm{e}\gamma - 4)$.

It should be noted that while in the real corticothalamic system the period of an oscillation of geniculate membrane potentials may well be shorter than the rise time of a single corticothalamic PSP (due to superposition of many depolarizing and hyperpolarizing PSPs), the frequency would in fact be limited by the time it takes a cortical neuron to respond to a feature passing its receptive field. There is no representation of this fact in the present model and the limit $\langle T \rangle \to 0$ should thus not be taken too serious. Moreover, too fast rates of change of GRC membrane potentials are not consistent with the approximation of instantaneous stimulus/response events we have made; cf. subsection 3.3.1.

3.4.4 Variance of Adaptation Dynamics

To estimate whether the trajectories of the RTDs stay bounded when their mean values converge we have to check whether their variances converge to finite values as well. We will analyze the dynamic map for the second moments of x and y defined in subsection 3.4.2. From equations (3.55) and

(3.57) we get

$$\begin{pmatrix} \langle x^2\rangle_j \\ \langle xy\rangle_j \\ \langle y^2\rangle_j \end{pmatrix} = \underbrace{\begin{pmatrix} a_2 - \gamma b_2 + \gamma^2 c_2 & b_2 - 2\gamma c_2 & c_2 \\ -\gamma a_2 + \frac{\gamma^2}{2} b_2 & a_2 - \gamma b_2 & \frac{1}{2} b_2 \\ \gamma^2 a_2 & -2\gamma a_2 & a_2 \end{pmatrix}}_{=:M_2} \begin{pmatrix} \langle x^2\rangle_{j-1} \\ \langle xy\rangle_{j-1} \\ \langle y^2\rangle_{j-1} \end{pmatrix} + \begin{pmatrix} u_{j-1} \\ v_{j-1} \\ w_{j-1} \end{pmatrix} , \tag{3.81}$$

with

$$\left.\begin{array}{rcl} a_2 & := & \left\langle \mathrm{e}^{-2r/\tau} \right\rangle \\ b_2 & := & \left\langle \frac{2r}{\tau} \mathrm{e}^{1-2r/\tau} \right\rangle \\ c_2 & := & \left\langle \left(\frac{r}{\tau}\right)^2 \mathrm{e}^{2-2r/\tau} \right\rangle \end{array}\right\} \in (0,1) , \tag{3.82}$$

and

$$\begin{aligned} u_j \; := \; & \Big(2\gamma^2 \mu c_2 \Delta + \gamma b_2 \langle s\rangle - \gamma\mu b_2 \Delta - 2\gamma^2 c_2 \langle s\rangle\Big) \langle x\rangle_j \\ & + \left(2\gamma c_2 \langle s\rangle - 2\gamma\mu c_2 \Delta\right) \langle y\rangle_j \\ & + \gamma^2 c_2 \Delta^2 + \gamma^2 c_2 \left\langle s^2 \right\rangle - 2\gamma^2 c_2 \Delta \langle |s| \rangle , \end{aligned} \tag{3.83}$$

$$\begin{aligned} v_j \; := \; & \Big(\gamma^2 \mu b_2 \Delta + \gamma a_2 \langle s\rangle - \gamma\mu a_2 \Delta - \gamma^2 b_2 \langle s\rangle\Big) \langle x\rangle_j \\ & + \left(\gamma b_2 \langle s\rangle - \gamma\mu b_2 \Delta\right) \langle y\rangle_j \\ & + \frac{1}{2}\gamma^2 b_2 \Delta^2 + \frac{1}{2}\gamma^2 b_2 \left\langle s^2 \right\rangle - \gamma^2 b_2 \Delta \langle |s| \rangle , \end{aligned} \tag{3.84}$$

$$\begin{aligned} w_j \; := \; & \Big(2\gamma^2 \mu a_2 \Delta - 2\gamma^2 a_2 \langle s\rangle\Big) \langle x\rangle_j \\ & + \left(2\gamma a_2 \langle s\rangle - 2\gamma\mu a_2 \Delta\right) \langle y\rangle_j \\ & + \gamma^2 a_2 \Delta^2 + \gamma^2 a_2 \left\langle s^2 \right\rangle - 2\gamma^2 a_2 \Delta \langle |s| \rangle . \end{aligned} \tag{3.85}$$

The $\langle x\rangle_j$ and $\langle y\rangle_j$ converge to the values given in the previous subsection, and (u_j, v_j, w_j) will become constant. To check convergence of the second moments it is therefore enough to consider the eigenvalues of M_2. These are the roots of the characteristic polynomial

$$\nu^3 - \Big(3a_2 - 2\gamma b_2 + \gamma^2 c_2\Big)\nu^2 + \Big(3a_2^2 - \gamma^2 a_2 c_2 - 2\gamma a_2 b_2 + \frac{1}{2}\gamma^2 b_2^2\Big)\nu - a_2^3 = 0 , \tag{3.86}$$

and are rather lengthy expressions which need not be spelled out here. Depending on the stimulus parameters a_2, b_2, and c_2, there are one real and two complex conjugate eigenvalues, or three real eigenvalues. Let ν_1 be the eigenvalue that is always real, and $\nu_{2/3}$ the other two that may or may not be complex conjugate. Stimulus parameters a_2, b_2, c_2 that yield convergent second moments of the RTDs are precisely those that obey the constraints

$$|\nu_1| =: \mathrm{f}_1(a_2,\gamma b_2,\gamma^2 c_2) < 1\ , \quad \max\left(|\nu_2|\,,|\nu_3|\right) =: \mathrm{f}_2(a_2,\gamma b_2,\gamma^2 c_2) < 1\ , \tag{3.87}$$

with continuous functions f_1 and f_2 that do not depend on γ; cf. equation (3.86). The two surfaces defined by

$$\mathrm{f}_1(a_2,\gamma b_2,\gamma^2 c_2) = 1\ , \quad \mathrm{f}_2(a_2,\gamma b_2,\gamma^2 c_2) = 1 \tag{3.88}$$

are shown in Figure 3.8. Since convergence is obviously ensured for $\gamma = 0$, which yields $x_j \equiv y_j \equiv 0$ [cf. equation (3.42)], the parameter region that results in convergence of the second moments is the space *in between* the two surfaces that includes the axis $(a_2,\gamma b_2,\gamma^2 c_2) = (a_2,0,0)$, $a_2 \in (0,1)$. In the region beyond the intersection of the surfaces (see the bottom of Figure 3.8), i.e., for roughly $\gamma^2 c_2 > 9$, there are no combinations of parameters that yield convergent second moments.

For Poisson statistics of the times t_j the stimulus parameters a_2, b_2, c_2 lie on the curves plotted in Figure 3.9 for different values of γ; see appendix D. The curves run from $(a_2,\gamma b_2,\gamma^2 c_2) = (0,0,0)$, the limiting point for sparse and slow stimuli ($\langle r\rangle = \infty$), to $(a_2,\gamma b_2,\gamma^2 c_2) = (1,0,0)$, the limit of dense and fast stimuli ($\langle r\rangle = 0$). For γ small enough, the curves lie completely within the region of convergence. For larger γ, they are in the region of divergence except near the point $(a_2,\gamma b_2,\gamma^2 c_2) = (0,0,0)$. For $\langle r/\tau\rangle \ll 1$, which is the usual regime[2], the eigenvalues $\nu_{2/3}$ are complex conjugate and we have

$$\nu_1 = 1-\left(2-\frac{\mathrm{e}\gamma}{2}\right)\left\langle\frac{r}{\tau}\right\rangle + O\left(\left\langle\frac{r}{\tau}\right\rangle^{3/2}\right)\ , \tag{3.89}$$

$$\left|\nu_{2/3}\right| = 1-\left(2+\frac{\mathrm{e}\gamma}{4}\right)\left\langle\frac{r}{\tau}\right\rangle + O\left(\left\langle\frac{r}{\tau}\right\rangle^{3/2}\right)\ . \tag{3.90}$$

By inspection of equations (3.89) and (3.90) we find that for the second moments to converge it is necessary and sufficient that the feedback strength obeys the upper bound $\gamma < 4/\mathrm{e}$. In fact, Figure 3.9 shows that at least

---

[2] A conservative estimate of $\langle r/\tau\rangle$ may be obtained as follows. The diameter of RFs in the primary visual cortex is of order 1 degree; cf. section 2.1. Let us assume an arrangement of RFs that covers the visual field in a maximally sparse manner, that is, with a center-to-center distance of the same order. The extension of the coupled adaptive system should be about one order larger, i.e., 10 degrees in diameter. A single feature like a bar, in order to be processed by velocity-tuned neurons, should move at a minimum speed of, say, 1 degree/s; cf. chapter 2. It will then cross an RF center every second. Now, a stimulus as sparse as one feature per square degree will cross an RF center every 1/100 s = 10 ms. This is already one order of magnitude smaller than the order of τ, which is 100 ms.

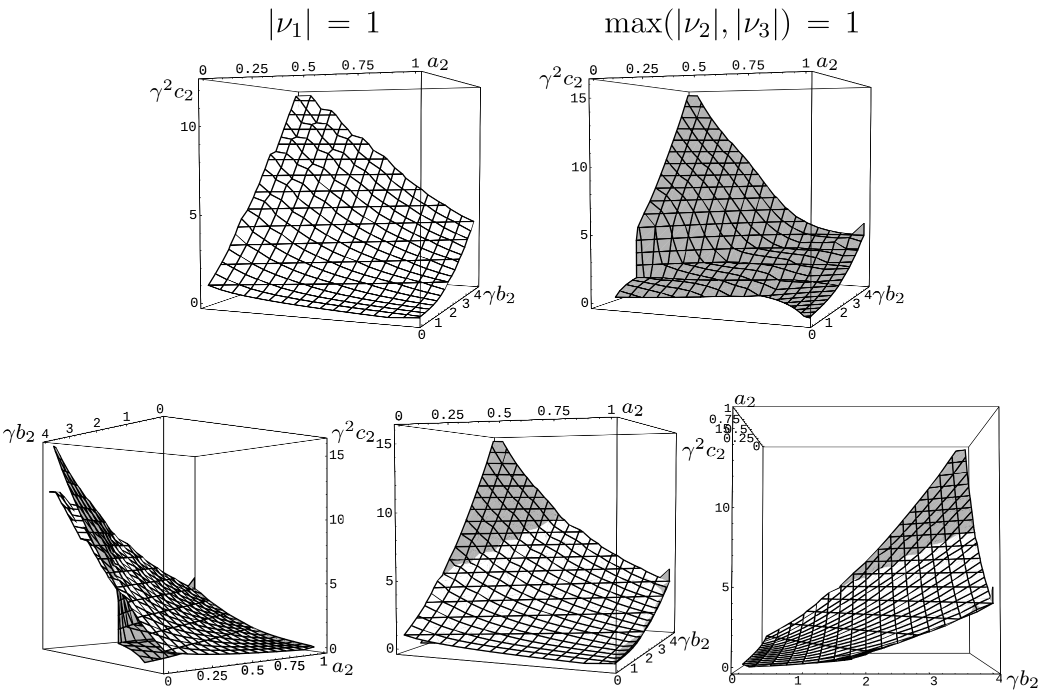

Figure 3.8: Surfaces of modulus one of the eigenvalues of M_2; see equation (3.81). These surfaces constrain values of the parameters a_2, γb_2, $\gamma^2 c_2$ that result in convergence of the second moments of the RTDs. ν_1 is the real eigenvalue, $\nu_{2/3}$ are complex conjugate in some parts of the parameter space, and real-valued in others. At the top of the figure the two surfaces defined respectively by $|\nu_1| = 1$ and $\max(|\nu_2|, |\nu_3|) = 1$ are shown. The bottom displays three different combined views of the two constraining surfaces. The parameter region of convergence of the second RTD moments is the space in between the two surfaces that includes the a_2-axis. In the region beyond the intersection of the surfaces, i.e., for roughly $\gamma^2 c_2 > 9$, there are no combinations of parameters that yield convergent second moments.

for $\gamma \leq 1.2$ the second moments converge not only for small $\langle r/\tau \rangle$, but for all $0 < \langle r/\tau \rangle < \infty$, corresponding to the entire curves running between $(a_2, \gamma b_2, \gamma^2 c_2) = (0, 0, 0)$ and $(a_2, \gamma b_2, \gamma^2 c_2) = (1, 0, 0)$ in parameter space; cf. Figure 3.9.

As shown in appendix D, the condition $\gamma < 4/\mathrm{e}$ is for Poisson statistics of the times t_j equivalent to $4a_1 > \gamma b_1$ for all $a_1 \in (0, 1)$. In the following we will assume this condition to hold. Our system is thus always in the regime of damped oscillations of the mean RTDs; cf. Figure 3.5.

After some lengthy but straightforward algebra we find for the asymptotic

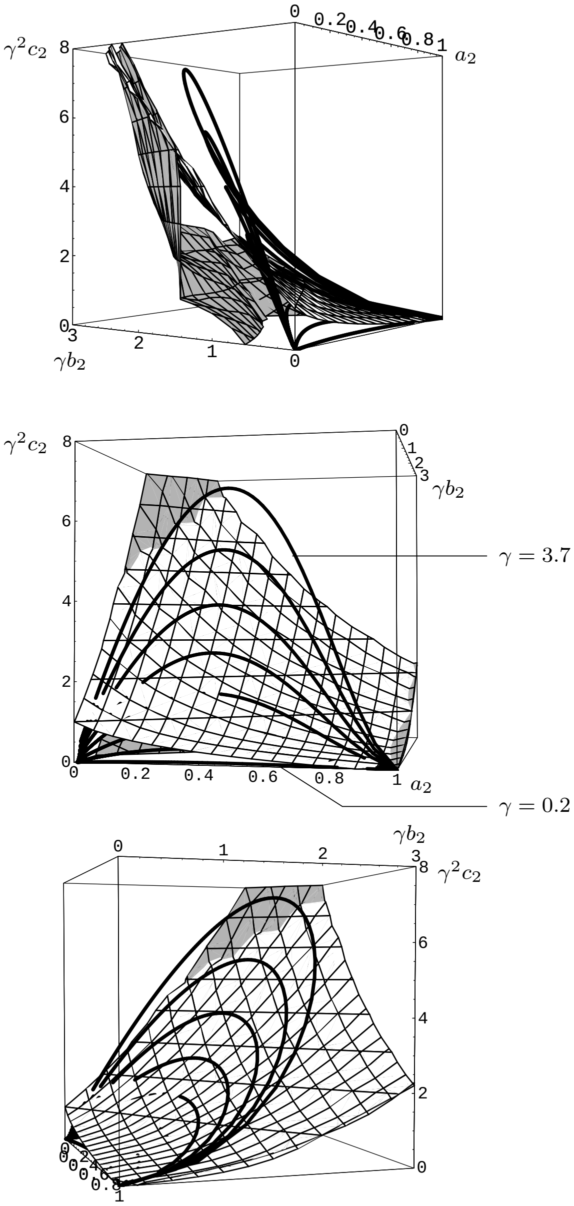

Figure 3.9: Three different views of the two constraining surfaces from Figure 3.8 combined with the parameter values for Poissonian stimulus/response times (thick curves). The Poissonian stimulus parameters are replicated for $\gamma = 0.2, 0.7, \ldots, 3.7$. The parameter region of convergence of the second RTD moments is the space in between the two surfaces. Convergence is thus ensured for all Poissonian stimuli, if $\gamma \leq 1.2$.

variance of x, and hence of the RTDs,

$$\mathrm{var}(x) = \left\langle x^2 \right\rangle - \langle x \rangle^2 = \left[(\langle |s| \rangle - \Delta)^2 + \mathrm{var}(|s|) \right] \rho_1 - \mu^2 (\langle s \rangle_o - \Delta)^2 \rho_2 \,, \quad (3.91)$$

with

$$\rho_1 \;:=\; \frac{\gamma^2 \left({b_2}^2 + 2c_2 - 2a_2 c_2 \right)}{2(1-a_2)^3 + 4\gamma\,(1-a_2)\,b_2 + \gamma^2 {b_2}^2 - 2\gamma^2\,(1+a_2)\,c_2} \,, \quad (3.92)$$

$$\rho_2 := \frac{\gamma^2 {b_1}^2}{\left[(1-a_1)^2+\gamma b_1\right]^2} \tag{3.93}$$

$$- \frac{2\gamma^2 \left[a_1(1-a_1)\left({b_2}^2+2c_2-2a_2c_2\right)+b_1(b_2-a_2b_2-2\gamma c_2)\right]}{\left[(1-a_1)^2+\gamma b_1\right]\left[2(1-a_2)^3+4\gamma(1-a_2)b_2+\gamma^2{b_2}^2-2\gamma^2(1+a_2)c_2\right]} .$$

While the mean $\langle x\rangle_j$ is proportional to $\langle s\rangle_o - \Delta$ [cf. equation (3.62)], the variance var(x) contains a term that is proportional to $(\langle s\rangle_o - \Delta)^2$, one that is proportional to $(\langle|s|\rangle - \Delta)^2$, and a third one that is proportional to var$(|s|)$. For Poisson statistics of the times t_j the coefficients $\rho_{1/2}$ simplify to (see appendix D)

$$\rho_1 = \frac{(\mathrm{e}\gamma)^2}{4\mathrm{e}\gamma-(\mathrm{e}\gamma)^2+4\langle r/\tau\rangle} > 0 , \tag{3.94}$$

$$\rho_2 = \frac{(\mathrm{e}\gamma)^3(\mathrm{e}\gamma+2\langle r/\tau\rangle)}{(4\mathrm{e}\gamma-(\mathrm{e}\gamma)^2+4\langle r/\tau\rangle)(\mathrm{e}\gamma+\langle r/\tau\rangle)^2} > 0 . \tag{3.95}$$

It follows that the asymptotic variance of the RTDs (i) is larger for neurons with initial response time difference Δ closer to the object's passage time $\langle s\rangle_o$, (ii) is smaller for neurons with Δ closer to $\langle|s|\rangle$, (iii) increases with increasing var$(|s|)$, that is, with increasing diversity of speeds in the stimulus, and (iv) decreases with increasing object weight μ, so strong objects not only give rise to strong mean adaptation [cf. equation (3.67)], but also to small fluctuations.

3.4.5 Stationary States and Diffusion-Sustained Oscillations

We have shown in the two previous subsections that there is a region of stimulus parameters where the means and variances of the RTDs converge to finite values. Averages do not tell us, however, what *individual* trajectories of RTD$^{(\pm)}(t_j)$ look like. In this subsection we want to address this issue.

Let us start by looking at the time course of adaptation for three different stimuli in Figure 3.10. For details on the computer simulations see appendix G. Roughly, a system of four classes of cortical neurons with adaptation dynamics RTD$^{(c,\pm)}(t)$ $(c = 1, 2, 3, 4)$ is adapted to stimuli with different object weights μ. The graphs show the dynamics of the four response time differences RTD$^{(c,+)}(t)$ $(c = 1, 2, 3, 4)$ of neurons encoding motion in the object's direction. The background consists of features moving parallel and opposite to the object with speeds drawn randomly from a speed density spanning speeds lower and higher than the object's speed. The top graph shows the case $\mu = 1$, i.e., no background in the stimulus, the middle graph an example for $\mu = 4/5$, and the bottom graph for $\mu = 1/3$, that is, twice as many features in the background as in the object component of the stimulus. Evidently, only in the no-background case is there convergence of the RTDs to a stationary state. As background is added to the stimulus, ongoing oscillations develop. These oscillations are more pronounced with a stronger background. We now derive the occurrence of sustained oscillations and their dependence upon the background component.

Let us first deal with the short-time behavior of individual trajectories (x_j, y_j). We ask what they look like for the first few j. The variances

$$\mathrm{var}_j(x) := \left\langle x^2 \right\rangle_j - \langle x \rangle_j^2 \ , \quad \mathrm{var}_j(y) := \left\langle y^2 \right\rangle_j - \langle y \rangle_j^2 \tag{3.96}$$

are zero initially. They increase to finite values no faster than the fastest converging linear combination of second moments, i.e., like $\mathrm{e}^{-j/\zeta}$ with

$$\zeta := -1 \Big/ \ln \left(\min_{i=1,2,3} |\nu_i| \right) \ . \tag{3.97}$$

We have to compare ζ with the period P of the oscillation of the mean values $(\langle x \rangle_j, \langle y \rangle_j)$ in order to see whether this oscillation shows up in individual realizations (x_j, y_j). From equations (3.72), (3.89), and (3.90) we get

$$\frac{P}{\zeta} = \frac{(8 + \mathrm{e}\gamma)\pi}{2(\mathrm{e}\gamma)^{1/2}} \left\langle \frac{r}{\tau} \right\rangle^{1/2} + O\left(\left\langle \frac{r}{\tau} \right\rangle \right) \ . \tag{3.98}$$

Thus, for $\langle r/\tau \rangle$ small enough $P/\zeta \ll 1$ and the oscillation of the means $\langle x \rangle_j$, $\langle y \rangle_j$ is fast as compared to the growth time of the fluctuations $\mathrm{var}_j(x)$, $\mathrm{var}_j(y)$ about the means. Individual realizations (x_j, y_j) are then well described by their means for several periods of the oscillation. Put differently, an oscillation then shows up in individual realizations (x_j, y_j), at least for the first few j. The transition from an oscillation-driven to a fluctuation-driven dynamics of the RTDs with increasing interstimulus times $\langle r/\tau \rangle$ is illustrated in Figure 3.11.

It remains to establish the long-time behavior of trajectories (x_j, y_j). Introducing

$$\xi_j := \frac{x_j - \langle x \rangle_\infty}{\langle s \rangle_o - \Delta} \ , \quad \eta_j := \frac{y_j - \langle y \rangle_\infty}{\langle s \rangle_o - \Delta} \ , \tag{3.99}$$

we can rewrite equation (3.71) as

$$\begin{pmatrix} \langle \xi \rangle_j \\ \langle \eta \rangle_j \end{pmatrix} = M_1^j \begin{pmatrix} -\alpha \\ -\beta \end{pmatrix} \ , \tag{3.100}$$

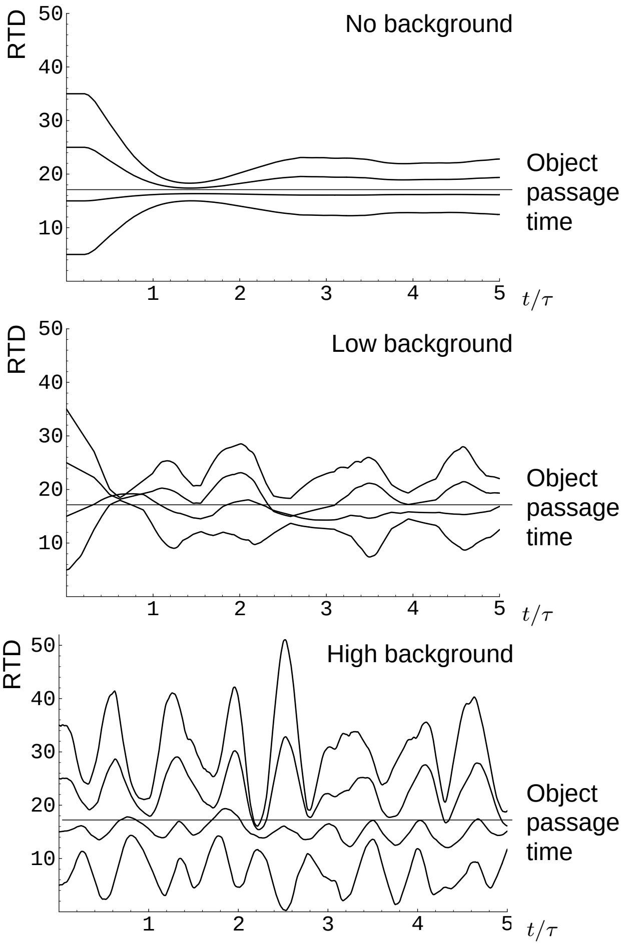

Figure 3.10: Computer simulations of the adaptation dynamics for the response time differences $\mathrm{RTD}^{(c,\pm)}(t)$ of 4 classes of neurons ($c = 1, 2, 3, 4$). The time scale is set by τ, the rise time of corticothalamic postsynaptic potentials; cf. equation (3.1). The stimulus is a coherently moving object without a background ($\mu = 1$, $\langle r/\tau \rangle = 0.075$, top), with a moderate background ($\mu = 4/5$, $\langle r/\tau \rangle = 0.015$, middle), and with a strong background ($\mu = 1/3$, $\langle r/\tau \rangle = 0.005$, bottom). Only the 4 trajectories $\mathrm{RTD}^{(c,+)}(t)$, i.e., representative of the neurons selective for the direction of object motion, are shown. The passage time of object features is indicated by the straight horizontal line in each graph. The adaptation dynamics converges to a stationary state close to the object's passage time without a background, and is increasingly oscillatory with increasing background strength. Other parameters: $s_o = 17$, $\langle |s| \rangle_b = 18.2$, $\mathrm{var}_b(|s|) = 19.1^2$, $\gamma = 0.2$. See appendix G for details on the computer simulations.

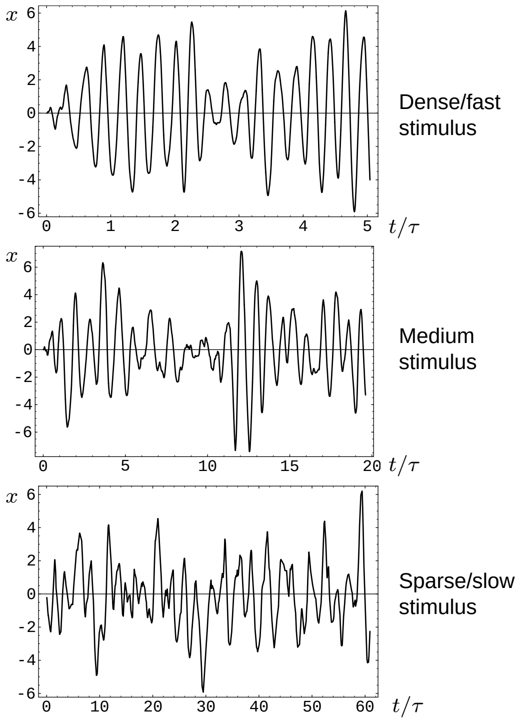

Figure 3.11: Transition from an oscillation-driven to a fluctuation-driven dynamics of response time differences (RTDs) with decreasing stimulus density or speed. The time scale is set by τ, the rise time of corticothalamic postsynaptic potentials; cf. equation (3.1). The plots show $x(t) = \mathrm{RTD}^{(+)}(t) - \mathrm{RTD}^{(+)}(0)$ for a single class of neuron. The stimulus consists of object and background with an object passage time $\langle s \rangle_o = \mathrm{RTD}^{(+)}(0)$, such that there is no drift of the shown RTDs, that is, $\langle x \rangle_\infty = 0$; cf. equation (3.62). As the mean interstimulus time $\langle r/\tau \rangle$ is increased from the top to the bottom graph, the RTD dynamics develops from an orderly oscillation into a pattern resembling a random walk. Top: $\langle r/\tau \rangle = 0.001$; middle: $\langle r/\tau \rangle = 0.01$; bottom: $\langle r/\tau \rangle = 0.1$. Note the different time scales in the graphs. Other parameters: $\mu = 1/3$, $s_o = 15$, $\langle |s| \rangle = 17.1$, $\mathrm{var}(|s|) = 15.6^2$, $\gamma = 0.2$. See appendix G for details on the computer simulations.

where the powers of M_1 are given by equation (3.70). The dynamics (3.100) of the means spirals into the origin of ξ-η space. Without damping of the oscillations the trajectories would lie on orbits defined by $\mathrm{q}(\xi, \eta) = \text{const.}$, with the quadratic form

$$\mathrm{q}(\xi, \eta) := \Big\langle (\xi, \eta), (KG)^\dagger KG(\xi, \eta) \Big\rangle = \frac{4\gamma a_1^2 \xi^2}{b_1} - 4\gamma a_1 \xi \eta + 4 a_1 \eta^2 \; ; \quad (3.101)$$

see Figure 3.12. To estimate the true degree of damping of individual trajectories (ξ_j, η_j) we calculate the ratio $\langle \mathrm{q}/\mathrm{q}_0 \rangle$ of the initial and asymptotic values

$$\mathrm{q}_0 := \mathrm{q}(\alpha, \beta) \ , \quad \langle \mathrm{q} \rangle := \langle \mathrm{q} \rangle_\infty \ . \tag{3.102}$$

From equation (3.81) we obtain the three second moments $\langle x^2 \rangle_\infty$, $\langle xy \rangle_\infty$, $\langle y^2 \rangle_\infty$ which are needed for the calculation of $\langle \mathrm{q} \rangle$. After some lengthy but straightforward algebra we find

$$\left\langle \frac{\mathrm{q}}{\mathrm{q}_0} \right\rangle = \frac{(\langle |s| \rangle - \Delta)^2 + \mathrm{var}(|s|)}{\mu^2 \left(\langle s \rangle_o - \Delta \right)^2} \bar{\rho}_1 - \bar{\rho}_2 \ , \tag{3.103}$$

where the coefficients are for Poisson statistics of t_j (see appendix D)

$$\begin{aligned} \bar{\rho}_1 &= \frac{2 \left(\mathrm{e}\gamma + \langle r/\tau \rangle \right)^2}{4\mathrm{e}\gamma - (\mathrm{e}\gamma)^2 + 4 \langle r/\tau \rangle} \ > \ 0 \ , & (3.104) \\ \bar{\rho}_2 &= \frac{2\mathrm{e}\gamma(\mathrm{e}\gamma + 2 \langle r/\tau \rangle)}{4\mathrm{e}\gamma - (\mathrm{e}\gamma)^2 + 4 \langle r/\tau \rangle} \ > \ 0 \ . & (3.105) \end{aligned}$$

Using the decomposition (3.59) and respecting that $\langle s \rangle_b = 0$, $\langle |s| \rangle_o = \langle s \rangle_o$ we obtain

$$\left\langle \frac{\mathrm{q}}{\mathrm{q}_0} \right\rangle = \tag{3.106}$$

$$\frac{\mu \left(\langle s \rangle_o - \Delta \right)^2 + (1-\mu) \left(\langle |s| \rangle_b - \Delta \right)^2 + \mu \, \mathrm{var}_o(s) + (1-\mu) \, \mathrm{var}_b(|s|)}{\mu^2 \left(\langle s \rangle_o - \Delta \right)^2} \bar{\rho}_1 - \bar{\rho}_2 \ ,$$

where $\mathrm{var}_{o/b}(|s|) := \langle s^2 \rangle_{o/b} - \langle |s| \rangle_{o/b}^2$. For $\mu = 1$ and an object in perfectly coherent motion, i.e., $\mathrm{var}_o(s) = 0$, we have

$$\left. \left\langle \frac{\mathrm{q}}{\mathrm{q}_0} \right\rangle \right|_{\mu=1} = \bar{\rho}_1 - \bar{\rho}_2 = \frac{2 \langle r/\tau \rangle^2}{4\mathrm{e}\gamma - (\mathrm{e}\gamma)^2 + 4 \langle r/\tau \rangle} < \frac{1}{2} \left\langle \frac{r}{\tau} \right\rangle \ll 1 \ . \tag{3.107}$$

Hence there is strong damping, and individual trajectories (x_j, y_j) converge to the steady mean state; cf. Figure 3.10 top. On the other hand,for $\mu \to 0$ at fixed $\mathrm{v}(s)$ [see equation (3.103)] or at fixed $\mathrm{v}_b(s)$ [see equation (3.106)] $\langle \mathrm{q}/\mathrm{q}_0 \rangle$ is dominated by a $1/\mu^2$-singularity. This means that at high background activity $\langle \mathrm{q}/\mathrm{q}_0 \rangle \gg 1$; there is no damping of individual trajectories (x_j, y_j). Since the adaptation dynamics is a temporally homogeneous Markov chain, at any time we find qualitatively the same situation as at the start of the process, implying that there is no qualitative change in the trajectories (x_j, y_j) on a long time scale; cf. Figure 3.10 bottom.

We have also checked numerically the variance $\langle \mathrm{q}^2 \rangle - \langle \mathrm{q} \rangle^2$, and found it to be of the same order of magnitude as $\langle \mathrm{q} \rangle^2$. This leaves open the question

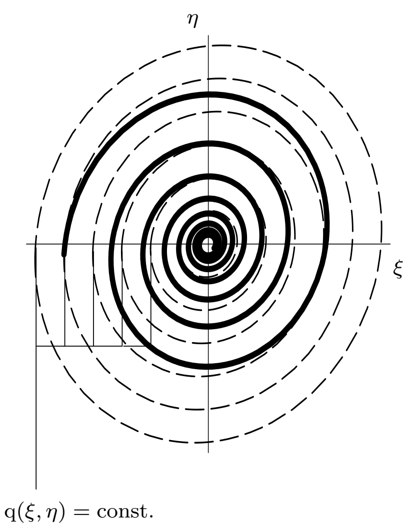

Figure 3.12: Trajectories of $(\langle\xi\rangle_j, \langle\eta\rangle_j)$ [bold spiral curve; cf. equation (3.100)] and orbits defined by $q(\xi, \eta) = \text{const.}$ [dashed ellipses; cf. equation (3.101)] corresponding to undamped oscillations of (ξ_j, η_j).

of whether there is a preferred orbit with $q = \text{const.}$ where the system spends most of the time.

We conclude that if μ and $\langle r/\tau\rangle$ are both small enough, i.e., if the background is strong and the total stimulus dense or fast enough, the RTDs show a sustained oscillation with a mean period given by equations (3.73) and (3.65), or by (3.79). In Figure 3.13 we compare mean oscillation periods observed in computer simulations with the mean period (3.79) of mean RTDs. The match is perfect for small $\langle r/\tau\rangle$, that is, in the regime where oscillations are rather regular. For increasing interstimulus times $\langle r/\tau\rangle$, when the random-walk component of RTD dynamics grows stronger (cf. Figure 3.11), the measured values eventually drop below the curve given by (3.79), indicating that fluctuations cause RTDs to jitter around their mean values faster than the oscillatory component of the dynamics alone. For details on the computer simulations and sampling of oscillation periods see appendix G.

As a particular scenario, consider that when background is added to any given stimulus, both the object weight μ and the mean interstimulus time $\langle r/\tau\rangle$ decline towards zero and sustained oscillations eventually develop.

If μ is close to one, on the other hand, the RTDs converge to a stationary state. The remaining case of small μ and rather large $\langle r/\tau\rangle$ is quite uninteresting. It corresponds to a stimulus consisting of a sparse background without any significant object, which may be identified with mere noise. Adaptation will be weak and look rather erratic in this case; cf. equation (3.67) and Figure 3.11 bottom.

Let us rephrase the above mathematics by saying that the ongoing oscillations are the result of an interplay between two contrary drives. One is

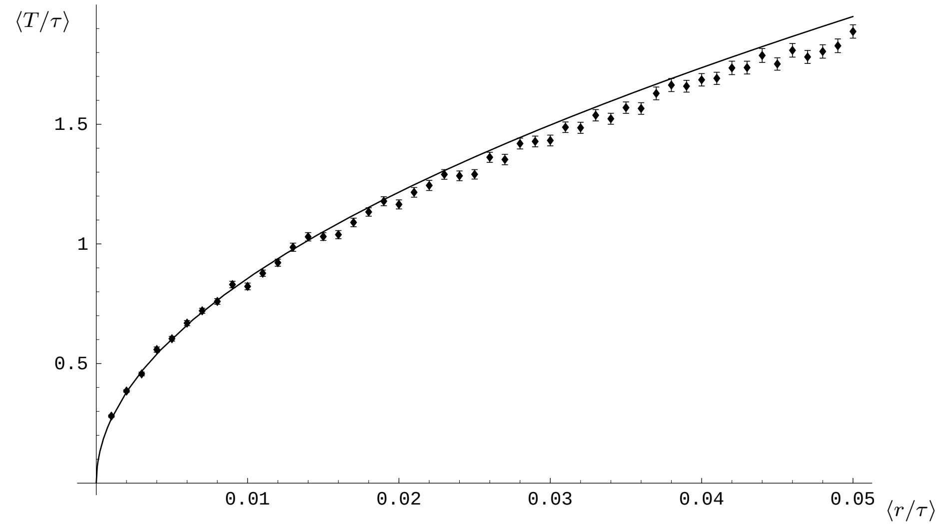

Figure 3.13: Comparison of mean oscillation periods of mean response time differences (RTDs) as given by equation (3.79) (solid line; cf. Figure 3.7) with mean periods of simulated RTD dynamics (diamond symbols; bars indicate standard errors) in the regime of diffusion-sustained oscillations. The match is perfect for small $\langle r/\tau \rangle$, where oscillations are rather regular. As oscillations are increasingly degraded by fluctuations for larger $\langle r/\tau \rangle$ (cf. Figure 3.11), the observed 'jitter period' drops below the period of the mean RTD. Parameters: $\mu = 1/3$, $s_o = 15$, $\langle |s| \rangle = 17.1$, $\mathrm{var}(|s|) = 15.6^2$, $\gamma = 0.2$. See appendix G for details on the computer simulations and sampling of oscillation periods.

the tendency of the system to relax in a damped oscillation to its stationary state. The other is the diffusion contributed by the background activity that drives the system away from its stationary state. For a strong background this diffusion is *strong* enough to keep the state at a significant distance away from the stationary state. For a dense or fast total stimulus the oscillation is *fast* enough to be not obscured by the diffusion process. We call the dynamics resulting from the coincidence of both conditions a *diffusion-sustained oscillation.*

One can heuristically understand the occurrence of diffusion-sustained oscillations by recalling that there are two populations of cortical neurons responsive to opposite directions of motion and producing feedback signals of opposite signs. Whenever some local feature stimulates a cortical neuron, RTDs of neurons encoding motion in the feature's direction are pulled towards the feature's passage time and, hence, *closer* to each other. On the other hand, due to the opposite signs of the feedback signals, RTDs of neurons encoding motion in the opposite direction are pushed *apart* from each other. Hence, if there are features moving both ways, there is an alternating convergence and divergence of RTDs, with the RTDs of neurons stimulated by object plus background features being at average closer together than RTDs of neurons stimulated by background features only.

3.4.6 Correlation of Adaptation Dynamics Between Cell Classes

The occurrence of ongoing oscillations in RTDs as derived in the last subsection motivates the question of how such oscillations are correlated. Correlation across space is trivial in the present model, since global lateral connections have been assumed to synchronize adaptation in a pool of cortical neurons that jointly represent an extended retinal area; cf. the model definition in section 3.3. Correlation of the response time differences $\mathrm{RTD}^{(c,\pm)}(t)$ across classes c of cortical neurons, on the other hand, is mediated by the stimulus.

For neurons of two classes $(c_1,+)$ and $(c_2,+)$ to be well tuned to an object's speed at the *same*, possibly periodic, times, $\mathrm{RTD}^{(c_1,+)}(t)$ and $\mathrm{RTD}^{(c_2,+)}(t)$ have to be *positively* correlated, if they are both smaller or larger, and *anti*-correlated, if one is smaller and the other larger than the object's passage time $\langle s\rangle_o$; cf. Figure 3.10. *Synchrony of adaptation* to an object's speed across classes of cortical neurons has important consequences on cortical activity and information processing, as will be detailed in subsections 3.5.1 and 3.5.3 in the discussion. Here we are interested in the inter-class correlations of RTDs in general and in the conditions for synchronous adaptation in particular.

Neuron classes c are characterized by the initial value Δ of their RTD; cf. definition (3.36). We denote the initial RTDs of two different classes $(c_1,+)$ and $(c_2,+)$ by Δ_1 and Δ_2. Accordingly, the two classes' dynamic variables (x,y) as defined in (3.37) and (3.41) are denoted (x_1,y_1) and (x_2,y_2) throughout this subsection. Although the index of x and y previously labeled stimulus/response events in chronological order, no confusion will arise from the notation used in this subsection.

The temporal evolution of the mixed-class moments $\langle x_1x_2\rangle$, $\langle 1/2(x_1y_2+x_2y_1)\rangle$, and $\langle y_1y_2\rangle$ is determined by the transition probabilities

$$\begin{aligned}\mathrm{p}_{\mathcal{S}}(x_1,y_1,x_2,y_2|x_1',y_1',x_2',y_2') \;=&\qquad\qquad (3.108)\\ \mu_+\int_{-\infty}^{\infty}\mathrm{d}s\,\mathrm{v}_+(s)\,\delta(x_1-x_1')\,\delta(x_2-x_2')&\\ \times\,\delta[y_1-y_1'-\gamma(s-x_1'-\Delta_1)]\;\delta[y_2-y_2'-\gamma(s-x_2'-\Delta_2)]&\end{aligned}$$

$$\begin{aligned} &+ \quad \mu_- \int_{-\infty}^{\infty} \mathrm{d}s\, \mathrm{v}_-(s)\, \delta(x_1 - x_1')\, \delta(x_2 - x_2') \\ &\qquad \times \delta[y_1 - y_1' - \gamma(s - x_1' + \Delta_1)]\ \delta[y_2 - y_2' - \gamma(s - x_2' + \Delta_2)] \ , \\ &\mathrm{p}_{\mathcal{R}}(x_1, y_1, x_2, y_2 | x_1', y_1', x_2', y_2') \ = \qquad (3.109) \\ &\qquad \int_0^{\infty} \mathrm{d}r\, \mathrm{u}(r)\, \delta\Big[x_1 - (x_1' + y_1' \frac{\mathrm{e}r}{\tau}) \mathrm{e}^{-r/\tau}\Big]\ \delta\Big[x_2 - (x_2' + y_2' \frac{\mathrm{e}r}{\tau}) \mathrm{e}^{-r/\tau}\Big] \\ &\qquad \times \delta\Big(y_1 - y_1' \mathrm{e}^{-r/\tau}\Big)\ \delta\Big(y_2 - y_2' \mathrm{e}^{-r/\tau}\Big) \ . \end{aligned}$$

Much like in subsection 3.4.2, we obtain from these transition probabilities for the mixed-class moments the dynamic map

$$\begin{pmatrix} \langle x_1 x_2 \rangle_j \\ \left\langle \frac{1}{2}(x_1 y_2 + x_2 y_1) \right\rangle_j \\ \langle y_1 y_2 \rangle_j \end{pmatrix} = M_{1,1} \begin{pmatrix} \langle x_1 x_2 \rangle_{j-1} \\ \left\langle \frac{1}{2}(x_1 y_2 + x_2 y_1) \right\rangle_{j-1} \\ \langle y_1 y_2 \rangle_{j-1} \end{pmatrix} + \begin{pmatrix} \hat{u}_{j-1} \\ \hat{v}_{j-1} \\ \hat{w}_{j-1} \end{pmatrix} \ , \tag{3.110}$$

where it turns out that $M_{1,1} = M_2$; cf. equation (3.81). In fact, this may be seen directly by comparing the transition probabilities (3.52), (3.53) with (3.108), (3.109). The vector components of the map are

$$\begin{aligned} \hat{u}_j \ &:= \ \gamma\mu\, (\alpha_j b_2 + 2\beta_j c_2 - 2\gamma\alpha_j c_2)\, (\langle s \rangle_o - \Delta_1)\, (\langle s \rangle_o - \Delta_2) \qquad (3.111) \\ &+ \ \gamma^2 c_2\, (\langle |s| \rangle - \Delta_1)\, (\langle |s| \rangle - \Delta_2) + \gamma^2 c_2\, \mathrm{var}(|s|) \ , \\ \hat{v}_j \ &:= \ \gamma\mu\, (\alpha_j a_2 + \beta_j b_2 - \gamma\alpha_j b_2)\, (\langle s \rangle_o - \Delta_1)\, (\langle s \rangle_o - \Delta_2) \qquad (3.112) \\ &+ \ \frac{1}{2}\gamma^2 b_2\, (\langle |s| \rangle - \Delta_1)\, (\langle |s| \rangle - \Delta_2) + \frac{1}{2}\gamma^2 b_2\, \mathrm{var}(|s|) \ , \\ \hat{w}_j \ &:= \ 2\gamma\mu\, (\beta_j - \gamma\alpha_j)\, a_2\, (\langle s \rangle_o - \Delta_1)\, (\langle s \rangle_o - \Delta_2) \qquad (3.113) \\ &+ \ \gamma^2 a_2\, (\langle |s| \rangle - \Delta_1)\, (\langle |s| \rangle - \Delta_2) + \gamma^2 a_2\, \mathrm{var}(|s|) \ . \end{aligned}$$

Because $M_{1,1} = M_2$ the mixed moments converge, if and only if the second moments do so; cf. subsection 3.4.4. We are interested in the asymptotic value

$$\langle x_1 x_2 \rangle \ := \ \langle x_1 x_2 \rangle_{\infty} \ . \tag{3.114}$$

The covariance between the two RTDs is

$$\mathrm{cov}(x_1, x_2) \ := \ \langle x_1 x_2 \rangle - \langle x_1 \rangle \langle x_2 \rangle \tag{3.115}$$

$$= \ \hat{\rho}_1\, (\langle s \rangle_o - \Delta_1)\, (\langle s \rangle_o - \Delta_2) + \hat{\rho}_2\, (\langle |s| \rangle - \Delta_1)\, (\langle |s| \rangle - \Delta_2) + \hat{\rho}_3\, \mathrm{var}(|s|) \ ,$$

with

$$\hat{\rho}_1 \ := \ \frac{\{2\gamma\mu\alpha(1 - a_2)b_2 + 2\gamma\mu\beta b_2^2 + 4\gamma\mu\, [\beta(1 - a_2) - \gamma\alpha]\, c_2\}}{2 + 6a_2^2 - 2a_2^3 + 4\gamma b_2 + \gamma^2 b_2^2 - 2\gamma^2 c_2 - 2a_2(3 + 2\gamma b_2 + \gamma^2 c_2)}$$

$$- \left[\frac{\mu\gamma b_1}{\gamma b_1 + (1-a_1)^2}\right]^2 , \tag{3.116}$$

$$\hat{\rho}_2 := \frac{\gamma^2 b_2^2}{2 + 6a_2^2 - 2a_2^3 + 4\gamma b_2 + \gamma^2 b_2^2 - 2\gamma^2 c_2 - 2a_2(3 + 2\gamma b_2 + \gamma^2 c_2)} , \tag{3.117}$$

$$\hat{\rho}_3 := \frac{\gamma^2 \left[2(1-a_2)c_2 + b_2^2\right]}{2 + 6a_2^2 - 2a_2^3 + 4\gamma b_2 + \gamma^2 b_2^2 - 2\gamma^2 c_2 - 2a_2(3 + 2\gamma b_2 + \gamma^2 c_2)} . \tag{3.118}$$

In order to have positive correlation between the two RTDs, if both neuron classes prefer speeds below or above an object's speed, and negative correlation, if one prefers speeds below and the other above the object's speed, it would be required that $\mathrm{cov}(x_1, x_2)$ is proportional to $(\langle s\rangle_o - \Delta_1)(\langle s\rangle_o - \Delta_2)$. By inspection of equation (3.115), however, we see that $\mathrm{cov}(x_1, x_2)$ also contains terms that are proportional to $(\langle|s|\rangle - \Delta_1)(\langle|s|\rangle - \Delta_2)$, and terms that are proportional to $\mathrm{var}(|s|)$. In general, therefore, arbitrary classes of cortical neurons do not synchronize their phases of close tuning to an object's speed.

Using the results of subsection 3.4.4 we can explicate the correlation

$$\mathrm{cor}(x_1, x_2) := \frac{\mathrm{cov}(x_1, x_2)}{\sqrt{\mathrm{var}(x_1)\mathrm{var}(x_2)}} . \tag{3.119}$$

For the general case, however, this is a rather lengthy expression that is not easily interpretable. Instead, we discuss the correlation for the case of Poissonian stimulus/response times t_j. To this end, we introduce the complex vectors

$$\boldsymbol{v}_i := \begin{pmatrix} \left(\gamma \mathrm{e} + \left\langle \frac{r}{\tau} \right\rangle\right) (\langle|s|\rangle - \Delta_i) \\ \mathrm{i}\mu\sqrt{\gamma \mathrm{e}\left(\gamma \mathrm{e} + 2\left\langle \frac{r}{\tau}\right\rangle\right)}\,(\langle s\rangle_o - \Delta_i) \\ \left(\gamma \mathrm{e} + \left\langle \frac{r}{\tau}\right\rangle\right)\sqrt{\mathrm{var}(|s|)} \end{pmatrix} , \quad i = 1, 2 , \tag{3.120}$$

and the bilinear form

$$((v_1, v_2, v_3), (u_1, u_2, u_3)) := v_1 u_1 + v_2 u_2 + v_3 u_3 , \tag{3.121}$$

which is *not* positive definite on complex vector spaces. For Poissonian stimulus/response times we get

$$\mathrm{cor}(x_1, x_2) = \frac{(\boldsymbol{v}_1, \boldsymbol{v}_2)}{\sqrt{(\boldsymbol{v}_1, \boldsymbol{v}_1)\,(\boldsymbol{v}_2, \boldsymbol{v}_2)}} ; \tag{3.122}$$

cf. appendix D. It now turns out that in the regime of diffusion-sustained oscillations, where μ^2 is small, the *sign* of the correlation is in fact largely determined by $(\langle|s|\rangle - \Delta_1)(\langle|s|\rangle - \Delta_2)$; cf. equation (3.120). Without loss of generality, let us assume that $\Delta_1 < \Delta_2$ and introduce the variables

$$D \;:=\; \frac{1}{2}(\Delta_1 + \Delta_2) - \langle s\rangle_o \;, \tag{3.123}$$

$$C \;:=\; D - (\Delta_1 - \langle s\rangle_o) \;=\; (\Delta_2 - \langle s\rangle_o) - D \;>\; 0 \;, \tag{3.124}$$

$$S \;:=\; \langle|s|\rangle - \langle s\rangle_o \;. \tag{3.125}$$

We can now ask the question: Given a certain stimulus parameter S and a certain distance D from the mean object passage time $\langle s\rangle_o$, how far must a neuron's initial RTD be from D, i.e., how large is the minimum value of C, such that neuron classes below $D-C$ are anti-correlated with neuron classes above $D+C$? Denoting this particular value of C by $\hat{C}$, the RTD *gap* between anti-correlated populations of neurons around D is thus $2\hat{C}$. To answer this question we have to investigate the change of sign of the correlation. Its sign is determined by the numerator of expression (3.122). Substituting D, C, and S into (3.122), we obtain

$$\operatorname{cor}(x_1, x_2) \;= \tag{3.126}$$

$$\frac{1}{\sqrt{\cdots}}\Big\{ - C^2 \left[\left(\gamma^2\mathrm{e}^2 + 2\gamma\mathrm{e}\left\langle\frac{r}{\tau}\right\rangle\right)(1-\mu^2) + \langle r/\tau\rangle^2\right]$$

$$+ (D-S)^2\left(\gamma\mathrm{e} + \left\langle\frac{r}{\tau}\right\rangle\right)^2 - \mu^2\gamma\mathrm{e}D^2\left(\gamma\mathrm{e} + 2\left\langle\frac{r}{\tau}\right\rangle\right) + \left(\gamma\mathrm{e} + \left\langle\frac{r}{\tau}\right\rangle\right)^2 \operatorname{var}(|s|)\Big\} \;.$$

Response time differences of neurons are thus anti-correlated, if and only if

$$C \;>\; \hat{C} \;:= \tag{3.127}$$

$$\sqrt{D^2 + [S^2 - 2DS + \operatorname{var}(|s|)]\,\frac{(\gamma\mathrm{e} + \langle r/\tau\rangle)^2}{(\gamma^2\mathrm{e}^2 + 2\gamma\mathrm{e}\,\langle r/\tau\rangle)(1-\mu^2) + \langle r/\tau\rangle^2}} \;.$$

In particular, the smallest gap between anti-correlated populations of neurons occurs around $D = S$, that is, between classes with initial RTDs around $\langle|s|\rangle$,

$$\hat{C}_{\min} \;:=\; \hat{C}\Big|_{D=S} \;= \tag{3.128}$$

$$\left\{S^2\left[1 - \frac{(\gamma\mathrm{e} + \langle r/\tau\rangle)^2}{(\gamma^2\mathrm{e}^2 + 2\gamma\mathrm{e}\,\langle r/\tau\rangle)(1-\mu^2) + \langle r/\tau\rangle^2}\right]\right.$$

$$\left. + \operatorname{var}(|s|)\frac{(\gamma\mathrm{e} + \langle r/\tau\rangle)^2}{(\gamma^2\mathrm{e}^2 + 2\gamma\mathrm{e}\,\langle r/\tau\rangle)(1-\mu^2) + \langle r/\tau\rangle^2}\right\}^{1/2} \;.$$

Note that the coefficient of S^2 in the radical argument is always positive, and zero only if $\mu = 0$.

Finally, coming back to the issue of synchrony of adaptation to an object's speed, the gap around the object's passage time $\langle s \rangle_o$ is $2\hat{C}$ with

$$\hat{C}\Big|_{D=0} = \sqrt{\frac{(\gamma \mathrm{e} + \langle r/\tau \rangle)^2 [S^2 + \mathrm{var}(|s|)]}{(\gamma^2 \mathrm{e}^2 + 2\gamma \mathrm{e} \, \langle r/\tau \rangle)\,(1-\mu^2) + \langle r/\tau \rangle^2}}\,. \tag{3.129}$$

It thus turns out that the maximum number of neurons can be recruited for synchronous adaptation to an object's speed, if $S = 0$, that is, for a stimulus with $\langle s \rangle_o = \langle |s| \rangle$, and as $\mu \to 0$, that is, for a weak object in the stimulus. The gap between anti-correlated classes of neurons increases with $\mathrm{var}(|s|)$, i.e., with the diversity of speeds in the stimulus. For illustration, Figure 3.14 compares a time course of adaptation with $S = 0$ and $\mathrm{var}(|s|) = 0$ (top) to one with $S > 0$ and a rather large $\mathrm{var}(|s|) > 0$ (bottom).

3.4.7 Crossing of Response Time Differences: Disruption of Adaptation

The dynamics (3.19) for the RTDs that is decoupled for different neuron classes c is a valid description of the full dynamics given in equations (3.12) through (3.15) only as long as the RTDs for different classes do not cross over, i.e., as long as condition (3.17) holds. As soon as RTDs of classes $c-1$ and $c+1$ cross, the system will produce PSP amplitudes $A_i^{(c)}$ of the wrong sign [cf. equation (3.15)] and adaptation will be disrupted. In the full system dynamics, however, due to the finite slope of the sigmoidal σ at zero, the amplitudes $A_i^{(c)}$ become small, if $\mathrm{RTD}^{(c-1,+)}(t)$ and $\mathrm{RTD}^{(c+1,+)}(t)$ get close to each other. As a result, wrong amplitudes $A_i^{(c)}$ are only *small* for *slightly* crossed RTDs, and the system tolerates slight crossing without disruption of the adaptation course. An example of adaptation dynamics where disruption occurs following repeated crossing of RTDs is given in Figure 3.15.

After having derived and discussed the solutions of (3.19) in the past subsections, we now have to take care of their consistency with the full dynamics (3.12) through (3.15) by giving conditions on the stimulus and system parameters for the trajectories $\mathrm{RTD}^{(c,+)}(t)$ to not cross over. These conditions constrain not only the validity of the solutions obtained previously, but also the range of parameters for which successful adaptation occurs. In the latter sense, they are additional to those for the convergence of the first and second moments of RTDs derived in subsections 3.4.3 and 3.4.4, respectively.

Since the RTDs' dynamics is a stochastic process, the event of RTD crossing is probabilistic. The most appropriate analytic treatment would therefore

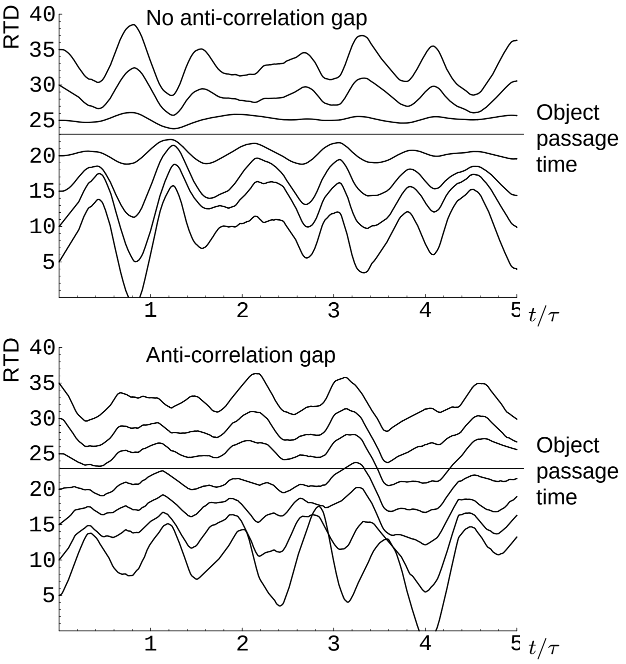

Figure 3.14: Computer simulations of the adaptation dynamics for the response time differences $\mathrm{RTD}^{(c,\pm)}(t)$ of 7 classes of neurons ($c = 1, \ldots, 7$). The time scale is set by τ, the rise time of corticothalamic postsynaptic potentials; cf. equation (3.1). The stimulus consists of an object and a background component. Only the 7 trajectories $\mathrm{RTD}^{(c,+)}(t)$, i.e., representative of the neurons selective for the direction of object motion, are shown. The passage time of object features is indicated by the straight horizontal line in each graph. The two graphs compare the dynamics resulting from a stimulus consisting of features moving all at the same speed in two opposite directions [$\mathrm{var}(|s|) = 0$, $S = 0$, top] with the dynamics resulting from a stimulus that comprises features moving at a large range of speeds [$\mathrm{var}(|s|) = 22.3^2$, $S = 1.24$, bottom]; cf. equation (3.125). In the top scenario the inter-class correlation of the RTDs reverses sign precisely at the object's passage time. As a result, RTDs of all classes approach the object's passage time in perfect *synchrony*. In the bottom scenario all RTDs close to the object's passage time are positively correlated. Synchrony of adaptation to the object's passage time is thus not possible across all 7 classes of neurons. Other parameters: $\mu = 1/3$, $s_o = 23$, $\langle |s| \rangle = 24.2$, $\langle r/\tau \rangle = 0.004$, $\gamma = 0.06$. See appendix G for details on the computer simulations.

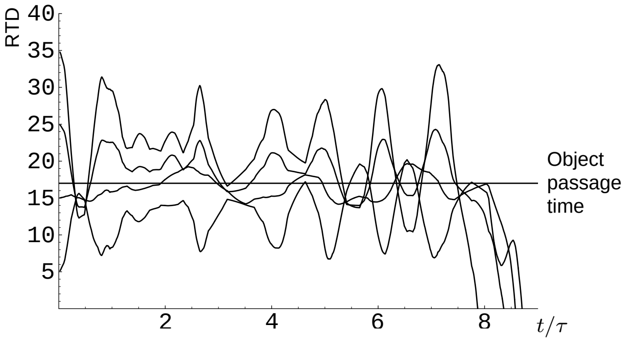

Figure 3.15: Example of an adaptation process that leads to crossing of the response time differences $\mathrm{RTD}^{(c,+)}(t)$ of 4 classes of neurons ($c = 1, 2, 3, 4$) representing the direction of an object's motion. The passage time of object features is indicated by the straight horizontal line in the graph. The time scale is set by τ, the rise time of corticothalamic postsynaptic potentials; cf. equation (3.1). In the example shown the RTDs are slightly crossed several times before adaptation is finally disrupted. Crossing with a dominant object in the stimulus occurs, if the feedback coupling γ is too large or the stimulus parameter a_1 is too close to one, i.e., $\langle r/\tau\rangle$ is too small, corresponding to a very fast or dense stimulus. Parameters: $\mu = 4/5$, $s_o = 17$, $\langle|s|\rangle = 17.2$, $\mathrm{var}(|s|) = 8.5^2$, $\langle r/\tau\rangle = 0.01$, $\gamma = 0.2$. See appendix G for details on the computer simulations.

be to calculate the probability of the crossing event as a function of time and stimulus parameters. This, however, turns out to be unfeasible. Instead, we want to estimate under which stimulus conditions crossing is likely to occur. To this end, we will investigate when the *mean* trajectories of the RTDs cross in the course of adaptation.

There are good reasons for analyzing the mean dynamics, if one is interested in crossing of RTDs. In the usual regime of the system's operation we have $\langle r/\tau\rangle \ll 1$; see the previous footnote 2 on page 89. In the last subsection we have found that, then, individual trajectories $\mathrm{RTD}^{(c,\pm)}(t)$ are well described by their means for several periods of their oscillation; cf. equation (3.98). Moreover, for μ close to one we have also found in the last subsection that there is strong damping of RTD oscillations [cf. equation (3.107)]. For any damped oscillation, crossing, if it occurs, is restricted to the *first* cycle of oscillation, where the amplitude is largest. The mean trajectories hence are good approximations to individual trajectories during the initial, and often *critical*, phase of adaptation.

The exception is the regime of diffusion-sustained oscillations, where $\langle r/\tau\rangle \ll 1$ and μ is not close to one; see subsection 3.4.5. In that case it is not possible to predict the amplitudes of late cycles of the oscillation. Ensuring no crossing in early cycles is necessary, but not sufficient for a RTD dynamics free of crossing. We will return to this issue at the end of this subsection.

If μ is small and $\langle r/\tau \rangle$ rather large, the input is just noise and adaptation is weak and erratic; cf. equation (3.67) and Figure 3.11 bottom. RTD trajectories may cross in that case, if the feedback coupling strength γ is large enough.

Generally, crossing of the mean RTD trajectories indicate a high probability for the event of crossing of individual trajectories. *Necessary and sufficient* conditions for a *mean* adaptation dynamics free of crossing can thus be interpreted as *necessary* for *individual* adaptation dynamics free of crossing.

By inspection of equation (3.62) we see that the mean RTD dynamics does not cross, if and only if the mean degree of adaptation obeys $\alpha_j \leq 1$ for all $j \in \mathbb{N}$, or

$$\alpha_{\hat{j}} := \max_{j \in \mathbb{N}} \alpha_j \ \leq \ 1 \ . \tag{3.130}$$

Since α_j always converges in a *damped* oscillation to $\alpha \leq 1$ [cf. equation (3.67)], it assumes its maximum within the first cycle of the oscillation, that is, $\hat{j} \in \mathbb{N}$ is an index of some event within the first oscillation period.

The evolution of α_j is given by equations (3.70) and (3.71). The angle ϕ defined in (3.70) gives the angular increment of α_j per cortical response event. ϕ is a function of the parameters a_1 and γb_1, which is plotted in Figure 3.16 for $\gamma b_1 \leq 4a_1$, the region where ϕ is defined and where the first and second moments of the RTDs converge; cf. Figure 3.5 and subsections 3.4.3 and 3.4.4. For $\gamma b_1 \approx 4a_1$ we have $\phi \approx \pi$, and thus $\hat{j} = 1$. Condition (3.130) becomes in that case

$$\alpha_1 = \mu \gamma b_1 \leq 1 \ . \tag{3.131}$$

This constraint on the parameters is illustrated in Figure 3.17 for different values of μ by horizontal lines. The condition holds below the line for the corresponding value of μ.

As we increase the stimulus density or speed, thus moving towards the point $a_1 = 1, b_1 = 0$, we have $\phi \rightarrow 0$. In this limit a continuous approximation of the dynamics of α_j with $j \in \mathbb{R}_+$ seems adequate, and $\hat{j}$ is the first positive solution of the equation

$$\frac{\partial}{\partial j} \alpha_j \ = \ 0 \ . \tag{3.132}$$

We will verify the adequacy of the continuous approximation below. After

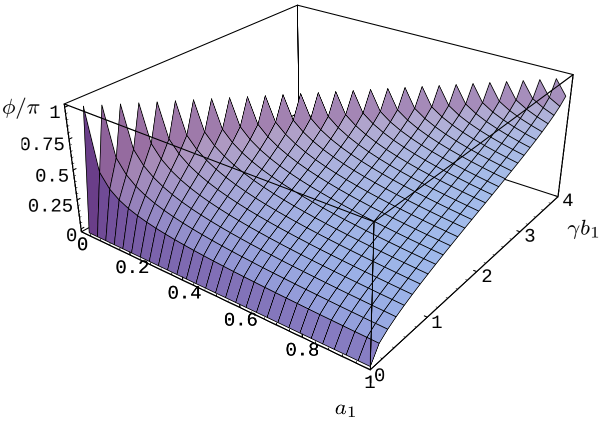

Figure 3.16: Plot of ϕ in units of π as function of a_1 and γb_1. ϕ is defined for $\gamma b_1 \leq 4a_1$; cf. equation (3.70) and Figure 3.5. In particular, $\phi = \pi$ for $\gamma b_1 = 4a_1$, and $\phi = 0$ for $\gamma b_1 = 0$.

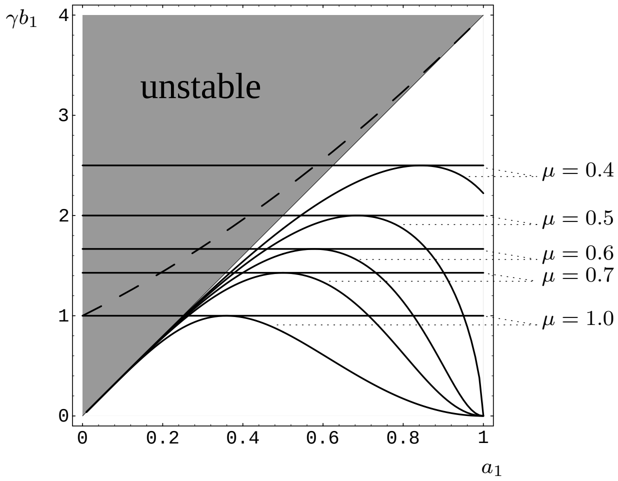

Figure 3.17: Plots of the constraints on the parameters a_1 and γb_1 for adaptation dynamics without crossing of the mean response time differences (RTDs). In the shaded region the first or second moments diverge; cf. Figure 3.5 and subsections 3.4.3, 3.4.4. For each value of μ, the parameters a_1 and γb_1 have to lie in the area below the corresponding curve to the right of its maximum, and below its horizontal tangent to the left of the maximum. The constraining curves terminate in $a_1 = 1$, $\gamma b_1 = 0$ for $\mu \geq 1/2$, and in $a_1 = 1$, $\gamma b_1 > 0$ for $\mu < 1/2$. Their slope in $a_1 = 1$, $\gamma b_1 = 0$ is zero for $\mu > 1/2$, and infinite for $\mu = 1/2$.

some lengthy but straightforward algebra we find

$$\hat{j} = \frac{\frac{\pi}{2} - \psi}{\phi} \;, \tag{3.133}$$

with

$$\psi \;:=\; \arg\left[\gamma b_1 + 2a_1^2 - 2a_1 - \mathrm{i}\sqrt{\gamma b_1(4a_1 - \gamma b_1)}\right] + \arg\left(\phi - \mathrm{i}\ln a_1\right) \;<\; \frac{\pi}{2} \;. \tag{3.134}$$

We can rearrange condition (3.130) to read

$$\begin{aligned} &\mathrm{F}(a_1, \gamma b_1) \;:= \\ &\mu\, a_1^{\frac{\pi/2-\psi}{\phi}} \left[\left(2a_1^2 - 2a_1 + \gamma b_1\right)\sqrt{\gamma b_1(4a_1 - \gamma b_1)}\,\cos\psi - \gamma b_1\,(4a_1 - \gamma b_1)\,\sin\psi\right] \\ &\quad + \mu\gamma b_1\,(4a_1 - \gamma b_1) - (4a_1 - \gamma b_1)\,\left[(1-a_1)^2 + \gamma b_1\right] \;\leq\; 0 \;. \end{aligned} \tag{3.135}$$

Note that by utilizing the continuous approximation for j, condition (3.135) is actually *more restrictive* than the real condition (3.130), which is only imposed for $j \in \mathbb{N}$. We will therefore investigate a posteriori the continuous values of $\hat{j}$ that effectively delimit the region of parameters by imposing the condition $\alpha_{\hat{j}} < 1$ or, equivalently, (3.135).

Obviously, there is no crossing of RTDs for $\gamma b_1 = 0$, since $\gamma = 0$ means no feedback. We thus seek solutions $\gamma b_1 = \mathrm{C}_\mu(a_1)$ of $\mathrm{F}(a_1, \gamma b_1) = 0$, such that

$$\gamma b_1 \;\leq\; \mathrm{C}_\mu(a_1) \quad\Longrightarrow\quad \mathrm{F}(a_1, \gamma b_1) \;\leq\; 0 \;. \tag{3.136}$$

These have to be determined numerically and are plotted in Figure 3.17 for different values of μ. We stress that the continuous approximation is very bad close to the line $\gamma b_1 = 4a_1$, because there $\phi \approx \pi$. In that limit the true, and less-constraining, condition is given by (3.131); cf. Figure 3.17. It will become clear shortly, where precisely in parameter space condition (3.131) gives the correct constraint.

Although we cannot give the curves $\gamma b_1 = \mathrm{C}_\mu(a_1)$ in an explicit analytical form, one can make a couple of analytical assertions on them. Developing these assertions will occupy the rest of this subsection. Longer proofs are relocated to appendix E. To start with, since $a_1 \in [0,1]$ and $\hat{j} > 0$ we know that

$$\lim_{(a_1,\gamma b_1)\to(0,0)} a_1^{\hat{j}} \;\in\; [0,1] \;, \quad \lim_{(a_1,\gamma b_1)\to(1,0)} a_1^{\hat{j}} \;\in\; [0,1] \;, \tag{3.137}$$

where the precise values of the limits depend on the path taken to the points $(a_1, \gamma b_1) = (0,0)$ and $(1,0)$, respectively. It follows that $\mathrm{F}(0,0) = \mathrm{F}(1,0) = 0$.

However, as can be seen from Figure 3.17, the point $a_1 = 1$, $\gamma b_1 = 0$ does not always lie on the curve $\gamma b_1 = \mathrm{C}_\mu(a_1)$.
Assertion 1: *The curve $\gamma b_1 = \mathrm{C}_\mu(a_1)$ terminates in $a_1 = 1$, $\gamma b_1 = 0$, if and only if $\mu \geq 1/2$, i.e.,*

$$\mathrm{C}_\mu(1) \left\{ \begin{array}{ccl} = & 0 & \text{if } \mu \geq 1/2, \\ > & 0 & \text{if } \mu < 1/2. \end{array} \right. \tag{3.138}$$

To prove this assertion, one may verify by patient calculation that

$$\lim_{\gamma b_1 \to 0+} \frac{\partial}{\partial z} \mathrm{F}(1, z) \bigg|_{z=\gamma b_1} = 4\,(2\mu - 1) \ . \tag{3.139}$$

Since $\mathrm{F}(1, 0) = 0$, equation (3.139) implies that, if and only if $\mu < 1/2$, there is some $\epsilon > 0$ such that for $0 < \gamma b_1 < \epsilon$ the condition (3.135) is satisfied.

When looking at the curves in Figure 3.17 one can see that $a_1 = 1$, $\gamma b_1 = 0$ is a critical point as far as crossing of mean RTDs is concerned. The slopes of $\mathrm{C}_{\mu>1/2}(a_1)$ seem to approach zero as $a_1 \to 1$. For Poissonian stimulus/response times we know that the parameters a_1 and γb_1 lie on the parabola

$$\gamma b_1 = \gamma\, \mathrm{e}\, a_1\, (1 - a_1) \ , \tag{3.140}$$

plotted in Figure 3.6 left; cf. appendix D. In the point $a_1 = 1$, $\gamma b_1 = 0$ the parabola has a slope of $-\gamma\mathrm{e} < 0$. So, as $a_1 \to 1$, eventually we have $\gamma b_1 > \mathrm{C}_{\mu>1/2}(a_1)$ and condition (3.135) will be violated, no matter how small the feedback coupling γ is. On the other hand, the slope of $\mathrm{C}_{\mu=1/2}(a_1)$ seems to diverge to $-\infty$ as $a_1 \to 1$, implying that the parabola stays *below* the curve for a_1 close to 1, no matter how large γ is. Finally, we have $\mathrm{C}_{\mu<1/2}(1) > 0$, such that, again, $\gamma b_1 < \mathrm{C}_{\mu<1/2}(a_1)$ as $a_1 \to 1$ for all γ. We point out that ψ, the derivatives $\partial\mathrm{F}/\partial a_1$ and $\partial\mathrm{F}/\partial(\gamma b_1)$, and the quotient of the derivatives are undefined in $(a_1, \gamma b_1) = (0, 0)$ and $(1, 0)$, and that their limits *depend on the path* taken to these points. In particular, one cannot appeal to the implicit-function theorem to obtain the derivatives $\mathrm{dC}_\mu/\mathrm{d}a_1$ at these points. Nonetheless, in appendix E we proof the observations of this paragraph.
Assertion 2: *For Poissonian stimulus/response times, there exists $\epsilon > 0$ such that*

$$\gamma b_1 \ < \ \mathrm{C}_\mu(a_1) \quad \text{for } a_1 \in [1 - \epsilon, 1) \quad \Longleftrightarrow \quad \mu \ \leq \ \frac{1}{2} \ . \tag{3.141}$$

Although condition (3.131) is *sufficient* to avoid crossing of mean RTDs only close to the line $\gamma b_1 = 4a_1$, it is *necessary* everywhere in parameter space. Put differently, the constraining curves $\mathrm{C}_\mu(a_1)$ obtained from the continuous approximation have to lie completely *below* the lines $\gamma b_1 = 1/\mu$; cf. Figure

3.17. In appendix E we, moreover, prove that the maxima of the curves $\mathrm{C}_\mu(a_1)$ lie in fact *on* these lines, as long as μ is not too small.
Assertion 3: *There exist $\hat{\mu} < 1/2$ and $\hat{a}(\mu) \in (0,1)$ such that*

$$\mathrm{C}_\mu[\hat{a}(\mu)] \;=\; \max_{a_1 \in (0,1)} \mathrm{C}_\mu(a_1) = \frac{1}{\mu} \quad \Longleftrightarrow \quad \mu > \hat{\mu} \; . \tag{3.142}$$

In Figure 3.17 we see that there is in fact only one maximum on each curve $\mathrm{C}_{\mu \geq 1/2}$. In the proof of assertion 3 (cf. appendix E) we learn that to the left of the maximum, that is, for $a_1 < \hat{a}$, we get $\hat{j} < 1$, while to the right of it, that is, for $a_1 > \hat{a}$, we get $\hat{j} > 1$. This implies that for $a_1 < \hat{a}$ the condition on the parameters that is necessary and sufficient for avoiding crossing of the mean RTDs is given by $\gamma b_1 < 1/\mu$, as a stimulus/response event index of $\hat{j} < 1$ is not sensible. For $a_1 > \hat{a}$, on the other hand, the condition is approximated by $\gamma b_1 < \mathrm{C}_\mu(a_1)$. For $a_1 \to 1$ on the curve C_μ the discrete angular increment ϕ drops to zero [see Figure 3.16] and the continuous event index $\hat{j}$ grows to infinity, if $\mu \geq 1/2$. This makes the difference between the true, discrete condition (3.130) and its continuous approximation (3.135) vanish. In particular, our results on the occurrence of mean RTD crossing close to the point $a_1 = 1$, $\gamma b_1 = 0$ for $\mu > 1/2$, and its absence for $\mu = 1/2$ (cf. assertion 2) have been obtained in the limit where the continuous approximation becomes exact.

The above analysis has revealed that for $\mu \leq 1/2$ there is no mean RTD crossing for all stimuli, if the feedback coupling γ is not too large, and for all γ, if the stimulus is dense or fast enough, that is, with a_1 close to one. With the means not crossed, however, the probability for RTD crossing increases with the asymptotic *variance* of the RTDs; cf. equation (3.91). In particular, μ small and a_1 close to one is the regime of diffusion-sustained oscillations; see the previous subsection. The variance of the RTDs may grow large, indicative of growing amplitudes of oscillation, and crossing may occur after many cycles.

3.4.8 Corticogeniculate Delays

In order to be able to formulate the loop dynamics as a Markov chain in subsection 3.4.2, we have neglected corticothalamic delays. The preliminary justification for doing so has been that the delays are more than one order of magnitude smaller than the rise time τ of corticothalamic PSPs (Tsumoto et al., 1978; Tsumoto & Suda, 1980; von Krosigk et al., 1999). We still have to be concerned, however, about *structural stability* of the dynamics analyzed above with respect to small delay perturbations. In other words, we have to ask whether the statements made about the dynamics in the previous subsections remain qualitatively valid when delays are introduced into the corticothalamic loop. To this end, we shall extend the previously studied dynamics to incorporate first-order delay effects. This will result in a higher-dimensional dynamic map. We then show that the dynamics essentially reduces to the one derived without regard for delays when only zero delays occur. By continuity of eigenvalues and asymptotic values in the delays within the extended model, we can then conclude that for small delays there is only a small quantitative, and no qualitative, change in RTD dynamics. All what has been said on the patterns of adaptation dynamics will thus turn out to remain true for small delays. We moreover calculate first-order corrections for the asymptotic mean degree of adaptation and for the mean oscillation period of RTDs.

Expanding equation (3.19) to first order in the delays d_i/τ, we have to note that $\mathrm{PSP}(t-t_i)$ is not differentiable at $t = t_i$; cf. equation (3.1). We can take advantage of the fact, however, that $d_i \geq 0$ and write

$$\begin{aligned} \mathrm{PSP}(t-t_i-d_i) &= \mathrm{PSP}(t-t_i) + d_i \lim_{d\to 0+} \frac{\mathrm{PSP}(t-t_i-d) - \mathrm{PSP}(t-t_i)}{d} + O(d_i^2) \\ &= \mathrm{PSP}(t-t_i) + \frac{d_i}{\tau}\left(1-\frac{t}{\tau}\right) \mathrm{e}^{1-t/\tau}\,\Theta(t-t_i) + O\left[\left(\frac{d_i}{\tau}\right)^2\right] \,, \end{aligned} \tag{3.143}$$

that is, we take the derivative of $\mathrm{PSP}(t-t_i)$ from the left. Substituting (3.143) into the dynamic equation (3.19) and performing some transformations analogous to (3.40) we end up with the stochastic iteration

$$\begin{pmatrix} x_j \\ y_j \\ z_j \end{pmatrix} = \mathcal{R}'(r_{j-1}) \circ \mathcal{S}'(s_{j-1}, d_{j-1}) \begin{pmatrix} x_{j-1} \\ y_{j-1} \\ z_{j-1} \end{pmatrix} \,, \quad x_0 = y_0 = z_0 = 0 \,, \tag{3.144}$$

$$\mathcal{S}'(s,d): \quad \begin{pmatrix} x \\ y \\ z \end{pmatrix} \mapsto \begin{pmatrix} x \\ y + \gamma\{s - [x + (\mathrm{sgn} s)\Delta]\}\left(1+\frac{d}{\tau}\right) \\ z + \gamma\{s - [x + (\mathrm{sgn} s)\Delta]\}\frac{d}{\tau} \end{pmatrix} \,, \tag{3.145}$$

$$\mathcal{R}'(r): \quad \begin{pmatrix} x \\ y \\ z \end{pmatrix} \mapsto \begin{pmatrix} \left(x + \mathrm{e}y\frac{r}{\tau} - \mathrm{e}z\right)\mathrm{e}^{-r/\tau} \\ y\mathrm{e}^{-r/\tau} \\ z\mathrm{e}^{-r/\tau} \end{pmatrix} \,. \tag{3.146}$$

The dimension of the dynamic map is increased by one compared to the case without delays; cf. equation (3.42). The maps for the moments of x, y, and z in this subsection will have accordingly higher dimensions than those for the moments of x and y without delays. This underlines the necessity to check structural stability of the dynamics derived previously.

Treating the stochastic dynamic map (3.144) for (x, y, z) analogous to the map (3.42) for (x, y) in subsection 3.4.2, we can derive dynamic maps for the moments of x, y, and z. Under the action of $\mathcal{S}'(s, d)$ the moments change according to

$$\begin{aligned}
\left\langle x^n y^m z^l \right\rangle_{\mathcal{S}'} \quad = \quad & \qquad\qquad\qquad\qquad\qquad\qquad\qquad\qquad\qquad\qquad (3.147) \\
\sum_{\substack{h+i+j+k=m \\ j \text{ even}}} \binom{m}{h,i,j,k} & \sum_{\substack{h'+i'+j'+k'=l \\ j' \text{ even}}} \binom{l}{h',i',j',k'} (-1)^{i+i'} \gamma^{h+i+j+h'+i'+j'} \Delta^{j+j'} \\
& \left\langle s^{h+h'} \right\rangle \left\langle \left(1-\frac{d}{\tau}\right)^{h+i+j} \left(\frac{d}{\tau}\right)^{h'+i'+j'} \right\rangle \left\langle x^{n+i+i'} y^k z^{k'} \right\rangle \\
+ \sum_{\substack{h+i+j+k=m \\ j \text{ odd}}} \binom{m}{h,i,j,k} & \sum_{\substack{h'+i'+j'+k'=l \\ j' \text{ odd}}} \binom{l}{h',i',j',k'} (-1)^{i+i'} \gamma^{h+i+j+h'+i'+j'} \Delta^{j+j'} \\
& \left\langle s^{h+h'} \right\rangle \left\langle \left(1-\frac{d}{\tau}\right)^{h+i+j} \left(\frac{d}{\tau}\right)^{h'+i'+j'} \right\rangle \left\langle x^{n+i+i'} y^k z^{k'} \right\rangle \\
+ \sum_{\substack{h+i+j+k=m \\ j \text{ even}}} \binom{m}{h,i,j,k} & \sum_{\substack{h'+i'+j'+k'=l \\ j' \text{ odd}}} \binom{l}{h',i',j',k'} (-1)^{i+i'+1} \gamma^{h+i+j+h'+i'+j'} \Delta^{j+j'} \\
\left(\mu_+ \left\langle s^{h+h'} \right\rangle_+ - \mu_- \left\langle s^{h+h'} \right\rangle_-\right) & \left\langle \left(1-\frac{d}{\tau}\right)^{h+i+j} \left(\frac{d}{\tau}\right)^{h'+i'+j'} \right\rangle \left\langle x^{n+i+i'} y^k z^{k'} \right\rangle \\
+ \sum_{\substack{h+i+j+k=m \\ j \text{ odd}}} \binom{m}{h,i,j,k} & \sum_{\substack{h'+i'+j'+k'=l \\ j' \text{ even}}} \binom{l}{h',i',j',k'} (-1)^{i+i'+1} \gamma^{h+i+j+h'+i'+j'} \Delta^{j+j'} \\
\left(\mu_+ \left\langle s^{h+h'} \right\rangle_+ - \mu_- \left\langle s^{h+h'} \right\rangle_-\right) & \left\langle \left(1-\frac{d}{\tau}\right)^{h+i+j} \left(\frac{d}{\tau}\right)^{h'+i'+j'} \right\rangle \left\langle x^{n+i+i'} y^k z^{k'} \right\rangle \ .
\end{aligned}$$

Mean values of quantities involving the corticothalamic delay d are taken with respect to the density of such delays. We do not need to specify any density for the delays, but keep in mind that typical values of d are more than an order of magnitude smaller than τ. We also have to remember that, due to the expansion (3.143) of the delayed PSP we have used, any results will be valid only to first order in $\langle d/\tau \rangle$.

Under the action of $\mathcal{R}'(r)$ the moments change according to

$$\left\langle x^n y^m z^l \right\rangle_{\mathcal{R}'} \quad = \tag{3.148}$$

$$\sum_{i=0}^{n}\binom{n}{i}\sum_{j=0}^{n-i}\binom{n-i}{j}(-\mathrm{e})^j\left\langle\left(\frac{\mathrm{e}r}{\tau}\right)^i \mathrm{e}^{-(n+m+l)r/\tau}\right\rangle\left\langle x^{n-i-j}y^{m+i}z^{l+j}\right\rangle\ .$$

Mean Delayed Adaptation Dynamics

Analogous to what we have done in subsection 3.4.3, we introduce the dynamic variables

$$\alpha_j := \frac{\langle x\rangle_j}{\langle s\rangle_o-\Delta}\ ,\quad \beta_j := \frac{\langle y\rangle_j}{\langle s\rangle_o-\Delta}\ ,\quad \gamma_j := \frac{\langle z\rangle_j}{\langle s\rangle_o-\Delta}\ . \tag{3.149}$$

The dynamics of the mean RTDs can now be written as

$$\begin{pmatrix}\alpha_j\\ \beta_j\\ \gamma_j\end{pmatrix} = M_1'\begin{pmatrix}\alpha_{j-1}\\ \beta_{j-1}\\ \gamma_{j-1}\end{pmatrix} + \gamma\mu\begin{pmatrix} b_1-\left\langle\frac{d}{\tau}\right\rangle(\mathrm{e}a_1+b_1)\\ \left(1-\left\langle\frac{d}{\tau}\right\rangle\right)a_1\\ \left\langle\frac{d}{\tau}\right\rangle a_1\end{pmatrix}\ , \tag{3.150}$$

with the stimulus parameters a_1 and b_1 as defined in (3.64) and the matrix

$$M_1' = \begin{pmatrix} a_1-\gamma b_1 & b_1 & -\mathrm{e}a_1\\ -\gamma a_1 & a_1 & 0\\ 0 & 0 & a_1\end{pmatrix} + \gamma\left\langle\frac{d}{\tau}\right\rangle\begin{pmatrix}\mathrm{e}a_1+b_1 & 0 & 0\\ a_1 & 0 & 0\\ -a_1 & 0 & 0\end{pmatrix}\ . \tag{3.151}$$

Because $a_1 < 1$, it is now evident that for $\langle d/\tau\rangle = 0$ the dynamics stably converges into the subspace spanned by the $\langle x\rangle$ and $\langle y\rangle$ components[3], where it is exactly the same as we have derived without regarding delays; cf. equation (3.63). This implies, by continuity in $\langle d/\tau\rangle$, that for small $\langle d/\tau\rangle$ the mean dynamics and the conditions for its stability are slightly modified versions of those derived in subsection 3.4.3.

Variance and Inter-Class Correlation of Delayed Adaptation Dynamics

The dynamics of the second moments of x, y, and z is

$$\begin{pmatrix}\langle x^2\rangle_j\\ \langle xy\rangle_j\\ \langle y^2\rangle_j\\ \langle xz\rangle_j\\ \langle yz\rangle_j\\ \langle z^2\rangle_j\end{pmatrix} = M_2'\begin{pmatrix}\langle x^2\rangle_{j-1}\\ \langle xy\rangle_{j-1}\\ \langle y^2\rangle_{j-1}\\ \langle xz\rangle_{j-1}\\ \langle yz\rangle_{j-1}\\ \langle z^2\rangle_{j-1}\end{pmatrix} + \begin{pmatrix}u'_{j-1}\\ v'_{j-1}\\ w'_{j-1}\\ u''_{j-1}\\ v''_{j-1}\\ w''_{j-1}\end{pmatrix}\ . \tag{3.152}$$

---

[3] Note that, of course, $\langle z\rangle_j = 0$ for all j, if all delays are zero; cf. equations (3.144) through (3.146). However, it is the *stability* with respect to delay perturbations that matters.

Fortunately, for investigating structural stability of the delay-free dynamics (3.81) of the second moments we do not need to spell out the matrix M_2' or the vector $(u_j', v_j', w_j', u_j'', v_j'', w_j'')$. The latter depends on the first moments $\langle x\rangle_j$, $\langle y\rangle_j$, and $\langle z\rangle_j$ and converges, if they converge. Here it is sufficient to take a look at

$$M_2'\Big|_{\langle d/\tau\rangle=\langle(d/\tau)^2\rangle=0} = \tag{3.153}$$

$$\begin{pmatrix} a_2-\gamma b_2+\gamma^2 c_2 & b_2-2\gamma c_2 & c_2 & -2\mathrm{e}a_2+\gamma\mathrm{e}b_2 & -\mathrm{e}b_2 & \mathrm{e}^2 a_2 \\ -\gamma a_2+\frac{\gamma^2}{2}b_2 & a_2-\gamma b_2 & \frac{1}{2}b_2 & \gamma\mathrm{e}a_2 & -\mathrm{e}a_2 & 0 \\ \gamma^2 a_2 & -2\gamma a_2 & a_2 & 0 & 0 & 0 \\ 0 & 0 & 0 & a_2-\frac{\gamma}{2}b_2 & \frac{1}{2}b_2 & -\mathrm{e}a_2 \\ 0 & 0 & 0 & -\gamma a_2 & a_2 & 0 \\ 0 & 0 & 0 & 0 & 0 & a_2 \end{pmatrix},$$

with the stimulus parameters a_2, b_2, and c_2 as defined in (3.82). By comparison with equation (3.81), it is evident that the dynamics of the second moments $\langle x^2\rangle_j$, $\langle xy\rangle_j$, and $\langle z^2\rangle_j$ with zero delays is identical to the dynamics derived without regard to delays, if and only if the moments $\langle xz\rangle_j$, $\langle yz\rangle_j$, and $\langle z^2\rangle_j$ stably converge to zero[4]. This, in turn, is determined by the lower right submatrix

$$\begin{pmatrix} a_2-\frac{\gamma}{2}b_2 & \frac{1}{2}b_2 & -\mathrm{e}a_2 \\ -\gamma a_2 & a_2 & 0 \\ 0 & 0 & a_2 \end{pmatrix} \tag{3.154}$$

of (3.153). Its eigenvalues are

$$\nu_{4/5} = a_2 - \frac{\gamma}{4}b_2 \pm \frac{1}{2}\sqrt{\frac{\gamma^2}{4}b_2^2 - 2\gamma a_2 b_2}\ , \tag{3.155}$$

$$\nu_6 = a_2\ . \tag{3.156}$$

Since $|\nu_6| < 1$, convergence requires that $|\nu_{4/5}| < 1$, that is, $\gamma b_2 < 2(a_2+1)^2$. In general, this is a condition for convergence in the delayed corticothalamic loop that is *additional* to those derived for the undelayed loop. For Poisson statistics of the times of responses to local stimuli, however, we know that a_2 and b_2 lie on the parabola

$$b_2 = \mathrm{e}a_2(1-a_2)\ ; \tag{3.157}$$

see appendix D. Together with the condition $\gamma < 4/\mathrm{e}$ derived in subsection 3.4.4 for the convergence of $\langle x^2\rangle_j$, $\langle xy\rangle_j$, and $\langle y^2\rangle_j$, this implies

$$\gamma b_2 < 4a_2 < 2(a_2+1)^2 \tag{3.158}$$

---

[4] Note that, of course, $\langle xz\rangle_j = \langle yz\rangle_j = \langle z^2\rangle_j = 0$ for all j, if all delays are zero; cf. equations (3.144) through (3.146). See, however, the previous footnote 3 on page 113.

(see appendix D), that is, $|\nu_{4/5}| < 1$. Thus, for Poisson statistics there is no extra condition to ensure structural stability of the zero-delay dynamics of second moments.

Analogous to the situation without delays, M_2' determines stability also of the class-mixed moments; cf. subsection 3.4.6. The inter-class correlation derived in subsection 3.4.6, therefore, is the correct zeroth-order correlation for the dynamics with delays.

At this point we have demonstrated structural stability of the dynamics investigated in the preceding subsections neglecting delays.

Delay Correction for Asymptotic Mean Degree of Adaptation

From equations (3.150) and (3.151) we get for the asymptotic mean degree of adaptation with corticothalamic delays

$$\alpha' := \alpha'_\infty = \alpha - \gamma\mu \frac{(1-a_1)^2(\mathrm{e}a_1 + b_1)}{\left[(1-a_1)^2 + \gamma b_1\right]^2} \left\langle \frac{d}{\tau} \right\rangle + O\left(\left\langle \frac{d}{\tau} \right\rangle^2 \right) , \qquad (3.159)$$

where α is the asymptotic mean degree of adaptation without any delays given by (3.67). It turns out that delays *degrade* the mean degree of adaptation to an object's speed.

Delay Correction for Mean Oscillation Period

For the eigenvalues of M_1' we get

$$\begin{aligned} \lambda'_{1/2} &= \lambda_{1/2} + \frac{\gamma(\mathrm{e}a_1 + b_1)}{2} \left[1 \mp \mathrm{i} \frac{2a_1 - \gamma b_1}{\sqrt{\gamma b_1 (4a_1 - \gamma b_1)}} \right] \left\langle \frac{d}{\tau} \right\rangle \\ &\quad + O\left(\left\langle \frac{d}{\tau} \right\rangle^2 \right) , \qquad (3.160) \\ \lambda'_3 &= a_1 , \qquad (3.161) \end{aligned}$$

where $\lambda_{1/2}$ are the eigenvalues of M_1 defined in (3.65). This expansion is valid only for $\gamma b_1 \neq 4a_1$. For $\gamma b_1 = 4a_1$ an expansion in powers of $\sqrt{\langle d/\tau \rangle}$ would be appropriate. However, as derived previously, for convergence of the second moments we always require that $\gamma b_1 < 4a_1$; cf. subsection 3.4.4. In this regime the pairs of eigenvalues $\lambda_{1/2}$ and $\lambda'_{1/2}$ are each complex conjugate, such that the dynamics of the moments and, for $\langle r/\tau \rangle$ small enough, of individual RTDs is oscillatory; cf. equations (3.72) and (3.98). The period of

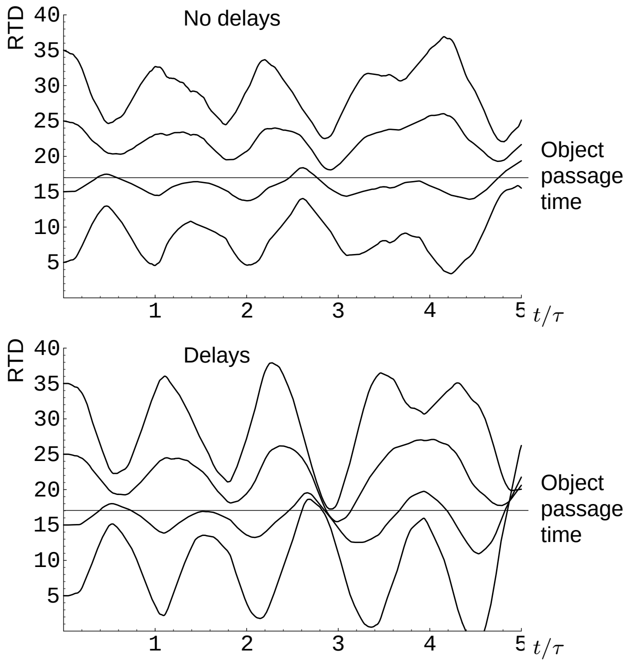

Figure 3.18: Computer simulations comparing the adaptation dynamics for the response time differences $\mathrm{RTD}^{(c,\pm)}(t)$ of 4 classes of neurons ($c = 1, 2, 3, 4$) without (top) and with delays (bottom) in the corticothalamic loop. The time scale is set by τ, the rise time of corticothalamic postsynaptic potentials; cf. equation (3.1). The delay for the simulation shown in the bottom graph is $d/\tau = 0.05$. For best comparison, precisely the same stimulus consisting of an object and a background component has been used for both simulations. The passage time of object features is indicated by the straight horizontal line in each graph. With and without delays the system is in the regime of diffusion-sustained oscillations. As predicted by equation (3.160), the oscillation period is slightly longer with the delays in the loop. Parameters: $\mu = 1/3$, $s_o = 17$, $\langle |s| \rangle = 17.8$, $\mathrm{var}(|s|) = 15.6^2$, $\langle r/\tau \rangle = 0.01$, $\gamma = 0.1$. See appendix G for details on the computer simulations.

oscillation with corticothalamic delays is

$$P' = \frac{2\pi}{\arg(\lambda_1')} \ . \tag{3.162}$$

Inspection of (3.160), taking care of the two cases $\gamma b_1 \leq 2a_1$ and $2a_1 < \gamma b_1 < 4a_1$, yields that, to first order in $\langle d/\tau \rangle$, $\arg(\lambda_1') \leq \arg(\lambda_1)$. It thus turns out that delays *increase* the mean period of oscillation of RTDs. This is illustrated for diffusion-sustained oscillations in Figure 3.18.

3.5 Discussion

We have proven that the model system adapts the speed preferences of cortical layer 4 neurons to the speed of an object through the corticothalamic loop. As explained in section 3.2, this enables the system to perform object segmentation against a background and reduction of visual data to behaviorally relevant aspects of a stimulus.

The proposed adaptation mechanism could be characterized as *pre*-attentive, since it requires no 'act of will' and no information from higher brain areas where different objects or shapes are categorized. On the other hand, like attentional mechanisms, it does act as a kind of bottleneck, namely, as a bottleneck for information on visual motion. Multiple adaptive motion systems could act in parallel for different directions of motion, in different parts of the visual field, and on different spatial scales. From the perspective of efficiency, higher perceptual and attentive mechanisms can be envisaged best to operate on top of a representation level where object-unrelated activity is reduced, as provided by the adaptive motion system. Although at this point it is difficult to pin down the precise mechanisms of contextual effects on neuronal responses in the visual system, it seems clear that modulation related to object segmentation occurs as early as in the primary visual cortex (V1), at least in primates; see Lamme et al. (1998) and references therein.

Responses of cat area 17 neurons to moving stimuli are modulated by motion within a region extending far beyond their classical RF[5]. Both facilitatory and suppressive effects have been observed for addition of surround motion at the same velocity as the central motion (Hammond & MacKay, 1981; Gulyas et al., 1987; Casanova, 1993; Li & Li, 1994). The model presented here predicts that speed preferences are pulled *closer* to the speed of a stimulus moving in a region surrounding the classical RF. Whether this would result in facilitation or suppression of responses depends on the definition of the *reference* response. If the latter is measured in an unadapted state, surround motion at the velocity of the central motion should facilitate the response. If, on the other hand, it is measured under conditions of *optimal* adaptation to a stimulus moving inside the classical RF, the addition of further moving features in the surround may drive the RTDs to cross and disrupt the adaptation process; cf. condition (3.17) and subsection 3.4.7. Failure of adaptation to the stimulus moving inside the classical RF would show up as a 'suppressive' effect; cf. Figure 3.15. Often in experiments, the reference response is defined as the best response, that is, the response to

---

[5] The 'classical' RF of a neuron is the region of visual space that *must* be stimulated in order to produce a response. It is the same as the RF in the narrower sense used throughout this work.

the optimally moving stimulus. If speed adaptation is effective, however, the best response would indeed be seen under conditions of optimal adaptation. In future experiments it, therefore, may be important to be more careful with the definition of the reference response so as to uncover the true interaction between classical RF and surround.

Recently, Li et al. (1999) have investigated specifically those neurons in area 18 that show a *suppressive* surround effect in their experiment. The authors describe a *repulsion* of the neurons' preferences from the speed of surround motion. The shift in preference is towards lower speeds, if the surround motion is faster, and towards higher speeds, if it is slower than the neuron's preference without any surround motion. While the fact of a shift of speed preference in response to a large-field motion stimulus supports the basic idea advanced in this work, it is unclear how to relate the details of their observations to our theoretical results. There are at least four problems. First, Li et al. selected only neurons with a suppressive surround effect for their study. Neurons that participate in speed adaptation as proposed here should certainly show response facilitation by surround motion under some conditions; see the last paragraph. Second, their results have been obtained in area 18 of the cat. To area 18 the direct geniculate Y-projection is strong, not the direct X-projection we have discussed in chapter 2 and on which our reasoning concerning dynamic cortical velocity tuning has been based. Third, the indirect X-projection to area 18 via area 17 takes at least two synapses more than the X-projection to geniculate recipient cells in area 17. Velocity tuning in area 18 may thus be differently affected by adaptation than in area 17. Fourth, related to what has been discussed in the last paragraph, it is not clear whether the tuning properties as measured in their experiment should be interpreted as unadapted tuning, or rather as the 'effective' tuning observed after adaptation to different stimuli.

A critical experimental test of a control loop such as the one analyzed here is to look for changes in spatiotemporal RF structure on a timescale of, say, 100 ms in response to moving, especially large-field, stimuli. It would be interesting to study reverse correlations in the speed or temporal-frequency domain, analogous to work that has uncovered dynamic orientation tuning in the monkey (Ringach et al., 1997).

Great care must be taken when extrapolating from cats to primates. No lagged relay cells have been described in the primate LGN so far. On the other hand, a recent study (Valois & Cottaris, 1998) does suggest a set of geniculate inputs to directionally selective simple cells in macaque striate cortex that is essentially analogous to the lagged-nonlagged set envisaged for cat simple cells. If indeed primates employ a similar system at the lowest level of motion analysis, the corticogeniculate loop would implement at this level the classical Gestalt principle of 'common fate', which recognizes common motion as a powerful cue for object segmentation in humans (Wertheimer, 1958; Julesz, 1971).

Some interesting properties that are not directly related to the computational goal of object segmentation, but nonetheless linked to the basic design of the system, have shown up in its analysis. We now discuss them in relation to experimental data.

3.5.1 Spatiotemporal Patterns of Cortical Activity

The response time differences $\mathrm{RTD}^{(c,\pm)}(t)$ of all layer 4 neurons in the system are correlated, both across space and classes c. The correlation across space is the result of the lateral connectivity of the system. The correlation across classes is mediated by the stimulus; cf. subsection 3.4.6.

If RTDs converge on a stationary state, they do so simultaneously; cf. Figure 3.10 top. Even for diffusion-sustained oscillations of RTDs we have shown in subsection 3.4.6 that, depending on the stimulus, all or part of the neuronal classes $(c,+)$ synchronize the phases of closest match of their RTD to the object's passage time; cf. Figure 3.10 bottom. In phases when many classes are closely tuned to the object's passage time, object features elicit a strong *class-averaged* response $\langle R^{(+)} \rangle$,

$$\left\langle R^{(\pm)} \right\rangle (s,t) \; := \; \frac{1}{n} \sum_{c=1}^{n} \mathrm{f}\left[|s - \mathrm{RTD}^{(c,\pm)}(t)| \right] \quad ; \tag{3.163}$$

cf. equation (3.13). In phases when most RTDs diverge from the object's passage time, on the other hand, they also diverge from each other, since there is no attractor of RTDs besides the object's passage time; cf. Figure 3.10 bottom. Hence there are no strong class-averaged responses $\langle R^{(\pm)} \rangle$, neither to object, nor to background features.

It turns out that each time course of adaptation is associated with a certain spatiotemporal pattern of cortical activity. For an adaptation time course such as shown at the top of Figure 3.10 there are permanent strong class-averaged responses $\langle R^{(+)} \rangle$ to object features as soon as the RTDs have converged to the object's passage time. On the other hand, an oscillatory time course as shown at the bottom of the figure is associated with alternating phases of weak and strong responses $\langle R^{(+)} \rangle$, the strong responses being restricted to object features. In fact, the dynamic RTDs act as a *pacemaker* for distributed cortical activity. A periodic time structure is imposed that tends to synchronize the firing of layer 4 cells representing the object. As an illustration of this point, we show in Figure 3.19 the adaptation dynamics and associated spatiotemporal pattern of activities of an array of cortical neurons exposed to a stimulus comprising an object and a strong background component.

In summary, an object is represented in spatially distributed cortical activity that has an oscillatory and synchronous spatiotemporal structure, if the background activity is strong, and no temporal structure, if the background activity is weak. It is important to note that background activity in the present sense may be associated with the stimulus, with ocular microtremor (see subsection 3.5.3 below), or with neuronal noise. The oscillations may show up in single cell activity or in multi-unit activity, depending on the nature of the stimulus and the size of RFs. In particular, single neurons show periodic activity, if their responses last longer than one period of oscillation of the RTDs. Their response then comprises several 'elementary' response events of the kind marked by a single dot in Figure 3.19.

There is indeed evidence for temporal structure in the response of neurons in primate middle temporal (MT) area to moving random dot stimuli with a strong incoherent component, while no temporal structure was observed for mainly coherent random dot motion (Bair & Koch, 1996). For neither kind of stimulus, though, a preferred frequency of oscillation was found in the activity data analyzed by Bair & Koch (1996). In terms of the present model, this may be due to the summation by MT neurons of inputs from areas V1 and V2 that oscillate independently at various frequencies.

More detailed modeling is required to compare the oscillations and synchronization that arise in the loop model under certain conditions with recent data on persistent oscillations in area 17 that are preferentially evoked by *moving* stimuli (Bringuier et al., 1997; Castelo-Branco et al., 1998). In the loop model, oscillations may arise from visual stimulation *at* geniculocortical synapses, showing up as periodic excitatory synaptic potentials in cortical neurons. Because of the slow potentials that modulate the GRC states we would expect such oscillations to be at the lower end of the observed frequency spectrum (below, say, 30 Hz); cf. Figure 3.19. Clearly, since periodic synaptic potentials are not restricted to layer 4 (Bringuier et al., 1997), intracortical connections have also a role to play, certainly in the propagation of the periodic activity.

3.5.2 Figure-Ground Segregation

According to Gestalt terminology, in a visual scene of two distinguishable parts the *figure* is the one which constitutes the minority, the *ground* is what constitutes the majority component (note that the *ground* is not necessarily the same as the *background* in our sense). Usually retinal motion of the figure indicates motion of an object in the environment, while retinal motion of the

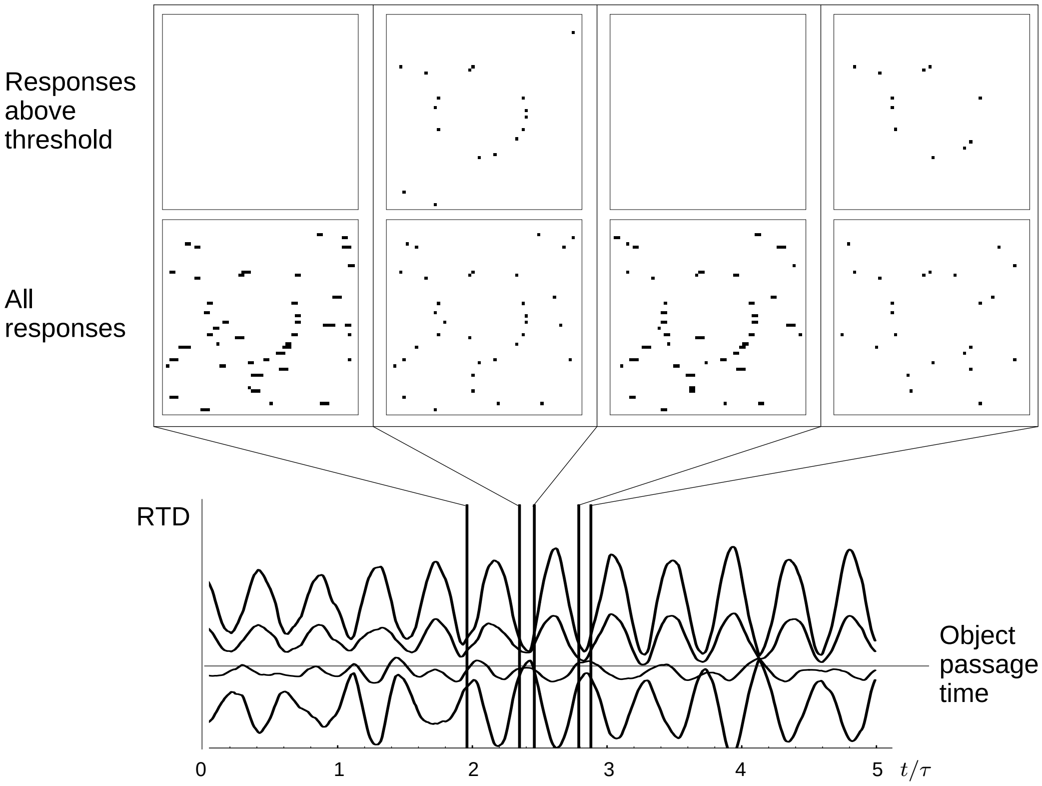

Figure 3.19: Computer simulations of the adaptation dynamics for the response time differences $\mathrm{RTD}^{(c,\pm)}(t)$ of 4 classes of cortical neurons ($c = 1, 2, 3, 4$) (bottom) and their associated spatiotemporal pattern of activity (top). Their receptive fields are arranged in an array of 60×60 retinal locations with 8 neurons per location. The time scale is set by τ, the rise time of corticothalamic postsynaptic potentials; cf. equation (3.1). The system is stimulated by 15 dots placed on a circle, all moving at a *common* velocity to the right (object), and 30 dots moving at various random speeds (exceeding or less than the object's speed) either to the left or to the right (directionally unbiased background). At the bottom of the figure we show the 4 trajectories $\mathrm{RTD}^{(c,+)}(t)$, i.e., representative of the neurons selective for the direction of object motion. The passage time of object dots is indicated by the straight horizontal line in the graph. Whenever the neurons' preferences, that is, response time differences (RTDs), get *close to* the object's passage time (corresponding to the object's speed), object dots elicit a strong response in neurons that represent their actual retinal positions. The corresponding array of activity is shown in the panels at the top of the figure.

Figure 3.19: The lower row of panels displays *all* responses that occur within the indicated intervals of time; the upper row displays only those responses where the class-averaged activity $\langle R^{(+)} \rangle$ [see equation (3.163)] for a location *exceeds* a certain threshold. Nearly all supra-threshold activity is related to object features, demonstrating the segmentation of the object against the background. Spurious supra-threshold activity derives from responses to background dots that by chance have speeds very close to the object's speed. The supra-threshold activity is oscillatory and synchronous. If τ, the rise time of corticothalamic postsynaptic potentials [cf. equation (3.1)], is taken to be 100 ms, the oscillation frequency is roughly 25 Hz in this example. The feedback strength is $\gamma = 0.25$.

ground is often induced by self-motion of the observer, e.g., by eye or head movement. The visual system is normally able to distinguish the two kinds of motion, providing for perception of a stable visual world.

There is evidence for the utilization of extra-retinal signals to compensate for eye and head movements in the perception of heading direction (Royden et al., 1994; Bradley et al., 1996; Crowell et al., 1997). On the other hand, it is well known that a stationary subject viewing a coherent large-field motion stimulus after a few seconds has the impression of self-motion in the reverse direction (Büttner & Henn, 1981; Straube & Brandt, 1987). Moreover, there is a series of classical psychophysical experiments, reviewed in Kaufman (1974) and in Van Essen & Anderson (1990), whose results can be summarized as follows. First, the perception of motion of an object is greatly facilitated, if a *larger* stationary reference stimulus is given. Second, motion of an object in the presence of a *smaller* stationary reference is not easily perceived. Instead, at low speeds motion of the *reference* in the reverse direction is inferred ('induced motion'). These facts suggest some *visually* driven mechanism that contributes to a different processing of figure and ground motion.

As explicated in the previous subsection, cortical activity associated with the proposed adaptation mechanism inherently distinguishes stimuli with small and large weights μ of moving objects by the presence or lack of temporal structure, respectively. This difference could be read out by subsequent processing stages, e.g., by neurons that are good coincidence detectors, and other neurons that are stronger driven by a high mean input rate. The former would function as 'figure channels', the latter as 'ground channels'. In order to explain in the current framework the perceptions of relative motion reported above (Kaufman, 1974; Van Essen & Anderson, 1990), one has to assume that only activity in 'figure channels' is interpreted by the visual system as signaling motion of objects in the environment.

Consistent with the idea of 'figure channels' is the finding of Peterhans & Baumann (1994) and Peterhans (1997) of neurons in primate area V2 that prefer coherent motion of a row of dots against a background of stationary dots to both coherent motion and stationarity of the *whole* field of dots. As the authors suggest, area V2 might extract form information from motion cues. Within our current framework of adaptive motion processing, this would mean that V1 *detects* an object through common motion and V2 then *analyzes* its shape.

In agreement with the concept of 'ground channels', neurons in primate area MT respond best to fields of dots extending over their classical RF and moving *coherently* into their preferred direction, and are suppressed by the addition of motion in other directions (Snowden et al., 1991; Qian & Andersen, 1994; Bair & Koch, 1996). The data on MT neurons really look more complicated, though. Allman et al. (1985) found that MT responses to the optimal coherent motion within a neuron's classical RF are commonly suppressed by addition of the same coherent motion in a large surrounding region. When interpreting their results in relation to the present model, however, there is the same problem of the definition of the reference response as we have mentioned above for experiments in area 17 of the cat. In their experiments motion inside the classical RF was always adjusted to be *optimal* in the context of a *stationary* surround stimulus. In terms of the present model, this would mean that V1 neurons projecting to a MT neuron are optimally adapted to the motion in their classical RF by that particular combination of stimuli. Now, if more motion in the same direction and extending over a large area of the visual field is added, the mean interstimulus time $\langle r/\tau \rangle$ will drop. According to subsection 3.4.7, then, this procedure may easily drive RTDs to cross and disrupt adaptation; cf. Figure 3.15. As a result, MT neurons will be out of tune with the stimulus speed and their responses decline. Addition of motion with less speed has less severe effects, consistent with the data of Allman et al. (1985). It certainly needs further experiments, such as simultaneous stimulation of the classical RF and the surround by slower or sparser dot patterns, to establish whether there are really distinct center and surround regions working in antagonism, or rather areas over which adaptation acts homogeneously, or perhaps a combination of the two. The same care must be taken when interpreting results in the light of the present model from analogous studies in primate areas V1 and V2; see, e.g., Allman et al. (1990).

The general notion that areas V2 and MT may perform different aspects of motion processing is supported anatomically by the existence of separate projections from V1 to these areas (Zeki & Shipp, 1988; Felleman & van

Essen, 1991).

There is evidence for a systematic spatial variation and columnar organization of the neural response characteristics to wide-field motion stimuli in area MT (Born & Tootell, 1992). Response suppression by uniform wide-field motion is interdigitated with response facilitation. This apparent functional specialization within area MT persists beyond MT (Tanaka et al., 1986; Komatsu & Wurtz, 1988; Tanaka et al., 1993; Eifuku & Wurtz, 1998; Berezovskii & Born, 2000). It remains to be established whether these two streams of processing could subserve the function of representing figure motion versus ground motion in the way that 'figure channels' and 'ground channels' would do.

3.5.3 Fixational Eye Movements

An important side effect of the adaptation mechanism is that it can account for visual stabilization during fixational eye movements. During fixation, erratic eye movements, called *microtremor*, occur with a frequency content ranging from roughly 25 to 100 Hz in humans, with the dominant component usually above 70 Hz (Eizenman et al., 1985; Spauschus et al., 1999; Bolger et al., 1999). They cause retinal slips that are in principle detectable by velocity-tuned neurons in the primary visual cortex. Nonetheless, no such motion is perceived during fixation. The reason may lie in the fact that fixational eye movements provide motion signals that are directionally *unbiased* on the timescale of the corticogeniculate control loop ($\sim$ 100 ms). Since unbiased motion, that is, a stimulus with object weight $\mu = 0$, does not lead to adaptation to any particular velocity [cf. equation (3.67)], none of the moving features is highlighted. Now, if the brain relies on the activity of adaptively speed-tuned neurons to infer coherent motion, no such motion will be inferred from fixational eye movements. Stabilization of the visual world is thus achieved because successive motion signals cancel out in the control loop.

Interestingly, this stabilization mechanism explains the recently reported 'jitter after-effect' (Murakami & Cavanagh, 1998). An observer is first exposed to dynamic noise for 30 s, and then fixates a larger area of static noise. The perception is a coherent jitter of the static noise that follows fixational eye movements, specifically, in the region that has *not* been exposed to the prior random motion. The explanation in terms of the present model relies on the fact that responses of velocity-selective neurons are reduced (fatigued) after stimulation for 30 s [also called 'adaptation', but unrelated to the adaptation of speed preferences proposed here; see Hammond et al. (1988)]. Let us consider two models of cortical response reduction, one multiplicative and one subtractive, that is,

$$R_i' = \kappa R_i \ , \quad R_i'' = \max(R_i - K, 0) \ , \tag{3.164}$$

where $0 < \kappa < 1$ and $0 < K < 1$, such that R_i' and R_i'' are the reduced responses to event i. According to equation (3.10), then, the respective amplitudes of corticogeniculate potentials [cf. equation (3.2)] are

$$A_i' = \gamma\, \mathrm{A}(\kappa R_i)\, \sigma\, [\kappa(R_i^> - R_i^<)] \ , \quad A_i'' = \gamma\, \mathrm{A}(R_i - K)\, \sigma(R_i^> - R_i^<) \ . \tag{3.165}$$

Generally, the function A is monotonically decreasing from a maximum value of $\mathrm{A}(0)$ to its minimum $\mathrm{A}(1) = 0$, and σ is sigmoidal between -1 and $+1$ with $\sigma(0) = 0$; cf. subsection 3.3.2. It follows that $A_i' = 0$ for $\kappa = 0$ and $\kappa = 1/R_i$. Although for $R_i < 1$ the value $1/R_i > 1$ is outside the range of κ we have in mind, continuity implies that there is a maximum of A_i for some value $\kappa \in [0, 1/R_i]$, and that this maximum will be at larger κ for higher responses R_i, $R_i^>$, $R_i^<$. Put differently, for any fixed response reduction $\kappa < 1$, there will be an increase in PSP amplitude, i.e., $A_i' > A_i$, if the responses R_i, $R_i^>$, $R_i^<$ are high enough, and a reduction, i.e., $A_i' < A_i$, if they are lower. For the subtractive model of cortical response reduction we have larger PSP amplitudes, $A_i'' > A_i$, if $R_i > 0$, and unchanged amplitudes, $A_i'' = A_i$, if $R_i = 0$.

The motion stimulus induced by ocular microtremor is characterized by a certain mean passage time $\langle |s| \rangle$. From the last paragraph we conclude that, while the mean adaptation with reduced cortical responses remains zero (because μ remains zero), the *fluctuations* of RTDs close enough to $\langle |s| \rangle$ increase. In fact, for close enough RTDs the effect is similar, although not equivalent, to increasing the amplitudes A_i by strengthening the corticothalamic coupling parameter γ; cf. equation (3.10). More precisely, the variance $\mathrm{var}(x) \to \infty$ as $\gamma \to 4/\mathrm{e}-$; cf. subsection 3.4.4. For multiplicative response reduction increased fluctuations of RTDs are restricted to a smaller neighborhood of $\langle |s| \rangle$ than for subtractive response reduction, because higher responses are required in the case of multiplicative response reduction; see the last paragraph.

In subsection 3.4.6 we have shown that the gap between anti-correlated RTDs is smallest around $\langle |s| \rangle$ and for $\mu = 0$; cf. equation (3.128). For the motion stimulus induced by erratic eye movements the gap is

$$2\, \hat{C}_{\min} \bigg|_{\mu=0} = 2\, \sqrt{\mathrm{var}(|s|)} \ . \tag{3.166}$$

As passage times s induced by fixational eye movements are generally brief (Eizenman et al., 1985; Spauschus et al., 1999; Bolger et al., 1999), we can assume that $\mathrm{var}(|s|)$ is rather small, that is, smaller than true motion stimuli usually give rise to. The gap $2\,\hat{C}_{\min}$ is thus small, implying that the mean induced passage time $\langle |s| \rangle$ will be approached *synchronously* by correlated fluctuations of many RTDs. Of course, when cortical responses are reduced according to equation (3.164), the results of subsection 3.4.6 apply only to zeroth order.

In Figure 3.20 we show computer simulations of the adaptation dynamics with normally responsive neurons (top), and with reduced response amplitudes for part of the neurons, both for multiplicative (middle) and subtractive (bottom) response reduction. The stimulus is jitter motion and mimics motion as induced by fixational eye movements. The normal-response condition demonstrates visual stabilization (see above), the condition with partial response reduction simulates the 'jitter after-effect' (Murakami & Cavanagh, 1998), where part of the cortical neurons have been fatigued. As a result of strong fluctuations of RTDs which tend to approach the induced passage time $\langle |s| \rangle$ synchronously (cf. Figure 3.20 middle and bottom), there are periods when the system is much closer tuned to the speed of eye-induced motion than under normal conditions (cf. Figure 3.20 top). Normally responsive neurons, that is, neurons outside the region of reduced (fatigued) responsiveness, now exhibit *enhanced* class-averaged responses $\langle R^{(\pm)} \rangle$ [cf. equation (3.163)] to eye-induced motion. Thus the same mechanism that ensures perceptual stabilization during normal fixation will now signal jitter motion as reported by Murakami & Cavanagh (1998).

3.5.4 Encoding Stimulus Speed

In a system of neurons with steady speed tuning absolute speed is encoded straightforwardly in the population activity of neurons with different tuning. Evidently, this is not true of our model system. Instead, speed differences relative to an object's speed are represented with high accuracy due to the clustering of tuning curves around the object's speed; cf. Figure 3.1 bottom.

There is an interesting experiment by Watamaniuk et al. (1993) that demonstrates the influence of dot density in random dot kinematograms on perceived speed: the *higher* the dot density, the *higher* the perceived speed. Suppose now that speed estimation had to be based on the outputs of adaptively velocity-tuned neurons. As expressed by equation (3.67) and Figure 3.6, at fixed μ the statistics of interstimulus times r determines the mean degree of adaptation of the neurons to the stimulus. Since the interstimulus times decrease with both increasing stimulus speed and stimulus density, a perceptual interaction between the two as observed by Watamaniuk et al. would have to be expected. In other words, their results are consistent with

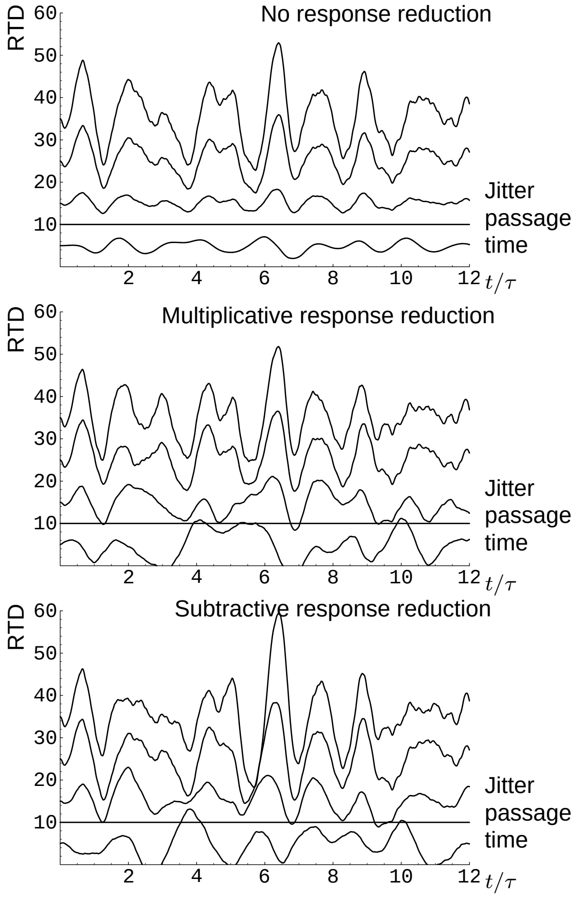

Figure 3.20: Demonstration of visual stabilization during fixation (top) and of the 'jitter after-effect' (Murakami & Cavanagh, 1998; middle and bottom) in computer simulations of the corticogeniculate loop model. The stimulus mimics fixational eye movements and is a jitter consisting of alternating episodes of motion in opposite directions with a jitter passage time of $s_{\text{jitter}} = \pm 10$, indicated by the straight horizontal line in each graph. The length l of each episode is drawn independently according to the Weibull density $\mathrm{p}(l) = l/100 \exp(-l^2/200)$ with a maximum probability for $l = 10$ stimulus events, and rounded to the nearest integer. Thus the jitter motion reverses direction at time intervals of on average $5\sqrt{2\pi}\langle r/\tau \rangle = 0.063$, which is fast on the time scale of the plots in this figure. We arbitrarily show one direction population of the response time differences $\mathrm{RTD}^{(c,\pm)}(t)$ $(c = 1, 2, 3, 4)$; both populations ("±") look qualitatively the same, as there is no object in the stimulus $(\mu = 0)$ and, hence, no drift of the RTDs. The top graph shows adaptation for normal fixation. Fluctuating RTDs approach the eye-induced passage time s_{jitter} synchronously, but no RTD gets close to s_{jitter}; hence, no cortical neuron responds strongly to the eye-induced motion.

Figure 3.20: The middle graph shows adaptation to exactly the same stimulus with 1/3 of cortical responses (randomly selected) reduced multiplicatively to 75 %. The fluctuations of the RTDs near the jitter passage time s_{jitter} are now stronger. Amongst the corresponding cortical neurons, those that have remained normally responsive now exhibit enhanced responses to the jitter motion. The bottom graph shows adaptation, again, to exactly the same stimulus but with subtractive reduction of 1/3 of neuronal responses (randomly selected) by 25 % of the maximum response. Fluctuations are now stronger for all RTDs. The system, again, exhibits enhanced responses to the jitter motion. Other parameters: $\langle r/\tau \rangle = 0.005$, $\gamma = 0.03$. See appendix G for more details on the computer simulations.

the idea that estimation of speed is to some degree based on the output of neurons that adapt their velocity tuning in the way proposed here.

Another set of experiments (Clymer, 1973; Smith & Edgar, 1994; Schrater & Simoncelli, 1998) has demonstrated *repulsion* of perceived speed away from the speed of an adapting stimulus. Again, this is just what is to be expected, if speed is estimated from responses of neurons that shift their speed preferences *towards* the speed of the adapting stimulus, which is the basic operation of the present model.

The human absolute measure of speed is not very accurate, which might not be a severe perceptual deficit. Detecting relative motion and exploiting it for object segmentation seems to be much more important than a mere determination of speed itself.

3.5.5 Unaddressed Issues and Possible Model Extensions

There are several directions in which one may extend the present model of the corticogeniculate loop in order to explore issues that have been left aside. Perhaps the most urgent question that has not been addressed here is how a control loop for adaptive velocity tuning could react sensibly to the presentation of multiple objects in motion. Of a system for object segmentation one would require that each object is represented as being distinct from the others. The loop model was analytically treated in a linear approximation; cf. equation (3.16). Within this approximation, the sole target of adaptation is always $\langle s \rangle/\mu$, regardless of how many objects are present in the stimulus; cf. equation (3.62). Multiple objects that move at different speeds into the same direction or that move in opposite directions thus cannot be selected for enhanced representation by the velocity-tuned neurons. A nonlinear system needs to be analyzed to see, if the population of cortical neurons can split such that different parts become tuned to different object velocities. If, on the other hand, different objects move into different directions, they are picked up by different direction populations of velocity-tuned neurons. Successful object segmentation then depends on the directional tuning characteristics and on the interactions that are assumed between the different direction populations. In the limiting case of narrow directional tuning and no interaction between the populations, we are left with a collection of independent systems as analyzed above, some of which are stimulated by a single object. Adaptation then proceeds in each population as has been demonstrated here. In particular, in the regime of diffusion-sustained oscillations cortical neurons responsive to parts of the same object tend to fire in synchrony, while those responsive to different objects fire without correlation between them.

The choice of interactions between direction populations has to be made consistent with data on motion integration across different directions, such as data on perceived global flow and transparent or rigid plaid motion; see, e.g., Watamaniuk et al. (1989), Braddick (1993), Stoner & Albright (1993), and Kim & Wilson (1993). In particular, for segmentation it should be possible to bind different features of the same object regardless of their orientation. Several authors have proposed that binding is encoded in correlation of firing of neurons that respond to related parts of a stimulus (von der Malsburg, 1981; von der Malsburg, 1986; Abeles, 1982; Eckhorn et al., 1988; Engel et al., 1992). Diffusion-sustained oscillations may realize just this in a control loop for velocity tuning that incorporates interactions between different direction populations. Visual cortical areas beyond the primary visual cortex are likely to be involved, as they are believed to be the stage where the so-called 'aperture problem' is solved[6].

We here have dealt only with translatory motion. It is well-known, however, that more complex velocity fields, such as resulting from object and observer motion in depth and motion of non-rigid objects, are utilized by the visual system as cues for object segmentation; cf. section 3.1. Again, higher visual cortical areas, notably area MST in primates, are likely to be involved in representing such patterns of motion; see, e.g., Zemel & Sejnowski (1998). With regard to segmentation of multiple objects in complex motion, it would be interesting to study a model that includes stages of convergence of out-

---

[6] By 'aperture problem' one denotes the simple fact that it is impossible to judge the true two-dimensional direction of retinal motion of, say, a bar from viewing only a part of the bar that excludes the bar's ends. Since simple cells respond only to bar orientation, and not to the location of the bar's ends (even if inside their RF), they are blind to the two-dimensional direction of motion. Rather, simple cells only represent the component of motion that is orthogonal to a bar's orientation.

puts from different direction populations as analyzed here. Neurons of the higher stages could be envisaged to either only collect the adapted signals of the lower stage or to influence the adaptation process in the lower stage by way of their feedback connections. In this context it is interesting to note that intracortical feedback connections terminate in layer 6 (and layer 1) of the primary visual cortex, that is, in the same layer that projects back to the LGN (Zeki & Shipp, 1988). Statistical detection and enhanced representation even of complex, object-related, patterns of motion may thus result from the basic mechanism of adaptive velocity tuning that has been explored here.

Appendix A

Biophysical Neuron Models

Since Hodgkin & Huxley (1952) have revolutionized both electrophysiology and models of excitable membranes with their work on the squid giant axon, there has been a common approach to detailed modeling of neurons of various types. The essential electrical properties of neuronal membranes have been found to be captured by the type of circuit shown in Figure A.1, often referred to as the ‘equivalent circuit’. According to this circuit model, the membrane potential V of a cell obeys the differential equation

$$\frac{\mathrm{d}V}{\mathrm{d}t} = \frac{1}{C}\sum_{i=1}^{n} I_i \ , \tag{A.1}$$

where I_i are the currents through the different types of ion channels in the membrane, and C is the membrane capacitance. The art of building a neuron model is to find good empirical, quantitative descriptions of all the relevant ion currents. It was the achievement of Hodgkin & Huxley (1952) to have provided the first successful mathematical account of voltage-dependent ion channels.

Equation (A.1) describes a point-like neuron. If the spatial dimension is relevant, e.g., because the neuron is of complex geometry or the types of ion channels vary significantly over the cell’s surface, different local models, called *compartments*, of the kind (A.1) must be coupled by current-exchange according to the cell’s topology. In this work we use a single-compartment model. Neurons that are well-described by single-compartment models, like the thalamic relay neurons investigated in this work (Huguenard & McCormick, 1992; McCormick & Huguenard, 1992), are called *electrically compact.*

The way Hodgkin & Huxley (1952) have modeled the Na^+ and K^+ ion channels of the squid giant axon has become the paradigm for a large range of ionic currents. We here introduce the general concepts, the characteristic

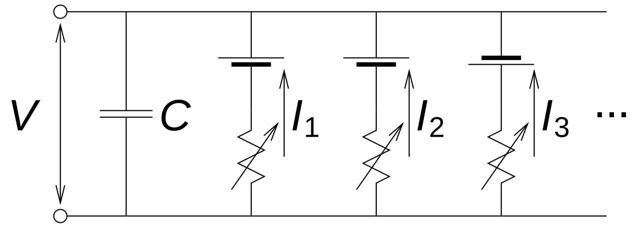

Figure A.1: Model circuit for the electrical properties of a cell's membrane, often referred to as the 'equivalent circuit'. V is the membrane potential, C is the membrane capacitance, and I_i are ion currents. The characteristics of ion currents are determined by their reversal potential (batteries) and their conductance that may in general depend on the membrane potential, on intracellular ion concentrations, or on the time elapsed after reception of an input spike (variable resistors).

functions, the parameters, and the common notation, along with modifications that are necessary for some channels. Characteristic functions and parameter values for the model of thalamic relay neurons (Huguenard & McCormick, 1992; McCormick & Huguenard, 1992) employed in this work can be found in appendix C. For a detailed exposition of data and theory on ion channels and excitable membranes the reader is referred to Tuckwell (1988a, 1988b) and Hille (1992).

Within the Ohmic approximation, the ion currents are described by

$$I_i = g_i \, m_i^{p_i} \, h_i^{q_i} \, (V_i - V) \ , \tag{A.2}$$

with the *reversal potential* V_i, the maximal conductance g_i, the *gates* m_i and h_i, and some positive, usually integer, constants p_i and q_i. The reversal potential V_i is given by the Nernst potential for ions of type i,

$$V_i = \frac{kT}{z_i e} \ln\left(\frac{c_{i,\mathrm{e}}}{c_{i,\mathrm{i}}}\right) \ , \tag{A.3}$$

where $c_{i,\mathrm{e}}$ and $c_{i,\mathrm{i}}$ are the ion's concentrations in the extra- and intracellular space, respectively, and z_i is its valence. As usually, e is the elementary charge, k is the Boltzmann constant, and T is the absolute temperature. The gates m_i and h_i are dynamic variables that assume values between zero and one according to differential equations that involve the membrane potential V; see below.

It must be stressed that expressions of type (A.2) are primarily *empirical fits* to the voltage dependence of ionic currents. Nonetheless, an oversimplified but intuitive physical interpretation of (A.2) is that ion currents flow through an ensemble of channels of type i that have p_i m-gates and q_i h-gates each. The gates are open and closed with certain probabilities. An individual channel allows ions to pass only if *all* its gates are in the open state.

In what follows we will drop the index i for notational simplicity. With the given picture of ionic gates in mind, we may 'understand' the dynamics of the gates m and h. Transitions between the open and closed states are governed by the transition rates $\alpha_{m/h}$ and $\beta_{m/h}$,

$$\frac{\mathrm{d}m}{\mathrm{d}t} = \alpha_m(V)\,(1-m) - \beta_m(V)\,m \; , \tag{A.4}$$

$$\frac{\mathrm{d}h}{\mathrm{d}t} = \alpha_h(V)\,(1-h) - \beta_h(V)\,h \; . \tag{A.5}$$

The rates, in turn, are functions of the membrane potential V. Instead of transition rates, one may specify the gates' asymptotic values m_∞ and h_∞, and time constants $\tau_{m/h}$. Their relation to the transition rates is

$$m_\infty(V) = \frac{\alpha_m(V)}{\alpha_m(V)+\beta_m(V)} \; , \tag{A.6}$$

$$h_\infty(V) = \frac{\alpha_h(V)}{\alpha_h(V)+\beta_h(V)} \; , \tag{A.7}$$

$$\tau_{m/h}(V) = \frac{1}{\alpha_{m/h}(V)+\beta_{m/h}(V)} \; . \tag{A.8}$$

By convention, the m-gate is usually the one that opens ($m_\infty \approx 1$) at higher and closes ($m_\infty \approx 0$) at lower membrane potentials; for the h-gate the situation is just the other way round. The m-gate is called the *activation gate*, the h-gate the *inactivation gate*. Accordingly, a current is said to *activate* when the m-gate opens; it is said to *inactivate* when the h-gate closes. As a typical example, Figure A.2 displays plots of the gates' asymptotic values and time constants for the transient Na^+ current I_{Na}; see equations (C.1) through (C.5) in appendix C. It can be understood from these plots (see the Figure caption) that the current I_{Na} is prominently involved in the production and propagation of a neuron's *action potentials*, or *spikes*.

For the firing pattern of thalamic relay neurons, the transient and low-threshold Ca^{2+} current I_{T} is of particular importance; see section 1.2 and equations (C.29) through (C.33) in appendix C. Analogous to the production of Na^+ spikes by I_{Na}, the Ca^{2+} current I_{T} produces Ca^{2+} spikes (that, in turn, can promote Na^+ spikes). In Figure A.3 we show plots of the gates' asymptotic values and time constants for I_{T}.

Some types of ion channels do not inactivate, i.e., they have $q = 0$. A somewhat unusual current of this type is the h-current I_{h}; see equations

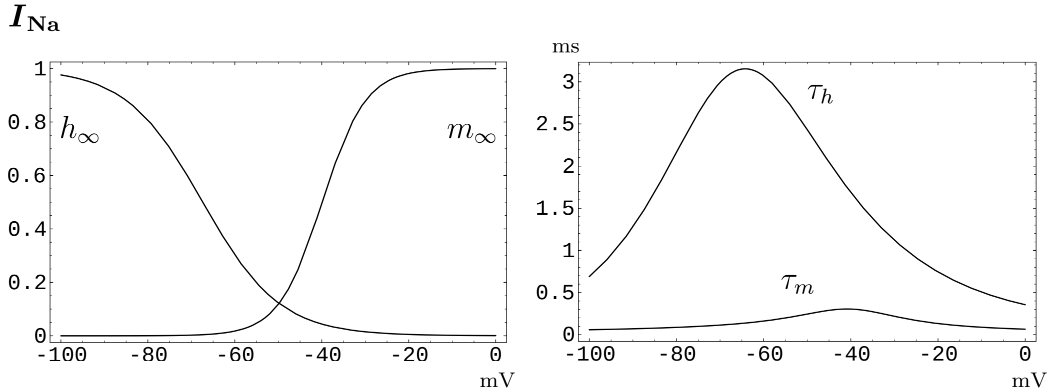

Figure A.2: Plots of asymptotic values (left) and time constants (right) of the gates for the transient Na^+ current I_{Na}; see equations (C.1) through (C.5) in appendix C. The m-gate is the activation gate, the h-gate the inactivation gate. The effect of I_{Na} is to initiate action potentials once the cell's membrane is sufficiently depolarized. As can be seen from the left plots, when the membrane potential increases from a resting level of -70 mV to roughly -50 mV, the m-gate starts opening (activation). At the same time, the h-gate starts closing (inactivation). In the right plots we see that activation is much faster than inactivation. The net effect is a transient opening of both m- and h-gates. As the Na^+ concentration in the cell's interior is much lower than in the exterior space, an influx of Na^+ into the cell results. Importantly, Na^+ influx leads to additional depolarization. Activation of I_{Na} is thus a self-reinforcing effect. The cell is repolarized to lower potentials, and the action potential is terminated, by inactivation of I_{Na} and activation of K^+ currents; see appendix C.

(C.41) through (C.43) in appendix C. Unlike for I_{Na} and I_{T}, the activation gate of I_{h} opens when the cell is *hyper*polarized[1]. The h-current is, therefore, said to be 'hyperpolarization-activated'.

An ion channel that neither inactivates nor de-activates, i.e., $p = q = 0$, is called a *leak* channel. Leak channels are characterized by a constant conductance g; cf. equation (A.2).

Within the picture of open and closed m- and h-gates we can reason that the asymptotic values m_∞ and h_∞ have to obey the Boltzmann equilibrium distribution for the open and closed states. Since this equilibrium is dependent upon the membrane potential V, some *gating charge* $z_{m/h}e$ has to be moved in the electric field in order to switch between the open and closed

---

[1] Alternatively, one might say that for I_{h} we have $p = 0$ and the current is always activated. For some reason, this way of looking at it is not favored.

I_{T}

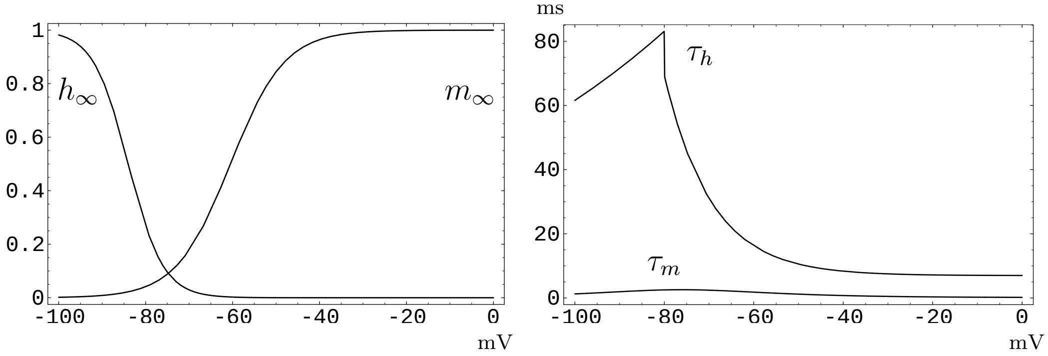

Figure A.3: Plots of asymptotic values (left) and time constants (right) of the gates for the transient and low-threshold Ca^{2+} current I_{T}; see equations (C.29) through (C.33) in appendix C. The m-gate is the activation gate, the h-gate the inactivation gate. The effect of I_{T} is to initiate Ca^{2+} spikes after sufficient hyperpolarization of the cell's membrane to open the h-gate (de-inactivation). The series of events during the production of a Ca^{2+} spike is analogous to the one for the Na^+ spike; cf. Figure A.2.

states of the m/h-gates. Let $W_{m/h}$ be the conformational energy increase associated with channel opening at $V = 0$. The equilibrium ratio of the numbers of open and closed channels in an ensemble at membrane potential V then is

$$\frac{n_{m/h}^{\mathrm{open}}}{n_{m/h}^{\mathrm{closed}}} = \exp\left(-\frac{W_{m/h} - z_{m/h}eV}{kT}\right) , \tag{A.9}$$

implying that

$$m_\infty(V) = \frac{n_m^{\mathrm{open}}}{n_m^{\mathrm{open}} + n_m^{\mathrm{closed}}} = \frac{1}{1 + \exp[(W_m - z_m eV)/kT]} , \tag{A.10}$$

$$h_\infty(V) = \frac{n_h^{\mathrm{open}}}{n_h^{\mathrm{open}} + n_h^{\mathrm{closed}}} = \frac{1}{1 + \exp[(W_h - z_h eV)/kT]} . \tag{A.11}$$

In fact, equations (A.10) and (A.11) represent commonly, although not exclusively, used fits to the voltage dependence of m_∞ and h_∞, respectively. The valence $z_{m/h}$ of the gating charge then turns out to be some effective, possibly fractional, number.

Equations (A.10) and (A.11) indicate a temperature dependence of m_∞ and h_∞. Likewise, the time constants $\tau_{m/h}$ and the maximal conductance g depend upon temperature. The time constants become shorter and the conductance larger with increasing temperature. The amounts of change depend on the specific channel, but often a time constant will reduce to roughly 1/3 and a conductance will increase about 1.5-fold, Ca^{2+} conductances 3-fold, when the temperature is increased by 10 degrees.

For some ion channels the Ohmic description (A.2) for the ion current I does not provide a satisfactory approximation. In those cases Goldman's constant-field equation

$$I = g\, m^p\, h^q\, \frac{V z^2 e^2}{kT}\, \frac{c_\mathrm{i} - c_\mathrm{e} \exp(-zeV/kT)}{1 - \exp(-zeV/kT)} \tag{A.12}$$

often is a better choice (Tuckwell, 1988a). Here c_i and c_e are the ion's concentrations in the intra- and extracellular space, respectively, and z is its valence. For the thalamic relay neuron, the Ca^{2+} currents are modeled according to equation (A.12); see appendix C.

Ion channels that have a conductance which depends on the membrane potential V, as introduced here, are called *voltage-gated* channels. There are other ion currents, like the Ca^{2+}-activated K^+ current I_C, with a conductance depending on the membrane potential *and* the intracellular concentration of Ca^{2+} ions; see equations (C.38) through (C.40) in appendix C. They are, accordingly, called *voltage- and Calcium-gated* currents. Their transition rates α and β [cf. equations (A.4) and (A.5)] are functions of membrane voltage and intracellular Ca^{2+} concentration. Moreover, *receptor-gated* channels can be found, e.g., at synapses, where they provide for transmission of chemical signals. All three types of channels are used for the model of thalamic relay neurons studied in this work; see appendix C and subsection 2.2.1.

Appendix B

The Spike-Response Model of a Neuron

The spike-response model has been introduced by Gerstner & van Hemmen (1992); see also Gerstner & van Hemmen(1994). Its basic idea is to reproduce a neuron's spiking behavior by a *threshold process* on its membrane potential. The evolution of a model neuron's membrane potential is given by the *linear response* to presynaptic input spikes and to spikes generated by the cell itself. Spikes are represented as point events and all that matters are the *times* of spike generation in the neurons. Justification for these modeling assumptions is obtained from the observation of real neurons. Moreover, the spike-response model can be understood as the systematic first-order approximation to the celebrated, but computationally much more expensive, Hodgkin-Huxley model (Hodgkin & Huxley, 1952; Kistler et al., 1997); see appendix A. We here introduce the principles and parameters of the spike-response model. Numeric values for the parameters are given elsewhere; see the descriptions of specific simulations in subsection 2.2.1 and appendix F.

The dynamic variable of the neuron model is usually denoted by h and is reminiscent of a neuron's membrane potential. In the deterministic version of the model, a spike is triggered whenever h crosses a given *threshold* θ from below. Probabilistic versions define a function $\mathrm{q}(h - \theta)$ that gives the rate of spikes, in the sense of an (inhomogeneous) Poisson process, depending on the distance of the 'membrane potential' h from the threshold θ. The function $\mathrm{q}(h - \theta)$ drops to zero as $h - \theta$ approaches $-\infty$. In the simulations presented in this work we have used external sources of noise, i.e., other neurons' inputs, and thus have employed the deterministic version of the spike-response model, that is, with the hard threshold θ.

The 'membrane potential' h is the sum of two terms,

$$h(t) \;=\; h_{\text{syn}}(t) + h_{\text{ref}}(t) \ , \tag{B.1}$$

the *synaptic* contribution h_{syn} and the *refractory* contribution h_{ref}. The synaptic term describes the response at the cell's soma to past synaptic input at times $t_1, t_2, \ldots, t_m < t$,

$$h_{\text{syn}}(t) \;=\; \sum_{i=1}^{m} w_i \, \epsilon(t - t_i) \ . \tag{B.2}$$

Here $\epsilon(t)$ is the unary postsynaptic potential. Different choices for $\epsilon(t)$ are possible. In particular, for $\epsilon(t) = \exp(-t/\tau)\,\Theta(t)$ we recover the widely-used *integrate-and-fire model* as a special case. A more realistic model is obtained for $\epsilon(t)$ being an alpha function,

$$\epsilon(t) \;=\; \frac{t}{\tau_{\text{exc/inh}}} \exp\!\left(1 - \frac{t}{\tau_{\text{exc/inh}}}\right) \Theta(t) \ . \tag{B.3}$$

We have chosen the alpha function with rise times τ_{exc} and τ_{inh} for excitatory and inhibitory input, respectively. Additionally, conduction and synaptic delays may be incorporated. The amplitudes w_i of postsynaptic potentials [see equation (B.2)] are reflections of the 'weight' of the different transmitting synapses. The 'weight' is positive for an excitatory, and negative for an inhibitory synapse. They are collectively referred to as w_{exc} and w_{inh}, respectively.

The refractory term in equation (B.1) describes the refractory phase that a neuron enters after generation of a spike. During the refractory phase a neuron is less likely to generate another spike. This behavior is implemented as a transient reduction in the 'membrane potential' h. Within the linear approximation we get

$$h_{\text{ref}}(t) \;=\; w_{\text{ref}} \sum_{i=1}^{n} \eta(t - t^i) \ , \tag{B.4}$$

where $t^1, t^2, \ldots, t^n < t$ are the times of past spike generation by the neuron, and $\eta(t) \leq 0$ is the refractory potential. Different choices for $\eta(t)$ are possible. For the simulations in the present work we have used

$$\eta(t) \;:=\; \begin{cases} 0 & \text{if } t < 0, \\ -\infty & \text{if } 0 \leq t < T_{\text{ref}}, \\ -\exp\!\left(-\frac{t}{\tau_{\text{ref}}}\right) & \text{if } T_{\text{ref}} \leq t. \end{cases} \tag{B.5}$$

During the time interval T_{ref} after each generated spike no further spikes can be triggered, no matter how large h_{syn} gets. T_{ref} is called the *absolute refractory period*. It reflects the time it takes a neuron's Na$^+$ channel to de-inactivate; cf. appendix A.

Appendix C

Model of Thalamic Relay Neurons

In accordance with Huguenard & McCormick (1992) and McCormick & Huguenard (1992), and with information privately communicated by J. R. Huguenard we have set the membrane area at $A = 29000\ \mu\mathrm{m}^2$, the membrane capacitance at $C = 0.29$ nF, and have implemented the ionic currents listed below. We have adapted the model to 37 degrees Celsius and all equations refer to this temperature. Moreover, V denotes the membrane potential in mV, I_i the ionic currents in nA, and $\tau_{m/h}$ the gating time constants in ms. The concentrations $c_{\mathrm{Ca,L/T/e}}$ of Ca^{2+} ions are measured in mol/l. m_∞ and h_∞ are dimensionless, asymptotic gating variables. For an introduction to biophysical neuron models and of the notation used here see appendix A.

Transient Na^+ current $\boldsymbol{I}_{\mathbf{Na}}$

$$m_\infty = \frac{1}{1 + 0.681\ \exp[-(V+38)/5]}\ , \tag{C.1}$$

$$h_\infty = \frac{1}{1 + 129\ \exp[(V+55)/15]/\{1+\exp[(17-V)/21]\}}\ , \tag{C.2}$$

$$\tau_m = \frac{0.227\,\{\exp[(V+38)/5]-1\}}{(V+38)\{0.091\ \exp[(V+38)/5]+0.062\}}\ , \tag{C.3}$$

$$\tau_h = \frac{0.227}{0.016\ \exp[-(V+55)/15] + 2.07/\{1+\exp[(17-V)/21]\}}\ , \tag{C.4}$$

$$I_{\mathrm{Na}} = 12.8\,m^3\,h\,(41-V)\ . \tag{C.5}$$

Persistent Na$^+$ current I_{Nap}

$$\begin{aligned} m_\infty &= \frac{1}{1+\exp[-(V+49)/5]} \,, && \text{(C.6)} \\ \tau_m &= \frac{0.227\,\{\exp[(V+38)/5]-1\}}{(V+38)\{0.091\,\exp[(V+38)/5]+0.062\}} \,, && \text{(C.7)} \\ I_{\text{Nap}} &= 0.00744\,m\,(41-V) \,. && \text{(C.8)} \end{aligned}$$

Rapidly inactivating K$^+$ current I_{A1}

$$\begin{aligned} m_\infty &= \frac{1}{1+\exp[-(V+60)/8.5]} \,, && \text{(C.9)} \\ h_\infty &= \frac{1}{1+\exp[(V+78)/6]} \,, && \text{(C.10)} \\ \tau_m &= \frac{0.227}{\exp[(V+35.8)/19.7]+\exp[-(V+79.7)/12.7]} + 0.084 \,, && \text{(C.11)} \\ \tau_h &= \begin{cases} \frac{0.227}{\exp[(V+46)/5]+\exp[-(V+238)/37.5]} & \text{if } V < -63, \\ 4.31 & \text{elsewhere,} \end{cases} && \text{(C.12)} \\ I_{\text{A1}} &= 0.644\,m^4\,h\,(-105-V) \,. && \text{(C.13)} \end{aligned}$$

Rapidly inactivating K$^+$ current I_{A2}

$$\begin{aligned} m_\infty &= \frac{1}{1+\exp[-(V+36)/20]} \,, && \text{(C.14)} \\ h_\infty &= \frac{1}{1+\exp[(V+78)/6]} \,, && \text{(C.15)} \\ \tau_m &= \frac{0.227}{\exp[(V+35.8)/19.7]+\exp[-(V+79.7)/12.7]} + 0.084 \,, && \text{(C.16)} \\ \tau_h &= \begin{cases} \frac{0.227}{\exp[(V+46)/5]+\exp[-(V+238)/37.5]} & \text{if } V < -73, \\ 13.6 & \text{elsewhere,} \end{cases} && \text{(C.17)} \\ I_{\text{A2}} &= 0.429\,m^4\,h\,(-105-V) \,. && \text{(C.18)} \end{aligned}$$

Slowly inactivating K$^+$ current I_{K2a}

$$\begin{aligned} m_\infty &= \frac{1}{1+\exp[-(V+43)/17]} \,, && \text{(C.19)} \\ h_\infty &= \frac{1}{1+\exp[(V+58)/10.6]} \,, && \text{(C.20)} \end{aligned}$$

$$\begin{aligned}
\tau_m &= \frac{0.227}{\exp[(V-81)/25.6]+\exp[-(V+132)/18]}+2.25\ , && \text{(C.21)}\\
\tau_h &= \frac{0.227}{\exp[(V-1329)/200]+\exp[-(V+130)/7.1]}+27.2\ , && \text{(C.22)}\\
I_{\mathrm{K2a}} &= 0.129\, m^4\, h\,(-105-V)\ . && \text{(C.23)}
\end{aligned}$$

Slowly inactivating K$^+$ current I_{K2b}

$$\begin{aligned}
m_\infty &= \frac{1}{1+\exp[-(V+43)/17]}\ , && \text{(C.24)}\\
h_\infty &= \frac{1}{1+\exp[(V+58)/10.6]}\ , && \text{(C.25)}\\
\tau_m &= \frac{0.227}{\exp[(V-81)/25.6]+\exp[-(V+132)/18]}+2.25\ , && \text{(C.26)}\\
\tau_h &= \begin{cases} \frac{0.227}{\exp[(V-1329)/200]+\exp[-(V+130)/7.1]}+27.2 & \text{if } V<-70,\\ 2020 & \text{elsewhere,}\end{cases} && \text{(C.27)}\\
I_{\mathrm{K2b}} &= 0.0857\, m^4\, h\,(-105-V)\ . && \text{(C.28)}
\end{aligned}$$

Transient and low-threshold Ca^{2+} current I_{T}

$$\begin{aligned}
m_\infty &= \frac{1}{1+\exp[-(V+60.5)/6.2]}\ , && \text{(C.29)}\\
h_\infty &= \frac{1}{1+\exp[(V+84)/4]}\ , && \text{(C.30)}\\
\tau_m &= \frac{0.181}{\exp[-(V+132)/16.7]+\exp[(V+16.8)/18.2]}+0.111\ , && \text{(C.31)}\\
\tau_h &= \begin{cases} 0.249\,\exp[(V+467)/66.6] & \text{if } V<-80,\\ 0.249\,\{\exp[-(V+22)/10.5]+28\} & \text{elsewhere,}\end{cases} && \text{(C.32)}\\
I_{\mathrm{T}} &= 681\, m^2\, h\, V\, \frac{c_{\mathrm{Ca,e}}\,\exp(-0.0748\,V)-c_{\mathrm{Ca,T}}-c_{\mathrm{Ca,L}}}{1-\exp(-0.0748\,V)}\ . && \text{(C.33)}
\end{aligned}$$

Here $c_{\mathrm{Ca,e}} = 0.002$ mol/l is the (fixed) extracellular concentration of Ca^{2+} ions, and $c_{\mathrm{Ca,T}}$ and $c_{\mathrm{Ca,L}}$ are the intracellular concentrations of Ca^{2+} as contributed by the Ca currents I_{T} and I_{L} (see below), respectively. The contribution by the T-current is modeled by

$$\frac{\mathrm{d}c_{\mathrm{Ca,T}}}{\mathrm{d}t} = \frac{0.0518}{A}\,\frac{\mathrm{mol}}{\mathrm{l\,nA\,ms}}\,I_{\mathrm{T}} - \frac{1}{\mathrm{ms}}\,c_{\mathrm{Ca,T}}\ , \qquad \text{(C.34)}$$

as long as $c_{\mathrm{Ca,T}} > 5\cdot 10^{-8}$ mol/l. The dynamics of $c_{\mathrm{Ca,T}}$ is constrained to never drop below $5\cdot 10^{-8}$ mol/l.

Long-lasting and high-threshold Ca^{2+} current $\boldsymbol{I}_{\mathbf{L}}$

$$\begin{aligned}
m_\infty &= \frac{1}{1+\exp[-(10+V)/10]}\ , && \text{(C.35)}\\
\tau_m &= 0.227\Bigg/\left[\frac{1.6}{1.43\,\exp(-0.072\,V)+1}\right.\\
&\qquad \left.+\frac{0.02\,(V-1.31)}{0.783\,\exp(0.186567\,V)-1}\right]\ , && \text{(C.36)}\\
I_{\mathrm{L}} &= 1360\,m^2\,V\,\frac{c_{\mathrm{Ca,e}}\,\exp(-0.0748\,V)-c_{\mathrm{Ca,T}}-c_{\mathrm{Ca,L}}}{1-\exp(-0.0748\,V)}\ . && \text{(C.37)}
\end{aligned}$$

The Ca concentrations $c_{\mathrm{Ca,e}}$, $c_{\mathrm{Ca,T}}$ and $c_{\mathrm{Ca,L}}$ have the same meanings as above. The intracellular concentration $c_{\mathrm{Ca,L}}$ is modeled exactly like $c_{\mathrm{Ca,T}}$, that is, by equation (C.34) with 'T' replaced by 'L' and with the same minimum concentration.

Ca^{2+}-activated K^{+} current $\boldsymbol{I}_{\mathbf{C}}$

$$\begin{aligned}
m_\infty &= \frac{1}{1+4\cdot 10^{-7}/c_{\mathrm{Ca,L}}\,\exp(-V/12)}\ , && \text{(C.38)}\\
\tau_m &= \frac{0.227}{0.1\,\exp(-V/24)+250000\,c_{\mathrm{Ca,L}}\,\exp(V/24)}\ , && \text{(C.39)}\\
I_{\mathrm{C}} &= 1.06\,m\,(-105-V)\ . && \text{(C.40)}
\end{aligned}$$

The Ca^{2+} concentration $c_{\mathrm{Ca,L}}$ has the same meaning as above.

Hyperpolarization-activated cation current $\boldsymbol{I}_{\mathbf{h}}$

$$\begin{aligned}
m_\infty &= \frac{1}{1+\exp[(V+75)/5.5]}\ , && \text{(C.41)}\\
\tau_m &= \frac{0.227}{\exp(-0.086\,V-14.59)+\exp(0.0701\,V-1.87)}\ , && \text{(C.42)}\\
I_{\mathrm{h}} &= 0.0213\,m\,(-43-V)\ . && \text{(C.43)}
\end{aligned}$$

Leak Na^{+} current $\boldsymbol{I}_{\mathbf{Naleak}}$

$$I_{\mathrm{Naleak}} = 0.000266\,(41-V)\ . \qquad \text{(C.44)}$$

Leak K^{+} current $\boldsymbol{I}_{\mathbf{Kleak}}$

$$I_{\mathrm{Kleak}} = g_{\mathrm{Kleak}}\,(-105-V)\ , \qquad \text{(C.45)}$$

where g_{Kleak} has been varied between 0.00106 μS and 0.0159 μS in order to yield resting membrane potentials between -61 mV and -76 mV; see subsection 2.2.6.

Appendix D

Stimulus Parameters for Poissonian Stimulus Events

In the absence of accurate data, it is reasonable to assume the times t_j at which visual features drive cortical neurons to fire to obey Poisson statistics. For the density u of interstimulus times r this means

$$\mathrm{u}(r) = \frac{\mathrm{e}^{-r/\langle r \rangle}}{\langle r \rangle} \; . \tag{D.1}$$

In order to reformulate and uncover dependencies between the stimulus parameters a_i, b_i, c_i introduced in equations (3.64) and (3.82), we calculate the mean values

$$\begin{aligned} \left\langle \left(\frac{r}{\tau}\right)^k \mathrm{e}^{-r/\tau} \right\rangle &= \left(-\frac{\partial}{\partial z}\right)^k \left\langle \mathrm{e}^{-zr/\tau} \right\rangle \bigg|_{z=1} = \left(-\frac{\partial}{\partial z}\right)^k \int_0^\infty \mathrm{d}r\, \mathrm{u}(r)\, \mathrm{e}^{-zr/\tau} \bigg|_{z=1} \\ &= \left(-\frac{\partial}{\partial z}\right)^k \frac{1}{1 + z\, \langle r/\tau \rangle} \bigg|_{z=1} \; . \end{aligned} \tag{D.2}$$

Hence the stimulus parameters turn out to be

$$a_1 = \frac{1}{1 + \langle r/\tau \rangle} \; , \quad b_1 = \frac{\mathrm{e}\, \langle r/\tau \rangle}{(1 + \langle r/\tau \rangle)^2} \; , \tag{D.3}$$

$$a_2 = \frac{1}{1 + 2\, \langle r/\tau \rangle} \; , \quad b_2 = \frac{2\mathrm{e}\, \langle r/\tau \rangle}{(1 + 2\, \langle r/\tau \rangle)^2} \; , \quad c_2 = \frac{2\mathrm{e}^2\, \langle r/\tau \rangle^2}{(1 + 2\, \langle r/\tau \rangle)^3} \; .$$

There are now dependencies between these parameters. In particular, we have

$$b_i = \mathrm{e}\, a_i\, (1 - a_i) \; , \quad i = 1, 2 \; , \tag{D.4}$$

such that the stimulus parameters a_1, b_1 lie on the parabolas plotted in the left graph of Figure 3.6.

In subsection 3.4.4 we have established that the necessary and sufficient condition for the second moments to converge is $\gamma < 4/\mathrm{e}$ for small $\langle r/\tau \rangle$. Multiplying equation (D.4) by γ, we see that this bound implies for Poisson statistics

$$\gamma b_i < 4\, a_i\, (1 - a_i) < 4\, a_i \quad \text{for } a_i \in (0, 1),\ i = 1, 2. \tag{D.5}$$

In particular, the loop system is in the regime of damped oscillation of the mean RTDs for all $a_1 \in (0, 1)$; cf. Figure 3.5. Conversely, $\gamma b_i < 4a_i$ for all $a_i \in (0, 1)$ together with equation (D.4) implies $\gamma < 4/\mathrm{e}$.

Appendix E

Proof of Two Assertions on Crossing of Mean Response Time Differences

We here present the proofs of assertions 2 and 3 on crossing of mean response time differences (RTDs) that are formulated in subsection 3.4.7. (Assertion 1 of subsection 3.4.7 is briefly proven there.)

Proof of Assertion 2

In order to prove assertion 2 we have to make use of equation (3.140) and investigate the sign of

$$\lim_{a_1 \to 1} \mathrm{F}\left[a_1, \gamma\, \mathrm{e}\, a_1\, (1 - a_1)\right] \ . \tag{E.1}$$

Since $\mathrm{F}(1,0) = 0$, the sign of (E.1) depends on the sign of

$$\lim_{a_1 \to 1-} \frac{\mathrm{d}}{\mathrm{d}z} \mathrm{F}\left[z, \gamma \mathrm{e} z(1 - z)\right] \bigg|_{z=a_1} \tag{E.2}$$

$$= \lim_{a_1 \to 1-} \left[\frac{\partial \mathrm{F}(z,z')}{\partial z} + \frac{\partial \mathrm{F}(z,z')}{\partial z'} \left(\gamma \mathrm{e} - 2\gamma \mathrm{e} z\right) \right]_{z=a_1, z'=\gamma \mathrm{e} a_1 (1-a_1)} .$$

With patience and some calculus one finds

$$\lim_{a_1 \to 1-} \frac{\partial \mathrm{F}(z,z')}{\partial z} \bigg|_{z=a_1, z'=\gamma \mathrm{e} a_1 (1-a_1)} = 0 \ , \tag{E.3}$$

and

$$\lim_{a_1\to 1-} \left.\frac{\partial \mathrm{F}(z,z')}{\partial z'}\right|_{z=a_1,z'=\gamma e a_1(1-a_1)} \;=\; 4\,(2\mu-1)\ . \tag{E.4}$$

[This is the same limit as obtained on a different path in (3.139).] The last two limits, substituted into equation (E.2), indeed imply assertion 2.

Proof of Assertion 3

Despite the fact that the implicit-function theorem is not applicable, we can derive the slope of $\mathrm{C}_\mu(a_1)$ in the point $a_1 = 0$, $\gamma b_1 = 0$. Because of (3.137) we know that

$$\mathrm{F}(a_1,\gamma b_1) \;=\; \gamma b_1 - 4a_1 + o(a_1,\gamma b_1)\ ; \tag{E.5}$$

cf. equation (3.135). This directly implies

$$\left.\frac{\mathrm{dC}_\mu}{\mathrm{d}a_1}\right|_{a_1=0} \;=\; 4\ , \tag{E.6}$$

as can be verified in Figure 3.17. Of course, the derivative of $\mathrm{C}_\mu(a_1)$ at the point $a_1 = 0$ is taken from the right side only. (Note that the line $\gamma b_1 = 4a_1$ is another solution of $\mathrm{F}(a_1,\gamma b_1) = 0$ that starts from the point $a_1 = 0$, $\gamma b_1 = 0$ with slope 4, a fact that, again, shows that the conditions for the implicit-function theorem are not satisfied.)

We now have to show that for μ large enough there is a value of $a_1 \in (0,1)$, to be called $\hat{a}$, such that

$$\left.\hat{\jmath}\right|_{\substack{a_1=\hat{a}\\ \gamma b_1=\mathrm{C}_\mu(\hat{a})}} \;=\; 1\ ; \tag{E.7}$$

cf. equations (3.133) and (3.134). Let us investigate the two limits taken along the curve $\gamma b_1 = \mathrm{C}_\mu(a_1)$

$$\lim_{\substack{a_1\to 0\\ \gamma b_1=\mathrm{C}_\mu(a_1)}} \hat{\jmath}\ , \qquad \lim_{\substack{a_1\to 1\\ \gamma b_1=\mathrm{C}_\mu(a_1)}} \hat{\jmath}\ . \tag{E.8}$$

From (E.6) we know that

$$\lim_{\substack{a_1\to 0\\ \gamma b_1=\mathrm{C}_\mu(a_1)}} \arg\left[\gamma b_1 + 2a_1^2 - 2a_1 - \mathrm{i}\sqrt{\gamma b_1(4a_1-\gamma b_1)}\right] \;=\; 0\ , \tag{E.9}$$

$$\lim_{\substack{a_1\to 0\\ \gamma b_1=\mathrm{C}_\mu(a_1)}} \phi \;=\; \pi\ . \tag{E.10}$$

Taking furthermore into account that

$$\lim_{a_1 \to 0} \arg\left(\phi - \mathrm{i} \ln a_1\right) \; = \; \pi/2 \; , \tag{E.11}$$

we can conclude from equations (3.133) and (3.134) that

$$\lim_{\substack{a_1 \to 0 \\ \gamma b_1 = \mathrm{C}_\mu(a_1)}} \hat{\jmath} \; = \; 0 \; . \tag{E.12}$$

For the second of the limits (E.8) we have to distinguish the case $\mu \geq 1/2$ from $\mu < 1/2$; cf. equation (3.138). For $\mu \geq 1/2$ we have the limits

$$\lim_{\substack{a_1 \to 1 \\ \gamma b_1 = \mathrm{C}_{\mu \geq 1/2}(a_1)}} \arg\left(\phi - \mathrm{i} \ln a_1\right) \; \in \; [0, \pi/2] \; , \tag{E.13}$$

$$\lim_{\substack{a_1 \to 1 \\ \gamma b_1 = \mathrm{C}_{\mu \geq 1/2}(a_1)}} \phi \; = \; 0 \; . \tag{E.14}$$

where the precise value of the first limit depends on the path taken to the point $a_1 = 1$, $\gamma b_1 = 0$, i.e., on the analytically not known curve $\mathrm{C}_{\mu \geq 1/2}$. While this does not bother us here, we need the ansatz

$$\mathrm{C}_{\mu \geq 1/2}(a_1) \; = \; c(1 - a_1)^\kappa + o[(1 - a_1)^\kappa] \; , \quad a_1 \leq 1, c > 0, \kappa > 0 \; , \tag{E.15}$$

in order to calculate the remaining limit

$$\begin{aligned} \arg\left[\gamma b_1 + 2a_1^2 - 2a_1 - \mathrm{i}\sqrt{\gamma b_1(4a_1 - \gamma b_1)}\right] & \xrightarrow{\substack{a_1 \to 1 \\ \gamma b_1 = \mathrm{C}_{\mu \geq 1/2}(a_1)}} \\ \arg\left[c(1 - a_1)^\kappa - 2(1 - a_1) - \mathrm{i}\sqrt{4c(1 - a_1)^\kappa}\right] & \\ = \arg\left[\sqrt{c}(1 - a_1)^{\kappa/2} - \frac{2}{\sqrt{c}}(1 - a_1)^{1-\kappa/2} - 2\mathrm{i}\right] & \\ \xrightarrow{a_1 \to 1} \begin{cases} -\pi/2 & \text{for } \kappa < 2, \\ \arctan(\sqrt{c}) - \pi & \text{for } \kappa = 2, \\ -\pi & \text{for } \kappa > 2. \end{cases} & \end{aligned} \tag{E.16}$$

With the help of these limits we can conclude from equations (3.133) and (3.134) that

$$\lim_{\substack{a_1 \to 1 \\ \gamma b_1 = \mathrm{C}_{\mu \geq 1/2}(a_1)}} \hat{\jmath} \; = \; \infty \; , \tag{E.17}$$

independent of the exponent κ in the ansatz (E.15), that is, independent of the path the curve $\mathrm{C}_{\mu \geq 1/2}(a_1)$ takes to the point $a_1 = 1$, $\gamma b_1 = 0$.

For $\mu < 1/2$, on the other hand, we get the end point $a_1 = 1$, $\gamma b_1 > 0$ of the curve $\mathrm{C}_{\mu<1/2}$ as a function of μ by solving

$$\mathrm{F}(1, \gamma b_1) \;=\; 0 \tag{E.18}$$

for γb_1; cf. equation (3.135). Equation (E.18) can be rewritten as

$$\mu \left[\frac{1}{2} \left(\frac{\gamma b_1}{\sqrt{4 - \gamma b_1}} + \sqrt{4 - \gamma b_1} \right) + 1 \right] \;=\; 1 \; . \tag{E.19}$$

Its solution is

$$\gamma b_1 \;=\; 4 \, \frac{1 - 2\mu}{(1 - \mu)^2} \; , \quad 0 \leq \mu < \frac{1}{2} \; , \tag{E.20}$$

and can be substituted into expression (3.133) to give

$$\hat{j} \Big|_{a_1 = 1, \gamma b_1(\mu)} \;=\; \frac{\frac{\pi}{2} + \arctan[\mu^2/(1 - 2\mu)]}{\arg\left(\mu^2 + 2\mu - 1 + 2\mathrm{i}\mu\sqrt{1 - 2\mu}\right)} \; . \tag{E.21}$$

In particular, it now turns out that

$$\hat{j} \Big|_{a_1 = 1, \gamma b_1(\mu = 0)} \;=\; \frac{1}{2} \; , \quad \lim_{\mu \to 1/2-} \hat{j} \Big|_{a_1 = 1, \gamma b_1(\mu)} \;=\; \infty \; . \tag{E.22}$$

Concluding the proof, we obtain the result that $\hat{j}$ varies continuously from zero at $a_1 = 0$ to infinity at $a_1 = 1$ on the curves $\mathrm{C}_{\mu \geq 1/2}$, implying that there is at least one point on these curves where $\hat{j} = 1$. At this point $\mathrm{C}_{\mu \geq 1/2}$ assumes its maximum $1/\mu$. The same is true of the curves $\mathrm{C}_{\mu<1/2}$, as long as μ is not too small.

Appendix F

Computer Simulations of Corticogeniculate Feedback

We have simulated the local cortical feedback pathway depicted in Figure 3.3 left, consisting of three groups of layer 4 neurons, one interneuron, and two corticothalamic neurons that feedback onto geniculate relay cells (GRCs). Each of the layer 4 groups comprises 10 neurons that have each been modeled as Poissonian spike sources. The other neurons have been modeled as spike-response neurons; see appendix B. Note that each of the spike-response neurons, i.e., the interneuron and the two corticothalamic neurons, can equivalently represent a *group* of spike-response neurons with accordingly down-scaled synaptic output weights.

The layer 4 neurons' responses to a local feature passing their receptive fields has been modeled as a transient rise of their firing rates according to

$$\mathrm{R}(t) \;=\; \begin{cases} R\left(1 - \frac{1}{100\ \mathrm{ms}}|t - 100\ \mathrm{ms}|\right) & \text{if } 0 < t < 200\ \mathrm{ms}, \\ 0 & \text{elsewhere,} \end{cases} \tag{F.1}$$

where the amplitude R assumes the values denoted in Figure 3.4 and its caption as $R^{>}$, R, and $R^{<}$ for the three groups of layer 4 neurons, respectively.

Using the notation of appendix B, the parameters for the spike-response neurons and the network in the simulations are given in Table F.1. Synaptic delays have always been set at 2.0 ms. All time constants lie within physiological ranges. None of the parameters is critical and qualitatively identical results are obtained within a wide range of parameters.

The postsynaptic potential (PSP) in a GRC following the layer 4 responses (F.1) has been calculated as the sum

$$\overline{\mathrm{PSP}}(t) \;:=\; \sum_{f=1}^{F_1} \mathrm{PSP}(t - t_f^{(1)}) - \sum_{f=1}^{F_2} \mathrm{PSP}(t - t_f^{(2)}) \;, \tag{F.2}$$

θ	w_{exc} layer 4	w_{exc} layer 6	w_{inh}	w_{ref}
1.0	0.3	5.0	6.0	1.5

τ_{exc}	τ_{inh}	τ_{ref}	T_{ref}
3.0 ms	6.0 ms	10.0 ms	2.0 ms

Table F.1: Neuron and network parameters used in the simulations of corticothalamic feedback. See appendix B for an explanation of the parameters and Figure 3.3 left for a sketch of the network structure. Note that the high values of w_{exc} for the two layer 6 neurons and of w_{inh} for the interneuron should be interpreted as the weight of the all-over excitation/inhibition exerted by each of the three *groups* of neurons represented (equivalently) by just single neurons in the model. In contrast, w_{exc} for layer 4 neurons is the weight of excitation exerted by each of 30 (3 groups of 10 each) stochastically firing *individual* neurons.

where $t_1^{(1)}, \ldots, t_{F_1}^{(1)}$ and $t_1^{(2)}, \ldots, t_{F_2}^{(2)}$ are the times of spikes fired by each of the two corticothalamic neurons, and the unary potentials $\mathrm{PSP}(t - t_f^{(k)})$ are given by equation (3.1) with a rise time of $\tau = 100$ ms. Longer rise times yield similar results. Significantly shorter rise times prevent the building up of higher amplitudes and alter the shape of $\overline{\mathrm{PSP}}(t)$; see below. In accordance with the model of the corticothalamic loop depicted in Figure 3.3 left, the two cortical inputs to GRCs contribute to the net potential $\overline{\mathrm{PSP}}(t)$ with opposite signs. We have determined the mean amplitude A of $\overline{\mathrm{PSP}}(t)$, averaged over 100 response events of the type (F.1), as a function of the response amplitudes $R^{>}$, R, $R^{<}$ for the three groups of layer 4 neurons; cf. Figure 3.4.

Since the time window $\max\{t_{F_1}^{(1)}, t_{F_2}^{(2)}\} - \min\{t_1^{(1)}, t_1^{(2)}\}$ during which corticothalamic feedback spikes are initiated by a layer 4 response event (F.1) turn out to be typically much shorter than the rise time τ of the unary PSPs, the sum (F.2) is well approximated by

$$\overline{\mathrm{PSP}}(t) \approx A \, \frac{t - t'}{\tau'} \, \exp\left(1 - \frac{t - t'}{\tau'}\right) \Theta(t - t') \; . \tag{F.3}$$

Here $t' \in [\min\{t_1^{(1)}, t_1^{(2)}\}, \max\{t_{F_1}^{(1)}, t_{F_2}^{(2)}\}]$ is the effective time of the stimulus/response event and $\tau' > \tau$ is the effective rise time of corticothalamic PSPs. We now arrive at equation (3.2) for a GRC's membrane potential by labeling effective stimulus/response times by $t_1, t_2, \ldots$, the corresponding PSP amplitudes by $A_1, A_2, \ldots$, dropping the prime on the effective rise time τ', and introducing corticothalamic delays.

Appendix G

Computer Simulations of the Corticogeniculate Loop

In the model of the corticogeniculate loop, the time scale is set by the rise time τ of the corticogeniculate postsynaptic potentials defined in equation (3.1). All dynamics and characteristic times are given in units of τ. The passage times s of local features in the stimulus and the cortical neurons' preferences, that is, their response times differences (RTDs), are only meaningful relative to each other. They cannot be compared to τ, as we have not made any assumptions on the size of receptive fields. The units of s and $\mathrm{RTD}^{(c,\pm)}(t)$ are thus arbitrary.

The dynamics of the simulated system is given by equations (3.12) through (3.15) with

$$\begin{aligned}
\mathrm{f}(\delta s) &:= \begin{cases} 1-\left(\frac{\delta s}{40}\right)^2 & \text{if } \delta s < 40, \\ 0 & \text{elsewhere,} \end{cases} && \text{(G.1)} \\
\mathrm{A}(R) &:= 40\sqrt{1-R}\ , && \text{(G.2)} \\
\sigma(\delta R) &:= \tanh(20\,\delta R)\ , && \text{(G.3)}
\end{aligned}$$

and with delays $d_i = 0$ except where stated differently. In particular, we have

$$\mathrm{A}\left[\mathrm{f}(\delta s)\right] = \begin{cases} |\delta s| & \text{if } |\delta s| < 40, \\ 40 & \text{elsewhere.} \end{cases} \qquad \text{(G.4)}$$

The parameters are not critical and different parameters yield similar results. However, the width of the passage-time-tuning function f and, hence, of the linear range of the combination $\mathrm{A} \circ \mathrm{f}$ should not be made too small such that each class of cortical neuron can 'see' a significant part of the whole speed statistics in the stimulus.

With the exception of the simulation shown in Figure 3.19 (see the figure caption), we have created the stimuli in the following way. The time intervals r between successive stimulus/response events have been drawn from the exponential density (D.1) with some fixed value for $\langle r \rangle$, given in the respective figure captions, thus realizing a Poisson process for the stimulus/response times. The stimulus/response times have been restricted only by the precision of the machine representation of floating point numbers. In this way, the numerical simulations have proceeded in 'quasi-continuous' time. Unless stated otherwise, the passage times s of local features have been drawn from the density

$$\mathrm{v}(s) \;=\; \mu\,\mathrm{v}_o(s) + (1-\mu)\,\mathrm{v}_b(s) \;= \tag{G.5}$$

$$\mu\,\delta(s-s_o) + (1-\mu)\,\frac{1}{2\,\ln(s_{\max}/s_{\min})\,|s|}\,\Theta\left(|s|-s_{\min}\right)\,\Theta\left(s_{\max}-|s|\right)\ ,$$

independently for each stimulus event. Here $0 < s_{\min} < s_{\max}$ denote the minimum and maximum values of $|s|$ of background features, and s_o the passage time of object features. We always have chosen $s_{\min} < s_o < s_{\max}$. The density (G.5) takes into account that features moving across the retina are sampled with a frequency proportional to their speed. The stimulus parameters that are relevant and that are given in the caption of the figures presenting simulation results are

$$\langle s \rangle \;=\; \mu\, s_o\ , \tag{G.6}$$

$$\langle |s| \rangle \;=\; \mu\, s_o + (1-\mu)\,\langle |s| \rangle_b \;=\; \mu\, s_o + (1-\mu)\frac{s_{\max}-s_{\min}}{\ln(s_{\max}/s_{\min})}\ , \tag{G.7}$$

$$\mathrm{var}(|s|) \;=\; (1-\mu)\,\mathrm{var}_b(|s|) \;=\; (1-\mu)\frac{s_{\max}^2-s_{\min}^2}{2\,\ln(s_{\max}/s_{\min})}\ . \tag{G.8}$$

In particular, we have used $s_{\min} = 10$ and $s_{\max} = 30$ to yield for the background component alone

$$\langle |s| \rangle_b \;\approx\; 18.2048\ , \quad \mathrm{var}_b(|s|) \;\approx\; 364.096 \;\approx\; 19.1^2\ , \tag{G.9}$$

and $s_{\min} = 10$ and $s_{\max} = 50$ to yield

$$\langle |s| \rangle_b \;\approx\; 24.8534\ , \quad \mathrm{var}_b(|s|) \;\approx\; 745.602 \;\approx\; 27.3^2\ . \tag{G.10}$$

In order to measure the period of the RTDs under conditions of diffusion-sustained oscillations (and compare it to the analytical period of the mean RTDs; cf. subsection 3.4.5 and Figure 3.13), we have simulated a single trajectory $\mathrm{RTD}^{(+)}(t)$ with the dynamics given by equation (3.19) for a range of values for $\langle r/\tau\rangle$ and without delays. The RTD's resting value has been chosen as $\mathrm{RTD}^{(+)}(0) = s_o$, such that there is no drift of $\mathrm{RTD}^{(+)}(t)$, that is,

$$\lim_{t\to\infty}\langle \mathrm{RTD}^{(+)}(t)\rangle = \mathrm{RTD}^{(+)}(0) \; ; \tag{G.11}$$

cf. equation (3.62). The resulting dynamics is a more or less orderly, ongoing oscillation around $\mathrm{RTD}^{(+)}(0)$; cf. Figure 3.11. As *periods* we have sampled the time intervals between successive crossings of $\mathrm{RTD}^{(+)}(t)$ of the value $\mathrm{RTD}^{(+)}(0)$ from below[1]. Note that this is not the same as analyzing the power spectrum of $\mathrm{RTD}^{(+)}(t)$. The power spectrum is the Fourier transform of the autocorrelation function which in turn is related to the covariance function $\mathrm{cov}(x_j, x_{j+k})$; cf. equation (3.74). The period of the latter has been shown in subsection 3.4.3 to be identical to the period of the mean $\langle x\rangle_k$. Hence there is no use in comparing these two quantities in a computer simulation.

---

[1] Of course, the intervals between crossings from above yield identical statistics of the period.

Appendix H

List of Abbreviations

The following is a list of abbreviations used in the text. Most of them are part of the neurobiological standard terminology.

AMPA	α-amino-3-hydroxy-5-methyl-4-isoxalone propionic acid
GABA	γ-aminobutyric acid
GRC	geniculate relay cell
LGN	lateral geniculate nucleus
MT	middle temporal area
NMDA	N-methyl-D-aspartate
PGN	perigeniculate nucleus
PSP	postsynaptic potential
RF	receptive field
RGC	retinal ganglion cell
RTD	response time difference
V1	primary visual cortex
V2	secondary visual cortex

Bibliography

Abeles, M. (1982). *Local Cortical Circuits.* Springer.

Ahmed, B., Anderson, J. A., Douglas, R. J., Martin, K. A. C., & Nelson, J. C. (1994). Polyneuronal innervation of spiny stellate neurons in cat visual cortex. *J. Comp. Neurol.*, 341, 39–49.

Albrecht, D. G. & Geisler, W. S. (1991). Motion selectivity and the contrast-response function of simple cells in the visual cortex. *Vis. Neurosci.*, 7, 531–546.

Allman, J., Miezin, F., & McGuinness, E. (1985). Direction- and velocity-specific responses from beyond the classical receptive field in the middle temporal visual area (MT). *Perception*, 14, 105–126.

Allman, J., Miezin, F., & McGuinness, E. (1990). The effects of background motion on the responses of neurons in the first and second cortical visual areas (V-I and V-II). In G. M. Edelman, W. E. Gall, & W. M. Cowan (Eds.), *Signal and Sense: Local and Global Order in Perceptual Maps* (pp. 131–141). New York: Wiley.

Alonso, J. M., Usrey, W. M., & Reid, R. C. (1996). Precisely correlated firing in cells of the lateral geniculate nucleus. *Nature*, 383, 815–819.

Bair, W. & Koch, C. (1996). Temporal precision of spike trains in extrastriate cortex of the behaving Macaque monkey. *Neural Comput.*, 8, 1185–1202.

Baker, F. H. & Malpeli, J. G. (1977). Effects of cryogenic blockade of visual cortex on the responses of lateral geniculate neurons in the monkey. *Exp. Brain. Res.*, 29, 433–444.

Bal, T., von Krosigk, M., & McCormick, D. A. (1995). Synaptic and membrane mechanisms underlying synchronized oscillations in the ferret LGNd in vitro. *J. Physiol. (Lond.)*, 483, 641–663.

Berezovskii, V. K. & Born, R. T. (2000). Specificity of projections from wide-field and local motion-processing regions within the middle temporal visual area of the owl monkey. *J. Neurosci.*, 20, 1157–1169.

Bloomfield, S. A. & Sherman, S. M. (1988). Postsynaptic potentials recorded in neurons of the cat's lateral geniculate nucleus following electrical stimulation of the optic chiasm. *J. Neurophysiol.*, 60, 1924–1945.

Bolger, C., Bojanic, S., Sheahan, N. F., Coakley, D., & Malone, J. F. (1999). Dominant frequency content of ocular microtremor from normal subjects. *Vision Res.*, 39, 1911–1915.

Born, R. T. & Tootell, R. B. H. (1992). Segregation of global and local motion processing in primate middle temporal visual area. *Nature*, 357, 497–499.

Braddick, O. J. (1993). Segmentation versus integration in visual motion processing. *Trends Neurosci.*, 16, 263–268.

Bradley, D. C., Maxwell, M., Andersen, R. A., Banks, M. S., & Shenoy, K. V. (1996). Neural mechanisms of heading perception in primate visual cortex. *Science*, 273, 1544–1547.

Bringuier, V., Fregnac, Y., Baranyi, A., Debanne, D., & Shulz, D. E. (1997). Synaptic origin and stimulus dependency of neuronal oscillatory activity in the primary visual cortex of the cat. *J. Physiol. (Lond.)*, 500, 751–774.

Büttner, U. & Henn, V. (1981). Circularvection: Psychophysics and single-unit recordings in the monkey. *Annals of the New York Academy of Science*, 374, 274–283.

Casanova, C. (1993). Responses of cells in cat's area 17 to random dot patterns: influence of stimulus size. *Neuroreport*, 4, 1011–1014.

Castelo-Branco, M., Neuenschwander, S., & Singer, W. (1998). Synchronization of visual responses between the cortex, lateral geniculate nucleus, and retina in the anesthetized cat. *J. Neurosci.*, 18, 6395–6410.

Cleland, B. G. (1983). Sensitivity to stationary flashing spots of the brisk classes of ganglion cells in the cat retina. *J. Physiol. (Lond.)*, 345, 15–26.

Cleland, B. G. & Harding, T. H. (1983). Response to the velocity of moving visual stimuli of the brisk classes of ganglion cells in the cat retina. *J. Physiol. (Lond.)*, 345, 47–63.

Cleland, B. G., Harding, T. H., & Tulunay-Keesey, U. (1979). Visual resolution and receptive field size: Examination of two kinds of cat retinal ganglion cell. *Science*, 205, 1015–1017.

Cleland, B. G., Harding, T. H., & Tulunay-Keesey, U. (1983). Response to the length of moving visual stimuli of the brisk classes of ganglion cells in the cat retina. *J. Physiol. (Lond.)*, 345, 27–45.

Clymer, A. B. (1973). *The effect of seen movement on the apparent speed of subsequent test velocities: Speed tuning of movement.* PhD thesis, Columbia University, NY.

Contreras, D., Dossi, R. C., & Steriade, M. (1993). Electrophysiological properties of cat reticular thalamic neurones in vivo. *J. Physiol. (Lond.)*, 470, 273–294.

Cox, C. L., Zhou, Q., & Sherman, S. M. (1998). Glutamate locally activates dendritic outputs of thalamic interneurons. *Nature*, 394, 478–482.

Crick, F. & Koch, C. (1998). Constraints on cortical and thalamic projections: The no-strong-loops hypothesis. *Nature*, 391, 245–250.

Crook, J. M., Kisvarday, Z. F., & Eysel, U. T. (1998). Evidence for a contribution of lateral inhibition to orientation tuning and direction selectivity in cat visual cortex: reversible inactivation of functionally characterized sites combined with neuroanatomical tracing techniques. *Eur. J. Neurosci.*, 10, 2056–2075.

Crowell, J. A., Banks, M. S., Shenoy, K. V., & Andersen, R. A. (1997). Self-motion path perception during head and body rotation. *Invest. Ophthalmol.*, 38, 481.

Crunelli, V. & Leresche, N. (1991). A role for gabab receptors in excitation and inhibition of thalamocortical cells. *Trends Neurosci.*, 14, 16–21.

DeAngelis, G. C., Ohzawa, I., & Freeman, R. D. (1993). Spatiotemporal organization of simple-cell receptive fields in the cat's striate cortex. II. Linearity of temporal and spatial summation. *J. Neurophysiol.*, 69, 1118–1135.

DeAngelis, G. C., Ohzawa, I., & Freeman, R. D. (1995). Receptive-field dynamics in the central visual pathways. *Trends Neurosci.*, 18, 451–458.

Douglas, R. J., Koch, C., Mahowald, M., Martin, K. A. C., & Suarez, H. H. (1995). Recurrent excitation in neocortical circuits. *Science*, 269, 981–985.

Eckhorn, R., Bauer, R., Jordan, W., Brosch, M., Kruse, W., Munk, M., & Reitboeck, H. J. (1988). Coherent oscillations: A mechanism of feature linking in the visual cortex? *Biological Cybernetics*, 60, 121–130.

Eifuku, S. & Wurtz, R. H. (1998). Response to motion in extrastriate area MSTl: Center-surround interactions. *J. Neurophysiol.*, 80, 282–296.

Eizenman, M., Hallett, P. E., & Frecker, R. C. (1985). Power spectra for ocular drift and tremor. *Vision Res.*, 25, 1635–1640.

Emerson, R. C. (1997). Quadrature subunits in directionally selective simple cells: spatiotemporal interactions. *Vis. Neurosci.*, 14, 357–371.

Emerson, R. C. & Huang, M. C. (1997). Quadrature subunits in directionally selective simple cells: counterphase and drifting grating responses. *Vis. Neurosci.*, 14, 373–385.

Engel, A. K., König, P., Kreiter, A. K., Schillen, T. B., & Singer, W. (1992). Temporal coding in the visual cortex: New vistas on integration in the nervous system. *Trends Neurosci.*, 15, 218–226.

Felleman, D. J. & van Essen, D. C. (1991). Distributed hierarchical processing in the primate cerebral cortex. *Cereb. Cortex*, 1, 1–47.

Ferster, D., Chung, S., & Wheat, H. (1996). Orientation selectivity of thalamic input to simple cells of cat visual cortex. *Nature*, 380, 249–252.

Field, D. J. (1994). What is the goal of sensory coding? *Neural Comput.*, 6, 559–601.

Funke, K. & Eysel, U. T. (1992). EEG-dependent modulation of response dynamics of cat dLGN relay cells and the contribution of corticogeniculate feedback. *Brain Res.*, 573, 217–227.

Geisert, E. E., Langsetmo, A., & Spear, P. D. (1981). Influence of the corticogeniculate pathway on response properties of cat lateral geniculate neurons. *Brain Res.*, 208, 409–415.

Gerstner, W. & van Hemmen, J. L. (1992). Associative memory in a network of 'spiking' neurons. *Network*, 3, 139–164.

Gerstner, W. & van Hemmen, J. L. (1994). Coding and information processing in neural networks. In E. Domany, J. L. van Hemmen, & K. Schulten (Eds.), *Models of neural networks II* (pp. 1–93). New York: Springer-Verlag.

Glees, P. & Clark, W. E. L. G. (1941). The termination of optic fibres in the lateral geniculate nucleus of the monkey. *J. Anat.*, 75, 295–308.

Godwin, D. W., Vaughan, J. W., & Sherman, S. M. (1996). Metabotropic glutamate receptors switch visual response mode of lateral geniculate nucleus cells from burst to tonic. *J. Neurophysiol.*, 76, 1800–1816.

Guido, W., Lu, S.-M., & Sherman, S. M. (1992). Relative contributions of burst and tonic responses to the receptive field properties of lateral geniculate neurons in the cat. *J. Neurophysiol.*, 68, 2199–2211.

Guido, W., Lu, S.-M., Vaughan, J. W., Godwin, D. W., & Sherman, S. M. (1995). Receiver operating characteristic (ROC) analysis of neurons in the cat's lateral geniculate nucleus during tonic and burst response mode. *Vis. Neurosci.*, 12, 723–741.

Guido, W. & Weyand, T. (1995). Burst responses in thalamic relay cells of the awake, behaving cat. *J. Neurophysiol.*, 74, 1782–1786.

Guillery, R. W. (1995). Anatomical evidence concerning the role of the thalamus in corticocortical communication: A brief review. *J. Anat.*, 187, 583–592.

Gulyas, B., Lagae, L., Eysel, U., & Orban, G. A. (1990). Corticofugal feedback influences the responses of geniculate neurons to moving stimuli. *Exp. Brain. Res.*, 79, 441–446.

Gulyas, B., Orban, G. A., Duysens, J., & Maes, H. (1987). The suppressive influence of moving textured backgrounds on responses of cat striate neurons to moving bars. *J. Neurophysiol.*, 57, 1767–1791.

Hammond, P. & MacKay, D. M. (1981). Modulatory influences of moving textured backgrounds on responsiveness of simple cells in feline striate cortex. *J. Physiol. (Lond.)*, 319, 431–442.

Hammond, P., Mouat, G. S., & Smith, A. T. (1988). Neural correlates of motion after-effects in cat striate cortical neurones: Monocular adaptation. *Exp. Brain. Res.*, 72, 1–20.

Hammond, P. & Pomfrett, C. J. (1990). Directionality of cat striate cortical neurones: Contribution of suppression. *Exp. Brain. Res.*, 81, 417–425.

Hamos, J. E., Van Horn, S. C., Raczkowski, D., Uhlrich, D. J., & Sherman, S. M. (1985). Synaptic connectivity of a local circuit neuron in lateral geniculate nucleus of the cat. *Nature*, 317, 618–621.

Hartveit, E. & Heggelund, P. (1990). Neurotransmitter receptors mediating excitatory input to cells in the cat lateral geniculate nucleus. II. Nonlagged cells. *J. Neurophysiol.*, 63, 1361–1372.

Hassenstein, B. & Reichardt, W. (1956). Systemtheoretische Analyse der Zeit-, Reihenfolgen- und Vorzeichenauswertung bei der Bewegungsperzeption des Rüsselkäfers *chlorophanus*. *Zeitschrift für Naturforschung*, 11 b, 513–524.

Heggelund, P. & Hartveit, E. (1990). Neurotransmitter receptors mediating excitatory input to cells in the cat lateral geniculate nucleus. I. Lagged cells. *J. Neurophysiol.*, 63, 1347–1360.

Hille, B. (1992). *Ionic channels of excitable membranes*. Sunderland, Massachusetts: Sinauer Associates Inc.

Hirsch, J. A., Alonso, J.-M., Reid, R. C., & Martinez, L. M. (1998). Synaptic integration in striate cortical simple cells. *J. Neurosci.*, 18, 9517–9528.

Hochstein, S. & Shapley, R. M. (1976a). Linear and nonlinear spatial subunits in Y cat retinal ganglion cells. *J. Physiol. (Lond.)*, 262, 265–284.

Hochstein, S. & Shapley, R. M. (1976b). Quantitative analysis of retinal ganglion cell classifications. *J. Physiol. (Lond.)*, 262, 237–264.

Hodgkin, A. L. & Huxley, A. F. (1952). A quantitative description of membrane current and its application to conduction and excitation in nerve. *J. Physiol. (Lond.)*, 117, 500–544.

Hoffmann, K.-P., Stone, J., & Sherman, S. M. (1972). Relay of receptive-field properties in dorsal lateral geniculate nucleus of the cat. *J. Neurophysiol.*, 35, 518–531.

Hubel, D. H. & Wiesel, T. N. (1961). Integrative action in the cat's lateral geniculate body. *J. Physiol. (Lond.)*, 155, 385–398.

Huguenard, J. R. & McCormick, D. A. (1992). Simulation of the currents involved in rythmic oscillations in thalamic relay neurons. *J. Neurophysiol.*, 68, 1373–1383.

Huguenard, J. R. & Prince, D. A. (1994). Intrathalamic rhythmicity studied in vitro: Nominal T current modulation causes robust anti-oscillatory effects. *J. Neurosci.*, 14, 5485–5502.

Humphrey, A. L. & Weller, R. E. (1988a). Functionally distinct groups of X-cells in the lateral geniculate nucleus of the cat. *J. Comp. Neurol.*, 268, 429–447.

Humphrey, A. L. & Weller, R. E. (1988b). Structural correlates of functionally distinct X-cells in the lateral geniculate nucleus of the cat. *J. Comp. Neurol.*, 268, 448–468.

Jagadeesh, B., Wheat, H. S., & Ferster, D. (1993). Linearity of summation of synaptic potentials underlying direction selectivity in simple cells of the cat visual cortex. *Science*, 262, 1901–1904.

Jagadeesh, B., Wheat, H. S., Kontsevich, L. L., Tyler, C. W., & Ferster, D. (1997). Direction selectivity of synaptic potentials in simple cells of the cat visual cortex. *J. Neurophysiol.*, 78, 2772–2789.

Jahnsen, H. & Llinás, R. (1984a). Electrophysiological properties of guinea-pig thalamic neurons: An *in vitro* study. *J. Physiol. (Lond.)*, 349, 205–226.

Jahnsen, H. & Llinás, R. (1984b). Ionic basis for the electroresponsiveness and oscillatory properties of guinea-pig thalamic neurons *in vitro*. *J. Physiol. (Lond.)*, 349, 227–247.

Johansson, G. (1973). Visual perception of biological motion and a model for its analysis. *Perceptual Psychophysics*, 14, 201–211.

Jones, E. G. (1985). *The Thalamus.* New York: Plenum Press.

Julesz, B. (1971). *Foundations of Cyclopean Perception.* Chicago: University of Chicago Press.

Kalil, R. E. & Chase, R. (1970). Corticofugal influence on activity of lateral geniculate neurons in the cat. *J. Neurophysiol.*, 33, 459–474.

Katz, L. C. (1987). Local circuitry of identified projection neurons in cat visual cortex brain slices. *J. Neurosci.*, 7, 1223–1249.

Kaufman, L. (1974). *Sight and mind, an introduction to visual perception.* New York: Oxford University Press.

Kim, J. & Wilson, H. R. (1993). Dependence of plaid motion coherence on component grating directions. *Vision Res.*, 33, 2479–2489.

Kistler, W. M., Gerstner, W., & van Hemmen, J. L. (1997). Reduction of the Hodgkin-Huxley equations to a single-variable threshold model. *Neural Comput.*, 9, 1015–1045.

Koch, C. (1987). The action of the corticofugal pathway on sensory thalamic nuclei: A hypothesis. *Neurosci.*, 23, 399–406.

Koffka, K. (1935). *Principles of Gestalt Psychology.* New York: Harcourt, Brace & World.

Komatsu, H. & Wurtz, R. H. (1988). Relation of cortical areas MT and MST to pursuit eye movements. I. Localization and visual properties of neurons. *J. Neurophysiol.*, 60, 580–603.

Kontsevich, L. L. (1995). The nature of the inputs to cortical motion detectors. *Vision Res.*, 35, 2785–2793.

Krauzlis, R. J. (1994). The visual drive for smooth eye movements. In A. T. Smith & R. J. Snowden (Eds.), *Visual detection of motion* (pp. 437–473). Academic Press.

Kwon, Y. H., Esguerra, M., & Sur, M. (1991). NMDA and non-NMDA receptors mediate visual responses of neurons in the cat's lateral geniculate nucleus. *J. Neurophysiol.*, 66, 414–428.

Lamme, V. A. F., Supèr, H., & Spekreijse, H. (1998). Feedforward, horizontal, and feedback processing in the visual cortex. *Curr. Opinion Neurobiol.*, 8, 529–535.

Li, C. Y., Lei, J. J., & Yao, H. S. (1999). Shift in speed selectivity of visual cortical neurons: A neural basis of perceived motion contrast. *Proc. Natl. Acad. Sci. USA*, 96, 4052–4056.

Li, C. Y. & Li, W. (1994). Extensive integration field beyond the classical receptive field of cat's striate cortical neurons – classification and tuning properties. *Vision Res.*, 34, 2337–2355.

Livingstone, M. S. & Hubel, D. H. (1981). Effects of sleep and arousal on the processing of visual information in the cat. *Nature*, 291, 554–561.

Lo, F. S. & Sherman, S. M. (1994). Feedback inhibition in the cat's lateral geniculate nucleus. *Exp. Brain. Res.*, 100, 365–368.

Lu, S.-M., Guido, W., & Sherman, S. M. (1992). Effects of membrane voltage on receptive field properties of lateral geniculate neurons in the cat: Contributions of the low-treshold Ca^{2+} conductance. *J. Neurophysiol.*, 68, 2185–2198.

Maex, R. & Orban, G. A. (1996). Model circuit of spiking neurons generating directional selectivity in simple cells. *J. Neurophysiol.*, 75, 1515–1545.

Mastronarde, D. N. (1987a). Two classes of single-input X-cells in cat lateral geniculate nucleus. I. Receptive-field properties and classification of cells. *J. Neurophysiol.*, 57, 357–380.

Mastronarde, D. N. (1987b). Two classes of single-input X-cells in cat lateral geniculate nucleus. II. Retinal inputs and the generation of receptive-field properties. *J. Neurophysiol.*, 57, 381–413.

Mastronarde, D. N., Humphrey, A. L., & Saul, A. B. (1991). Lagged Y-cells in the cat lateral geniculate nucleus. *Vis. Neurosci.*, 7, 191–200.

McCarley, R. W., Benoit, O., & Barrionuevo, G. (1983). Lateral geniculate nucleus unitary discharge in sleep and waking: State- and rate-specific aspects. *J. Neurophysiol.*, 50, 798–818.

McClurkin, J. W. & Marrocco, R. T. (1984). Visual cortical input alters spatial tuning in monkey lateral geniculate nucleus cells. *J. Physiol. (Lond.)*, 348, 135–152.

McClurkin, J. W., Optican, L. M., & Richmond, B. J. (1994). Cortical feedback increases visual information transmitted by monkey parvocellular lateral geniculate nucleus neurons. *Vis. Neurosci.*, 11, 601–617.

McCormick, D. A. (1992). Neurostransmitter actions in the thalamus and cerebral cortex and their role in neuromodulation of thalamocortical activity. *Prog. Neurobiol.*, 39, 337–388.

McCormick, D. A. & Feeser, H. R. (1990). Functional implications of burst firing and single spike activity in lateral geniculate relay neurons. *Neuroscience*, 39, 103–113.

McCormick, D. A. & Huguenard, J. R. (1992). A model of the electrophysiological properties of thalamocortical relay neurons. *J. Neurophysiol.*, 68, 1384–1400.

McCormick, D. A. & von Krosigk, M. (1992). Corticothalamic activation modulates thalamic firing through glutamate "metabotropic" receptors. *Proc. Natl. Acad. Sci. USA*, 89, 2774–2778.

McLean, J. & Palmer, L. A. (1989). Contribution of linear spatiotemporal receptive field structure to velocity selectivity of simple cells in area 17 of the cat. *Vision Res.*, 29, 675–679.

McLean, J., Raab, S., & Palmer, L. A. (1994). Contribution of linear meachanisms to the specification of local motion by simple cells in areas 17 and 18 of the cat. *Vis. Neurosci.*, 11, 295–306.

Miller, R. (1996). Cortico-thalamic interplay and the security of operation of neural assemblies and temporal chains in the cerebral cortex. *Biol. Cybern.*, 75, 263–275.

Mineiro, P. & Zipser, D. (1998). Analysis of direction selectivity arising from recurrent cortical interactions. *Neural Comput.*, 10, 353–371.

Movshon, J. A. (1975). The velocity tuning of single units in cat striate cortex. *J. Physiol. (Lond.)*, 249, 445–468.

Mukherjee, P. & Kaplan, E. (1995). Dynamics of neurons in the cat lateral geniculate nucleus: In vivo electrophysiology and computational modeling. *J. Neurophysiol.*, 74, 1222–1243.

Mukherjee, P. & Kaplan, E. (1998). The maintained discharge of neurons in the cat lateral geniculate nucleus: Spectral analysis and computational modeling. *Vis. Neurosci.*, 15, 529–539.

Murakami, I. & Cavanagh, P. (1998). A jitter after-effect reveals motion-based stabilization of vision. *Nature*, 395, 798–801.

Murthy, A. & Humphrey, A. L. (1999). Inhibitory contributions to spatiotemporal receptive-field structure and direction selectivity in simple cells of cat area 17. *J. Neurophysiol.*, 81, 1212–1224.

Murthy, A., Humphrey, A. L., Saul, A. B., & Feidler, J. C. (1998). Laminar differences in the spatiotemporal structure of simple cell receptive fields in cat area 17. *Vis. Neurosci.*, 15, 239–256.

Nakayama, K. (1985). Biological image motion processing: A review. *Vision Res.*, 25, 625–660.

Nieuwenhuys, R., Voogd, J., & van Huijzen, C. (1988). *The Human Central Nervous System*. Berlin Heidelberg: Springer-Verlag.

Orban, G. A., Kennedy, H., & Maes, H. (1981a). Response to movement of neurons in areas 17 and 18 of the cat: Direction selectivity. *J. Neurophysiol.*, 45, 1059–1073.

Orban, G. A., Kennedy, H., & Maes, H. (1981b). Response to movement of neurons in areas 17 and 18 of the cat: Velocity sensitivity. *J. Neurophysiol.*, 45, 1043–1058.

Pape, H. C., Budde, T., Mager, R., & Kisvarday, Z. F. (1994). Prevention of Ca(2+)-mediated action potentials in GABAergic local circuit neurones of rat thalamus by a transient K+ current. *J. Physiol. (Lond.)*, 478, 403–422.

Peterhans, E. (1997). Functional organization of area V2 in the awake monkey. In J. H. Kaas, K. Rockland, & A. Peters (Eds.), *Cerebral Cortex*, volume 12 (pp. 335–357). New York: Plenum Press.

Peterhans, E. & Baumann, R. (1994). Elements of form processing from motion in monkey prestriate cortex. *Soc. Neurosci. Abstr.*, 20, 1053.

Qian, N. & Andersen, R. A. (1994). Transparent motion perception as unbalanced signals: II. Physiology. *J. Neurosci.*, 14, 7367–7380.

Reid, R. C. & Alonso, J. M. (1995). Specificity of monosynaptic connections from thalamus to visual cortex. *Nature*, 378, 281–284.

Reid, R. C., Soodak, R. E., & Shapley, R. M. (1991). Directional selectivity and spatiotemporal structure of receptive fields of simple cells in cat striate cortex. *J. Neurophysiol.*, 66, 505–529.

Reinagel, P., Godwin, D., Sherman, S. M., & Koch, C. (1999). Encoding of visual information by LGN bursts. *J. Neurophysiol.*, 81, 2558–2569.

Richard, D., Gioanni, Y., Kitsikis, A., & Buser, P. (1975). A study of geniculate unit activity during cryogenic blockade of the primary visual cortex in the cat. *Exp. Brain. Res.*, 22, 235–242.

Ringach, D. L., Hawken, M. J., & Shapley, R. (1997). Dynamics of orientation tuning in macaque primary visual-cortex. *Nature*, 387, 281–284.

Royden, C. S., Crowell, J. A., & Banks, M. K. S. (1994). Estimating heading during eye movements. *Vision Res.*, 34, 3197–3214.

Saul, A. B. & Humphrey, A. L. (1990). Spatial and temporal response properties of lagged and nonlagged cells in the cat lateral genicualte nucleus. *J. Neurophysiol.*, 64, 206–224.

Saul, A. B. & Humphrey, A. L. (1992a). Evidence of input from lagged cells in the lateral geniculate nucleus to simple cells in cortical area 17 of the cat. *J. Neurophysiol.*, 68, 1190–1207.

Saul, A. B. & Humphrey, A. L. (1992b). Temporal-frequency tuning of direction selectivity in cat visual cortex. *Vis. Neurosci.*, 8, 365–372.

Schmielau, F. & Singer, W. (1977). The role of visual cortex for binocular interactions in the cat lateral geniculate nucleus. *Brain Res.*, 120, 354–361.

Schrater, P. R. & Simoncelli, E. P. (1998). Local velocity representation: Evidence from motion adaptation. *Vision Res.*, 38, 3899–3912.

Sherman, S. M. (1996). Dual response modes in lateral geniculate neurons: Mechanisms and functions. *Vis. Neurosci.*, 13, 205–213.

Sherman, S. M. & Guillery, R. W. (1996). Functional organization of thalamocortical relays. *J. Neurophysiol.*, 76, 1367–1395.

Sherman, S. M. & Koch, C. (1986). The control of retinogeniculate transmission in the mammalian lateral geniculate nucleus. *Exp. Brain. Res.*, 63, 1–20.

Sherman, S. M. & Koch, C. (1990). Thalamus. In G. M. Shepherd (Ed.), *The synaptic organization of the brain* (pp. 246–278). Oxford University Press.

Sillito, A. M., Jones, H. E., Gerstein, G. L., & West, D. C. (1994). Feature-linked synchronization of thalamic relay cell firing induced by feedback from the visual cortex. *Nature*, 369, 479–482.

Singer, W. (1994). A new job for the thalamus. *Nature*, 369, 444–445.

Smith, A. T. & Edgar, G. K. (1994). Antagonistic comparison of temporal frequency filter outputs as a basis for speed perception. *Vision Res.*, 34, 253–265.

Snowden, R. J., Treue, T., Erickson, R. G., & Andersen, R. A. (1991). The response of area MT and V1 neurons to transparent motion. *J. Neurosci.*, 11, 2768–2785.

Spauschus, A., Marsden, J., Halliday, D. M., Rosenberg, J. R., & Brown, P. (1999). The origin of ocular microtremor in man. *Exp. Brain Res.*, 126, 556–562.

Steriade, M. (1992). Basic mechanisms of sleep generation. *Neurology*, 42, 9–18.

Steriade, M. & Contreras, D. (1995). Relations between cortical and thalamic cellular events during transition from sleep patterns to paroxysmal activity. *J. Neurosci.*, 15, 623–642.

Steriade, M. & Llinás, R. (1988). The functional states of the thalamus and the associated neuronal interplay. *Physiol. Rev.*, 68, 649–742.

Steriade, M. & McCarley, R. W. (1990). *Brainstem Control of Wakefulness and Sleep*. New York: Plenum Press.

Steriade, M., McCormick, D. A., & Sejnowski, T. J. (1993). Thalamocortical oscillations in the sleeping and aroused brain. *Science*, 262, 679–685.

Stoner, G. R. & Albright, T. D. (1993). Image segmentation cues in motion processing: Implications for modularity in vision. *J. Cog. Neurosci.*, 5, 129–149.

Stratford, K. J., Tarczy-Hornoch, K., Martin, K. A., Bannister, N. J., & Jack, J. J. (1996). Excitatory synaptic inputs to spiny stellate cells in cat visual cortex. *Nature*, 382, 258–261.

Straube, A. & Brandt, T. (1987). Importance of the visual and vestibular cortex for self-motion perception in man (circularvection). *Human Neurobiol.*, 6, 211–218.

Suarez, H., Koch, C., & Douglas, R. (1995). Modeling direction selectivity of simple cells in striate visual cortex within the framework of the canonical microcircuit. *J. Neurosci.*, 15, 6700–6719.

Tanaka, K., Hikosaka, K., Saito, H., Yukie, M., Fukada, Y., & Iwai, E. (1986). Analysis of local and wide-field movements in the superior temporal visual areas of the macaque monkey. *J. Neurosci.*, 6, 134–144.

Tanaka, K., Sugita, Y., Moriya, M., & Saito, H. (1993). Analysis of object motion in the ventral part of the medial superior temporal area of the macaque visual cortex. *J. Neurophysiol.*, 69, 128–142.

Tolhurst, D. J. & Heeger, D. J. (1997). Comparison of contrast-normalization and threshold models of the responses of simple cells in cat striate cortex. *Vis. Neurosci.*, 14, 293–309.

Toth, L. J., Kim, D. S., Rao, S. C., & Sur, M. (1997). Integration of local inputs in visual cortex. *Cereb. Cortex*, 7, 703–710.

Tsumoto, T., Creutzfeldt, O. D., & Legendy, C. R. (1978). Functional organization of the corticofugal system from visual cortex to lateral geniculate nucleus in the cat (with an appendix on geniculo-cortical mono-synaptic connections). *Exp. Brain. Res.*, 32, 345–364.

Tsumoto, T. & Suda, K. (1980). Three groups of cortico-geniculate neurons and their distribution in binocular and monocular segments of cat striate cortex. *J. Comp. Neurol.*, 193, 223–236.

Tuckwell, H. C. (1988a). *Introduction to theoretical neurobiology, Volume 1: Linear cable theory and dendritic structure.* Cambridge: Cambridge University Press.

Tuckwell, H. C. (1988b). *Introduction to theoretical neurobiology, Volume 2: Nonlinear and stochastic theories.* Cambridge: Cambridge University Press.

Valois, R. L. D. & Cottaris, N. P. (1998). Inputs to directionally selective simple cells in macaque striate cortex. *Proc. Natl. Acad. Sci. USA*, 95, 14488–14493.

Van Essen, D. C. & Anderson, C. H. (1990). Reference frames and dynamic remapping processes in vision. In E. L. Schwartz (Ed.), *Computational Neuroscience* (pp. 278–294). A Bradford Book, MIT Press.

von der Malsburg, C. (1981). *The correlation theory of brain function.* Technical Report 81-2, Max-Planck-Institute for Biophysical Chemistry.

von der Malsburg, C. (1986). Am I thinking assemblies? In G. Palm & A. Aertsen (Eds.), *Proceedings of the Trieste Meeting on Brain Theory* (pp. 161–176). Berlin, Heidelberg: Springer.

von Krosigk, M., Monckton, J. E., Reiner, P. B., & McCormick, D. A. (1999). Dynamic properties of corticothalamic excitatory postsynaptic potentials and thalamic reticular inhibitory postsynaptic potentials in thalamocortical neurons of the guinea-pig dorsal lateral geniculate nucleus. *Neurosci.*, 91, 7–20.

Watamaniuk, S. N., Grzywacz, N. M., & Yuille, A. L. (1993). Dependence of speed and direction perception on cinematogram dot density. *Vision Res.*, 33, 849–859.

Watamaniuk, S. N., Sekuler, R., & Williams, D. W. (1989). Direction perception in complex dynamic displays: The integration of direction information. *Vision Res.*, 29, 47–59.

Wertheimer, M. (1923). Untersuchungen zur Lehre von der Gestalt, II. *Psychologische Forschung*, 4, 310–350.

Wertheimer, M. (1958). Principles of perceptual organization. In D. C. Beardslee & M. Wertheimer (Eds.), *Readings in Perception* (pp. 115–135). Princeton, NJ: van Nostrand.

Wimbauer, S., Wenisch, O. G., Miller, K. D., & van Hemmen, J. L. (1997a). Development of spatiotemporal receptive fields of simple cells: I. Model formulation. *Biol. Cybern.*, 77, 453–461.

Wimbauer, S., Wenisch, O. G., van Hemmen, J. L., & Miller, K. D. (1997b). Development of spatiotemporal receptive fields of simple cells: II. Simulation and analysis. *Biol. Cybern.*, 77, 463–477.

Wörgötter, F., Suder, K., Zhao, Y., Kerscher, N., Eysel, U. T., & Funke, K. (1998). State-dependent receptive-field restructuring in the visual cortex. *Nature*, 396, 165–168.

Zeki, S. (1993). *A Vision of the Brain.* Oxford: Blackwell Scientific.

Zeki, S. & Shipp, S. (1988). The functional logic of cortical connections. *Nature*, 335, 311–317.

Zemel, R. S. & Sejnowski, T. J. (1998). A model for encoding multiple object motions and self-motion in area MST of primate visual cortex. *J. Neurosci.*, 18, 531–547.

Zhan, X. J., Cox, C. L., Rinzel, J., & Sherman, S. M. (1999). Current clamp and modeling studies of low-threshold calcium spikes in cells of the cat's lateral geniculate nucleus. *J. Neurophysiol.*, 81, 2360–2373.